University of Southampton

Faculty of Engineering and the Environment

Engineering Sciences Unit

Study of Fatigue Crack Initiation and Propagation Mechanisms in an Advanced Ni-based Superalloy: Effects of Microstructures and Oxidation

By

Rong Jiang

Thesis for the degree of Doctor of Philosophy

April 2015

UNIVERSITY OF SOUTHAMPTON

ABSTRACT

FACULTY OF ENGINEERING AND THE ENVIRONMENT
ENGINEERING SCIENCES UNIT

Doctor of Philosophy

Study of Fatigue Crack Initiation and Propagation Mechanisms in an Advanced Ni-based Superalloy: Effects of Microstructures and Oxidation

By Rong Jiang

Low Solvus, High Refractory (LSHR) alloy is a latest generation of turbine disc alloy which contains relatively high Co and Cr levels compared with incumbent alloys, this provides a low solvus temperature for enhanced high temperature processing versatility, and the alloy is designed to operate at higher temperatures to achieve higher thrust-to-weight ratio and higher fuel efficiency. Understanding the fatigue performance of the LSHR alloy along with the coupled influences of deformation and oxidation damage is important for both its practical application and in further development of turbine disc alloys.

Short crack tests have been conducted on coarse grained (CG) and fine grained (FG) LSHR alloys by uninterrupted and interrupted three-point bending with a replication procedure at room temperature, 650 and 725 ^{o}C in air and vacuum under a sine waveform (20Hz) and/or 1-1-1-1 trapezoidal waveform to investigate fatigue crack initiation and early propagation. The results show that fatigue lives in the LSHR alloy are shortened by high temperature, high oxygen partial pressure and low frequency loading waveforms which are associated with more intergranular fracture mechanisms. At room temperature, where the effect of oxidation is absent, twin boundary (TB) cracking in relatively large grains dominates the crack initiation process along with occasional crack initiation due to slip band cracking. Activation of the primary slip systems parallel to the TB at matrix and twin and high resolved shear stress associated with high Schmid factor (SF) are required for TB crack initiation. Cracks preferentially propagate along slip bands associated with high SF slip systems after initiation. But cracks also propagate along slip bands associated with slip systems with lower SF if the inclination angle between the slip band ahead of the crack tip and the crack segment of the crack tip is small enough to enable a steady transition (or non-deflected growth) of cracks across the grain boundary (GB).

At elevated temperatures (i.e. 650 and 725 ^{o}C), fatigue crack initiation and early short crack propagation behaviour are closely related to coupled deformation-oxidation damages. Plentiful crack initiation mainly occurs at GBs and/or γ/γ′ interfaces (in the FG variant) with bulged Ni/Co-rich oxides and Cr/Ti/Al oxide intrusion due to oxide cracking. Cracks subsequently propagate along oxidised GBs at the surface and exhibit significant crack coalescence in the final stages of fatigue life. In terms of crack propagation in the depth direction, this is a consequence of the competing effects between mechanically-driven and oxidation-assisted crack propagation, and exhibits transgranular or intergranular or mixed inter-transgranular propagation.

Formation of bulged Ni/Co-rich oxides and Cr/Ti/Al oxide intrusion along grain boundaries is accompanied by dissolution of γ′ precipitates, and is closely related to the strain localisation which is associated with grain orientation and applied stress. The boundaries of high/low SF grains are preferential sites for bulged Ni/Co-rich oxides and Cr/Ti/Al oxide intrusion formation. Strain-assisted formation of internal GB Cr/Ti/Al oxide intrusion can facilitate coupled formation of GB bulged Ni/Co-rich oxides by providing abundant Ni and Co. Apart from the significant oxidation at grain boundaries and γ/γ′ interfaces, uniform surface oxide scale along with internal Al oxide particles form within grains and primary γ′.

Studies of long fatigue crack growth (FCG) behaviour in LSHR alloy at 650 and 725 ^{o}C in air and vacuum under trapezoidal waveforms of 1-1-1-1 and 1-20-1-1 indicate that a CG structure possesses better FCG resistance due to the enhanced slip reversibility promoted by planar slip as well as the reduction in grain boundary area. The fatigue performance of the LSHR alloy is significantly degraded by the synergistic oxidation effect brought about by high temperature, high oxygen partial pressure and dwell at the peak load, associated with increasingly intergranular fracture features and secondary grain boundary cracking. Secondary cracks are observed to be blocked or deflected around primary γ′, carbides and borides, and their occurrence closely relates to the roughness of the fracture surface, FCG rate and grain boundary oxidation. The apparent activation energy analysis provides a further insight into the underlying mechanism of the FCG under dwell-fatigue testing conditions, and confirms that oxidation fatigue is the dominant process contributing to the intergranular failure process. At high enough crack growth rates and at lower temperatures, mechanically-driven fatigue crack growth processes can outstrip crack-tip oxidation processes.

Table of contents

List of tables

List of figures

Declaration of Authorship

I, **Rong Jiang**, declare that the thesis entitled

Study of Fatigue Crack Initiation and Propagation Mechanisms in an Advanced Ni-based Superalloy: Effects of Microstructures and Oxidation

and the work presented in the thesis are both my own, and have been generated by me as the result of my original research. I confirm that:

- this work was done wholly or mainly while in candidature for a research degree at this University;
- where any part of this thesis has previously been submitted for a degree or any other qualification at this University or any other institution, it has been clearly stated;
- where I have consulted the published work of others, it has been clearly attributed;
- where the thesis is based on work done by myself jointly with others, I have made clear exactly what was done by others and what I have contributed myself;
- parts of this work have been published as:

S. Everitt, R. Jiang, N. Gao, M. J. Starink, J. W. Brooks and P. A. S. Reed, Comparison of fatigue crack propagation behaviour in two gas turbine disc alloys under creep–fatigue conditions: evaluating microstructure, environment and temperature effects, Materials Science and Technology 29 (2013): 781-787

R. Jiang, S. Everitt, M. Lewandowski, N. Gao, and P. A. S. Reed, Grain size effects in a Ni-based turbine disc alloy in the time and cycle dependent crack growth regimes, International Journal of Fatigue 62 (2014): 217-227.

R. Jiang, S. Everitt, N. Gao, K. Soady, J. W. Brooks, and P. A. S. Reed, Influence of oxidation on fatigue crack initiation and propagation in turbine disc alloy N18, International Journal of Fatigue 75 (2015): 89-99.

R. Jiang, N. Gao, and P. A. S. Reed, Influence of orientation-dependent grain boundary oxidation on fatigue cracking behaviour in an advanced Ni-based superalloy, Journal of Materials Sciences 50 (2015): 4379-4386.

F. Farukh, L. G. Zhao, R. Jiang, P. A. S. Reed, D. Proprentner, B. A. Shollock, Fatigue crack growth in a Nickel-based superalloy at elevated temperature - experimental studies, viscoplasticity modelling and XFEM predictions, Mechanics of Advanced Materials and Modern Processes 1 (2015), 1-13.

R. Jiang, N. Karpasitis, N. Gao, P. A. S. Reed, Effects of microstructures on fatigue crack initiation and short crack propagation at room temperature in an advanced disc superalloy, submitted to Materials Sciences and Engineering A (2015), accepted.

D. Proprentner, R. Jiang, F. Farukh, P. A. S. Reed, L. G. Zhao, B. A. Shollock, Fatigue Crack Propagation and the Role of Oxidation Ahead of the Crack Tip in an Advanced Ni-based Superalloy, Submitted to Internal Journal of Fatigue (2015), under revision.

Sign:

Date:

Acknowledgement

There are a great many people I wish to thank for their help either in my research programme or daily life. I would never be able to go so far and get this thesis done without their kindness and support.

First and foremost I would like to thank my supervisors at the University of Southampton to whom I am greatly indebted, Prof. Philippa Reed and Dr. Nong Gao, for their continuous patience, support and guidance over the last four years. They have both contributed a great deal to my development both as a researcher and as a person and for that I will be forever grateful. Prof. Ian Sinclair, the examiner of my 9-month report and transfer report, who inspired me to think broadly and deeply in my research programme, is greatly thanked.

I would also like to thank Dr. Shuncai Wang at the University of Southampton for training me on SEM and TEM, and Dr. John Walker at the University of Southampton for his assistance in TEM sample preparation. Dr. Michael Ward and Dr. Zabeada Aslam at the University of Leeds are acknowledged for their assistance in FIB-TEM-EDX analysis. Dr. Geoff West at Loughborough University is thanked for his help with EBSD characterisation.

I am also indebted to Michael Lewandowski and Dr. Andy Robinson at the University of Southampton, for teaching me how to use the Instron servo-hydraulic testing machine. Dave Beckett is highly thanked for his help in metallography and maintenance for the heating and vacuum systems attached to Instron testing machine. Without these help and support, my experimental work would have been even more challenging. I must also thank Binyan He and Angelos Evangelou at the University of Southampton for their help in fatigue tests and the helpful discussion and suggestions in terms of the experimental results analysis. Dr. Kath Soady is greatly thanked for her assistance when I embarked on the finite element simulation using Abaqus. Chao You, Yikun Wang and Haibin Zhu who helped me come over the problems I encountered during FE simulation are greatly acknowledged. I also have to thank the project students, who helped conduct the experiments and collect some of the data which have gone into writing this thesis: Ross Downer, Nick Karpasitis and Richard Whitehouse. I am appreciated for your efforts.

I am grateful for the supports provided by Peter Sellen and Chris Williams in fatigue sample preparation. I would also like to thank the administrative staff, particularly Sue Berger, for their frequent help. I would like to thank all my fellow students and friends in the Engineering Materials Research Group, who made my time at the University enjoyable by giving me welcome distractions from work, but of course also for helping me out with my research.

The University of Southampton, UK, Engineering and Physical Science Research Council, UK, and the China Scholarship Council, China are acknowledged for their financial support. NASA (particularly Dr. Tim Gabb) is thanked for supplying the LSHR alloy used in this study.

Finally, to my parents and sister who have always been supporting and encouraging me to confront all kinds of challenges, I will always be thankful for your love which pushed me on and helped shape the person I am today.

Nomenclature

AIM	Alicona Infinitefocus Microscopy
AOI	Areas of interest
APB	Anti-phase boundary
CG	Coarse grained
CRSS	Critical resolved shear stress
CSL	Coincidence site lattice
CTOD	Crack tip opening displacement
DCPD	Direct current potential drop
DIC	Digital image correlation
EBSD	Electron backscatter diffraction
EDX	Energy dispersive X-ray spectrometry
EPFM	Elastic-plastic fracture mechanics
ESR	Electro-slag remelting
fcc	Face centred cubic
FCG	Fatigue crack growth
FEG-SEM	Field emission gun scanning electron microscope
FG	Fine grained
FIB	Focus ion beam
GB	Grain boundary
GBE	Grain boundary engineering
HCF	High cycle fatigue
HIP	Hot isostatic pressing
LCF	Low-cycle fatigue
LEFM	Linear elastic fracture mechanics
LSHR	Low Solvus, High Refractory
NDT	Non-destructive testing
OM	Optical microscope
PBB	Plain bend bar
PBR	Pilling-Bedworth ratio
P/M	Powder metallurgy

PSB	Persistent slip band
SAGBO	Stress assisted grain boundary oxidation
SF	Schmid factor
SFE	Stacking fault energy
SIMS	Secondary ion mass spectrometry
TB	Twin boundary
TEM	Transmission electron microscope
VAR	Vacuum arc remelting
VIM	Vacuum induced melting
3D	Three dimensions

a	Crack depth at the notch root
a_M	Activity of the element M in the Ni-based superalloy
a_{MxOy}	Activity of oxide M_xO_y
a_{tran}	Transition crack lengths (from Stage I to Stage II type cracking)
b	Burgers vector
b	Width of samples
c	Half crack length at notch root surface
da/dN	Fatigue crack growth rate
f	Volume fraction of precipitates
f	Loading frequency
$f(W_p)$	Inelastic strain energy density
$\boldsymbol{g}$	Rotation matrix connecting the sample coordinates and crystal coordinates
l^{ε}	Slip direction for the slip system ε
m	Mole mass of oxide M_xO_y
n^{ε}	Slip plane normal for the slip system ε
n_m	strain hardening exponent
r	*R*adius of precipitate
$r_{p,cyclic}$	Cyclic plastic zone size
$r_{p,momotonic}$	Monotonic plastice zone size
v	Poisson ratio
w	Strain-energy density
w	Sample thickness

A	Surface area of the oxide nuclei
A'	Constant depending on materials
B_w	Correction factor for the finite dimension of the investigated specimens
D	Diffusion coefficient
D_g	Grain boundary diffusivity
E	Young's modulus
E_{app}	Apparent activation energy
$E(K)$	Elliptic integral of the second kind.
G	Shear modulus
ΔG	Overall Gibbs free energy change for oxide nucleation
ΔG_0	Standard Gibbs free energy of formation of M_xO_y
ΔG_f	Gibbs free energy of formation of M_xO_y
ΔG_V	Free energy for the formation of per unit volume of oxide
G_S	Strain energy as a consequence of the volume change due to oxide nucleation
ΔG_ε	Strain energy due to deformation brought about by cyclic loading
J	Non-linear elastic energy release rate
ΔJ	J integral range
L_{crystal}	Loading direction written in crystal coordinates
L_{sample}	Loading direction written in sample coordinates
K	Stress intensity factor
ΔK	Stress intensity factor range
$K_{closure}$	Crack closure stress intensity factor
ΔK_{eff}	Effective stress intensity factor range
K_{max}	Maximum applied stress intensity factor
ΔK_{th}	Threshold stress intensity factor range
$M_{f(\frac{\pi}{2})}$	Front face correction factor for crack shape
N	Loading cycle
N_f	Fatigue lifetime
P_{O2}	Oxygen partial pressure
Q	Activation energy
Q_g	Activation energy of GB diffusion in the strain/stress-free state
Q'_g	Effective activation energy of GB diffusion for strained/stressed state
R	Load ratio

R_a	Average roughness
R_g	Gas constant (8.31 J/mol K)
V	Volume of oxide nuclei
$Z_{crystal}$	Direction perpendicular to specimen surface written in crystal coordinates
α	Angle between a slip trace and the loading direction
α_c	Calculated inclination angle between the possible slip traces of the {111} slip planes and the tensile stress axis
α_m	Measured inclination angles between the main crack segment and tensile stress axis within each crack-initiating grain
β	Calculated inclined angle between the tensile stress axis and the slip trace corresponding to the slip system with highest SF
γ	Interface energy due to oxide nucleation
γ_{APB}	Anti-phase boundary energy
δ_t	Crack tip opening displacement
σ_0	Mean stress
σ_a	Stress amplitude
σ_{max}	Maximum stress
σ_{min}	Minimum stress
σ'_f	Fatigue strength coefficient
σ_y	Yield strength
$\Delta\sigma$	Stress range
ε_0	Mean strain
ε_a	Strain amplitude
ε_{max}	Maximum strain
ε_{min}	Minimum strain
$\Delta\varepsilon$	Strain range
ε'_f	Fatigue ductility coefficient
τ_c	Critical resolved shear stress for precipitate-cutting by dislocations
μ_c	Calculated SF for active primary slip system associated with crack initiation
μ_h	Highest SF in the crack- initiating grains
ρ	Density of oxide M_xO_y
$\varphi_1, \emptyset, \varphi_2$	Euler angles

Chapter 1 Introduction

1.1 Research background

Gas turbine engines, which are responsible for converting the chemical energy of fuel to thrust, are a critical component for a modern aircraft. Since the gas turbine engine was developed, great improvements in engine efficiency have been achieved due to advances in engine design, development of advanced materials and related material manufacture and processing techniques. The operating temperatures and pressures for gas turbine engines have increased significantly in the past half century, and continuing efforts are still being made to enhance the operating temperature of the gas turbine engine, particularly the turbine entrance temperature, to further improve the engine efficiency and thrust-to-weight ratio as well as to reduce the emission of green-house gases. This increased turbine entrance temperature means higher operating temperatures for turbine blades and discs, producing more stringent requirements for the high temperature mechanical properties and oxidation/corrosion resistance of the materials used in these areas [1, 2].

A turbine disc is one of the most safety-critical components in a gas turbine engine due to its harsh operating conditions. The alternating load at intermediate temperatures (400~750^{o}C) coupled with the aggressive environment usually causes combined damage arising from fatigue, creep and oxidation of the disc during the course of service [3, 4]. The temperature gradient across the disc from rim to bore requires location specific properties of the disc materials to optimise the overall fatigue-creep-oxidation performance, which in turn demands that the disc materials should possess good processing versatility so that the microstructures of the disc materials can be properly tailored to meet such requirements [5, 6].

Polycrystalline Ni-based superalloys have been widely used for disc materials due to their excellent combined properties, i.e. high strength at elevated temperatures, good resistance to fatigue, creep, oxidation and corrosion [1]. Among all the properties of polycrystalline Ni-base superalloys for turbine disc applications, fatigue is one of the most important, often limiting the overall service life. However, due to the increased operating temperatures of the turbine disc, creep and oxidation damage make an increasing contribution to the fatigue failure of Ni-based superalloys, especially under dwell-fatigue conditions, resulting in accelerated fatigue failure indicated by shorter fatigue life and/or faster crack propagation

rate [7-14]. Such a phenomenon is usually associated with intergranular fracture resulting from the interaction between grain boundary (GB) oxidation/embrittlement effects or GB cavitation and mechanical fatigue processes, and is a function of the microstructures of the investigated Ni-based superalloys and the service conditions [3, 12, 13, 15-17]. Generally, the microstructures corresponding to an improvement of fatigue performance and high temperature strength for Ni-based superalloys are usually associated with a *degradation* of the creep and oxidation resistance. Therefore, a trade-off in the addition of alloying elements in Ni-based superalloys needs to be made to optimise the fatigue-creep-oxidation performance and yet still obtain a good processing characteristic. A further trade-off also has to be made during processing of disc superalloys to obtain microstructures which can balance the fatigue performance and creep/oxidation resistance.

Low Solvus, High Refractory (LSHR) alloy is a latest generation powder metallurgy (P/M) Ni-based superalloy developed by NASA for turbine disc application at higher operating temperatures. The LSHR alloy combines the low solvus of ME3 brought about by the high Co content and the high temperature strength and creep resistance of Alloy 10 brought about by the high refractory element content [18-20]. The low solvus temperature of LSHR alloy allows more flexible solution heat treatment (e.g. dual microstructure heat treatments [5, 6]) to optimise the microstructures which in turn optimise the overall fatigue-creep-oxidation performance at the increased operating temperatures. However, the conflicting and interlinked requirements for these microstructures to improve fatigue-creep-oxidation performance require a deep understanding of the mechanisms of fatigue, creep and oxidation under service conditions and the main microstructural factors controlling these failure processes as well as the interplay of damage between fatigue, creep and oxidation processes. Study of crack initiation and propagation mechanisms with coupled influences of (fatigue/creep) deformation-oxidation damage in LSHR alloy is therefore necessary and helpful for further development of appropriate materials optimisation approaches in terms of alloying design and processing techniques to improve high temperature disc performance.

1.2 Research objectives

In this PhD research programme, the fatigue crack initiation and propagation mechanisms in the LSHR alloy over a range of temperatures will be investigated. The primary objectives are:

(1) To examine fatigue crack initiation and early propagation behaviour in LSHR alloy at room temperature and elevated temperatures, from which the critical microstructures for intrinsic fatigue crack initiation/propagation and extrinsic fatigue crack initiation/propagation under fatigue-oxidation conditions can be identified.
(2) To investigate the role of oxidation in crack initiation and early propagation and the interlinked influences between microstructure, deformation and oxidation.
(3) To systematically reveal the influence of microstructure, temperature, environment and loading waveform on cyclic- and time-dependent long fatigue crack growth (FCG) behaviour.
(4) To propose appropriate materials optimisation approaches to improve high temperature turbine disc performance.

1.3 Scope of this work

In Chapter 2, relevant literature addressing the fundamentals of Ni-based superalloys and the fatigue behaviour of Ni-based superalloys is reviewed. Chapter 3 presents the general microstructure features of LSHR alloy variants studied and their tensile and creep properties. Chapter 4 presents intrinsic fatigue crack initiation and early propagation at room temperature where effect of oxidation is absent, in combination with the evaluation of the influence of microstructures on this intrinsic crack initiation and propagation process. In Chapter 5, oxidation-assisted fatigue crack initiation and early propagation are examined, and the interlinking between microstructures, deformation/strain localisation and oxidation is analysed. Chapter 6 presents the interplay of microstructures, temperature, loading waveform/frequency and environment on cycle- and time-dependent long crack growth behaviour. In Chapter 7, the major conclusions obtained in this work are given. Finally, in Chapter 8, recommendations for future research are proposed.

Chapter 2 Literature review

2.1 Ni-based superalloys for turbine disc applications

2.1.1 Development of disc Ni-based superalloys

Ni-based superalloys are widely used for turbine disc application due to their excellent mechanical properties, fatigue and creep resistance at high temperature, good phase stability, in combination with superior corrosion and oxidation resistance. Generally, Ni-based superalloys mainly consist of γ phase and the strengthening γ′ phase, i.e. (Ni_3(Al, Ti)), both of which have a face centred cubic (fcc) crystal structure. Unlike other alloy systems, Ni-based superalloys have exceptional high temperature strength. The yield strength of Ni-based superalloy does not decrease significantly with increasing temperature. In some cases, the yield strength increases with increasing temperature due to formation of Kear–Wilsdorf locks at elevated temperature, which is usually associated with the cross-slip of dislocation from {111} plane to {001} plane [1, 21].

The properties of disc Ni-based superalloys are closely related to their composition. The alloying elements in Ni-based superalloys can be classified into three main categories, i.e. solid solution strengthening elements, such as Cr, Co, Mo and W, which strengthen the superalloys by formation of a local strain field due to the lattice distortion and decrease the stacking fault energy (SFE) (hence contributing to dissociated dislocations); precipitation strengthening elements, such as Nb, Al, Ti and Ta, which facilitate the formation of γ' phase and increase the anti-phase boundary (APB) energy; and grain boundary strengthening elements, such as Hf, C, B and Zr, which are inclined to segregate to grain boundaries where they may improve the cohesive strength and reduce the segregation of other impurities and undesired precipitation. The evolution of the composition of various Ni-based superalloys for turbine disc applications as they have developed over the past 60 years is shown in Table 2.1, where an increasing alloying level can be discerned as alloy development progresses. With the enhancement of alloying level in Ni-based superalloys, the temperature capability has shown a great improvement, approximately an increase of 2 ^{o}C annually, and approaches 750 ^{o}C in recent years, as shown in Fig. 2.1 [22]. Meanwhile, the initial cast and wrought superalloys are gradually replaced by P/M superalloys because of the severe elemental segregation during solidification caused by the heavy alloying. Furthermore, a novel heat

treatment method, i.e. dual microstructure heat treatment [23], has been designed to attain dual microstructures in a turbine disc which is optimized to withstand a relatively high operating temperature and low cyclic stress at the disc rim and a comparatively low operating temperature and high cyclic stress at the disc bore.

Table 2.1 Composition of Ni-based superalloys developed over the past 60 years [1, 6, 24-26]

Alloy	Cr	Co	Mo	W	Nb	Al	Ti	Ta	Fe	Hf	C	B	Zr	Ni
Waspaloy	19.5	13.5	4.3	—	—	1.3	3.0	—	—	—	0.08	0.006	—	Bal.
Inconel 706	16	—	—	—	2.9	0.2	1.8	—	40.0	—	0.03	—	—	Bal.
Inconel 718	19.0	—	3.0	—	5.1	0.5	0.9	—	18.5	—	0.04	—	—	Bal.
Allvac 718Plus	17.86	8.97	2.7	0.99	5.49	1.49	0.76	—	9.59	—	0.024	0.004	—	Bal.
Astroloy	15.0	17.0	5.3	—	—	4.0	3.5	—	—	—	0.060	0.03	—	Bal.
MERL-76	12.4	18.6	3.3	—	1.4	0.2	0.3	—	—	0.35	0.050	0.03	0.06	Bal.
Udimet 500	18.0	18.5	4.0	—	—	2.9	2.9	—	—	—	0.08	0.006	0.05	Bal.
Udimet 520	19.0	12.0	6.0	1.0	—	2.0	3.0	—	—	—	0.05	0.005	—	Bal.
Udimet 700	15.0	17.0	5.0	—	—	4.0	3.5	—	—	—	0.06	0.03	—	Bal.
Udimet 710	18.0	15.0	3.0	1.5	—	2.5	5.0	—	—	—	0.07	0.02	—	Bal.
Udimet 720	17.9	14.7	3.0	1.25	—	2.5	5.0	—	—	—	0.035	0.033	0.03	Bal.
Udimet 720Li	16.0	15.0	3.0	1.25	—	2.5	5.0	—	—	—	0.025	0.018	0.05	Bal.
Rene 95	14.0	8.0	3.5	3.5	3.5	3.5	2.5	—	—	—	0.15	0.010	0.05	Bal.
Rene 88DT	16.0	13.0	4.0	4.0	0.7	2.1	3.7	—	—	—	0.03	0.015	0.03	Bal.
N18	11.5	15.7	6.5	0.6	—	4.35	4.35	—	—	0.45	0.015	0.015	0.03	Bal.
RR 1000	15.0	18.5	5.0	—	1.1	3.0	3.6	2.0	—	0.5	0.027	0.015	0.06	Bal.
ME3	13.1	18.2	3.8	1.9	1.4	3.5	3.5	2.7	—	—	0.03	0.03	0.05	Bal.
Alloy 10	11.5	15	2.3	5.9	1.7	3.8	3.9	0.75	—	—	0.030	0.02	0.05	Bal.
LSHR	12.5	20.7	2.7	4.3	1.5	3.5	3.5	1.6	—	—	0.03	0.03	0.05	Bal.
TMW-4M3	13.5	25.0	2.8	1.2	—	2.3	6.2	—	—	—	0.02	0.02	0.03	Bal.

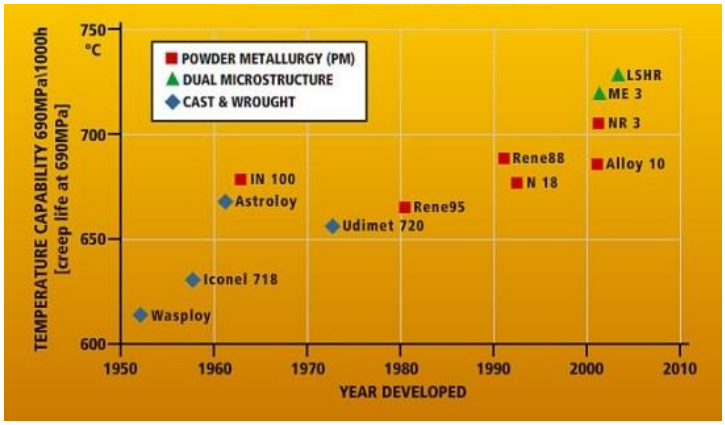

Fig. 2.1 Progress in turbine disc superalloys [22].

2.1.2 Processing of Ni-based superalloys

2.1.2.1 Ingot metallurgy

Turbine discs are fabricated by the machining of superalloy forgings, and the forgemasters are manufactured either by conventional ingot metallurgy that includes vacuum induced melting (VIM), electro-slag remelting (ESR) and vacuum arc remelting (VAR) or powder metallurgy [1, 24]. The selection of processing route is predominantly determined by the chemistry or alloying level of the chosen superalloy, although other factors should also be taken into consideration such as cost. For conventional ingot metallurgy, the specific procedure is illustrated in Fig. 2.2 [1]. It is shown that both ESR and VAR are used to purify superalloys after the VIM, and then the ingot is annealed to remove or reduce elemental segregation, followed by thermal-mechanical working before proceeding with the final forging operations.

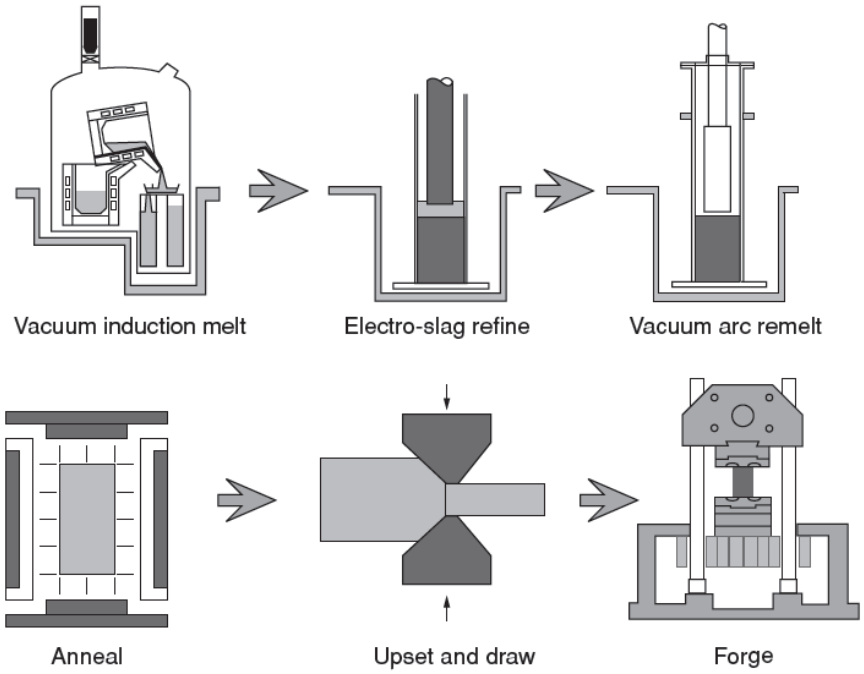

Fig. 2.2 The sequence of ingot metallurgy process for production of turbine disc alloys [1].

2.1.2.2 Powder metallurgy

However, ingot metallurgy is not suitable for processing heavily alloyed superalloys such as Rene 95 and RR1000 due to the significant solidification segregation and the cracking propensity during thermal-mechanical working. Under these circumstances, powder

metallurgy becomes more attractive and competitive in terms of eliminating elemental segregation. As shown in Fig. 2.3, VIM is also employed in the P/M processing route, followed by remelting and inert gas atomization to produce powder [1]. The obtained powder is sieved to remove large non-metallic inclusions inherited from the atomization, and then consolidated, degassed in combination with sealing followed by hot isostatic pressing (HIP) and/or extrusion. Compared with ingot metallurgy, higher cleanliness can be attained by power metallurgy although the processing route is significantly more complicated and incurs a greater cost.

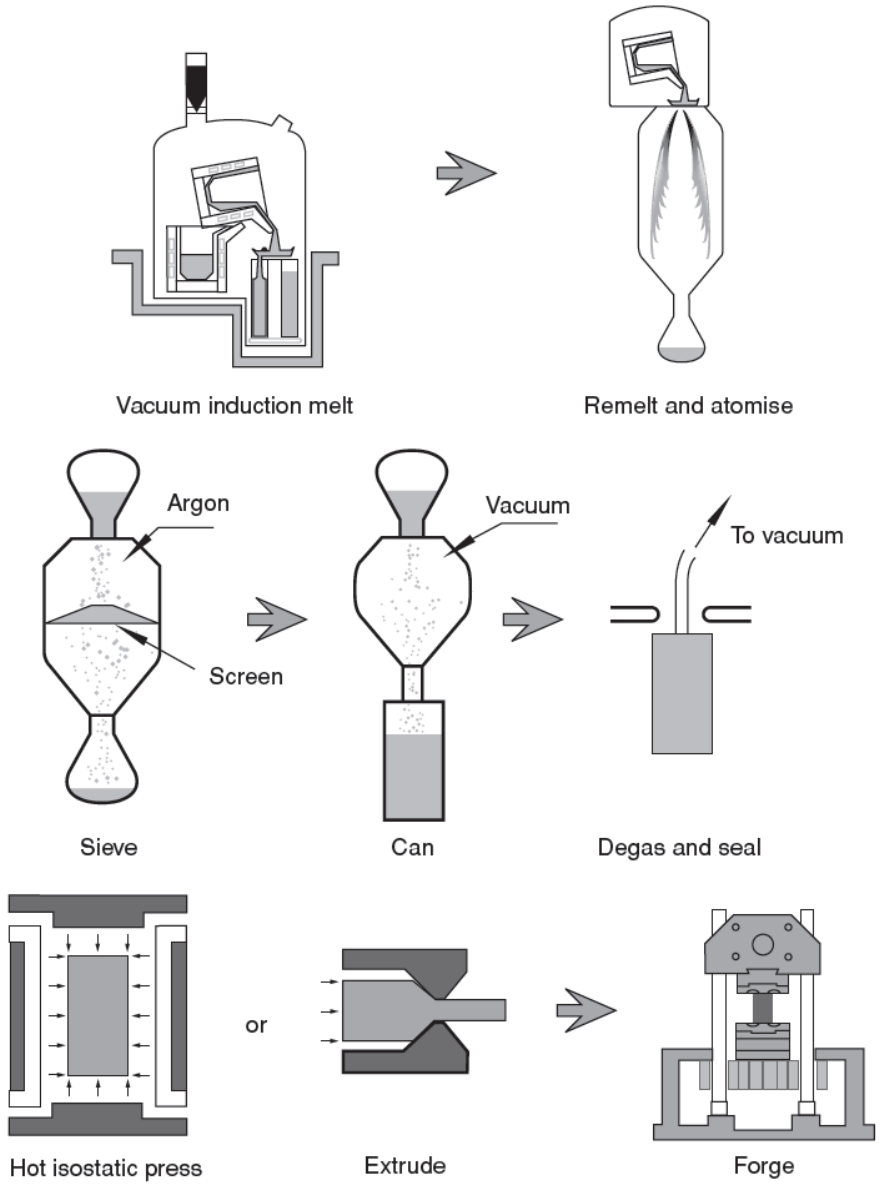

Fig. 2.3 The sequence of powder metallurgy process for production of turbine disc alloys [1].

2.1.2.3 Dual microstructure heat treatment

In order to maximize the associated mechanical properties as required at each location of the turbine disc (corresponding to fine grained (FG) microstructure at the disc bore and coarse grained (CG) microstructure at the disc rim), the dual microstructure heat treatment is employed to process the turbine disc. As shown in Fig. 2.4 [5], heat sinks consisting of solid metallic cylinders are placed on the top and bottom faces of the disc forging to introduce a temperature gradient over the turbine disc with the bore at lower temperature than the rim. An insulating jacket is used to further slow the temperature rise of the central portion of the disc forging. Thermocouples are used to monitor the temperature field with the aid of finite element modelling results. To perform the heat treatment, the forging and heat sinks are placed in a furnace maintained at a temperature above the γ′ solvus of LSHR alloy and taken out when the temperature at the disc rim exceeds the solvus but before the bore temperature reaches the solvus. After removal from the furnace the heat sinks are removed and the forging is cooled [6]. Based on NASA's approach, this kind of heat treatment method is successful in producing powder metallurgy dual microstructure turbine disc [5, 6].

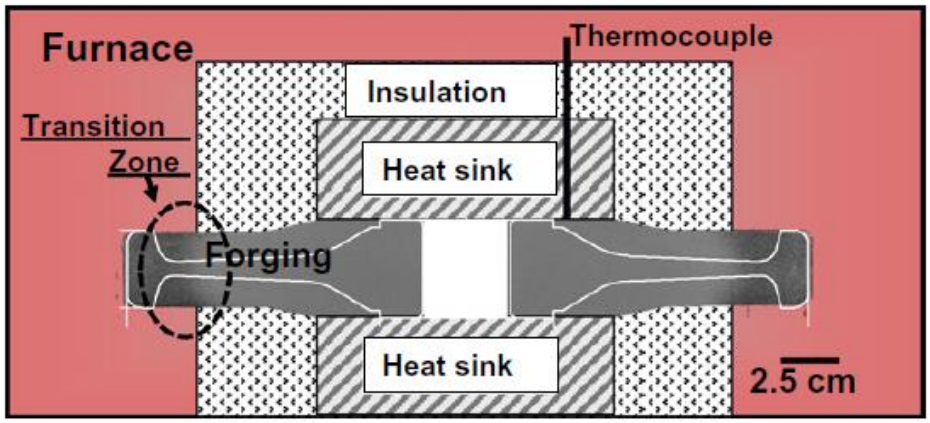

Fig. 2.4 Schematic of dual microstructure heat treatment assembly used for solution heat treatment of turbine disc [5].

2.1.2.4 Grain boundary engineering

Grain boundary is a very important microstructural characteristic in polycrystalline disc alloys. Not only the grain size (which determines the grain boundary area), but also the grain boundary character significantly influences the properties and performance of these disc alloys. It is well known that the small angle grain boundaries and the special grain boundaries

(as described by the coincidence site lattice (CSL) model) possess higher lattice coherency and lower grain boundary energy compared with random large angle grain boundaries, giving rise to better grain boundary attack resistance in an aggressive environment [27-30]. It is therefore believed that it is possible to improve the resistance of grain boundary related failure process in these disc alloys by increasing the fraction of small angle and special grain boundaries.

Grain boundary engineering (GBE) [31], which targets increasing the area fraction of small angle and special grain boundaries via thermomechanical processing, has been employed to process turbine disc alloys to improve the creep and intergranular fatigue crack initiation and propagation resistance [28, 29, 32, 33]. The thermomechanical processing usually involves several strain-annealing cycles to induce (1) strain by cold working and (2) strain-induced grain-boundary migration or static recrystallization during subsequent annealing. A dual aging heat treatment is always applied to GBEed Ni-based disc alloys to reprecipitate the γ′ [29]. The attainable small angle and special grain boundaries can be maximized by reasonably selecting the appropriate strain and strain rate during the cold working as well as the annealing temperature and time [29, 32]. However, a drawback in traditional thermomechanical processing procedures is that cold working is not involved in fabricating P/M turbine discs/alloys, which makes the increased special grain boundaries produced by thermomechanical processing less practical in industrial applications of disc manufacture. An attempt to increase the fraction of special grain boundaries, particularly Σ3 twin boundary (TB) in disc alloys via hot deformation at a temperature close to γ′ solvus has been recently conducted by Souai et al. [32], and the results show a dependence of the annealing twin on the strain level and strain rate, which opens the possibility of GBE via hot deformation in Ni-based disc alloys.

2.1.3 Heat treatment and microstructures

The properties of materials are dependent on the composition, processing and resultant microstructures. When the composition is fixed, the properties are mainly determined by the attainable microstructures via certain processing. As illustrated in Table 2.1, Ni-based superalloys are heavily alloyed, and thereby various phases may exist depending on the processing conditions, especially heat treatment conditions. In typical Ni-based superalloys for turbine disc application, the constituent phases include γ phase that forms a continuous

matrix, γ′ phase along with minor carbides and borides [1, 19]. Under certain conditions, the TCP phases such as μ, σ and Laves phases may exist as well [1, 34].

Currently, the most common and available Ni-based superalloys for turbine disc application are fabricated by the cast and wrought method and powder metallurgy, and both of these two processing technologies require a heat treatment, i.e. solution and aging heat treatment, to modify the microstructures after the extrusion and/or forging. It is well accepted that the performance of Ni-based superalloys in turbine disc applications is closely related to the final heat treatment which is able to significantly change the grain size of the matrix, as well as the size, amount and distribution of primary, secondary and tertiary γ′. In addition, the MC carbides formed during solidification may decompose to $M_{23}C$ or M_6C carbides depending on the heat treatment conditions employed [35].

The microstructures of turbine disc alloys after the solution and aging heat treatment basically determine the in-service creep and fatigue performance. Considerable research has been performed to reveal the relationship between the heat treatment, microstructures and related mechanical properties in a wide range of Ni-based superalloys over the decades. As shown in Table 2.2, the most commonly used heat treatments for a few typical P/M Ni-based superalloys are presented. The main parameters of heat treatment that have significant influence on the resultant microstructures are solutioning temperature, time and subsequent cooling rate, in combination with aging temperature and time [6, 8, 9, 36, 37]

The solutioning temperature is extremely critical to the grain size of the superalloys. When the solutioning temperature is higher than solvus of γ′ (known as a supersolvus solution heat treatment), primary γ′ will completely dissolve into the matrix, and no longer constrain grain boundaries, causing rapid grain growth; whereas when the solutioning temperature is lower than the solvus of γ′, normally 20-40 ^{o}C below the solvus of γ′ (known as a subsolvus solution heat treatment), approximately 10-20% primary γ′ can be retained, which act as barriers to grain boundary motion and confines grain growth, yielding uniform microstructures with grains near 5-10 μm in diameter [5]. This FG microstructure is able to meet the typical requirements of aeroengine turbine disc bore and web regions because of the high strength and good fatigue resistance at 400-550 ^{o}C. Conversely, the CG microstructures, typically 30-70 μm in diameter, caused by the absence of the pinning effect of retained primary γ′ in the supersolvus solutioning stage, are believed to be beneficial to the creep and

dwell fatigue resistance at 650-750 ^{o}C. These are the key properties for high performance aeroengine turbine disc rims.

Table 2.2 Typical heat treatments for several Ni-based superalloys in the literature

N18 [36]	4h 1165°C	→	air cool	→	24h 700°C	→	air cool	→	4h 800°C	→	air cool
RR1000 [8]	4h 1120°C	→	fan air cool	→	24h 650°C	→	air cool	→	16h 760°C	→	air cool
U720Li [9, 37]	4h 1105°C	→	oil quench	→	24h 650°C	→	air cool	→	16h 760°C	→	air cool
U720Li LG [9, 37]	4h 1135°C	→	air cool	→	24h 650°C	→	air cool	→	16h 760°C	→	air cool
CG LSHR [6]	3h 1170°C	→	fan cool	→	4h 855°C	→	air cool	→	8h 775°C	→	air cool
FG LSHR [6]	3h 1135°C	→	oil quench	→	4h 855°C	→	air cool	→	8h 775°C	→	air cool

It is generally accepted that the solvus of γ′ is important to the processing flexibility of solution heat treatment. The temperature gap between the solvus of γ′ and melting point of Ni-based superalloys, known as the heat treatment temperature window, determines the usable temperature range of solution heat treatment. The higher the solvus of γ′, the narrower the heat treatment temperature window is, which makes the Ni-based superalloys more difficult to be heat treated. The high solvus of γ′ also means the supersolvus solution temperature is close to the melting point of investigated superalloys, which causes significant grain growth at such high homogenization temperatures. Furthermore, the high solution temperature increases the propensity of quench cracking due to the greater residual thermal stresses, especially in large scale turbine discs [38].

Precipitation of secondary and tertiary γ′ during the cooling process and subsequent aging heat treatment is another distinctive characteristic of disc Ni-based superalloys. The volume, size, shape and distribution of secondary and tertiary γ′, which can be tailored by heat treatment, are very important to the mechanical properties of Ni-based superalloys. It is well established that the precipitation of secondary γ′ is strongly dependent on the cooling process followed by the solutioning step [18, 39, 40]. Generally, the slower the cooling rate, the larger the secondary γ′ is. According to Gabb's research [18], the size of secondary γ′ decreases monotonically with increasing cooling rate, and has little relation to the aging heat treatment. In terms of the morphology of secondary γ′, it is mainly cuboidal or near-circular apart from

some extreme conditions such as cooling extremely slowly from solutioning stage, in which dendritic secondary γ′ can be observed, and quite stable during aging heat treatment. Unlike secondary γ′, the size of tertiary γ′ is closely related to the aging temperature and time along with a slight influence of cooling rate from the solutioning temperature, and their morphology is mainly cuboidal or circular as well. In terms of volume fraction, both secondary and tertiary γ′ are influenced by the cooling rate and aging heat treatment, i.e. a high cooling rate from solutioning temperature and high aging temperature are able to enhance the volume fraction of secondary γ′. Furthermore, a high volume fraction of secondary γ' often results in a decrease in the volume fraction of tertiary γ'.

2.1.4 Strengthening mechanism and mechanical properties

The mechanical properties of Ni-based superalloys are strongly dependent on the microstructures, which in turn are determined by the chemical composition and corresponding processing routes. By choosing alloying elements and carefully designing the processing routes, the mechanical properties of Ni-based superalloys can be significantly improved by solid solution strengthening effects due to the lattice distortion caused by the difference between the radius of the Ni atom and alloying elements, precipitation hardening due to the formation of coherent and semi-coherent γ′ precipitates and grain boundary strengthening effects due to grain refinement and the increase in cohesion strength of a grain boundary [1].

2.1.4.1 Solid solution strengthening

Solid solution strengthening is a common strengthening mechanism of materials, and is widely employed to strengthen Ni-based superalloys. With the addition of solid solution strengthening elements such as Co, Cr, W and Mo, the crystal lattice is distorted to some extent depending on the amount of alloying elements in solid solution and the difference in the radius of alloying elements and Ni. The lattice distortion causes long-range internal stress which inhibits the motion of dislocations, causing the increase in strength. Apart from the lattice distortion, the atoms in solid solution will still cause a variation in elastic modulus in the surrounding crystal lattice, which exerts an additional interaction between the solute atom and dislocation and strengthens the materials further, although its effect is not as significant as that of the long-range internal stress field. Additionally, the solute atoms are able to segregate at stacking faults and around the dislocations, pinning dislocations and thereby

enhancing the strength of Ni-based superalloys.

2.1.4.2 Precipitation strengthening

Precipitation strengthening is the most important strengthening mechanism in the Ni-based superalloys, and the precipitated γ′ phase in Ni-based disc superalloys accounts for 40-55% volume fraction depending on the specific composition. The precipitation of coherent and/or semi-coherent γ′ causes lattice misfit around the γ′ phase due to the difference in lattice constant between γ and γ′ phases. The higher the degree of lattice misfit, the stronger the stress field is, which lowers the mobility of dislocations and thereby results in a more significant strengthening effect. During the deformation process, dislocations have to bypass the γ′ by shear cutting or Orowan looping or climb mechanism depending on the size of the precipitates and temperature, which also make contributions to the improved mechanical properties of Ni-based superalloys [41-44].

In Ni-based superalloys, the dislocation passing through the precipitates by a shear cutting mechanism is activated when following conditions are met: (1) the precipitates are coherent with the γ matrix and have the same slip plane with the matrix; (2) the size of precipitates is smaller than a critical size; and (3) the strength of precipitates is relatively low. It is well recognized that APB is an unstable high-energy structure that will be formed when a *a/2*<110>{111} dislocation passes through γ′ by this cutting mechanism and the required precipitate-cutting stress is expected to be proportional to the APB energy (γ_{APB}) and inversely proportional to the Burgers vector $\bar{b}$ of the dislocation. In order to remove the APB, the dislocations must travel through the γ′ precipitates in pairs, and such paired dislocations are termed a superdislocation which have been confirmed by transmission electron microscope (TEM) observation [41, 42].

The particle-cutting stress is also believed to be associated with the volume fraction and size of γ′ precipitates. In general, a higher volume fraction of γ′ precipitates always results in higher particle-cutting stress. In terms of the effects of precipitate size on the interaction between precipitates and dislocations, it is schematically shown in Fig. 2.5, and the paired dislocations cutting through γ′ precipitates can be classified as “weakly” and “strongly” coupled dislocations depending on the size of γ′ precipitates [1, 45].

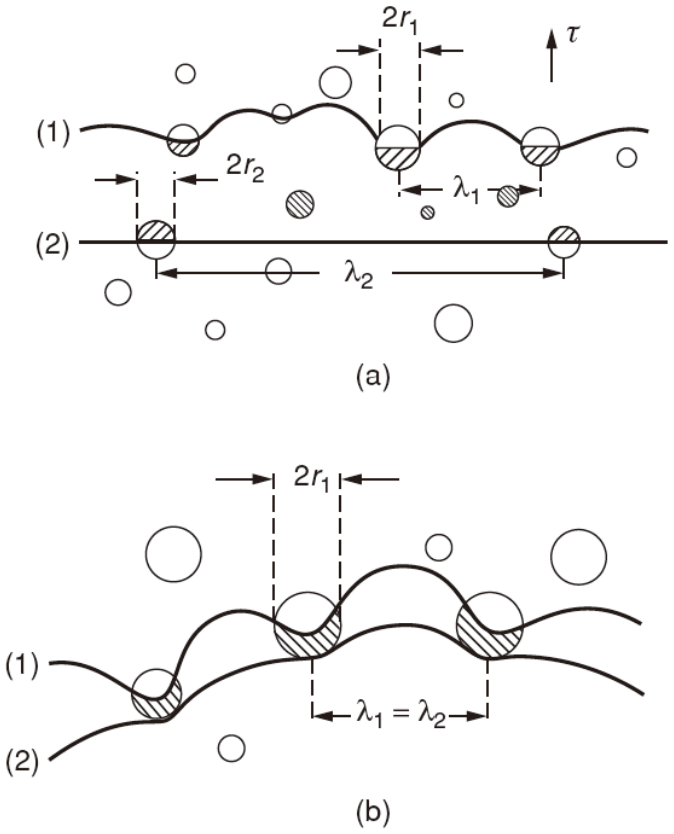

Fig. 2.5 Ordered γ′ precipitates being sheared by pairs of dislocations: (a) weak pair-coupling and (b) strong pair-coupling [1, 45]

When the size of γ′ precipitates is small in comparison with the spacing between the paired dislocations, particularly in the case of the under-aged condition, the second trailing dislocation is some way behind the first, leaving faulted particles between the two dislocations. The required critical resolved shear stress (CRSS) for this weakly coupled precipitates-dislocations interaction can be estimated by following equation [1]:

$$\tau_c = \frac{\gamma_{APB}}{2b}\left[\left(\frac{6\gamma_{APB} f r}{\pi T}\right)^{0.5} - f\right] \tag{2.1}$$

where τ_c is the critical resolved shear stress for precipitate-cutting by dislocations. γ_{APB} is APB energy, which is dependent on the specific composition and stoichiometry of γ′ precipitates. The reported APB energies for γ′ precipitates are summarised in Table 2.3 [46-49]. b is the Burgers vector, and f is the volume fraction of γ′ precipitates. r is the radius of γ′ precipitates with a uniform distribution.

Table 2.3 APB energies at the {100} and {111} planes for γ′ precipitates (or Ni_3Al alloys) reported in the literature [46-49]

Composition	(111) APB energy (mJ m^{-2})	(001) APB energy (mJ m^{-2})
Ni-22.9Al	169±22	104±11
Ni-24Al	176±11	135±18
Ni-25Al	195±13	160±20
Ni-26Al	219±17	184±16
Ni-24.7Al-1.0Ta	237±30	225±30
Ni-17.4Al-6.16Ti	250±31	250±30
Ni-24Al-0.25Hf	160	120
Ni-24Al-2Hf	190	170
Ni-22Al-3Hf	300±25	250±25

When the γ′ precipitates are large, particularly in the case of the over-aged condition, the spacing of the dislocation pairs becomes comparable to the particle diameter. Thus, any given precipitate may contain a pair of dislocations which are now "strongly coupled". In this situation, the required CRSS for precipitate-cutting can be estimated by following equation [1]:

$$\tau_c = \sqrt{\frac{3}{2}}\left(\frac{Gb}{r}\right) f^{0.5} \frac{w}{\pi^{1.5}} \left(\frac{2\pi\gamma_{APB} r}{wGb^2} - 1\right)^{0.5} \quad (2.2)$$

where G is shear modulus of γ′, and w is dimensionless constant which is expected to be of the order of unity. A distinguished difference between Equations 2.1 and 2.2 is that $r^{0.5}$ dependence is expected in the case of the weakly coupled dislocations, whereas $r^{-0.5}$ dependence is expected in the case of the strongly coupled dislocations. Therefore, the required CRSS for precipitate-cutting is supposed to increase with precipitate size initially and then to decrease with the increasing precipitate size after the critical size is reached.

As a consequence of the dislocations continuously cutting the γ′ precipitates, strain localization and preferential slip on the cutting plane become severe due to the reduction in the effective area of γ′ precipitate to resist further deformation especially when precipitates are relatively small. This preferential slip on the cutting plane usually results in softening in that direction and therefore concentration of slip, exhibiting a planar slip behaviour [50].

With the increasing precipitate size, it becomes more difficult for a dislocation cutting through the γ′ precipitates, and the precipitate-cutting mechanism will eventually be replaced by a looping mechanism when the precipitate size reaches a critical value. When a dislocation passes through the γ′ precipitate by the Orowan looping mechanism under external stress, a small dislocation loop will be left. These small dislocation loops increase the size of γ′ precipitates and decrease the effective spacing between γ′ precipitates, which increases the required stress to realize further dislocation motion and thereby enhance the strength of Ni-based superalloys [51]. The increase in yield strength can be expressed as [1]:

$$\Delta\tau = \frac{Gb}{2\pi L}\emptyset' ln\frac{L}{2b} \tag{2.3}$$

where L is the spacing between γ′ precipitates. $\emptyset' = \frac{1}{2}\left(1+\frac{1}{1+v}\right)$, where v is Poisson ratio.

Due to the increased internal resistance to succeeding dislocation bypassing precipitates by looping mechanism, dislocations are forced to move out to adjacent planes in the same slip system when the strain amplitude is small or to cross-slip on to other systems when the strain amplitude is large. These two processes usually result in a more homogeneous distribution of dislocations (wavy slip) in the matrix, and thereby they are associated with more homogeneous deformation behaviour [52]. In summary, the correlation between the increase in the CRSS and the precipitate size can be schematically shown in Fig. 2.6 [1].

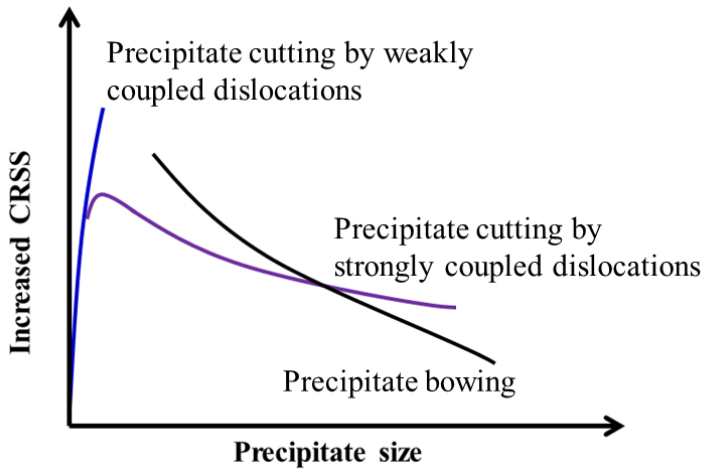

Fig. 2.6 Schematic representation of the increase in CRSS as a funtion of the mean precipitate size in Ni-based superalloys [1].

2.1.4.3 Grain boundary strengthening

Since those Ni-based superalloys targeted for turbine disc applications are polycrystalline structures, grain size has always been an important issue. It is well known that grain boundary is a high-energy region that connects two grains and contains a high density of defects such as vacancies, solute atoms and dislocations. During the deformation process, the grain boundary acts as a barrier to dislocation motion due to the misorientation, elastic anisotropy and plastic incompatibility in neighbouring grains, making slip transmission more difficult to occur and enhancing the mechanical properties of materials [53]. It is a well-established method therefore to increase the strength of materials by grain refinement. Based on the Hall-Petch equation, the yield or ultimate strength of materials is inversely proportional to the square root of the diameter of the grains. It is should be noted however that the migration and sliding of grain boundaries becomes increasingly significant along with enhanced grain boundary diffusion as the temperature increases, which reduces grain boundary strength markedly and stimulates the creep process [1, 54]. When a critical temperature is reached, the grain boundary strength is equivalent to the grain strength and then continues to decrease with the increasing temperature. Thus, the beneficial effect of grain refinement is dependent on the operating temperature of components as grain boundary failure modes (either creep or oxidation) start to come into play.

Apart from the modification of grain size which modifies the area of grain boundary to enhance the mechanical properties of superalloys, alloying elements are added to improve the grain boundary microstructure and its cohesion strength, which in turn further increases the strength of superalloys. As mentioned previously, the alloying elements such as B, C, Zr and Hf are added into Ni-based superalloys to improve cohesion strength of grain boundary, ease or eliminate detrimental elemental segregation at grain boundary, inhibit the precipitation of brittle and low melting point phases, and therefore increase the resistance to formation of cavitation and crack initiation and yield better creep and fatigue resistance. Moreover, the beneficial phases formed at grain boundaries due to the addition of grain boundary strengthening elements are capable of pinning the grain boundaries and thereby improving the creep performance [55, 56].

2.1.4.4 Temperature dependence of strengthening in the Superalloys

Unlike other alloy systems, the yield strength of Ni-based superalloys does not decrease

significantly with increasing temperature. In many cases, the yield strength increases with increasing temperature, until temperatures of about 800 ^{o}C are reached, as shown in Fig. 2.7 [1]. It is now widely accepted that the positive temperature dependence of yield strength in Ni-based superalloys is caused by the interaction between the applied stress and elastic anisotropy, and most importantly is caused by the anisotropy of the APB energy [1, 57, 58]. As shown in Table 2.3, the APB energy is lower on the {100} plane than the {111} plane. Upon deformation, the paired dislocations may individually dissociate with superpartial dislocations which contain stacking faults and are linked by an APB domain. As temperature increases, cross-slip becomes easier due to the extra thermal energy available, which promotes the cross-slip of the segments of the γ' superpartial dislocations from the {111} plane to the {001} plane, and allowing the APB domain along the {001} plane which lowers the APB energy. However, the {001} plane is not a favourable plane for dislocation motion, and thereby the superpartial dislocations are effectively locked, which is known as a Kear–Wilsdorf lock. As a result, the critical resolved shear stress for dislocation motion is increased at higher temperatures when this type of cross-slipping occurs. This hardening becomes more significant with increasing temperatures until a peak yield stress is reached. As temperature continues to increase (>800 ^{o}C), slip on {001} planes becomes easier and then the superpartial dislocations can unlock again, which results in a decrease of the yield strength on further increase in temperature [1, 59]. However, the full details of the mechanism of the temperature dependence of strengthening in Ni-based superalloys are still under investigation.

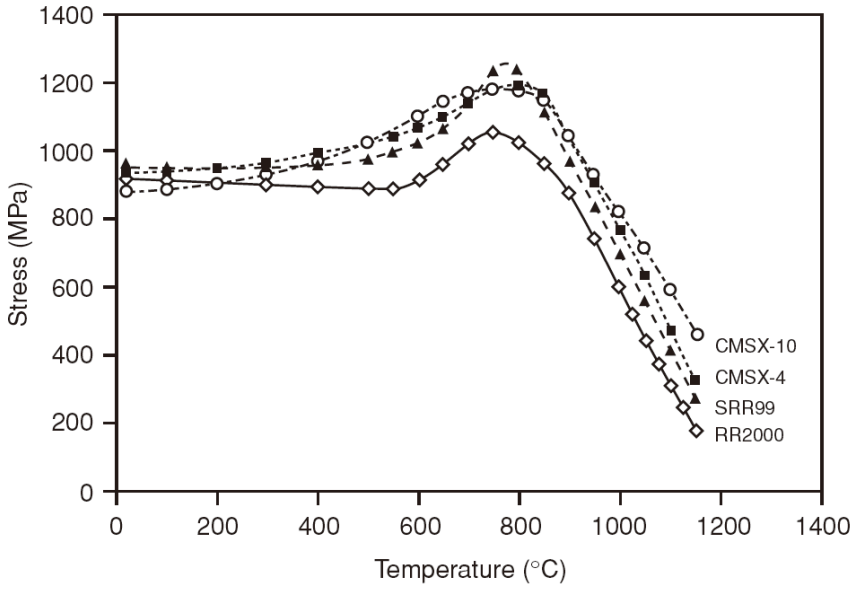

Fig. 2.7 Variation of the yield strength of several Ni-based superalloys with temperatures [1].

2.2 Fatigue of Ni-based superalloys

2.2.1 Introduction and terminology

Fatigue is an important failure mode of materials or components subjected to an alternating load that is usually lower than the yield strength of materials. The whole fatigue process includes fatigue crack initiation, propagation and final fracture. It is estimated that approximately 90% of the failure accidents of non-static industrial components are caused by the fatigue damage of materials, and thereby it is important to investigate the fatigue performance of materials, in light of benefits to safety, performance and subsequently the economy.

As illustrated in Suresh's book [60], there are four parameters used to describe to the features of cyclic load/strain exerted on materials. Taking a sinusoidal waveform load for instance which is shown in Fig. 2.8, these parameters can be defined as follows:

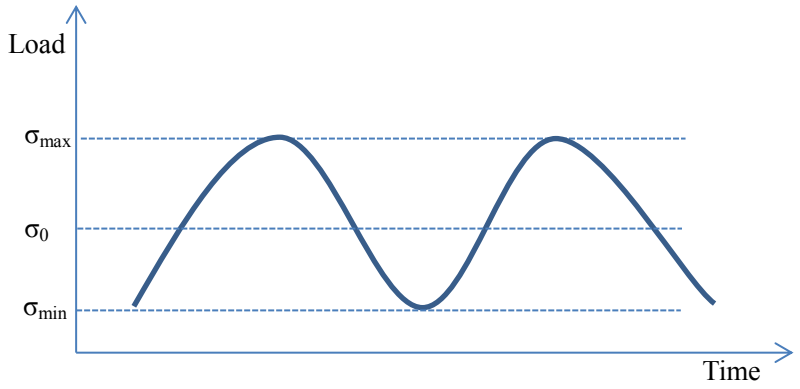

Fig. 2.8 Sinusoidal fatigue load cycle [60]

Mean stress: $\sigma_0 = \frac{\sigma_{max}+\sigma_{min}}{2}$ (2.4-a)

Mean strain: $\varepsilon_0 = \frac{\varepsilon_{max}+\varepsilon_{min}}{2}$ (2.4-b)

Stress amplitude: $\sigma_a = \frac{\sigma_{max}-\sigma_{min}}{2}$ (2.5-a)

Strain amplitude: $\varepsilon_a = \frac{\varepsilon_{max}-\varepsilon_{min}}{2}$ (2.5-b)

Stress range: $\Delta\sigma = \sigma_{max} - \sigma_{min}$ (2.6-a)

Strain range: $\Delta\varepsilon = \varepsilon_{max} - \varepsilon_{min}$ (2.6-b)

Load (stress) ratio: $R = \frac{\sigma_{min}}{\sigma_{max}}$ (2.7-a)

Strain ratio: $R = \frac{\varepsilon_{min}}{\varepsilon_{max}}$ (2.7-b)

Apart from the aforementioned parameters, the loading frequency *f* is also an important parameter to depict the applied load. In general, high loading frequency is usually associated with high slip density and homogeneous deformation but less environmental attack. On the contrary, low loading frequency is usually accompanied by low slip density and corresponds to heterogeneous deformation, but it is generally associated with more significant environmental attack [61, 62].

Normally, the loads acting on the materials or components, specifically on fatigue cracks relative to the orientation of crack faces and crack fronts, can be classified into three categories, as shown in Fig. 2.9 [53]:

- Mode 1: The opening mode in which the applied loads are perpendicular to the crack faces and the crack faces are separated in a direction normal to the plane of the cracks;
- Mode 2: The in-plane shear mode, where the loads are in the planes of the crack and the crack faces are sheared in a direction normal to the crack front;
- Mode 3: the tearing or anti-plane shear mode, where the loads are in the plane of the crack and the crack faces are sheared parallel to the crack front.

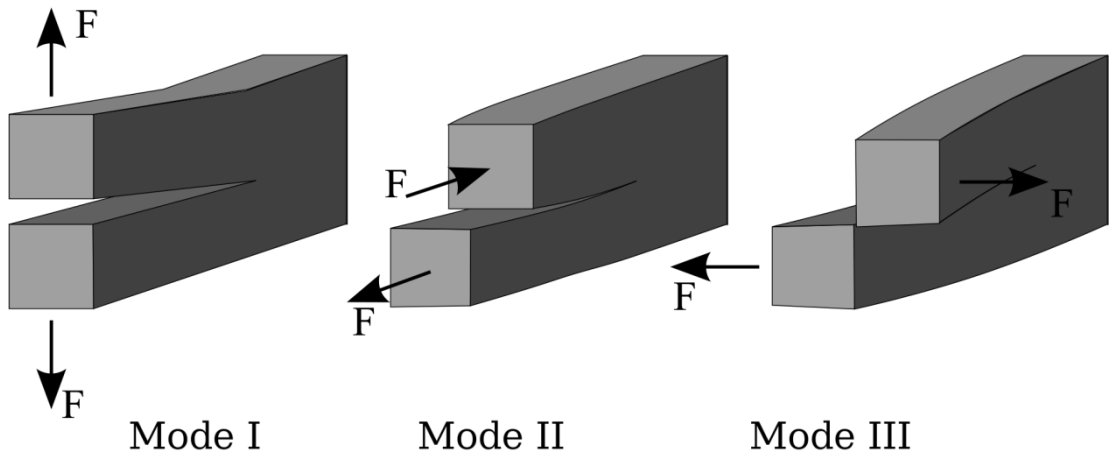

Fig. 2.9 Schematic representation of the three fundamental crack-opening modes: (a) opening mode, (b) in-plane shear mode, and (c) anti-plane shear mode [53].

2.2.2 Fatigue life approach

2.2.2.1 Total life approach

Since 19th century when the fatigue performance of materials became a research subject of interest, considerable theory and experimental methods have been documented to predict the lifetime of components. The earliest and most commonly used method in engineering is the Wohler curve or S-N curve that describes the relationship between the applied stress or strain amplitude and loading cycles. The schematic S-N curve is shown in Fig. 2.10 [63]. On the basis of such an S-N curve, the fatigue limit or endurance limit σ_e can be defined, i.e. the stress amplitude below which fatigue failure does not occur or at least does not occur within 10^7 cycles [64]. However, it should be mentioned that not all the materials possess a fatigue limit or endurance limit, e.g. fatigue life of materials with fcc crystal structure keeps increasing with the decreased stress/strain amplitude even beyond 10^7 cycles.

Around the beginning of the 20th century, Basquin found that the S_a-N_f plot could be linearized with full log coordinates, and thereby established the exponential description of fatigue lifetime (N_f) [65]:

$$\frac{\Delta\sigma}{2} = \sigma_a = \sigma_f'(2N_f)^b \tag{2.8}$$

where σ'_f is the fatigue strength coefficient and b is the fatigue strength exponent. The Basquin equation is frequently used to describe the stress-life in high cycle fatigue where the N_f is greater than 10^5 cycles, and the applied stresses are low and the plastic deformation of materials can be ignored.

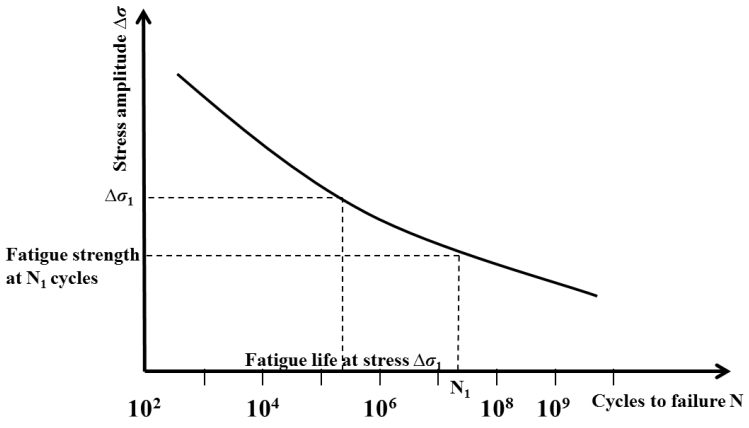

Fig. 2.10 Schematic S-N curve [63]

Quite similar to the Basquin equation, Coffin and Manson found that plastic strain-life data may also be linearized with log-log coordinates in the middle of 20th century, which is well known now as the Coffin-Manson equation [66, 67]:

$$\frac{\Delta\varepsilon_p}{2} = \varepsilon_a = \varepsilon_f'(2N_f)^c \tag{2.9}$$

where ε'_f is the fatigue ductility coefficient, and c is the fatigue ductility exponent. The Coffin-Manson equation is often used to express the strain-life relationship in low cycle fatigue where the N_f is less than 10^5 cycles, and stresses are high enough for significant plastic deformation to occur.

Given that the total strain amplitude, $\Delta\varepsilon/2$, can be expressed in terms of elastic strain amplitude $\Delta\varepsilon_e/2$ and plastic strain amplitude $\Delta\varepsilon_p/2$ as following equation [60]:

$$\frac{\Delta\varepsilon}{2} = \frac{\Delta\varepsilon_e}{2} + \frac{\Delta\varepsilon_p}{2} \tag{2.10}$$

By substituting Basquin and Coffin-Manson equation into above equation, the total fatigue life can be characterized by in terms of the elastic and plastic components of total strain as shown below [60]:

$$\frac{\Delta\varepsilon}{2} = \frac{\sigma_f'}{E}(2N_f)^b + \varepsilon_f'(2N_f)^c \tag{2.11}$$

The S-N curve, the Basquin equation, as well as the Coffin-Manson equation comprise the basis of total life approach design method in engineering components. In designing using an S-N curve, Basquin equation (stress-life data), and Coffin-Manson equation (strain-life data), the design code is against fatigue crack initiation rather than crack growth since stress-life and strain-life data are obtained from smooth, nominally defect-free specimens and much of the measured life is taken up by crack initiation rather than crack propagation. For this reason, the total life approach is useful for selecting materials where resistance to crack initiation is important, while it is unreliable in determining the resistance of a material to crack propagation. In applications where resistance to crack propagation is important, the damage-tolerant approach is adopted [2].

2.2.2.2 Damage-tolerant approach

As most engineering components contain flaws, such as machining marks, notches, and

holes, as well as material microstructural defects, a defect-tolerant lifing approach will allow for practical engineering situations. In the damage tolerance approach, components are assumed to contain flaws of an initial size a_0 that is dependent on the detection resolution of the non-destructive testing (NDT) technique. The components should be considered as safe and sound until the critical size a_c that causes fast failure or affects compliance beyond design tolerance is reached. The usable fatigue lives are determined by integration of an equation relating the crack growth rate to some characteristic driving force which can be determined on the basis of linear elastic fracture mechanics (LEFM) or elastic-plastic fracture mechanics (EPFM) [53, 60].

Among various fracture mechanics approaches developed to correlate fatigue crack growth with loading conditions, LEFM is widely employed to calculate the stress field ahead of crack tips in terms of the nominal applied stress and the flaw length when the plastic zone in front of the crack tip is considerably smaller compared with the flaw length.

The LEFM approach can be illustrated by the classical example of a sharp through thickness crack of length 2a in a thin elastic plate as shown in Fig. 2.11. The local stresses at polar co-ordinates (r, θ) close to the crack tip are given to a first approximation by [60]:

$$\sigma_{xx} = \frac{K}{\sqrt{2\pi r}}\left[\cos\frac{\theta}{2}\left(1 - \sin\frac{\theta}{2}\sin\frac{3\theta}{2}\right)\right] \tag{2.12}$$

$$\sigma_{yy} = \frac{K}{\sqrt{2\pi r}}\left[\cos\frac{\theta}{2}\left(1 + \sin\frac{\theta}{2}\sin\frac{3\theta}{2}\right)\right] \tag{2.13}$$

$$\sigma_{xy} = \frac{K}{\sqrt{2\pi r}}\left[\sin\frac{\theta}{2}\cos\frac{\theta}{2}\cos\frac{3\theta}{2}\right] \tag{2.14}$$

where K is the stress intensity factor, defined in terms of the applied stress σ and flaw length a as:

$$K = \sigma\sqrt{\pi a}\, f\left(\frac{a}{w}\right) \tag{2.15}$$

where $f\left(\frac{a}{w}\right)$ is the compliance function which allow for differing component geometry and shape.

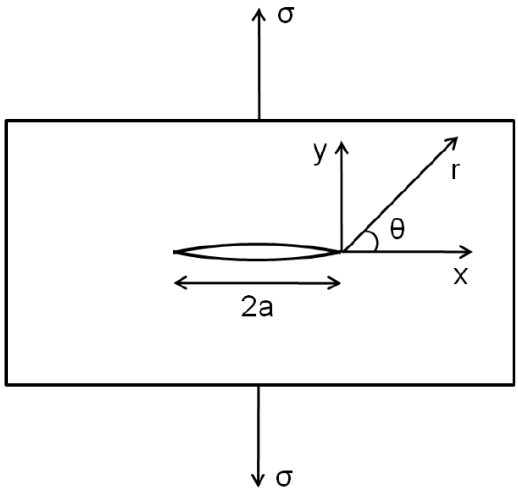

Fig. 2.11 Sharp crack in a thin elastic plate [60].

The stress intensity factor is a useful parameter in describing the stress state ahead of the crack tip and the driving force for crack propagation since it takes the contribution of crack size and applied stress into consideration and can be easily calculated by the specimen dimension and external loading conditions. It should be mentioned however that the stress intensity tends to infinity as r approaching to zero based on the above equation, which is unable to occur in reality due to the plastic yielding of materials that makes the LEFM invalid in describing very near crack-tip stress/strain states.

The concept of K has been adopted in fatigue theory to characterize crack growth behaviour. Instead of using an applied stress range $\Delta\sigma$, the stress intensity factor range ΔK is used. By plotting the fatigue crack growth rate da/dN against ΔK in log-log co-ordinates, a sigmoidal curve can be obtained which can be divided into three distinct regions, as depicted in Fig. 2.12 [53].

Region A is characterized by a low ΔK and very slow crack growth rate, and thereby a threshold stress intensity factor range ΔK_{th} is defined that is the smallest driving force to attain a detectable crack growth rate. Region B is the region of stable crack growth described by the Paris Equation:

$$\frac{da}{dN} = C\Delta K^m \tag{2.16}$$

where C and m are materials-specific constants determined experimentally.

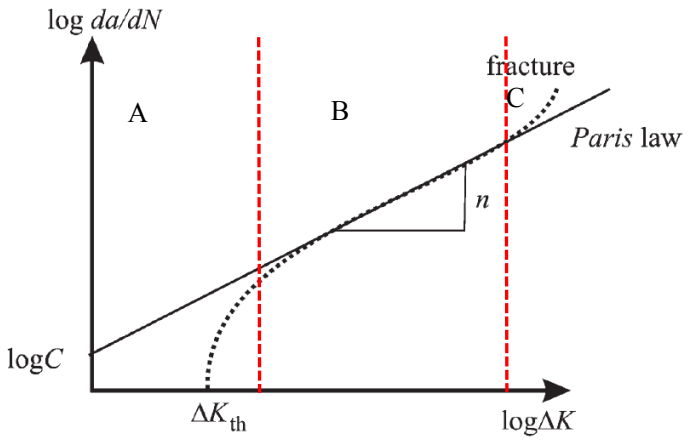

Fig. 2.12 Schematic representation of the *da/dN* vs. *ΔK* in a double-logarithmic plot with the Paris law represented as a straight line [53].

In region C, the crack growth rate accelerates rapidly towards final fast fracture or plastic collapse of the uncracked ligament at high *ΔK* level. The onset of fast crack growth under static loading is represented by the fracture toughness K_c being reached during cycling for the loading mode in question.

As mentioned previously, LEFM is applicable in dealing with the long crack growth problem where the length of the crack is far greater than the plastic zone and a quasi-elastic condition is realised. In the case of the short crack problem, the plastic zone size is comparable to the crack length, LEFM therefore becomes invalid because the deformation around the crack cannot be considered as elastic. According to Suresh's definition [60], there are four kinds of short cracks, i.e. microstructurally short cracks, mechanically short cracks, physically short cracks and chemically short cracks.

Microstructurally short cracks occur when the crack size is equivalent to microstructural characteristics of materials such as: grain size, precipitates or pores, or the spacing of reinforcement in composites. As the crack grows, the significant effect of the local variation in microstructures gradually diminishes and eventually becomes minimized when the crack length exceeds several grain diameters, as the crack tip is now sampling a much wider range of microstructure and effectively achieving a more averaged materials response. Such cracks may still be termed mechanically short cracks, as the crack propagation is driven by the plastic zone ahead of the crack tip, which is still comparable to crack length, hence LEFM still do not describe the crack-tip stress state adequately. With a further increase in the crack length, the size of the plastic zone at the crack tip may become negligibly small in relation to

the crack length, even though the crack length is still small compared with the component in which cracking occurs. This kind of crack may be named a physically short crack, in this case LEFM may now apply, but there has been insufficient development of crack wake to develop the closure levels typical in longer cracks. In terms of chemically short cracks, these may have developed a different crack-tip chemical process zone than is seen in longer cracks, despite being defined as physically short or typical long cracks by their propagation behaviour in the absence of the aggressive environment [53, 60]. Currently, there is no consistent and quantitative definition of short microstructural cracks, although a crack can be considered as a short crack as long as the radius of the plastic zone is larger than one-fiftieth of the crack length according to ASTM [53] or the crack length is less than a critical value, generally ten grain diameters long based on Taylor's definition [68].

Short cracks are characterized by their abnormal propagation behaviour, i.e. much faster crack growth rates are observed than one would expect on the basis of long crack growth data, e.g. they grow below the ΔK_{th} determined for long fatigue cracks, and exhibit highly fluctuating growth rate, which is mainly determined by the very specific local microstructural features at the crack tip such as size and orientation distribution of grains and precipitates and discontinuously varying contributions of crack-tip shielding due to the effects of crack closure, branching and coalescence. In light of the length scale of (microstructurally) short cracks and the significant influence of plastic zone, the material cannot be considered to be a continuum, and hence it is perhaps unsurprising that the LEFM (K/ΔK concept), where the crack-propagation rate depends on the combination of crack length and the remote mechanical stress, is not applicable. Using LEFM based long crack propagation data to deal with the short crack problem in engineering design, usually leads to unconservative life prediction which causes potential safety hazards. In such a situation, either the elastic plastic fracture mechanics approach or a more statistically derived approach is required [60].

To overcome the limitation of LEFM in analysing the stress state of short cracks where the influence of crack-tip plasticity is pronounced, the J integral, i.e. the non-linear elastic energy release rate has been employed [60]. The J-integral is a path independent line integral along a contour around the crack tip which represents the rate of change of potential energy with respect to crack advance. For a cracked body subjected to a purely mechanical monotonic load in the absence of a body force and crack face traction (illustrated in Fig. 2.13 [60]), the J-integral is defined by the following Equation:

$$J = \int_{\Gamma} (wdy - T\frac{\partial u}{\partial x}ds) \tag{2.17}$$

where T is the traction vector with the components of the stress tensor σ_{ij} normal to the integration path Γ, u is the respective displacement vector as shown in the Fig. 2.13, and w is the strain-energy density, and can be expressed as follows:

$$w = \int_0^{\varepsilon_{ij}} \sigma_{ij}\, d\varepsilon_{ij} \tag{2.18}$$

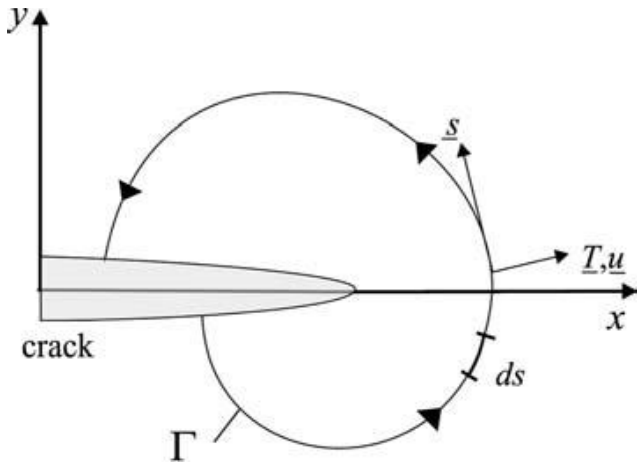

Fig. 2.13 Contour Γ encircling crack tip [60].

Similar to the range of stress intensity factor, the J integral range ΔJ can also be applied to cyclic-loading conditions. It can be applied to fatigue-crack propagation in a similar way to Paris' law for the propagation rate of long cracks vs. the range of the linear-elastic stress intensity factor range ΔK,

$$\frac{da}{dN} = C'\Delta J^{m'} \tag{2.19}$$

It should be noted that strictly speaking the fundamental assumption of the J-integral, that it is a non-linear elastic material (to mimic the elastic-plastic response on loading) means it cannot strictly be held to apply in a cyclic loading situation as unloading will not be reversible. Apart from the J integral, the crack tip opening displacement (CTOD), δ_t is an alternative parameter to characterize the fatigue crack growth driving force under elastic-plastic conditions. The CTOD is typically defined as the distance between two points on the upper and lower crack faces where two 45 ° lines are drawn from the crack tip and intercept. In EPFM, the calculation is based on the results for crack face displacements, whereas it can be related to K under LEFM conditions as shown in the following equation:

$$\delta_t = \frac{\Delta K^2}{\sigma_y E} \tag{2.20}$$

where σ_y and E are the yield strength and Young's modulus of investigated materials, respectively.

2.2.3 Cyclic deformation behaviour of Ni-based superalloys

2.2.3.1 Overview of cyclic deformation

Cyclic deformation behaviour in metallic materials, particularly Ni-based superalloys in this PhD programme, is a consequence of dislocation motion, which is predominantly accompanied by the slip or twinning of the crystal lattice. Although deformation can also occur via dislocation climb or grain boundary sliding under an extremely low frequency loading (which is more likely to be associated with creep processes), it is beyond the scope of this PhD programme, and thereby it is not considered in this section. It is well recognized that the dislocation motion under cyclic loading in Ni-based superalloys is not only closely related to their compositions and microstructures, but also dependent on the temperature, strain rate and strain amplitude [19, 25, 50, 69-72]. The cyclic deformation behaviour of Ni-based superalloys has been extensively reviewed in literature [4, 73, 74]. In this section, some key aspects of the cyclic deformation mechanisms in Ni-based superalloys are briefly discussed and reviewed as fatigue damage at any temperature is related to the deformation processes in combination with possible deformation-related environmental degradation.

As mentioned previously in Section 2.1.4.2, interaction between dislocations and γ′ precipitates is an important strengthening mechanism for Ni-based superalloys and is closely related to the deformation processes. Depending on the size of γ′ precipitates, paired dislocations bypass γ′ precipitates via shearing or Orowan looping mechanism [1]. The precipitate shearing mechanism is associated with planar slip and confines the dislocation motion within the activated slip plane, resulting in inhomogeneous deformation. This inhomogeneous deformation is most significant in the Ni-based superalloys with coarse grains and fine γ′ precipitates, usually indicating by the low slip band density but intense slip bands [8, 9, 37, 50, 75, 76]. Under the cyclic loading in a strain-controlled test, the precipitate shearing mechanism is mainly responsible for the cyclic softening observed in Ni-based superalloys [50, 72]. In contrast to shearing mechanism, Orowan looping mechanism is associated with wavy slip and more homogeneous deformation, especially in the Ni-based

superalloys with fine grains and coarse γ′ precipitates which exhibits high slip band density but less intense slip bands. The Orowan looping mechanism is considered as a reason for the observed cyclic hardening, although cross-slip of screw dislocation and formation of low energy dislocation configuration such as dislocation dipoles and dislocation jogs can also contribute to cyclic hardening [25, 70, 74, 75]. In fact, the cyclic softening and cyclic hardening observed in Ni-based superalloys vary from alloy to alloy, and also vary between different loading conditions [25, 69-71]. For instance, it is reported that continuous cyclic hardening at 400 ^{o}C is observed in TMW-4M3 (that is a new cast-and-wrought Ni-based superalloy with high Co (25.0 wt.%) and Ti (6.2 wt.%) content developed by NIMS, Japan) for turbine disc application whereas cyclic softening at 650 and 725 ^{o}C is examined [25]; however, a cyclic hardening followed by softening until fracture is found in U720Li at 25 and 650^{o}C when the strain amplitude is greater than 0.6% [70]. In addition, cyclic hardening during cyclic deformation increases with increasing strain amplitude accompanied by a decreased fatigue lifetime [69].

2.2.3.2 Cyclic deformation at low and intermediate temperatures

In general, at low and intermediate temperatures where the thermal activation enhanced cross-slip is limited, the predominant deformation occurs via shearing of γ′ precipitates by a pair of a/2 <110> dislocations at high strain rate or a/6 <112> partial dislocations along with intrinsic stacking faults in the precipitates at relatively low strain rate [1, 4]. This precipitate shearing mechanism occurs when the size of γ′ smaller than the critical size (~25nm [75]) for the transition from shearing to looping mechanism. The resultant cyclic hardening effect brought about by increase in dislocation density and slip band density may be offset by this precipitate shearing to some extent. Basically, the relatively low cyclic hardening is observed at low strain in terms of precipitate shearing on single slip band since relatively few active bands are required to carry the imposed strain. As the applied strain amplitude increases, the hardening becomes much more pronounced as there are multiple slip bands and dislocation debris at slip intersections as well as the formation of complicated dislocation networks (e.g. dislocation cells) [69].

If the γ′ precipitate is large enough, the shearing mechanism is overtaken by Orowan looping mechanism, which produces homogeneous deformation [50, 75]. As the cyclic loading proceeds, the number of dislocation loops left around each γ′ increases correspondingly until annihilation and creation of dislocations reach dynamic balance and

dislocation tangles form eventually. This dislocation structures are much more homogeneous in comparison to that observed in the alloys containing small shearable γ′ precipitates, even though slip bands are still observable. The more homogeneous dislocation structures usually result in more rapid work hardening and a higher response stress under a given strain range [75]. In addition, occurrence of mechanical twinning during cyclic deformation is also believed to be a contributor to the cyclic hardening at intermediate temperatures [77-79]

2.2.3.3 Cyclic deformation at high temperatures

As the temperature is increased, cross-slip is enhanced due to the additional thermal activation process, resulting in more homogeneous dislocation structures. The cross-slip of screw dislocations from {111} plane to {001} plane is expected to produce Kear-Wilsdorf lock which contributes to high temperature strength of Ni-based superalloys [1]. However, the cyclic softening is usually observed from the beginning of cyclic loading at high temperature, e.g. in Waspaloy at 800 ^{o}C [50], due to the reduced slip band density, slip band intersections and dislocation density. It is reported that spacing between slip bands is wider in comparison to that at low temperatures, and the dislocation density within the slip bands is much lower, which suggests that the applied plastic strain can be accommodated by fewer dislocations due to the increased mobility of dislocations at high temperatures. Moreover, formation of planar slip bands indicates that shearing of γ′ still occurs even at 800 ^{o}C which results in softening. Similar softening has also been seen in René 80 which has a higher volume fraction of γ′ and mismatch parameter compared with Waspaloy [28].

However, cyclic hardening is also observed at high temperatures. Deformation-induced coarsening of γ′ precipitates may occur, which promotes the occurrence of dislocation looping and thereby causes the continued deformation more difficult, resulting in a hardening effect [4]. In addition, due to the precipitation of carbides (or other precipitates) at dislocations or the segregation of solutes such as C and B at dislocations, which are known as dynamic strain aging [50, 80-82], can produce a pinning effect to hinder dislocation motion, leading to an increase in response stress (hardening effect).

2.2.4 Fatigue crack initiation

2.2.4.1 Overview of fatigue crack initiation

Generally, in Ni-based superalloys and other metallic materials, cracks mainly initiate at a

site which gives rise to a stress concentration, such as grain boundaries [83, 84] or twin boundaries [85, 86], slip bands [37, 85, 86], precipitates [83, 87], carbides [7] and metallurgical defects (non-metallic inclusion and pores) [9, 88, 89]. In most cases, the initiation of cracks is in relation to the strain localization that is usually associated with microstructural heterogeneity, and occurs at the surface if there are few sub-surface defects, except in the case in which the small material heterogeneities such as large grains, pores and non-metallic inclusions in the bulk increasingly govern the fatigue-crack-initiation process because of the small extent of plasticity and negligible significance of the plane stress condition, e.g. in the ultrahigh cycle fatigue [90]. At elevated temperatures, an oxidation-enhanced crack initiation is also widely observed in aggressive environments in Ni-based superalloys [19, 84, 91, 92].

2.2.4.2 Slip band crack initiation

Crack initiation from slip bands at a surface is closely associated with surface roughening behaviour which is usually caused by slip irreversibility as a consequence of dislocation annihilation, cross-slip of screw dislocations and climb of edge dislocations, piling-up of dislocations, transmission of dislocations across grain boundaries and dislocation shearing precipitates [53, 74]. Due to the slip irreversibility, the damage caused by the forward loading cannot be fully recovered during reversed loading, which leads to formation of persistent slip bands and results in strain localisation [74]. The irreversible slip along the persistent slip bands (PSB) usually results in intrusion and extrusion of slip bands which consist of the protrusion and act as stress concentrators at the surface, particularly in the tension condition, and causes crack initiation upon further loading [93-95]. An example of this slip band protrusion and cracking is shown in Fig. 2.14 [96]. Additionally, the larger local strain developed at the PSB/matrix interface observed by optical interferometry stimulates crack initiation to some extent at such regions [53, 97]. This slip band crack initiation is closely related to microstructures of Ni-based superalloys. Basically, the microstructures that promote planar slip, such as coarse grain and fine γ' along with low stacking fault energy as mentioned previously, have relatively high propensity to slip band crack initiation [8, 9, 37, 50, 75, 76].

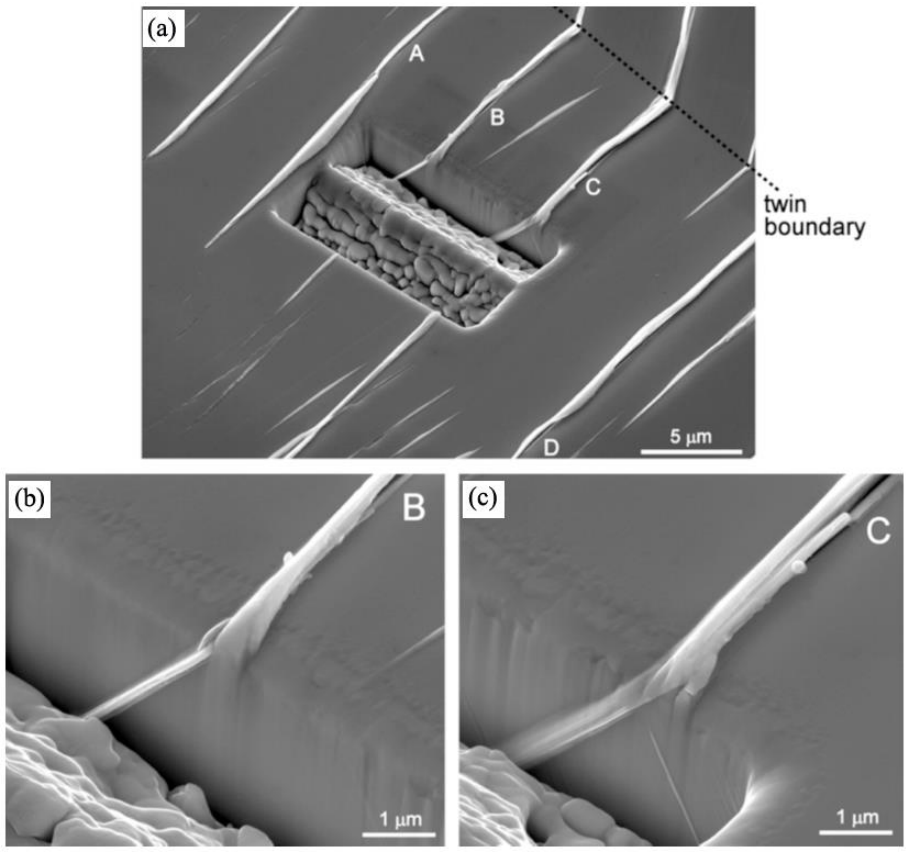

Fig. 2.14 Slip band protrusion and cracking formed in a 316L austenitic stainless steel under a cyclic load with a plastic strain amplitude of 1×10^{-3}: (a) overview of slip bands; (b) and (c) details of slip band protrusion and cracking [96].

Moreover, slip band crack initiation is also influenced by environment as reversed slip is hindered to some extent in the aggressive environments, where the chemisorption of oxidizing or embrittling species (or formation of an oxide film) on the freshly formed slip step makes reverse slip more difficult on the same slip plane upon load reversal. Thus the presence of an aggressive environment provides a mechanism of enhanced surface roughening as well as transport of the aggressive species into the near-surface volumes of the PSBs, thereby facilitating crack initiation. This mechanism is illustrated schematically in Fig. 2.15 [98]. However, such effects of environment on fatigue crack initiation as well as crack propagation and fatigue life almost disappear at really high strains, because the associated deformation events and speed of failure mechanisms are too gross to be significantly affected by the environment. In addition, at elevated temperatures, the yield strength of Ni-based superalloys decreases and the thermal activated processes such as climb are enhanced, which makes the multiple slip processes more easily happen, and thereby decrease the propensity of slip band cracking.

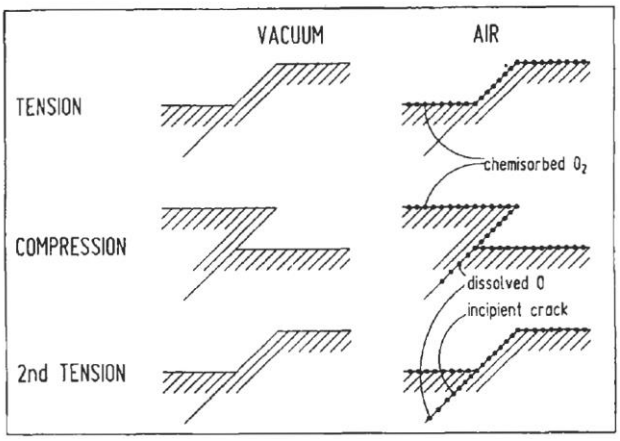

Fig. 2.15 Interaction of an aggressive species with freshly formed slip steps in fatigue, making reverse slip more difficult, entrapping the species in the materials and hastening crack initiation and Stage I growth [98].

2.2.4.3 Grain boundary crack initiation

At higher strain amplitudes, secondary slip systems and/or cross-slip can be activated in addition to primary slip systems and the single slip or planar slip is overtaken by multiple slip or wavy slip, which causes more homogeneous deformation in the materials. Under such circumstances, slip band cracking is not the main mechanism for crack initiation. Conversely, it is found that crack initiation at grain boundaries is a more common situation. It is generally believed that crack initiation at grain boundaries is determined by both the elastic anisotropy and plastic incompatibility of adjacent grains which are closely related to the crystallographic orientation of the grains [53]. Differences in crystallographic orientation of the grains cause stress peaks at the grain boundaries and triple lines that may exceed locally the yield strength and eventually cause fatigue initiation, just as shown schematically in Fig. 2.16 [53]. Normally, the "vulnerable" boundaries are identified as random large angle boundaries as slip bands cannot transfer through these boundaries, resulting in strong impingement of slip bands with grain boundaries (due to the impendence of dislocation motion and dislocation pile-ups). By contrast, the low angle grain boundaries and special grain boundaries (according to the CSL model using the Brandon criterion [99]) are believed to be more resistant to intergranular cracking as slip bands can transmit through these grain boundaries [74, 100, 101], and thereby minimize the stress concentration around these areas. According to Kim and Laird [102-104] and Zhang's [100, 105] work, the influence of plastic slip incompatibility across grain boundaries is predominant during crack initiation for high strain

amplitudes, i.e., low-cycle fatigue (LCF) conditions, whereas elastic anisotropy across grain boundaries becomes most significant during crack initiation at low and very low strain amplitudes, i.e., high cycle fatigue (HCF) and ultrahigh cycle fatigue.

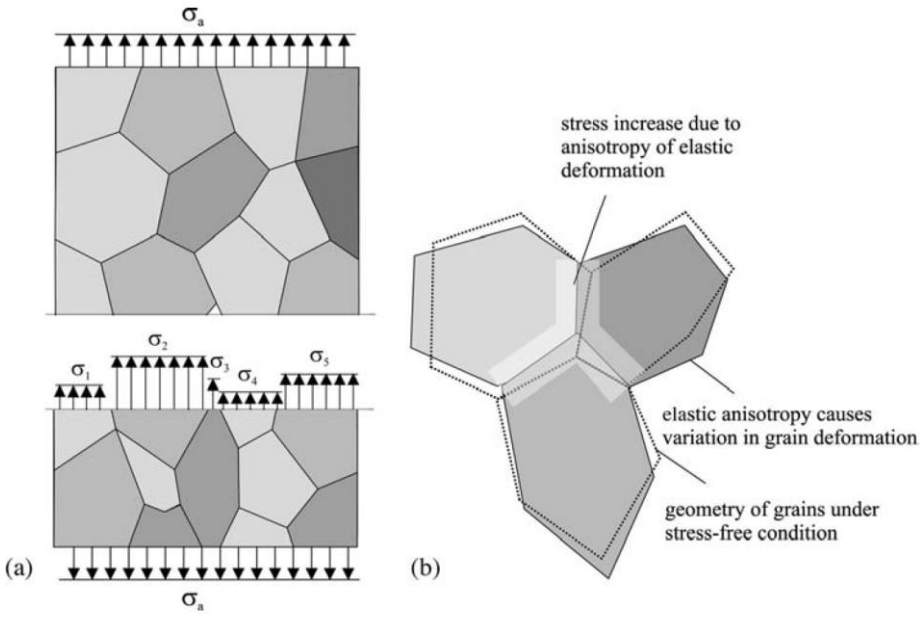

Fig. 2.16 Schematic representation of the influence of crystallographically anisotropic material properties: (a) inhomogeneous stress distribution (simplified for normal stresses only); (b) resulting anisotropy of elastic deformation [53].

Compared with low temperatures, intergranular crack initiation is more commonly observed at elevated temperatures in aggressive environments due to the degradation of grain boundary strength caused by grain boundary oxidation and/or embrittlement. The environmental attack induced intergranular crack initiation is microstructurally sensitive, i.e. finer microstructures are usually associated with more significant environmental attack (due to the larger area of grain boundaries which act as short-circuit diffusion paths for oxidising/embrittling species) and consequently more frequent intergranular crack initiation [19, 84, 91]. In the case of grain boundary oxidation, the growth stress which mainly arises from oxide nucleation and growth due to the volume differences between the oxides and the metals can be superimposed with the applied load, causing brittle cracking of oxides at grain boundaries and contributing to intergranular crack initiation. The volume difference between the oxide and the metal can be expressed by Pilling-Bedworth ratio (PBR) which is the ratio between the specific volume of oxide and the specific volume of the metal that is consumed in oxide formation. For Ni-based superalloys, the PBR for the common oxides is listed in

Table 2.4 [106].

Table 2.4 PBR between common oxides and alloying elements in Ni-based superalloys [106]

Oxide	NiO	Cr_2O_3	CoO	Al_2O_3	TiO_2	WO_3	Nb_2O_5	Ta_2O_5	ZrO_2
PBR	1.65	2.07	1.86	1.28	1.78	3.3	2.68	2.5	1.56

For those disc superalloys which are operated at intermediate temperatures, the most common oxides are NiO, Cr_2O_3, CoO, Al_2O_3 and TiO_2. The Ellingham diagram showing the free energies of formation for the selected oxides is presented in Fig. 2.17 [106, 107], which indicates the stability of these oxides, i.e. Al_2O_3> TiO_2> Cr_2O_3> CoO> NiO in a sequence of decreasing stability. Although Al_2O_3 is the most thermodynamically favourable to form at elevated temperatures, it should be noted that the frequently observed oxides in disc alloys consist of external Ni/Cr oxide scale along with internal Al_2O_3 scale. This configuration of oxide scales is mainly determined by the oxidation kinetics which are closely related to the cation and anion diffusion within the oxide scale and the alloy matrix. The faster formation of Ni and/or Cr oxides is probably due to the abundance of Ni and Cr in the alloy matrix and their relatively high migration rate in comparison to Al as indicated by the parabolic rate constants shown in Fig. 2.18 [106].

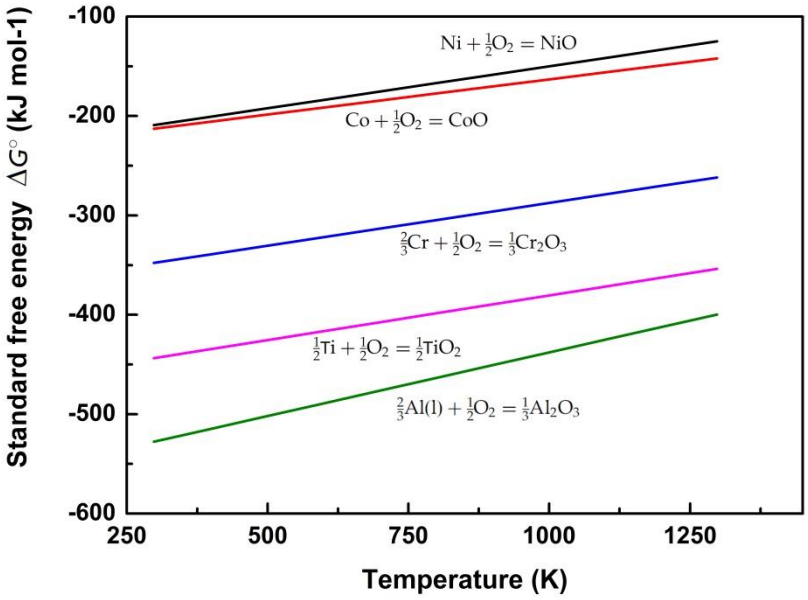

Fig. 2.17 Ellingham diagram showing the free energies of formation of the most common oxides found in disc Ni-based superalloys [106, 107].

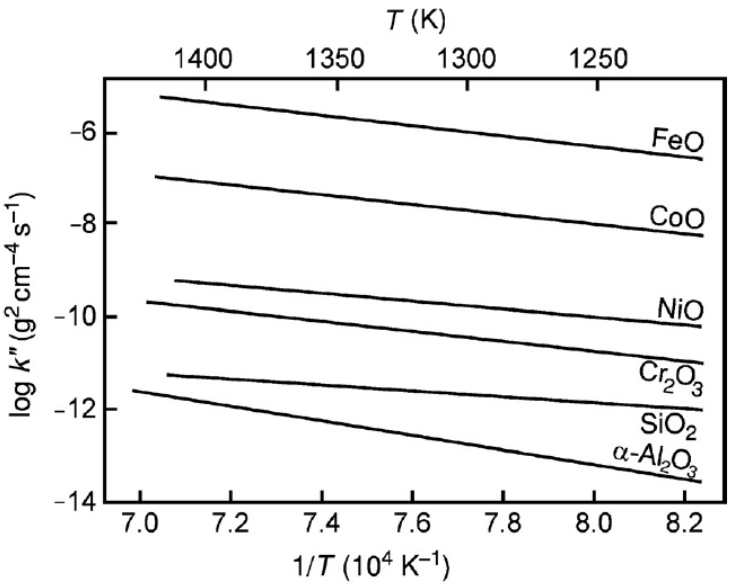

Fig. 2.18 Parabolic rate constants for the growth of several oxides [106].

In addition to high-temperature oxidation or corrosion effects, creep is the second key factor determining the fatigue life of Ni-based superalloys under long dwell fatigue conditions. Formation of cavities or pores at grain boundaries or triple points because of the combination of grain boundary sliding and vacancy diffusion towards areas of high hydrostatic tension during creep process stimulates intergranular crack initiation as well [53].

2.2.4.4 Twin boundary crack initiation

Twin boundary is a distinguished characteristic in polycrystalline Ni-based superalloys for turbine disc application due to the low stacking fault energy. It is commonly observed that cracks initiate from twin boundaries at low temperatures as the presence of TBs further increase the heterogeneity of the slip band distribution [86, 108, 109]. It is reported that concentrated slip bands form adjacent to twin boundaries due to the high elastic incompatibility stress, resulting in strain localisation that further causes crack initiation at twin boundaries [108]. However, there are still debates on the role of twin boundary in crack initiation as the improved resistance of twin boundaries to crack initiation has also been observed in other fcc metallic materials [110, 111]. It is generally believed that TBs are inherently stronger against intergranular cracking in materials with high SFE, while in low SFE materials (e.g. Ni-based superalloys), TBs accommodate much of the plastic deformation, leading to strain localisation and crack nucleation at the TBs [110]. But at elevated temperatures, it is widely accepted that twin boundaries are beneficial in improving

crack initiation resistance due to the enhanced resistance to environmental attack brought about the relatively high lattice coherence and relatively low TB energy compared with the random high angle grain boundaries [28-30, 32, 33, 112].

2.2.4.5 Crack initiation at inclusions, pores and carbides

In addition to slip band and grain boundary initiations, cracks are also inclined to initiate at the interface of inclusions/matrix due to their different elastic properties or different coefficients of thermal expansion, which are capable of raising the mechanical stress in the vicinity of the interface during mechanical or thermal loading. Of course, the level of this stress increase depends strongly on the size of the inclusions. Pore crack-initiation is also observed in Ni-based superalloys. Crack initiation at pores and inclusions are closely related to the test or in-service conditions. In general, low temperatures and low applied strain/stress result in relatively high propensity of pore and inclusion crack initiation [2, 19]. In addition, oxidation of precipitates, e.g. carbides, at elevated temperatures also causes crack initiation. It has been found in Connolley's work for example that the oxidation of Nb-carbides in Inconel 718 superalloy at 600 ^{o}C results in a significant volume expansion around the particles due to the different densities of the original carbides and oxidizing products, and thereby leads to crack initiation [7, 113].

2.2.5 Short crack propagation behaviour

2.2.5.1 Overview of short crack propagation

As discussed previously in Section 2.2.2.2, the term short crack or small crack is used to describe the kind of cracks whose plastic zone is comparable to the crack length and thereby LEFM is not applicable in describing the crack driving force/crack tip stress state. At low temperatures such small cracks grow along crystallographic slip planes, mostly inclined to an angle close to 45° with respect to the applied stress axis, driven by the maximum resolved shear stress (loading mode II) and strongly interact with local microstructural features. The crack itself and crack tip interaction region generally spans only several grain diameters, and hence short cracks cannot be detected by conventional methods of non-destructive materials testing, like ultrasonic testing or X-ray analysis, which are typically provided a resolution of the order of 0.5 mm. Although recently developed detection methodologies such as high resolution X-ray computed tomography or synchrotron radiation computed tomography can

provide a fine resolution (down in some circumstances to 0.8 μm) to discern short cracks in-situ non-destructively in three dimensions (3D), these approaches are best suited for polymer, carbon fibre reinforced carbon composites and some light metal and alloys such as aluminium alloys due to attenuation effects. Currently the most widespread method to investigate short fatigue crack growth behaviour is limited to surface observations via replicating the morphology of cracks with acetate or silicone compounds, and examining the resultant replica via optical and scanning electron microscopy.

In light of the importance of understanding short crack growth behaviour for engineering design and making a reasonable prediction of the lifetime of engineering components, a considerable amount of research has already been carried out in this area. In the remit of this study it is significant to note that the majority of a turbine disc's fatigue life is determined by the early stages of crack growth, such that short crack initiation and growth is the relevant fatigue condition for this service application. It is widely accepted that the most distinctive characteristics of short fatigue cracks are their abnormally high but greatly scattered growth rate below the stress intensity threshold of long crack observations and the strong interaction with local microstructural features. For fcc metallic materials, specifically Ni-based superalloys, short cracks at low temperatures often grow predominantly on {111} planes along <011> directions in individual grains until the activation of other secondary slip systems [1, 11]. At this point single slip is overtaken by multiple slip and the cracks grow in a direction perpendicular to the remote normal stress, thus the factors influencing the slip behaviour of materials and slip transmission across the grain boundaries can significantly influence the short crack propagation behaviour, such as the size and orientation distribution of the grains and precipitates. In addition, enhanced short crack propagation and coalescence have usually been observed at elevated temperatures due to the effects of stress assisted grain boundary oxidation (SAGBO) or dynamic embrittlement of grain boundaries [16, 19, 84].

2.2.5.2 Effects of grain size

It is well established that grain size has great influence on the strength of materials, either in static conditions or cyclic conditions, and impacts the dislocation motion during deformation. On the one hand, as the grain size increases, the free slip length for dislocations increases accordingly, and the amount of dislocations piling up or pairing along the slip band increases as well until either the grain boundary becomes ineffective as a barrier for the succeeding dislocations or dislocation sources in the adjacent grains are activated. Therefore,

the coarse grain is apt to promote planar slip, which makes Stage I or mode II short cracks grow more easily. In addition, the greater the grain size, the lower the number of grain boundaries acting as obstacles to slip transmission of dislocations, resulting in poor crack growth resistance. On the other hand, the enhanced planar slip in a coarse grained structure is associated with increased reversibility of slip giving lower damage accumulation and more tortuous crack paths [8, 9, 37].The typical influences of grain size on the short crack growth behaviour at room temperature or elevated temperatures can be found in Pang's research about disc alloy U720Li [9, 37]. In his work, fatigue crack initiation and short crack propagation behaviour in U720Li and its microstructural variants, i.e. U720Li-LG (large grain variant) and U720Li-LP (large intragranular coherent γ' precipitate variant) have been assessed by replicated short crack tests. It is found that crack propagation is highly faceted due to planar slip band cracking immediately after crack initiation followed by a transition to a flatter Stage II type crack path as crack length increases at room temperature. U720Li-LG shows a slightly improved crack growth resistance compared with as-received U720Li because of the increased slip reversibility, although its fatigue lifetime is less than that of U720Li-LP due to the relatively lower fatigue crack initiation resistance. At elevated temperature (650^{o}C), a transition from transgranular crack growth to oxidation-assisted intergranular crack growth can be observed after the short crack propagates beyond four to six grain diameters in air. U720Li-LG shows the most significant performance benefits in terms of overall fatigue lifetime under the test conditions as the larger grain size not only prolongs the initial slow transgranular crack growth after crack initiation but also improves high temperature oxidation-assisted intergranular crack growth resistance due to less embrittled grain boundaries and more tortuous crack paths.

2.2.5.3 Effects of grain orientation

It is worth mentioning however that short crack growth is a complicated function of microstructural factors. Apart from the grain size, the crystallographic orientation of grains (or GB misorientation) and respective slip planes impact the dislocation slip transmission and short crack growth behaviour to a significant extent. Initially, the interaction between short crack and grain boundary is observed in two dimensions due to the limitation of experimental equipment and processed by a two-dimension LEFM approximation. It is believed that the retardation effects of grain boundary on transgranular short crack growth (especially in HCF tests at relatively low temperatures) are determined by the crystallographic orientation of

neighbouring grains, i.e. the small angle grain boundaries are less effective to hinder the short crack growth, whereas boundaries with higher misorientation angles on average tend to cause larger crack deflections and result in larger crack-growth retardations (if the segregation, precipitation and oxidation of grain boundary are not taken into account). Additionally, at fixed grain-boundary misorientation angles, special boundaries are no more effective than random boundaries in impeding transgranular small crack growth [29, 112]. Furthermore, the spatial arrangement of slip planes in the adjacent grains or misorientation of neighbouring slip planes is a more critical influential factor on short crack growth compared with the misorientation of neighbouring grains according to Zhai's research [114], which is schematically shown in Fig. 2.19 and supported by a directed 3D observation of the interaction between short cracks and grain boundaries due to the recently employed application of focus ion beam (FIB) tomography [115-117]. It is pointed out that the grain boundary can still continue to exert an effective drag on the crack front due to fracture of the area "abc" on the grain boundary plane (Fig. 2.19) after the crack tip passes the grain boundary on the surface, until the crack crosses the whole grain boundary plane beneath the surface because of the normally semi-elliptical shape of a short fatigue crack. As a result, the growth rate of the crack tip inside a given grain on the sample surface is still significantly influenced by the grain boundary that it has just passed on the surface, in addition to the orientation of that grain.

The influences of grain orientation on intergranular short crack propagation are manifested by stress/strain assisted degradation (e.g. oxidation and corrosion) of grain boundary properties which is related to strain accumulation and stress concentration in the vicinity of grain boundaries. The orientation-dependent strain accumulation or stress concentration at grain or subgrain level can be measured by high resolution digital image correlation (DIC) in combination with electron backscatter diffraction (EBSD) [118], and can be simulated by crystal plasticity model [119, 120]. Generally, large misorientation between neighbouring grains or large differences in Schmid factor of the active primary slip systems in the neighbouring grains is associated with significant dislocation pile-ups and strain accumulation [118, 121], and thereby may facilitate the degradation processes of grain boundary properties induced by oxidation and/or corrosion. In addition, the grain boundary energy which is associated with grain orientation and the lattice coherence of the neighbouring grains also has influence on the grain boundary degradation processes and further influences the intergranular short crack propagation [27-29]. Based on the CSL model,

low angle grain boundaries and special grain boundaries with low CSL Σ value usually correspond to low grain boundary energy [99, 122, 123], which means these grain boundaries are more insensitive to environmental attack. For instance, the frequent observed crack initiation and early propagation at Σ3 twin boundaries (with a misorientation angle of 60^{o}) in Ni-based superalloys at low temperatures are closely related to the strain accumulation around this Σ3 twin boundaries [86, 118], whereas Σ3 twin boundaries show good resistance to short crack propagation at elevated temperatures due to the high lattice coherence and low grain boundary energy as well as more homogeneous deformation (at elevated temperatures).

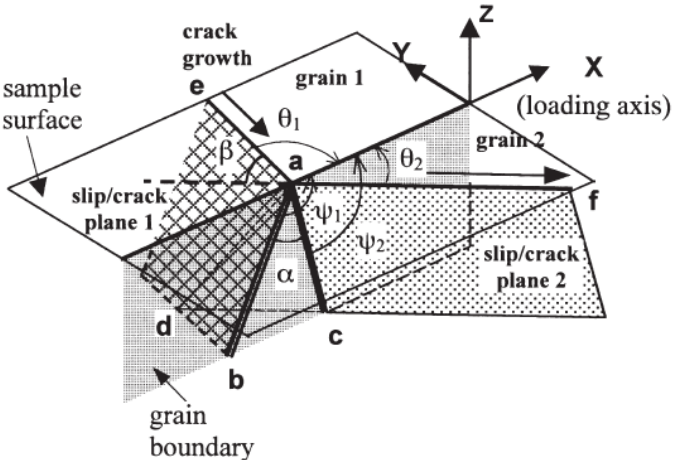

Fig. 2.19 Schematic diagram showing a crystallographic mechanism for crack growth along slip plane 1 in grain 1 on to slip plane 2 in grain 2. The crack growth is controlled by α and β [114].

2.2.5.4 Effects of precipitates

As illustrated in the preceding Section 2.1.4.2, γ′ precipitates are effective barriers for dislocation motion, and thereby they are also effective barriers for crack propagation. Depending on the γ′ size, dislocation-precipitate shearing or looping mechanism can occur, producing planar slip or wavy slip, which influences the early transgranular crack propagation. Moreover, the retained primary γ′ in P/M Ni-based superalloys after solution heat treatment produces elastic strain field which is expected to interact with cracks, and it may accelerate or decelerate early short crack propagation [8, 37]. With traditional metallurgical sectioning methods, it is found that the cracks can either cut through the γ′ precipitates or deflect at the interfaces of γ′ precipitates and matrix materials depending on the degree of coherence and the elastic–plastic properties of the respective particles with

respect to the surrounding matrix material. In some cases, the cracks are arrested by the precipitates and then stop growing for a few thousands of cycles before the crack growth resumes or even stop growing completely [37]. Recently, the interaction between short cracks and precipitates has been carefully investigated by 3D FIB tomography technique in a directionally solidified Ni-based superalloy [124]. It is reported that the crack tends to bypass the precipitates by forming steps in the crack plane and this behaviour depends on the mechanical properties of the precipitates with respect to the matrix material. However, in the cases where oxidation exists, the interfaces of precipitates/matrix are usually preferential path for early crack propagation due to the degradation of boundary properties [92].

2.2.5.5 Effects of temperatures

The microstructural contributions to short crack growth decrease with increasing test temperature. Generally speaking, the influences of temperature on short crack propagation are embodied by the influences of temperature on slip behaviour in Ni-based superalloys and possible stress relaxation/creep behaviour when long dwell load is employed. At higher temperatures, the additional thermal energy stimulates the activation of secondary slip and cross-slip, resulting in reduction of critical resolved shear stress and causing short cracks to grow less crystallographically. Studies regarding the influence of the temperature on short fatigue crack propagation behaviour in Waspaloy with an in-situ test in an SEM conducted by Stephens et al. [85] shows that the crack grows predominantly by slip band cracking at 25 °C and 500 °C. The surface crack profiles are much flatter at 500 °C than those observed at 25 °C owing to an increase in slip activity and the presence of cross-slip during crack extension, whereas crack growth proceeds primarily by a Stage II type of growth with very little crystallographic growth at 700 °C. In addition, the influences of temperature on short crack propagation may be coupled with the influences of environments, resulting in accelerated intergranular short crack propagation due to degradation of grain boundary properties.

2.2.5.6 Extrinsic short crack propagation

Interaction of the stress field of two mutually approaching short cracks may cause crack shielding and blunting, therefore decreasing the crack growth rate until the coalescence of short cracks happens [113]. It is reported that formation of micro-cracking field ahead of the crack tip can significantly contribute to crack propagation resistance [125]. In some cases

where initiation processes were very easy (e.g. cracking of multiple carbides [126]) subsequent crack growth was observed to be extremely slow, as the closely neighbouring cracks robbed surrounding crack tips of the required strain fields to propagate and lifetime was effectively controlled by coalescence events. Furthermore, crack closure induced by a plastic deformation left by the wake of propagating crack, a mutual displacement of the two crack faces or the asperity of fracture surface and a volume increase in the vicinity of the crack tip due to the oxidation or transformation also influences the short fatigue crack growth behaviour, although the effects of crack closure on the near-threshold crack growth behaviour are investigated more extensively [53, 127, 128].

2.2.6 Long crack growth behaviour

2.2.6.1 Overview of long crack growth

The growth behaviour of a long fatigue crack is the synergistic result of microstructure, temperature, environment in combination with loading mode, although the influences of microstructure become much less significant compared with short crack propagation. The resultant fracture mode can be transgranular or intergranular or a mixture of both of them depending on the specific in-service or testing conditions. Correspondingly, the fatigue behaviour can be termed as cycle-dependent fatigue or time-dependent fatigue on the basis of the degree of crack growth responding to the time-related effects. Generally, low temperature, high frequency in combination with vacuum or inert environment tend to produce cycle-dependent fatigue crack growth, whereas a high temperature, low frequency as well as aggressive environments promote time-dependent fatigue crack growth

2.2.6.2 Effects of grain size

After crack initiation, the crack-propagation direction changes from close to 45° to 90° with respect to the remote normal stress after passing through a few grains (Stage II crack growth). Even though the influences of microstructure on long crack propagation become less significant, improved fatigue crack growth resistance has still been observed in Ni-based superalloys with a coarse grained microstructure and large coherent precipitates under the same in-service or testing conditions, such as in P/M Astroloy [43], U720Li [129] and Inconel 718 [130]. This has been explained as being due to the longer slip paths and enhanced slip reversibility, as well as more significant crack deflection and crack closure

effects. This is despite the expected competing effects of fewer grain boundaries which can act as crack-growth barriers and a lower degree of discontinuity, which should make cracks able to propagate more continuously, resulting in poorer crack growth resistance [40, 76, 129-134].

2.2.6.3 Effects of temperature

At elevated temperatures, the fatigue crack growth rate is supposed to be increased due to the enhanced dislocation mobility (cross-slip and climb) and the decrease in the yield strength and elastic modulus of materials, which result in an increase of CTOD on the basis of Equation 2.20. Similarly to the stress intensity factor range ΔK, the CTOD is also considered as an indicator of fatigue crack growth driving force. An increase of CTOD normally results in faster crack growth. In addition, the higher diffusivity of aggressive species at high temperature is expected to make a contribution to a faster crack propagation rate as well due to the accelerated degradation of grain boundary properties [12, 13].

With the increasing temperature, the thermal-activated processes such as creep and stress relaxation become more evident. A great deal of research indicates that the activation of creep processes contributes to a deterioration in fatigue crack growth resistance and the transition from transgranular fracture to intergranular fracture due to the formation of voids at grain boundaries by grain boundary sliding and vacancy diffusion, especially when a long dwell is employed during the cyclic loading [44, 135, 136]. In contrast to creep, the activation of stress relaxation that is closely related to the size of precipitates is believed to reduce the fatigue crack growth rate because of the decreased crack growth driving force ahead of the crack tip. According to NASA's research [40, 137], the stress relaxation behaviour in LSHR alloy is predominantly determined by the tertiary γ′ even though their volume fraction is one order of magnitude lower than that of secondary γ′. Larger tertiary γ′ enhances stress relaxation during the dwell fatigue test [40], which improves fatigue crack growth resistance.

2.2.6.4 Effects of oxidation and dynamic embrittlement

Oxidation, particularly grain boundary oxidation or carbide oxidation is a common phenomenon for fatigue tests at elevated temperatures in air in Ni-based superalloys. This causes degradation of fatigue crack growth resistance accompanied by intergranular fracture [13, 43, 138]. A schematic diagram of the oxides formed around the crack wake and in the

crack tip is shown in Fig. 2.20 according to a recent study on RR1000 [17]. The oxides formed consist of external NiO/CoO layer and internal $Cr_2O_3/TiO_2/Al_2O_3$ layer. The oxides formed ahead of the crack tip not only lead to weakening of the grain boundaries, but also act as stress concentrators. In addition, the brittle nature of these oxides usually causes oxide cracking upon loading and unloading, and thereby accelerates the crack propagation.

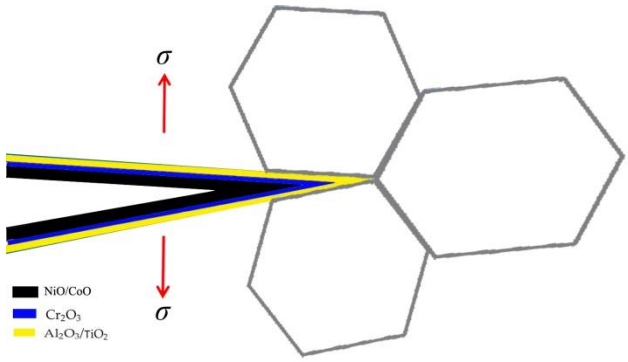

Fig. 2.20 Schematic diagram of the formed oxides around crack wake and ahead of the crack tip [17].

The degree of oxidation ahead of the crack tip is usually determined by the chemical composition of the alloys, the oxygen partial pressure or the content of aggressive species and the applied load/the accumulated inelastic strain at the crack tip [12, 13, 17, 139-144]. Based on Molins' work [13], there is a critical oxygen partial pressure (i.e. 10^{-1}Pa) beyond which oxidation assisted fatigue crack growth proceeds dramatically, and this critical oxygen partial pressure is closely related to the chromium content of the investigated superalloy (i.e. IN718). In this case it appeared there was little dependence on the mechanical loading such as the waveform, frequency and load amplitudes. It is reported that the intergranular embrittlement mechanism is a result of the formation of Ni-based oxide nuclei at the crack tip during the propagation stage, and the enhanced fatigue crack growth is closely related to the prolonged passivation time that is required to form protective oxide layer ahead of the crack tip or oxide/metal interface [12]. By making alloying modifications, to enhance chromia forming (reduce the passivation time), or by appropriate heat treatments leading to a quicker stress relaxation of the material near the crack tip, the crack growth resistance in an aggressive environment can be improved to some extent [12, 13].

It should be pointed out that the oxides formed ahead of the crack tip vary from alloy to

alloy due to the complicated compositions of turbine disc Ni-based superalloys [17, 140, 144], e.g. layered oxides in a thermodynamic sequence of CoO, NiO, Cr_2O_3, TiO_2 and Al_2O_3 formed in disc alloy RR1000 [17]. The degree of oxidation and/or the oxide intrusion ahead of the crack tip is dependent on the testing or in-service conditions, particularly the applied load and the local accumulated inelastic strain [17, 140, 144]. It is reported that the applied load does not change the nature of the oxidising products, but it enhances the oxidation process and produces a thicker oxide layer in comparison to the stress-free scenario [142, 143]. The enhanced oxidation effect associated with the applied load/accumulated inelastic strain is rationalised by the accelerated diffusion of oxide-forming elements aided by stress or the high densities of dislocation and vacancy brought about by the accumulated strain [62, 143]. As a consequence of the combined damage of oxidation and fatigue load, an accelerated crack growth has usually been observed. However, in some cases, a faster formation of a protective Cr_2O_3 layer is also observed as the defects induced by applied load facilitate diffusion of Cr and reduce the duration of the less protective transient oxidation period [145]. More details about the interaction between oxidation and crack propagation are reviewed by Leo Prakash et al. [3], Woodford [146] and Pineau et al. [4].

In addition, the penetration of an oxidizing or embrittling species such as oxygen or moisture into a grain boundary or phase boundary which is accomplished by stress-induced grain-boundary diffusion will cause a decrease in cohesion strength in those areas, which is known as dynamic embrittlement [15, 16, 147, 148]. It is widely accepted that this dynamic embrittlement also enhances crack propagation. The intergranular fracture in such cases can be attributed to a combination of stress-assisted grain-boundary diffusion of an embrittling species followed by interfacial decohesion at a small scale, which is shown in Fig. 2.21 schematically [53]. It is worth noting that the phenomenon of dynamic embrittlement which involves the penetration of grain boundaries by embrittling elements (e.g. oxygen atoms) is different from the phenomenon of SAGBO. The former results in decohesion of metallic grain boundaries, but SAGBO involves cracking of a bulk oxide at grain boundaries. The role of stress in SAGBO is to assist in the accommodation of the volume expansion that accompanies bulk oxide formation. In dynamic embrittlement the role of stress is to provide the driving force for the diffusion of embrittling atoms into the solid, usually along grain boundaries [15].

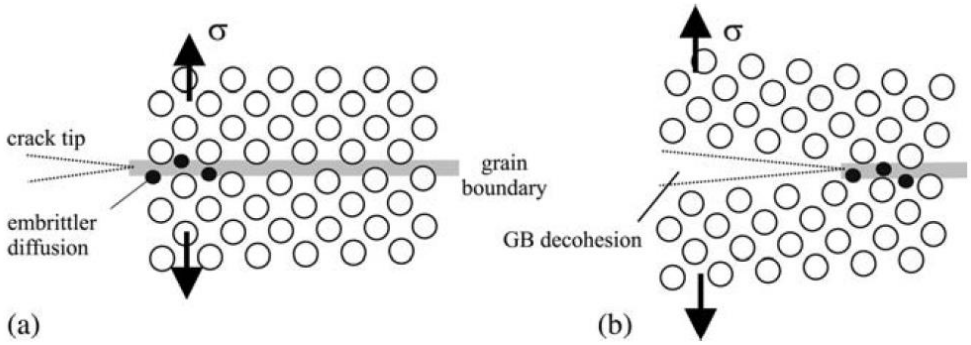

Fig. 2.21 Schematic representation of the dynamic embrittlement mechanism: (a) grain boundary diffusion of an embrittling element in the elastically stretched cohesive zone ahead the crack tip, followed by (b) local decohesion [53].

2.2.6.5 Effects of loading mode

Loading mode also has an influence on the fatigue crack growth. The loading mode can be described by the load amplitude, load ratio and frequency as mentioned previously in Section 2.2.1, as well as the dwell time at maximum and minimum load in the dwell-fatigue test. The larger the load amplitude, the faster the crack growth will be due to the enhanced crack driving force which can be easily understood to be due to the increase in stress intensity factor range. In terms of influence of load ratio, it is reported that increasing the load ratio generally lowers the value of ΔK_{th} and increases crack growth rates due to the absence of crack closure effects [149], and the influence of load ratio on ΔK_{th} is more significant in superalloys with coarse grained structure compared with fine grained structure superalloys [150]. When the crack growth data are plotted against an effective stress intensity range, ΔK_{eff}, rather than ΔK, the majority of the results obtained for differing load ratios fall within a small range of scatter and a similar value of ΔK_{th} is seen [151]. The effective stress intensity factor range, ΔK_{eff} is defined as:

$$\Delta K_{eff} = K_{max} - K_{closure} \tag{2.21}$$

where K_{max} is the maximum applied stress intensity factor, and $K_{closure}$ is the stress intensity factor below which crack face contact will occur. ΔK_{eff} is relevant only when the value of $K_{closure}$ is greater than K_{min}. In the case of significant oxidation-fatigue the contributions to closure effects may be two-fold: the oxide itself at the crack tip can act to enhance closure effects, and the increased surface roughness due to the increased intergranular crack growth modes can also contribute, i.e. both oxide and surface roughness induced closure effects may

be present. As a matter of fact, closure is only really likely to affect observed fatigue performance at the ΔK levels close to the threshold region.

The influence of frequency and dwell time on fatigue crack growth is correlated to temperature and environment effects. At room temperature, crack growth rates are generally not affected by loading frequency, particularly in vacuum or inert condition, whereas the crack growth rate is markedly influenced by loading frequency in air or aggressive environments at elevated temperatures particularly when the loading frequency is low [61, 152-154]. As shown in Fig. 2.22, the crack growth rates are largely independent of frequency due to a lack of time dependent processes in operation at high frequency and the corresponding fracture surface is usually transgranular and featureless [135]. As the loading frequency is lowered or the dwell time at maximum load is increased the contribution to crack growth from time dependent processes such as creep and oxidation becomes more significant although in some cases in which the stress relaxation is activated and the stress at the crack-tip may be sufficiently lowered to reduce crack growth rates. The fracture surface changes from transgranular to mixed-trans-intergranular or even fully intergranular.

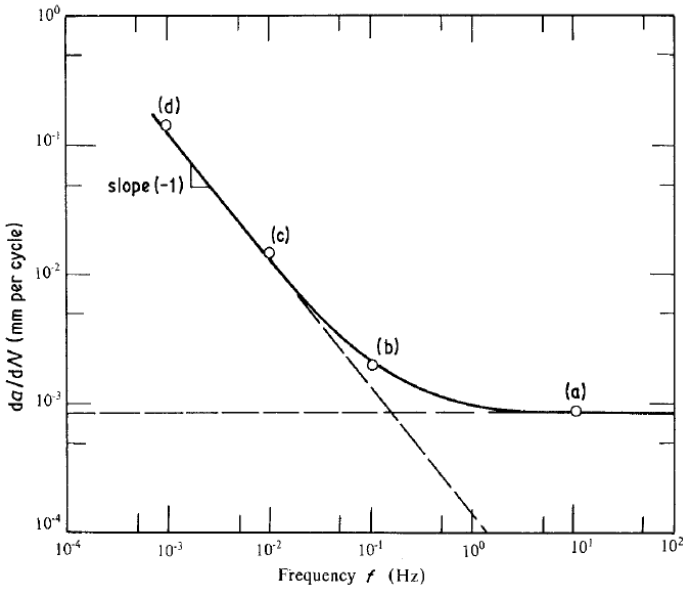

Fig. 2.22 Frequency dependence of crack growth per cycle at ΔK= 50 MPa√m when R=0.1 in Alloy AP1 [135].

2.4 Summary of literature review

- Ni-based superalloys have been widely used for aeroengine turbine disc due to their

excellent combined mechanical properties and good oxidation/corrosion resistances at elevated temperatures. By adapting proper alloying design, the processing versatilities and the overall performance of the disc alloys can be improved to a significant extent. However, a trade-off of the microstructures of the disc alloys still need to be made to balance the creep and fatigue performance. The microstructures such as fine grain and fine γ′ which correspond to good fatigue performance and tensile strength are usually associated with inferior creep and oxidation resistance. A dual microstructure heat treatment has been used to process turbine disc in an attempt to yield site-specific microstructures across the disc to optimize the fatigue-creep-oxidation resistance/performance.

- Cyclic deformation in Ni-based superalloys is closely related to microstructures, especially the size of γ′ precipitates. Generally, dislocations bypass γ′ precipitates via shear-cutting mechanism if the γ′ precipitates are smaller than a critical size, which is usually associated with cyclic softening. On the contrary, dislocations bypass γ′ precipitates via looping mechanism if the γ′ precipitates are large enough, which is usually associated with cyclic hardening. Lowering the SFE in the disc alloy systems favours the occurrence of the precipitate shear-cutting mechanism. The cyclic deformation in Ni-based superalloys also depends on the test conditions. The variety in the test temperature, the employed strain rate and strain amplitude during fatigue loading further complicate the cyclic deformation (cyclic softening and cyclic hardening) behaviour.
- Depending on whether crack initiation dominates the fatigue failure or crack propagation dominates the fatigue failure, the total-life approach or damage-tolerance approach is employed in the fatigue design of engineering components. The total-life approach is useful for selecting materials where resistance to crack initiation is important, whereas the damage-tolerant approach is adopted to deal with the cases where resistance to crack propagation is important.
- Cracks mainly initiate at a site which gives rise to a stress concentration, such as a grain boundary, twin boundary, slip bands, precipitates and metallurgical defects (non-metallic inclusion and pores). The crack initiation is closely related to strain localisation which is generally associated with the microstructural heterogeneity and its response to fatigue loading in the cases where oxidation/corrosion is absent. At elevated temperatures in the aggressive environments, oxidation/corrosion of grain boundaries and precipitates comes into effect, and the localised strain may facilitate

the oxidation/corrosion processes. As a result, crack initiation is expected to result from the competing (or combined) effects between oxidation/corrosion damage and mechanical damage due to strain localisation.

- Short fatigue cracks are characterized by their abnormally high but greatly scattered growth rate below the stress intensity threshold of long crack observations and the strong interaction with local microstructural features. The factors influencing the slip behaviour of Ni-based superalloys and slip transmission across the grain boundary can significantly influence the short crack propagation behaviour, such as the size of the grains and precipitates as well as grain misorientation. Aggressive environments make short crack propagation less microstructure-sensitive, exhibiting somehow more extrinsic propagation behaviour such as crack closure or crack coalescence. However, the microstructure-dependent deformation (mechanical damage) can exert influences on the oxidation/corrosion processes, which in turn influences the short crack propagation behaviour in aggressive environments.
- The growth behaviour of long fatigue crack is the synergistic result of microstructure, temperature, environment in combination with loading mode, although the influence of microstructure is expected to be less significant as that on short crack propagation. Depending on the loading conditions and environments, the damage arising from fatigue, creep and oxidation may happen simultaneously. Distinguishing the individual contribution of fatigue, creep and oxidation damage to crack growth and identifying the corresponding influential factors are challenging but necessary. Generally, low temperature, high loading frequency in combination with vacuum or inert environment tend to produce cycle-dependent fatigue crack growth, whereas high temperature, low frequency as well as aggressive environment promote time-dependent fatigue crack growth.

Chapter 3 Material characterisation

3.1 Introduction

Material microstructures are closely related to mechanical properties. Characterization of the microstructures of the LSHR alloy and its (static) mechanical properties is essential to understand fatigue crack initiation and propagation mechanisms under the dwell cyclic load conditions discussed in the following chapters. The tensile properties (or stress-strain response) are needed to estimate the local stress/strain distributions achieved in the dwell fatigue tests. Creep/stress relaxation may occur simultaneously during fatigue testing, and may make a significant difference to fatigue failure processes, especially at long dwell periods. Understanding of creep/stress relaxation behaviour is helpful to further assess the stress/strain evolution during the dwell period, and thus better reveal the fatigue failure mechanism.

In this chapter, the microstructures of the LSHR alloy were investigated by standard metallographic methodologies. Tensile tests at room temperature were conducted to obtain the stress-strain data, whereas high temperature tensile properties were extracted from reported NASA' data [155] and interpolated/extrapolated by a Ramberg-Osgood relationship for the stress-strain data at the temperatures of interest where no experimental data are available. The creep/stress relaxation properties were also extracted from reported NASA' data [18, 19, 40, 156] and summarized. Some aspects of the work detailed in this chapter have been published in the following paper:

R. Jiang, S. Everitt, M. Lewandowski, N. Gao, and P. A. S. Reed, International Journal of Fatigue 62 (2014): 217-227.

3.2 Material processing route

The materials used in this study were extracted from P/M LSHR alloy turbine disc which was fabricated by canning atomized LSHR alloy powder, and then hot isostatic pressing, extrusion and isothermal forging. Two different forging conditions were intentionally employed, to enable different grain sizes after heat treatment. The composition of the LSHR alloy is listed in Table 3.1. The specimens extracted from the disc processed in the first forging condition are referred as batch 1 LSHR alloy. Batch 1 LSHR alloy was then

supersolvus and subsolvus heat treated to yield CG and FG microstructures respectively, this was followed by the same dual stage aging to modify the precipitation behaviour of secondary and tertiary γ′. Hereinafter, the supersolvus heat treated batch 1 LSHR alloy is referred to CG LSHR alloy and the subsolvus heat treated batch 1 LSHR alloy is referred to FG LSHR alloy. The details of the heat treatment routes are shown in Table 3.2. The specimens extracted from a disc processed in the second forging condition are referred to batch 2 LSHR alloy, and the detailed heat treatment routes for this batch of LSHR alloy are shown in Table 3.3.

Table 3.1 Composition of LSHR alloy (in wt.%)

Cr	Co	Mo	Ti	Al	C	B	W	Zr	Ta	Nb	Ni
12.5	20.7	2.7	3.5	3.5	0.03	0.03	4.3	0.05	1.6	1.5	Bal.

Table 3.2 Heat treatment of batch 1 LSHR alloy

Supersolvus heat treatment	1135°C/1.5h, furnace cool	→	1171°C/1h, cooled 72°C/per minute	→	855°C/4h, Air cool	→	775°C/8h, Air cool
Subsolvus heat treatment	1135°C/1h, cooled 202 °C/per minute	→	855°C/4h, Air cool	→	775°C/8h, Air cool		

Table 3.3 Heat treatment of batch 2 LSHR alloy

Supersolvus heat treatment	1171°C/2h, cooled 72 °C/per minute	→	855°C/4h, Air cool	→	775°C/8h, Air cool

3.3 Experimental procedures

3.3.1 Microstructural characterization

The specimens for microstructural characterization were cut to a size of 10×10 mm^2 in cross section, and mounted in Bakelite, and then ground on 180, 800, 1200 and 4000 grit abrasive papers sequentially, followed by a 0.25 μm OPS polish on a Struers polishing machine. The LSHR alloy was etched by Kalling's reagent (80ml HCl + 40ml CH_3OH + 40g $CuCl_2$) for about 10s to reveal grain boundaries and primary γ′. A solution of 10% Orthophosphoric acid in H_2O was used to electro-etch secondary γ′ with a voltage of 2 V for 25s. An Olympus BX51 optical microscope (OM) and JEOL JSM 6500F field emission gun (FEG) scanning electron microscope (SEM) were employed to investigate the morphology

and size of γ grains, primary γ′ and secondary γ′ in the LSHR alloy.

EBSD mappings were carried out on un-etched mechanically polished specimens of the CG and FG LSHR alloys using an FEI Nova 600 Nanolab Dual-Beam FEG SEM/FIB system to observe the distribution of grain orientations. The EBSD mapping area was 400μm×400μm for the CG LSHR and 200μm×200μm for the FG LSHR. EBSD mapping on other disc alloys RR1000, N18, Inconel 718 as well as U720Li was also conducted to systematically compare the microstructural differences in these alloys. An EBSD scan for the batch 2 LSHR alloy was conducted using a JSM 6500F FEG-SEM. A grain boundary tolerance angle of 2^o was employed for EBSD mapping. A step size of 1μm was used for EBSD mapping for the CG LSHR and batch 2 LSHR specimens, and a step size of 0.5 μm was used for other specimens.

The grain size was analysed by the linear intercept method on the basis of ASTM E112-2004. In addition, the planimeter procedure was also used to determine the grain size, along with additional information about grain size distribution and circularity that is an indicator of grain shape. The size and shape of incoherent primary γ′ and coherent secondary γ′ were analysed by the planimeter procedure as well. The circularity is defined by:

$$\text{Circularity} = 4\pi A/P^2 \tag{3.1}$$

where A is the area of individual grain or γ′ precipitate, and P is the perimeter of an individual grain or γ′ precipitate.

The image analysis for statistics of the size and shape characteristic of the microstructures of the LSHR alloy was performed with Image Pro Plus 6.0 software, and a schematic diagram is shown in Fig. 3.1 to demonstrate the process of measurement. In order to measure the size characteristic of the microstructures, the scale of the relevant images is integrated into the software first, and then a drawing tool was used to trace each grain boundary or the phase boundary of each γ′ individually followed by a conversion of the selected grains into corresponding objects for size-measurement.

3.3.2 Tensile test

Tensile tests were conducted at room temperature for both CG and FG LSHR alloys on an Instron servo-mechanical testing machine. The dimension of the tensile specimen is shown in

Fig. 3.2. The specimen has a gauge cross section of 3mm×4mm with a gauge length of 13mm. A Vishay EA-15-125BZ-350/E strain gauge was attached to the specimen surface (within the gauge centre) with a ground finish produced by 1200 grit abrasive paper. The test was carried out according to Standard BS EN 10002-1-2001, using an initial test segment with displacement increased at a uniform rate of 0.065 mm/min, followed by a displacement increased at a uniform rate of 0.5 mm/min after the yield point was achieved.

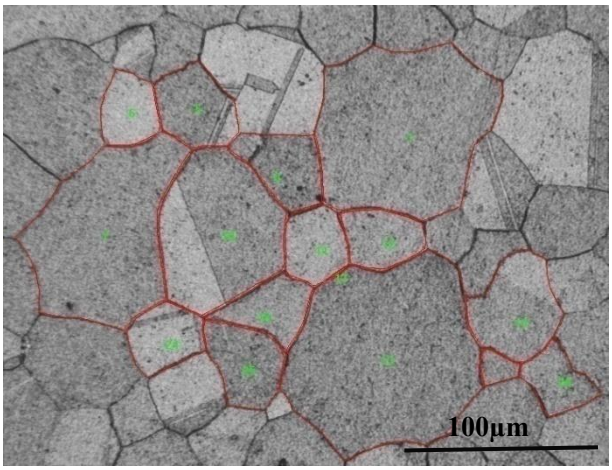

Fig. 3.1 Schematic diagram of grain size measurement in the LSHR alloy

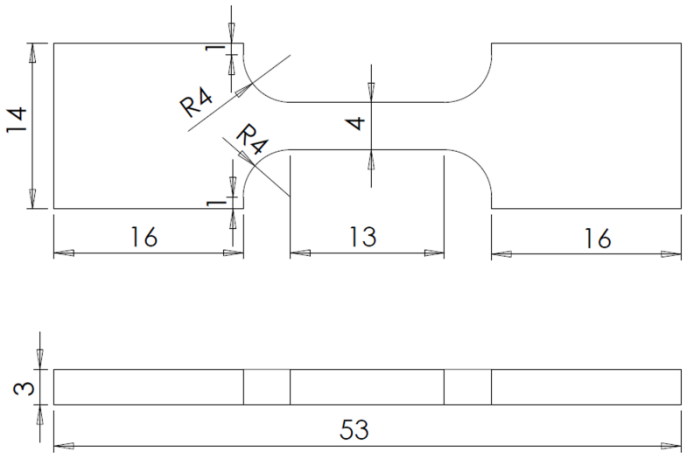

Fig. 3.2 Tensile test specimen dimension (in mm) for the LSHR alloy

High temperature tensile properties of LSHR alloy at 704, 760 and 815 ^{o}C were extracted from reported NASA' data [155], and then a Ramberg-Osgood equation as shown in Equation 3.2 [157] was used to fit the extracted stress-strain data to get the Ramberg-Osgood constants n_m and A'. The Ramberg–Osgood relation is commonly used to represent the monotonic as well as stabilised cyclic stress (σ) –strain (ε) curves. It provides a smooth continuous curve,

with no distinct yield point, describing the total strain in terms of stress. The fitted values of n_m and A' as well as E are listed in Table 3.4. The values of n_m and A' at 650 and 725°C were extrapolated and interpolated respectively, and were used to simulate the stress-strain data at these two temperatures using the Ramberg-Osgood relationship. The extrapolated and interpolated n_m and A' values are listed in Table 3.4 as well along with the Young's modulus at the investigated temperatures reported in literature [19, 155].

$$\varepsilon = \frac{\sigma}{E} + (\frac{\sigma}{A'})^{\frac{1}{n_m}} \tag{3.2}$$

where E is Young's modulus, and the E at the investigated temperatures can be found in literature [19, 155]. n_m is strain hardening exponent and A' is a constant depending on materials.

Table 3.4 Values of n_m, A' and E in Ramberg-Osgood equation for CG and 2nd batch LSHR alloys [19, 155]

Materials ID	Temperature (°C)	n_m	A'	Fitted E (GPa)	Reported E (GPa)
CG LSHR	704	0.0483	1366	175.02	184.33
	760	0.0451	1320.7	178.62	179.50
	815	0.0431	1196.7	166.25	176.33
	650	0.0506	1461.5		185.84
	725	0.0470	1347.3		180.80
2nd batch LSHR	704	0.0531	1445.8	182.48	187.00
	760	0.0442	1308.3	180.03	182.50
	815	0.0321	1112.5	177.98	175.33
	650	0.0639	1618.1		
	725	0.0498	1393.0		

3.4 Results

3.4.1 Microstructures

The microstructures of the LSHR alloy are presented in Fig. 3.3. As shown in Fig. 3.3 (a), the grain size of supersolvus heat treated (CG) LSHR is quite heterogeneous, and much coarser than that of the subsolvus heat treated (FG) LSHR (Fig. 3.3 (c)). Annealing twins can be discerned in the metallography. Although batch 2 LSHR was supersolvus heat treated for a longer time than CG LSHR, it exhibits smaller grain size and a great amount of twinning.

This difference may be caused by the differing forging procedures. Compared with CG LSHR, the grain size of the FG LSHR is more uniform and finer, with primary γ′ observed on the grain boundary which has acted as a barrier to grain growth during the sub-solvus solution heat treatment and results in the finer grains observed. In addition, a few primary γ′ precipitates are also observed within grains. The secondary γ′ is coarser with a more cuboidal morphology in the CG and batch 2 LSHR alloys as shown in Fig. 3.3 (b) and (f), whereas it is finer with a more circular morphology in the FG LSHR as shown in Fig. 3.3 (d). The size of secondary γ′ decreases in the sequence: batch 2 LSHR > CG LSHR > FG LSHR.

The grain orientations of the LSHR alloys characterized by EBSD are shown in Fig. 3.4, and no obvious texture is observed. A distinctive feature in the EBSD mapping is the large number of annealing twins, especially in the FG LSHR. These twins were formed during (static and dynamic) recrystallization process due to the hot working (i.e. forging and extrusion) employed for disc manufacture. The quantity of twin boundaries decreases in the sequence: FG LSHR > batch 2 LSHR > CG LSHR as shown in the band contrast map overlaid with special grain boundaries.

The size distributions of γ grains, primary and secondary γ′ precipitates in CG, FG and batch 2 LSHR alloys are shown in Table 3.5. The quantitative analysis of grain size was conducted with the linear intercept method and planimeter procedure. It is found that the *mean* grain sizes determined by the linear intercept method and planimeter procedure are quite similar to each other, which gives confidence in the findings. The significant differences in standard deviation are caused by the measurement method, i.e., the planimeter procedure measures each grain size individually, and therefore represents the actual scatter in individual grain sizes; while the linear intercept method measures the average size of grains which intercept a particular line, and then assesses the scatter in the set of averages obtained for a number of lines.

Table 3.5 Statistics results of size of grain, primary γ′ and secondary γ′ in the LSHR alloys

	Grain size (μm) Linear intercept method	Grain size (μm) Planimeter procedure	Primary γ′ (μm)	Secondary γ′ (nm)
CG LSHR	36.05±1.76	38.38±18.07	N/A	153± 29
FG LSHR	8.42±0.51	8.14±2.77	1.74±0.48	89± 15
Batch 2 LSHR	16.70±0.94	19.85±7.82	N/A	221± 28

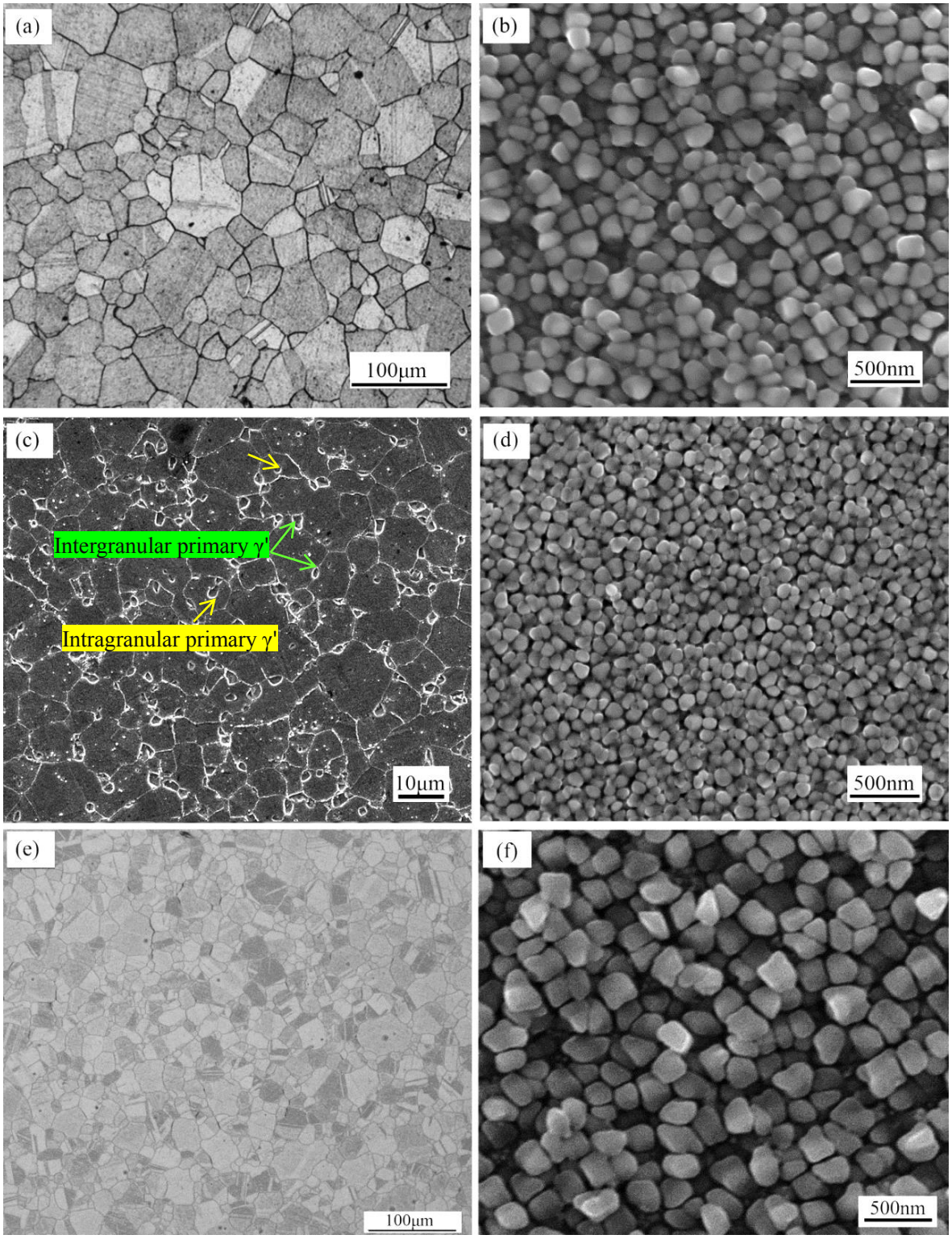

Fig. 3.3 Microstructures of (a) CG, (c) FG and (e) batch 2 LSHR alloys; secondary γ' in (b) CG, (d) FG and (f) batch 2 LSHR alloys.

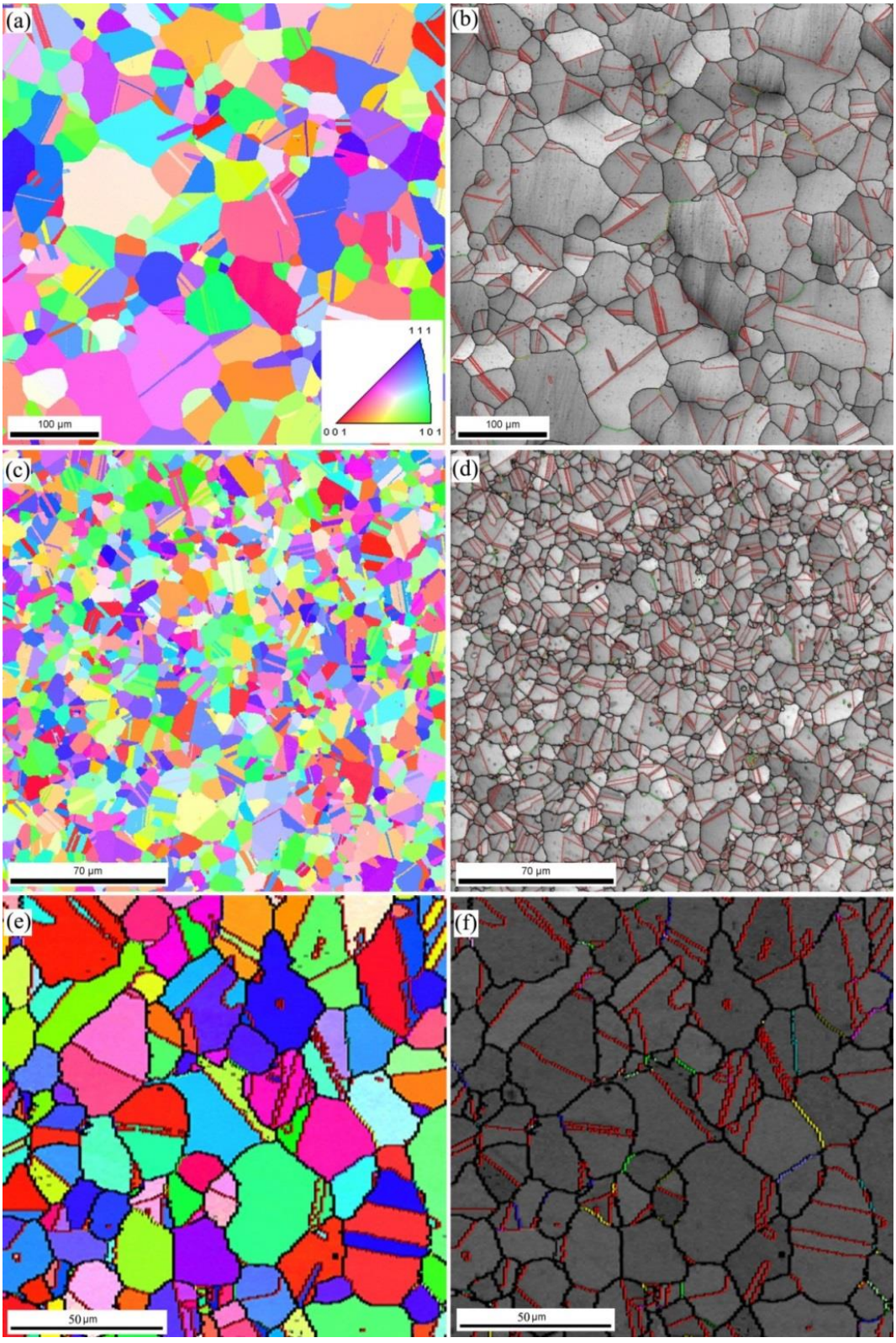

Fig. 3.4 Grain orientation map of (a) CG, (c) FG and (e) batch 2 LSHR alloys; and corresponding band contrast map overlaid with random large angle grain boundaries and special grain boundaries in (b) CG, (d) FG and (f) batch 2 LSHR alloys.

Fig. 3.5 presents the grain misorientation angle in the LSHR alloy, as well as other previously studied disc alloys (at University of Southampton) such as N18 [2], Inconel 718 [113], RR1000 and U720Li [158] extracted from the EBSD data by Orientation Imaging Microscopy software. A misorientation angle of 60 degree in the graph represents the misorientation angle of a twin boundary. As shown in the graph, the LSHR alloy has a much higher number fraction of twins than the other disc alloys. The higher number fraction of CG LSHR over FG LSHR is unexpected, because it appears that FG LSHR has more twins from the EBSD mapping shown in Fig. 3.4. This inconsistency may be caused by the γ/γ′ interfaces in the FG LSHR being considered as grain boundaries when calculating the number fraction of twins.

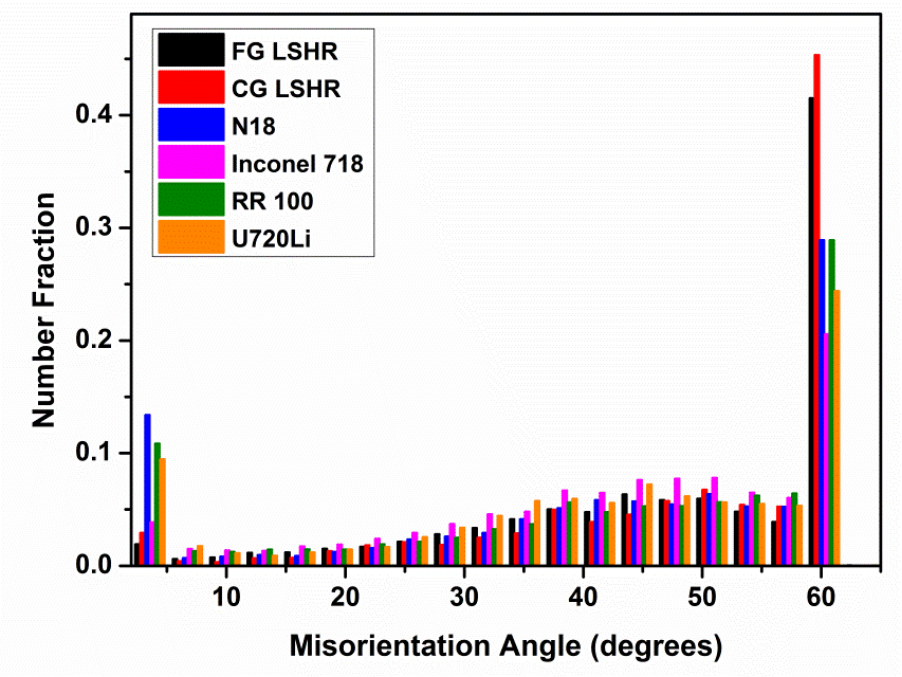

Fig. 3.5 Grain misorientation angle in the CG and FG LSHR alloys, as well as other previously studied turbine disc alloys at University of Southampton, i.e. N18, Inconel 718, RR1000 and U720Li.

The grain size distribution in the LSHR alloy is shown in Fig. 3.6. As shown in Fig. 3.6 (a), the grain size of the CG LSHR mainly ranges from 10 to 60 μm, along with approximately 15% extremely large grains (60-140 μm) as measured by grain number. In terms of grain size distribution expressed by area fraction, those grains which fall within a size range of 10-60 μm account for about 61% of measured area. It should be noted that the extremely large grains (60-140 μm) account for 39% of measured area although they only

account for 15% of measured grains by number fraction. The grain size of the FG LSHR (Fig. 3.6 (b)) mainly ranges from 4 μm to 12 μm with a more even distribution pattern compared with CG LSHR in terms of number frequency, whereas the grains within the 7 to 16 μm range account for about 85% of measured grain area although their contribution to number frequency is only about 60%. In the batch 2 LSHR alloy, the grain size range is much smaller compared with CG LSHR, even though it is also supersolvus heat treated. The grain size mainly ranges between 10 to 35 μm, accounting for about 90% of the measured grain numbers and 82% of the measured grain area. The circularity of γ grains, which is an indicator of shape characteristics of the microstructure, is calculated based on Equation 3.1, and the distribution of circularity is shown in Fig. 3.7. It is found that the circularity of both CG and FG LSHR are quite similar, with average values of 0.784 and 0.792, respectively. However, the circularity of the batch 2 LSHR is higher, and ~75% of measured grains have circularity close to 1, indicating a more regular (circular/cubic) geometry.

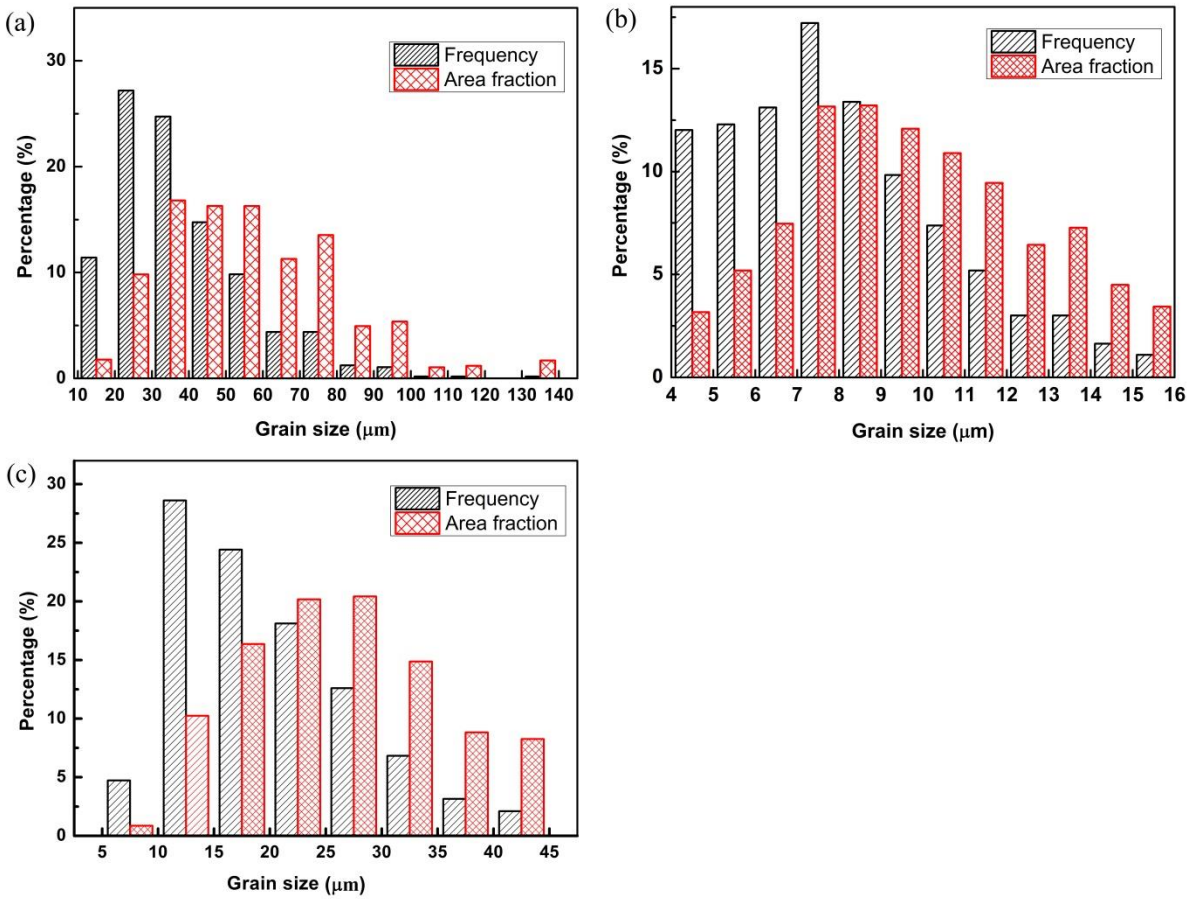

Fig. 3.6 Grain size distribution in (a) CG, (b) FG and (c) batch 2 LSHR alloys.

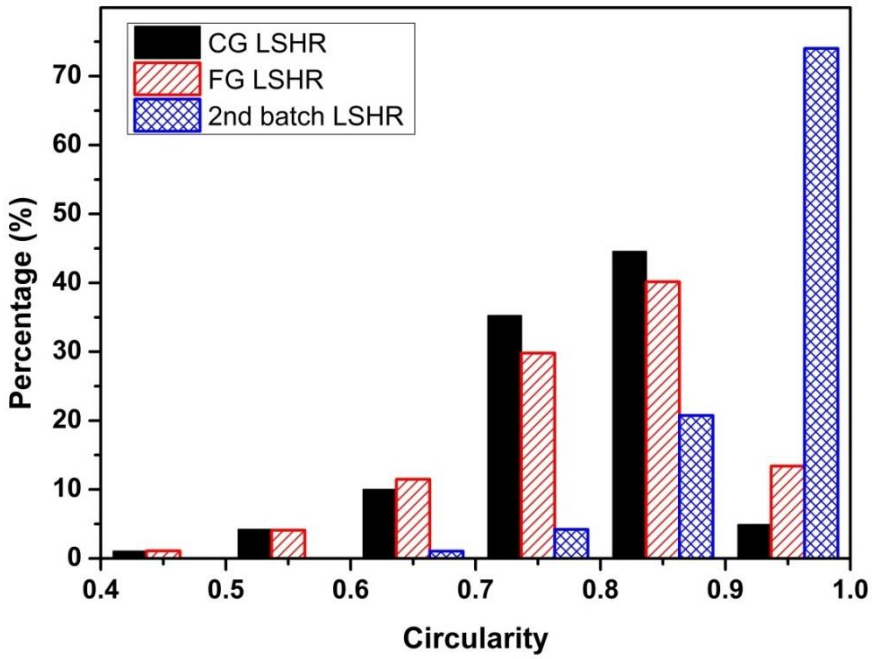

Fig. 3.7 Grain circularity distribution of CG, FG and batch 2 LSHR alloys.

The size distribution of γ′ precipitates is shown in Fig. 3.8. The size range of primary γ′ in the FG LSHR is 0.5 to 4.0 μm, with approximately 90% of the primary γ′ falling in the zone of 1.0 to 2.5 μm as shown in Fig. 3.8 (a). The size ranges of secondary γ′ in CG LSHR and FG LSHR (Figs. 3.8 (b) and (c)) are 70 to 270 nm and 40 to 150 nm respectively, with the main size distribution zone of 110 to 200 nm and 70 to 110 nm which include more than 85% of the secondary γ′. For the batch 2 LSHR, the secondary γ′ is much coarser. The size of secondary γ′ ranges from 140 nm to 320 nm and is mainly distributed within 180 to 280 nm, accounting for approximately 90% of the measured secondary γ′.

As shown in Fig. 3.9, the circularity of secondary γ′ is closer to 1 compared with primary γ′, especially in the FG LSHR, which indicates that the shape of the secondary γ′ is more regular and circular. The average circularity of primary γ′ in the FG LSHR is 0.850, and secondary γ′ in the CG, FG and batch 2 LSHR alloys are 0.909, 0.929 and 0.894 respectively.

Apart from the γ and γ′ phases, there are some other minor phases observed in the LSHR alloys according to the work conducted at NASA [155], but not specifically assessed in this study. It is reported that angular (W, Mo, Cr)$_3$B$_2$ with a size of 0.3 to 1.5 μm in diameter mainly precipitate within grains and sometimes at grain boundaries. Smaller (Ta, Nb, Ti)C particles between 0.2 and 0.5 μm in diameter are also observed within the grains. In addition, very fine (W, Cr)$_{23}$C$_6$ with a thickness between 0.05 and 0.2 μm have been discerned along

grain boundaries.

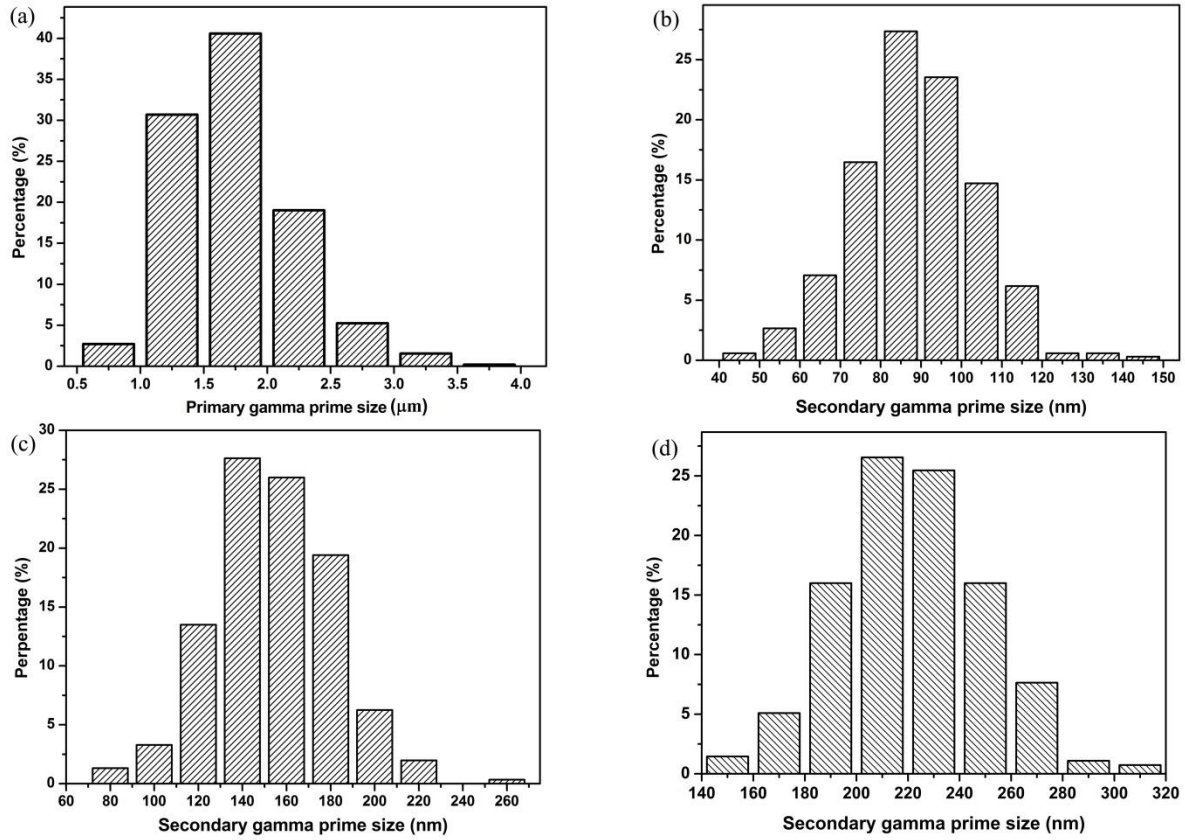

Fig. 3.8 Size distribution of (a) primary γ′ and (b) secondary γ′ in the FG LSHR; (c) secondary γ′ in the CG LSHR and (d) secondary γ′ in the batch 2 LSHR.

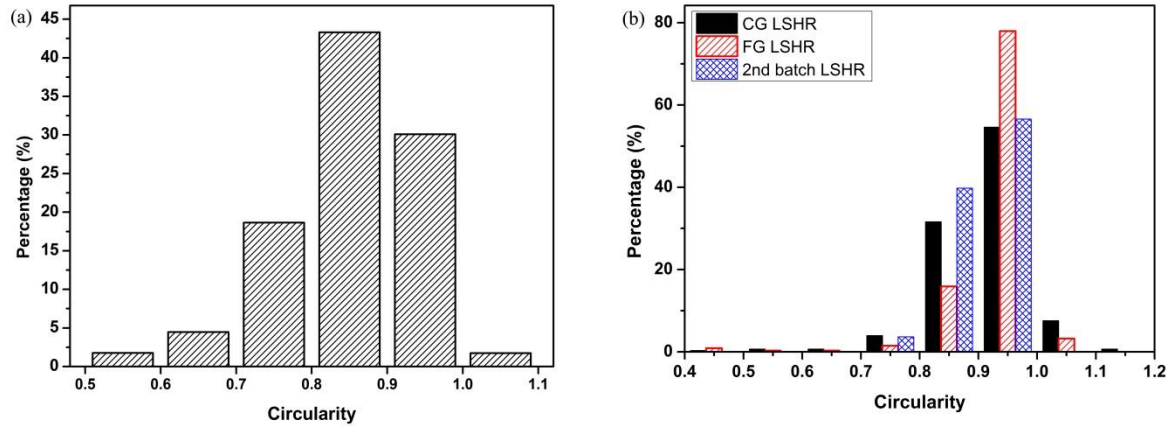

Fig. 3.9 Circularity distribution of (a) primary γ′ in the FG LSHR and (b) secondary γ′ in the CG, FG, and batch 2 LSHR alloys.

3.4.2 Tensile properties

Fig. 3.10 presents the tensile properties of CG and FG LSHR at room temperature. The tensile property of CG LSHR at 704 ^{o}C is also shown in comparison with the room temperature tensile behaviour. It is shown that no apparent yielding point is observed in both CG and FG LSHR alloys. It appears that CG LSHR exhibits a more significant strain hardening after yielding at room temperature compared with that at 704 ^{o}C. FG LSHR possesses higher yield strength than CG LSHR as indicated by the stress-strain curve. However, the experimental stress-strain curve of the FG LSHR does not show a linear regime within the expected elastic region and a drop in strain is observed in the curve after yielding, which is probably associated with the off-centre failure at one end of the parallel gauge (close to the shoulder curve transition) giving an anomalous stress-strain curve.

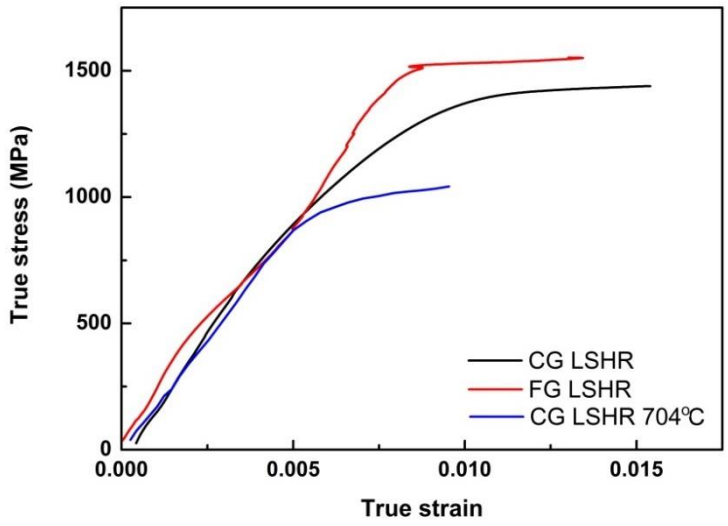

Fig. 3.10 Tensile properties of LSHR alloys at room temperature and 704 ^{o}C

As shown in Fig. 3.11, the tensile properties of CG LSHR at 704 ^{o}C calculated by the extrapolated Ramberg-Osgood equation is quite close to the experimental data, indicating the Ramberg-Osgood approximation gives a good prediction of the stress-strain data. The stress-strain data of CG LSHR at 650 and 725 ^{o}C extrapolated and interpolated respectively from the known tensile properties at 704, 760 and 815 ^{o}C according to Ramberg-Osgood relationship are also presented in this figure. It is found that the stress-strain data within the elastic regime are quite similar, but it can be seen that the yield strength decreases as temperature increases (as expected). Similar stress-strain data for batch 2 LSHR at elevated temperatures can also be obtained by conducting the extrapolation and interpolation with the

Ramberg-Osgood equation, which is shown in Fig. 3.12. The yield strength and ultimate tensile strength of LSHR alloy with different microstructural variants at temperatures of interest are summarised in Table 3.6. It can be seen in the table that the yield strength and ultimate tensile strength increase with the decreasing grain size at the same temperature, and decrease with increasing temperature in the investigated LSHR alloys.

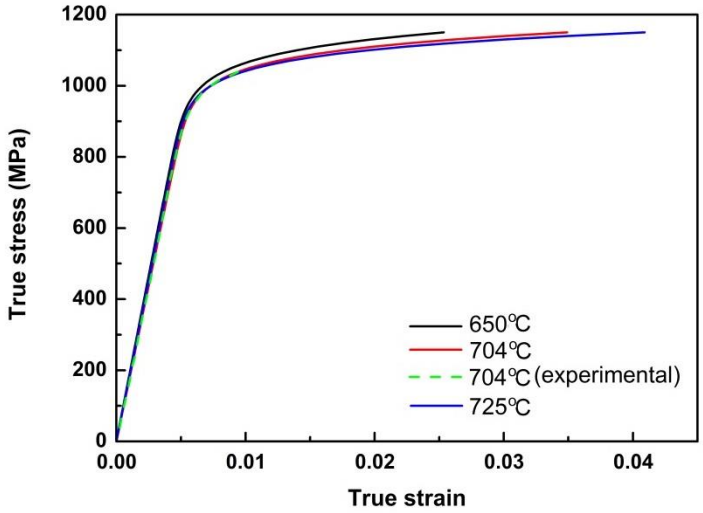

Fig. 3.11 Tensile properties of CG LSHR at elevated temperatures.

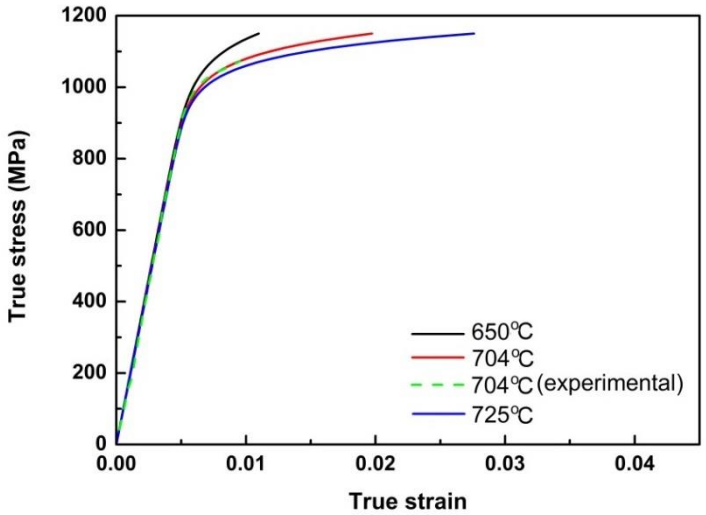

Fig. 3.12 Tensile properties of batch 2 LSHR at elevated temperatures.

3.4.3 Creep and stress relaxation behaviour

Table 3.7 presents the creep property and stress relaxation behaviour in the LSHR alloys at 704 ^{o}C, in combination with related yield and ultimate tensile strengths. It is evident that the

CG LSHR alloy possesses better creep resistance than the FG LSHR, and the beneficial effects of increased cooling rate on creep life can be discerned as well. A dramatic drop in remaining stress is captured due to stress relaxation when measured after 1 hour at a 1% total strain at 704 °C, indicating a marked stress relaxation during the long dwell period.

Table 3.6 Yield strength and ultimate tensile strength of LSHR alloys [19, 155]

	0.1% Yield strength (MPa)					Ultimate tensile strength (MPa)			
	RT	650°C	704°C	725°C	760°C	650°C	704°C	725°C	760°C
CG LSHR	1030	990	968	974	960		1298		1260
FG LSHR		1183	1170			1542	1457		
Batch 2 LSHR		1039	996	989	968		1322		1156

Table 3. 7 Creep properties and stress relaxation behaviour of LSHR alloys at 704 °C

	Cooling rate from solutioning	Yield strength (MPa)	Ultimate strength (MPa)	0.2% strain creep life (h)	Remaining stress (MPa)
CG LSHR[18, 40]	72 °C/min	996	1322		809
CG LSHR[18, 40]	202 °C/min	1105	1406		893
CG LSHR[18]	79 °C/min			305	
CG LSHR[18]	249 °C/min			570	
FG LSHR[156]	Fan cooled	1124	1324	34	

Note: 1) The stress used in the creep test is 690 MPa. 2) In the stress relaxation test, the remaining stress is recorded after 1 hour at 1% total strain. 3) The heat treatment in literature [18, 40] is as follows: supersolvus solutioning heat treatment at 1171 °C followed by 855°C/4h +775°C/8h. 4) the heat treatment in the literature [156] is as follows: subsolvus solutioning heat treatment at 1135 °C, followed by 855°C/4h +775°C/8h.

3.5 Discussion

3.5.1 Influence of processing routes on microstructures

Microstructures of the LSHR alloy as well as other P/M disc Ni-based superalloys can be deliberately tailored by modifying the thermo-mechanical processes such as forging and extrusion and subsequent heat treatments. Extrusion/forging processes during disc manufacture can introduce significant deformation and produce stored strain energy in the disc materials which are closely related to dynamic recrystallization and/or static recrystallization processes, and further influence the grain size [1, 98]. Generally, higher

extrusion/forging ratios are usually associated with more severe deformation and more stored strain energy, leading to a finer microstructure when other subsequent processing is kept identical as the deformation sub-microstructure and stored strain energy can facilitate grain nucleation and suppress (abnormal) grain growth due to the high grain nucleation rate and the competition for grain growth. Therefore, the finer grain size observed in the batch 2 LSHR is probably caused by a different forging process (probably a high forging ratio, but no information on the precise forging parameters was provided by NASA), although this batch LSHR alloy was supersolvus heat treated for a longer time than CG LSHR. In addition, it is noticed that secondary γ′ in batch 2 LSHR is coarser than that in CG LSHR although the cooling rate after the solutioning stage and aging heat treatment are the same. This difference in the size of secondary γ′ may also arise from the different forging processes as well as the difference in the solution heat treatment.

It is well established that the heat treatment is critical in determining both microstructures and properties of Ni-based superalloys. By solution heat treating Ni-based superalloys at a temperature higher or lower than the γ′ solvus which causes complete or partial dissolution of primary γ′, a wide range of grain sizes can be obtained as shown in Fig. 3.3. A coarse grain structure has been yielded by supersolvus heat treatment while a fine grain variant is produced by a subsolvus heat treatment. A serration of grain boundaries may be achieved due to the preferential grain growth and the subsequent dissolution of the large primary γ′ at grain boundaries during the supersolvus solution heat treatment [159]. In addition, the size of secondary γ′ is mainly controlled by the cooling process following the solutioning stage. As shown in NASA's research [18, 40], a slow cooling rate favours the formation of coarser secondary γ′ in supersolvus heat treated LSHR alloy whereas fast cooling is prone to form finer secondary γ′, which is consistent with the findings in this study. However, it should be noted that the formation of secondary γ′ is not only dependent on the cooling rate, but also correlates to the content of γ′ forming elements solutioning into the matrix. Although the tertiary γ′ has not been investigated explicitly in this study, the size of tertiary γ′ is mainly determined by the aging temperature and time in combination with a minor influence of cooling rate according to previous research by NASA [40]. Additionally, the volume fraction of secondary and tertiary γ′ are also affected by cooling rate and aging temperature as well as aging time, i.e. a high cooling rate following a solutioning treatment and low aging temperature tend to produce a high volume fraction of uniform, fine secondary γ' combined with a low volume fraction of uniform, fine tertiary γ', whereas lower cooling rates combined

with aging at high temperatures produce a lower volume fraction of coarser secondary γ' and a high volume fraction of coarser tertiary γ' [18].

3.5.2 Microstructures and tensile/creep properties

The tensile property and creep resistance of the LSHR alloy are closely related to the grain size and γ′ precipitates. Generally the yield strength and ultimate tensile strength increase with the decreasing grain size, which can be well described by the Hall-Petch equation, whereas the creep resistance is reduced by reducing the grain size. Finer secondary γ′ produced by fast cooling after solution heat treatment is associated with higher yield strength as shown in Table 3.7. Additionally, it is reported that the yield strength is also influenced by the volume fraction of secondary γ′ and tertiary γ′, whereas the ultimate tensile strength is found to be influenced by secondary γ′ size and volume fraction [18]. The high volume fraction of uniform, fine secondary γ′ in combination with low volume fraction of uniform, fine tertiary γ′ gives relatively high yield strength and creep resistance but relatively low ductility. On the contrary, the low volume fraction of coarser secondary γ′ along with high volume fraction of coarser tertiary γ′ gives relatively low yield strength and creep resistance but better ductility [18]. Moreover, the study of stress relaxation indicates that size of secondary γ′ shows a weak correlation with the stress relaxation behaviour, while the size of tertiary γ′ is found to be the most important microstructural variable which has the largest influence on the stress relaxation [40].

3.6 Summary

- Two batches of LSHR alloys processed by separate, different forging processing routes are used in this PhD programme. The microstructures of the LSHR alloys are closely related to the hot working (e.g. extrusion and forging) and solution/aging heat treatments.
- The LSHR alloy variants possess a relatively high fraction of twin boundaries compared with other turbine disc alloys, especially in the FG variant, this is believed to be due to the relatively high content of Co which is expected to reduce the stacking fault energy of this alloy system.
- Tensile properties of the LSHR alloys increase as the grain size decreases as expected from the Hall-Petch equation. The high volume fraction of fine secondary γ′ and low volume fraction of fine tertiary γ′ processed by fast cooling from the solutioning

temperature and aging at low temperature give relatively high tensile strength and creep resistance but relatively low ductility, and vice versa.

- A Ramberg-Osgood relationship is used to describe the stress-strain response in LSHR alloy at elevated temperatures and shows a good fit between the calculated and experimental data. The tensile properties of CG LSHR and batch 2 LSHR at 650 and 725 ^{o}C are thus extrapolated and interpolated respectively by using a suitable Ramberg-Osgood approximation.

Chapter 4 Fatigue crack initiation and early propagation behaviour at room temperature

4.1 Introduction

Fatigue crack initiation and short crack growth processes are important to optimise as they contribute to the majority of fatigue life of a turbine disc during the course of service. This is due to the high overall component stresses which result in a relatively small extent of fatigue crack propagation prior to fast fracture and thereby limit the fatigue life dependency to the short crack growth regime [8, 9, 37, 160]. Generally, the fatigue crack initiation is closely related to strain localisation developed in the materials or components. Cracks usually initiate from slip bands, twin boundaries, grain boundaries, precipitates (such as carbides, nitrides in the materials or components) and inclusions or pores formed during material processing as a result of the stress concentration and enhanced strain localisation at these regions. In terms of crack propagation, the early short crack propagation is significantly dependent on the evolution of the plastic zone ahead of the crack tip and the local microstructures. The observed growth rate for short cracks is quite fluctuating and abnormally high compared with that of a long crack under the same ΔK level due to the significant interaction between the cracks and its local microstructure. In addition, environmental attack can interact with the mechanical deformation processes when the materials or components are in aggressive environments, which further interacts with the crack initiation and early propagation processes.

Preliminary studies concerning LCF performance of the LSHR alloy at elevated temperatures in air indicate that the typical fatigue-initiation sites and the overall fatigue life of LSHR alloy are related to the microstructures, test temperatures and strain amplitudes employed [5, 19]. Specifically, cracks mainly initiate from internal inclusions and/or pores and occasionally initiate from crystallographic facets in FG LSHR at elevated temperatures (427 ^{o}C and 704 ^{o}C), which is usually associated with longer fatigue life. This has been observed when the applied total strain is less than 0.8%. Whereas cracks predominantly initiate from crystallographic facets of larger grains in the CG LSHR variant, which usually produces a shorter fatigue life at similar moderate strain amplitudes [5]. When higher strain amplitudes were applied by conducting LCF tests at higher temperature (704 ^{o}C), an

oxidation assisted crack initiation process was observed to come into effect, usually forming intergranular cracks, especially when a long dwell time was applied at the peak load during LCF tests [19]. However, it is difficult to distinguish the respective contributions from oxidation and strain localisation to crack initiation and propagation at elevated temperatures as the oxidation process is usually linked to the strain localisation process. Although we can significantly reduce the oxidation by conducting fatigue tests in vacuum at elevated temperatures, this still cannot rule out the influence of oxidation as the oxides such as Al_2O_3 and Cr_2O_3 can form in a very low oxygen partial pressure (10^{-30}~10^{-50}Pa) [106]. Moreover, the short crack propagation behaviour after initiation in the LSHR alloy, which is sensitive to the local microstructure adjacent to the crack tips, was not investigated in these studies published by NASA. As a result, a systematic assessment of crack initiation and subsequent short crack growth behaviour is necessary at both lower and elevated temperatures in order to evaluate the intrinsic (without environmental attack) and extrinsic (with environmental attack) fatigue cracking processes in appropriate microstructural variants of the LSHR alloy. This is expected to provide a better understanding of the fatigue crack initiation and propagation processes and to contribute to the ongoing development of optimised disc alloys. It should also be noted that the bore region of a turbine disc will experience lower temperatures in service and optimisation of turbine disc alloys requires good fatigue resistance at both low and high temperatures. In this chapter, crack initiation and subsequent short crack propagation behaviour in LSHR alloy at room temperature was investigated, and the effects of grain size, grain orientation and primary γ′ precipitate have been studied and are discussed. A companion study on crack initiation and short crack propagation in LSHR alloy at elevated temperatures will be presented in Chapter 5. Some aspects of the work detailed in this chapter have been published in the following paper:

R. Jiang, N. Karpasitis, N. Gao, and P. A. S. Reed, Effects of microstructures on fatigue crack initiation and short crack propagation at room temperature in an advanced disc superalloy, submitted to Materials Sciences and Engineering A (2015), accepted.

4.2 Experimental procedures

4.2.1 Short fatigue crack testing at room temperature

Fatigue tests were conducted on polished U-notch CG and FG LSHR specimens under three-point bend loading on an Instron 8501 servo-hydraulic testing machine at room

temperature with a 20 Hz sine waveform and a load ratio of 0.1. The applied load was calculated to produce a maximum nominal elastic stress of 1020 MPa at the notch root using simple elastic beam theory for the un-cracked ligament. The dimension of the U-notch specimen and the position of the loading rollers are shown in Fig. 4.1. The notch has a depth of 1.25 mm with a curvature radius of 2 mm. This notch type was chosen to provide an elastic stress concentration of around 2, i.e. representative of that seen in the fir tree root fixings used to secure blades to turbine discs. The notch was ground and then polished using dental felts by 1 μm diamond polishing paste before testing. Some of the tests were interrupted at certain intervals to make a replica of the notch root surface with a silicone compound (provided by Struers Ltd) to monitor crack evolution. Some tests were also halted before final failure to carry out more in-depth analysis of the crack growth morphology. During the replication process, the mean load of the fatigue test was applied to the specimen in order to partially open the cracks so that the crack length can be better captured on the replica.

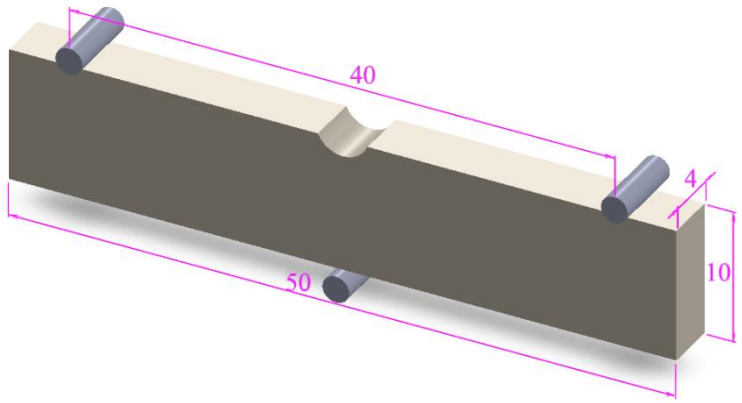

Fig. 4.1 Dimension of the U-notch specimen (in mm) and the positon of the loading rollers.

4.2.2 Assessment of crack evolution

A JEOL JSM 6500 FEG SEM was employed to examine the morphology of the fatigue fracture surface and notch root at an accelerating voltage of 15 kV. Optical microscope was used to observe crack evolution on the replicas. Both actual crack length and projected crack length were measured with Image J software. Definition of actual and projected crack length is schematically shown in Fig. 4.2. In most cases, only those cracks were measured that grew relatively long (> 10 times the average grain size) and were still sufficiently isolated to be unaffected by the proximity of other cracks at the end of the test. Crack growth rate was derived by the secant method, and then was plotted against stress intensity factor range, ΔK.

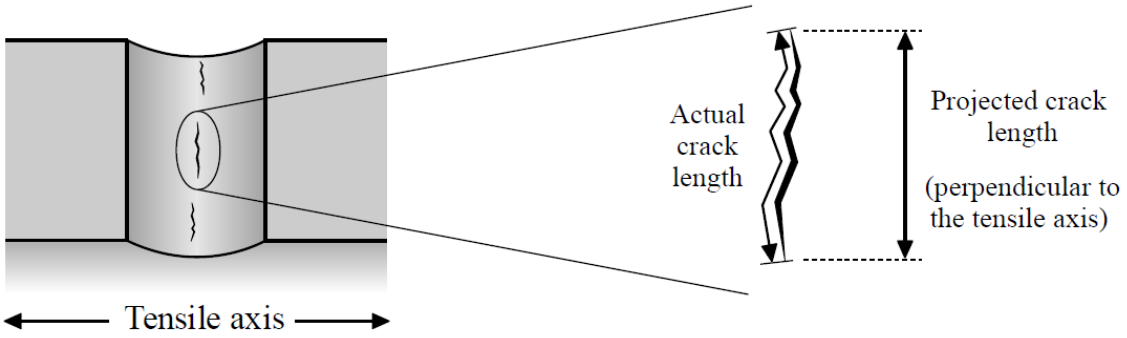

Fig. 4.2 Schematic diagram of the definition of actual and projected crack length.

Stress intensity factor values were calculated from the half surface crack length (c) using the empirical formula of Scott and Thorpe [161]. Details of the stress intensity factor calculation are presented in Appendix I. The interrupted CG LSHR specimen was metallographically sectioned and then the sectioned metallographic images were re-constructed in 3D using Avizo software to confirm the crack aspect ratio a/c (a is crack depth) to allow more accurate ΔK calculation as well as 3D crack tomography. During metallographic sectioning, micro-hardness indentions were introduced to the specimen surface to act as fiduciaries to align the 2D section images. The grinding/polishing depth was also estimated by the change of diagonal length of the indentions according to an established calibration. The stresses used for ΔK calculation were obtained by running elastic-plastic finite element modelling in Abaqus by simulating the loading roller with an appropriate pressure load and simulating the support roller with the restricted displacement in the vertical direction of the specimen. The contacting region with the rollers was assumed to be elastic to avoid non-convergence in the model.

4.2.3 EBSD characterisation of crack path

Additional testing was conducted on a plain bend bar (PBB) specimen with a dimension of 4 mm × 4 mm × 50 mm under a maximum load of 1550 N along with the same replication procedures and crack length measurement approaches. The achieved maximum strain in the PBB specimen is slightly lower than that in the U-notch specimen (0.0067 vs. 0.0078) based on the simulation by finite element. This specimen was used to evaluate the influence of grain orientation on crack initiation and early crack propagation by conducting EBSD analysis on the cracked regions at the centre of the top surface using HKL Channel 5 software provided by Oxford Instruments. The crack-initiating grain and early crack propagation region (in the

CG LSHR) can be identified via surface observation in combination with replicas using OM. In addition, EBSD analysis was also conducted in the regions containing crack-initiating grains and secondary cracks in the FG LSHR fractured specimen. This was due to the fact that it is difficult to track the crack-initiating grain in the FG LSHR via surface observation in combination with replicas using OM due to the small grain size and the inability to use high magnification objective lenses in OM due to the notch geometry. A grain boundary tolerance angle of 2^o was employed for EBSD mapping. A step size of 1μm was used during the EBSD mapping for CG LSHR and a step size of 0.5 μm was used for FG LSHR. After EBSD indexing, the three Euler angles ($\varphi_1, \emptyset, \varphi_2$) of the grains of interest were extracted to determine the rotation matrix $\boldsymbol{g}$ which connects the sample coordinates and crystal coordinates using following equation:

$$\boldsymbol{g} = \begin{bmatrix} cos\varphi_1 cos\varphi_2 - sin\varphi_1 sin\varphi_2 cos\emptyset & sin\varphi_1 cos\varphi_2 + cos\varphi_1 sin\varphi_2 cos\emptyset & sin\varphi_2 sin\emptyset \\ -cos\varphi_1 sin\varphi_2 - sin\varphi_1 cos\varphi_2 cos\emptyset & -sin\varphi_1 sin\varphi_2 + cos\varphi_1 cos\varphi_2 cos\emptyset & cos\varphi_2 sin\emptyset \\ sin\varphi 1 sin\emptyset & -cos\varphi 1 sin\emptyset & cos\emptyset \end{bmatrix} \quad (4.1)$$

By converting the loading direction from the sample coordinates to crystal coordinates using the rotation matrix and Equation 4.2,

$$L_{\text{crystal}} = \boldsymbol{g} L_{\text{sample}} \quad (4.2)$$

where L is a vector that represents the loading direction,

It is possible to determine the Schmid factor of the 12 primary slip systems (i.e. {111}<110>) in each grain of interest using following equation [118]:

$$Schmid\ Factor = |(L_{\text{crystal}} \cdot n^{\varepsilon})(L_{\text{crystal}} \cdot l^{\varepsilon})| \quad (4.3)$$

where L_{crystal} is the loading direction written in crystal coordinates, n^{ε} is the slip plane normal for the slip system ε, and l^{ε} is the slip direction for the slip system ε.

The slip traces corresponding to {111} slip planes in the cracked grains at the specimen surface were also calculated and the angle (α) between a slip trace and the loading direction was calculated using following equation [162]:

$$cos\alpha = (n^{\varepsilon} \times Z_{crystal}) \cdot L_{crystal} \quad (4.4)$$

where $Z_{crystal}$ is the direction perpendicular to specimen surface written in crystal coordinates.

The calculated angle α was used as a reference to identify the active slip systems associated with the actual crack segment within each cracked grain.

4.3 Results

4.3.1 Overall fatigue behaviour

Table 4.1 summarises the overall observations of the fatigue tests. As shown in the table, the fatigue life of the FG LSHR is nearly twice that of the CG LSHR for the U-notch specimens tested to failure. The equivalent estimated fatigue lifetime of the interrupted PBB specimen is higher than that of the U-notch specimen due to the absence of the stress concentration feature and the slightly smaller applied maximum strain. Crack initiation occurred after fewer cycles in the U-notch CG LSHR and a little later in the CG PBB specimen, as it took about 5000 and 10000 cycles respectively to produce observable cracks on replicas. Compared with the CG LSHR, FG LSHR possesses better crack initiation resistance indicated by the higher cycle number to first observable crack (denoted as fatigue crack initiation lifetime) and fewer cracks overall were observed at the end of the test. Observation of the fracture surfaces of the uninterrupted tests shows that the length of the crystallographic facets which are associated with Stage I crack propagation is approximately 10 times the average grain size in either the CG or FG LSHR variant according to 12 measurements made on the fracture surface in each case.

Table 4.1 Summary of the fatigue test results

Specimens	CG	CG	CG (PBB)	FG	FG
Test type	Tested to failure	Interrupted	Interrupted	Tested to failure	Interrupted
Fatigue lifetime/cycles at the end of the test	31482	26500	60000	57826	61500
Number of cycles to first observed crack		5000	10000		16000
Number of cracks at the end of the test		18	22		5
Extent of crystallographic faceting on fracture surface	333±38μm			105±15μm	

4.3.2 Fatigue crack initiation and propagation

Fig. 4.3 presents the morphology of the fracture surfaces of the CG and FG LSHR U-notch tests. Crystallographic facets which are associated with slip band cracking can be seen in Figs. 4.3 (a) and (d). Cracks initiate from crystallographic facets in both the CG or FG LSHR specimens, and the size of crack-initiating grains is usually larger than the average grain size. Cracks propagate along the crystallographic facets after initiation for a distance of about 10 times the average grain size until Stage II crack propagation sets in, forming a relatively flat feature on fracture surfaces as shown in Figs. 4.3 (c) and (f). A secondary crack on the fracture surface can be discerned close to the crack initiation site in Fig. 4.3 (b), and crack kinks which seem to be associated with crack deflection at TBs are observed on the crack path as indicated by the arrows. For the crack-initiated crystallographic facets in the FG LSHR, some of these are located next to primary γ′ as shown in Figs. 4.3 (d) and (e), although the role of primary γ′ in crack initiation is not clear. In addition, it seems that the FG LSHR possesses more crystallographic steps on the fracture surface, which is probably associated with the denser slip bands formed in the FG variant [130].

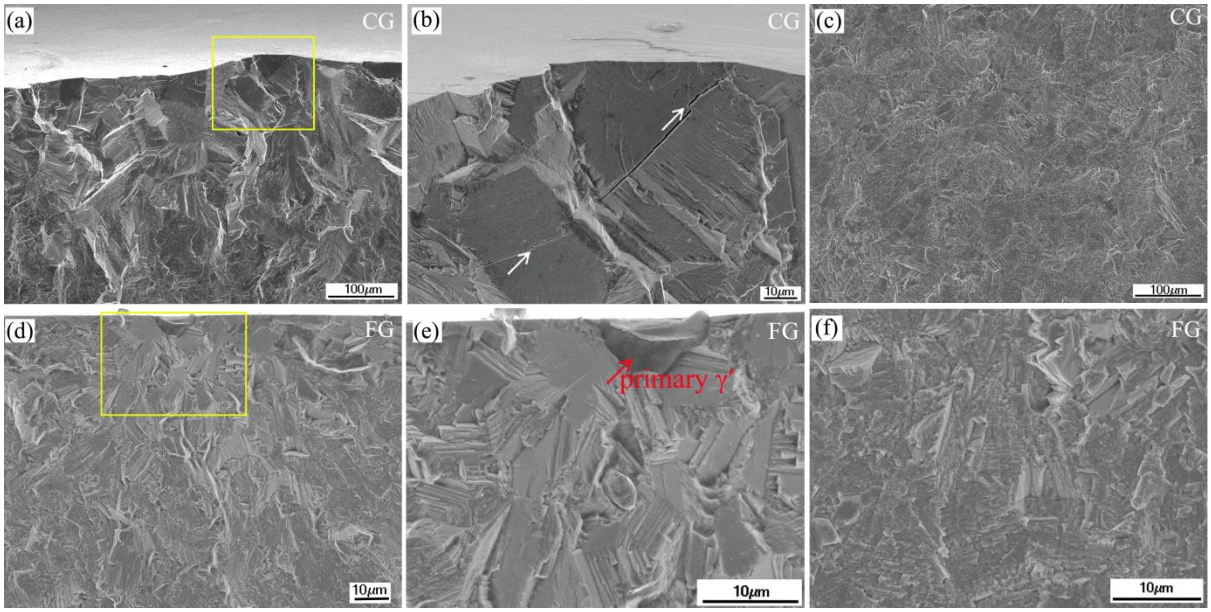

Fig. 4.3 (a) and (d) Morphology associated with Stage I crack growth on fracture surfaces in the CG and FG LSHR; (b) and (e) close-ups of the regions highlighted in (a) and (d) respectively; (c) and (f) morphology associated with Stage II crack growth on fracture surfaces in the CG and FG LSHR.

Interaction between the cracks and primary γ′ was investigated by etching the

microstructure in the notch in the interrupted FG LSHR specimen. As shown in Fig. 4.4 (a), few primary γ′ precipitates are cut by the crack path at the early crack propagation stage after initiation, except for one instance (indicated by the arrow). An occasional bowing of the crack path around a boride is observed as highlighted by the rectangle, and the crack by-passes the boride by cracking the interface of the matrix/boride. Some black replica silicone compounds remain around the crack after the replication process as they infiltrated into the crack and were difficult to remove. Figs. 4.4 (b) and (c) show the microstructure within the plastic zone ahead of the crack tip, within which intensive and intersecting slip bands in each grain can be clearly seen, indicating the occurrence of multiple slip. The slip bands usually terminate at grain boundaries or at the interfaces of γ matrix/primary γ′. Most primary γ′ precipitates within the plastic zone appear to be intact, indicating a beneficial effect of primary γ′ on resisting crack propagation.

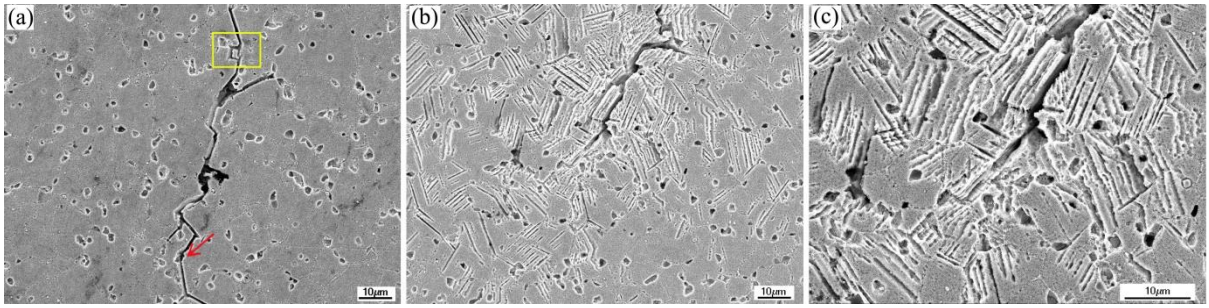

Fig. 4.4 (a) Microstructure around crack path adjacent to crack initiation site in the FG LSHR; (b) microstructure ahead of a crack tip in the FG LSHR and (c) high magnification of crack tip region shown in (b).

Evolution of the primary cracks (i.e. the most fatal crack which caused failure) in the interrupted tests for both CG and FG LSHR U-notch specimens obtained from the observation of the replicas is shown in Figs. 4.5 - 4.6, respectively. As shown in Fig. 4.5, slip bands can be observed, and crack coalescence is captured. Conversely, the primary crack grows continuously (no crack coalescence is observed) in the FG LSHR after crack initiation as shown in Fig. 4.6.

The measured lengths (*2c*) of the primary cracks and the relatively isolated secondary cracks on the specimen surface in each interrupted test are presented in Figs. 4.7 (a) and (b) respectively. The measured crack lengths corresponding to Stage I crack growth in the CG and FG LSHR based on the observation of fracture surfaces are multiplied by 2 times the

reciprocal of the crack aspect ratio (a/c), and then are plotted in the figures as indicated by the dotted lines. As shown in the graphs, accelerated and decelerated crack growth can be observed, and also crack arrest is discerned (e.g. CG C1a and CG C6a (PBB)). It is found that a crack propagates at a higher speed in the FG LSHR indicated by the steeper slope in the curve of crack length vs. loading cycle when the stage II crack propagation mode becomes dominant. Whilst it seems that the FG LSHR shows a comparable crack growth to the CG LSHR during the stage I crack propagation period. For the CG LSHR, crack coalescence can be observed during crack propagation, which is rarely seen in the FG LSHR. However, the expected acceleration of crack propagation after coalescence is not always observed as demonstrated by the coalescence of crack CG C1b and CG C1c in the U-notch specimen and the coalescence of crack CG C6a (PBB) and CG C6b (PBB) in the PBB specimen. Fig. 4.7 (c) shows the evolution of the tortuosity (actual crack length/projected crack length) of the measured cracks, from which it can be found that the crack tortuosity is generally higher in the CG LSHR than that in the FG LSHR, even though the value of the tortuosity is quite scattered and varies from crack to crack.

Fig. 4.5 Evolution of the primary crack in the interrupted test for the CG LSHR U-notch specimen.

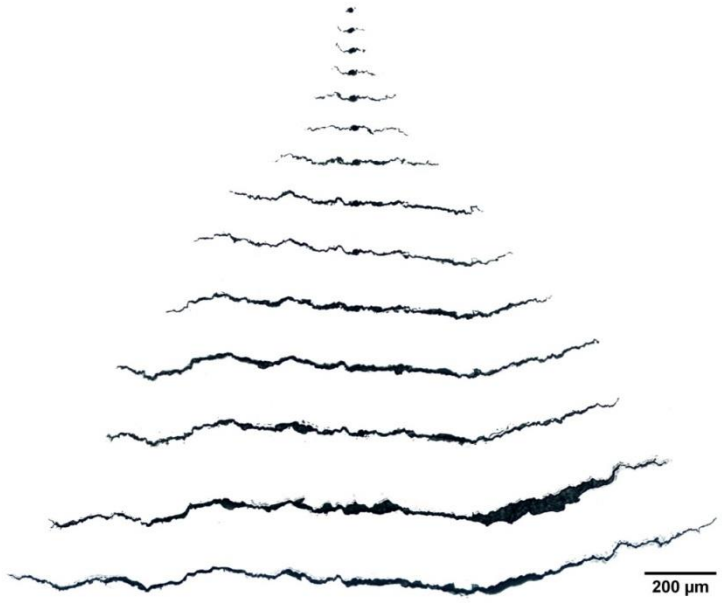

Fig. 4.6 Evolution of the primary crack in the interrupted test for the FG LSHR U-notch specimen.

Two metallographic sectioned slices and the overall 3D tomography of crack CG C1 in the U-notch interrupted specimen are presented in Fig. 4.8. As shown in the microstructures around the crack path at the notch surface (Fig. 4.8 (a)) and 28µm beneath notch surface (after removal of notch root material Fig. 4.8 (b)), the crack coalescence sites can be clearly seen, which can also be verified by the primary crack evolution as shown in Fig. 4.5. Intensive slip bands are observed at the crack coalescence regions due to the interaction of the plastic zones of the two approaching cracks. A zig-zag crack path is discerned followed by a significant crack deflection at the crack tip of CG C1a at the notch surface (Fig. 4.8 (a)) when the crack passes through a grain boundary. A more clearly defined zig-zag crack path is shown in Fig. 4.9. A similar zig-zag crack path and crack deflection are observed underneath the notch surface. Moreover, a marked inclination angle between the crack segments at the crack tip of CG C1a at the notch surface and 28µm underneath the notch surface can be seen from the inset SEM images, and such an inclination of crack plane in depth direction is probably correlated to the temporary crack arrest observed for crack CG C1a as shown in Fig. 4.7 (a). The obtained crack tomography is shown in a video in Fig. 4.8 (c), from which the tortuous nature of the crack plane in 3D can be seen. Although the cracks CG C1a and C1b appear to coalesce at the notch surface as shown in Fig. 4.8 (a), they are still separated from each other underneath the notch surface as shown in the crack tomography. On the contrary, the cracks CG C1b and C1c coalesce at both surface and depth. The measured average aspect ratio of the crack from the crack tomography is 0.918, which was used for subsequent ΔK

calibration. It should be noted here that the crack aspect ratio may vary from specimen to specimen, and even vary from crack to crack in the same specimen. The crack aspect ratio of 0.918 (which is used for ΔK calculation of all the cracks of interest) is still an assumption for simplicity.

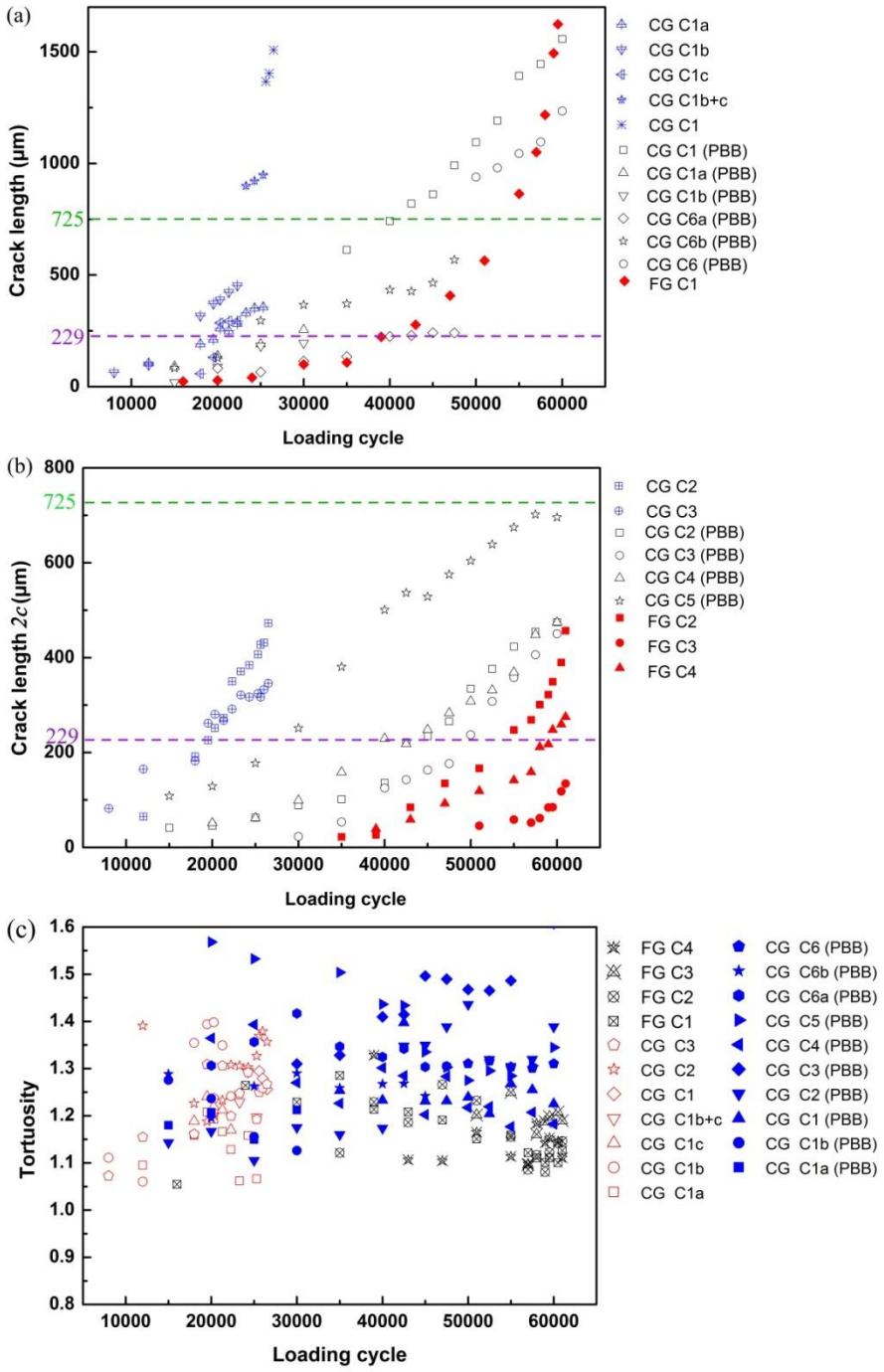

Fig. 4.7 (a) Primary and (b) secondary crack length evolution in the interrupted tests for the CG and FG LSHR alloys; the dotted lines indicate the measured Stage I crack growth length based on the observation of fracture surface; and (c) evolution of the tortuosity of the measured cracks.

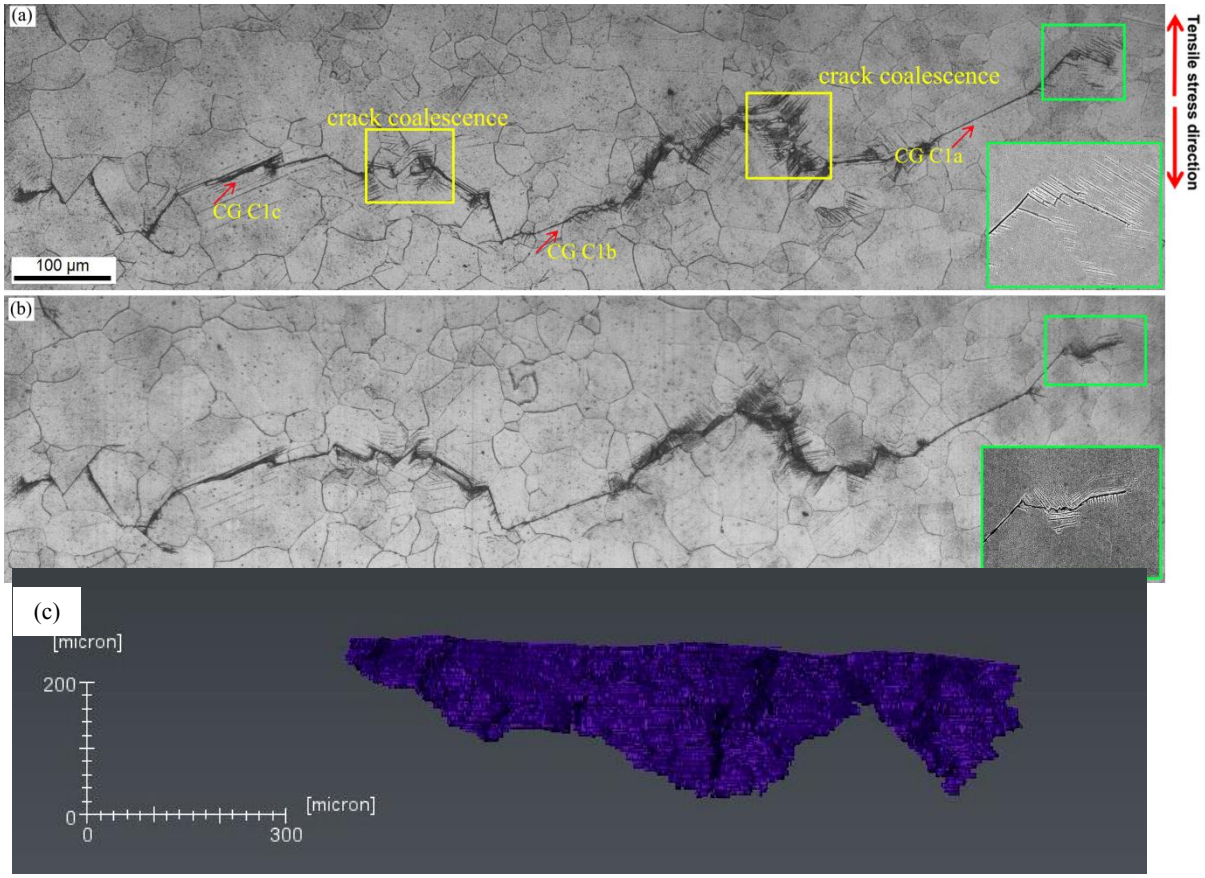

Fig. 4.8 Microstructure around crack CG C1 at (a) the notch surface and (b) 28μm underneath the notch surface; and (c) tomography of CG C1.

As shown in Fig. 4.9, it is found that the zig-zag crack growth route results from the intersection of slip lines/bands. Due to the tortuous nature of the zig-zag crack path, premature contact of the crack wake can be observed, and this premature contact may reduce the crack growth driving force, resulting in a temporary crack arrest.

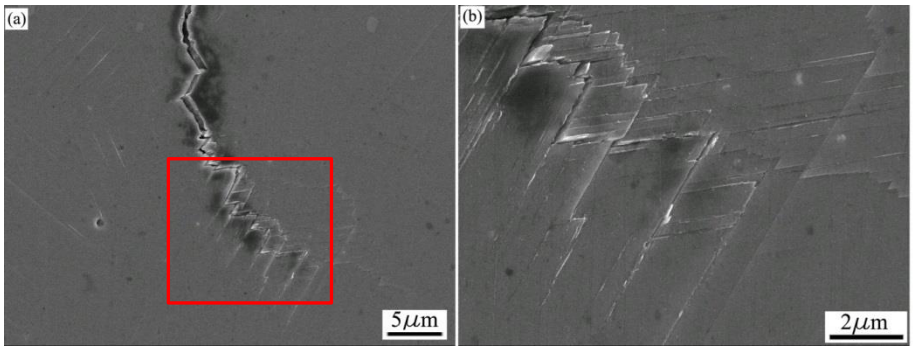

Fig. 4.9 (a) Morphology of the zig-zag crack propagation path ahead of a crack tip in the CG LSHR U-notch specimen, and (b) close-up of the crack tip shown in (a).

Crack growth rate for each measured crack in the CG and FG LSHR are plotted against calculated ΔK as shown in Fig. 4.10. The long crack growth rates along with the fitting lines according to the published Paris law behaviour [60] for both CG and FG LSHR at room temperature are also plotted for comparison with short crack growth behaviour. Typical small crack growth behaviour is seen, i.e. fluctuating and relatively higher crack growth rates at the same nominal ΔK compared to the established long crack data. This is clearly observed in both the CG and FG LSHR alloys at low ΔK level. It seems that the crack growth rates in the CG LSHR are more variable than in the FG LSHR, which may be related to the greater number of cracks and the more tortuous crack paths observed in the CG LSHR. At higher ΔK levels corresponding to longer crack lengths, the crack growth rates appear to lie closer to long crack growth data. The discrepancy between the crack growth rate at high ΔK level for short and long cracks may arise from the difference in the specimen geometry overall constraint and employed load ratio [19]. Although the fatigue life of the FG LSHR is higher as shown previously in Table 4.1, the crack once initiated propagates at a higher speed in the FG LSHR, especially at the relatively high ΔK level for the small crack or long crack data. When ΔK level is low (~ <12MPa√m), the crack growth rate in the FG LSHR is comparable to that in the CG LSHR. Such crack growth behaviour indicates that the higher resistance to crack initiation and the equivalent resistance to early short crack propagation contribute to the higher fatigue lifetime observed in the FG LSHR test.

4.3.3 Influence of grain orientation on crack initiation and propagation

EBSD analysis was conducted around the cracks (CG C1~C6 (PBB)) on the top central surface of the PBB specimen to particularly investigate the influence of grain orientation on crack initiation and early crack propagation processes. The PBB specimen orientation was selected to allow easier EBSD evaluation. The crack-initiating grains are identified by tracking down the cracks on the replicas to the stage just after initiation and then comparing the crack segment just after initiation on the replica and the corresponding area containing the crack path on the final investigated specimen surface.

Fig. 4.11 (a) shows the microstructure around crack CG C1 (PBB) and Fig. 4.11 (b) shows the corresponding grain orientation map overlapped with the random high angle grain boundaries, special grain boundaries and crack paths. It is found that cracks initiate from TBs in the relatively large grains as indicated by the arrows. Crack segments which are parallel to TBs can also be observed during propagation. The same TB crack initiation was also

observed in other cracked regions along with occasional crack initiation due to slip band cracking.

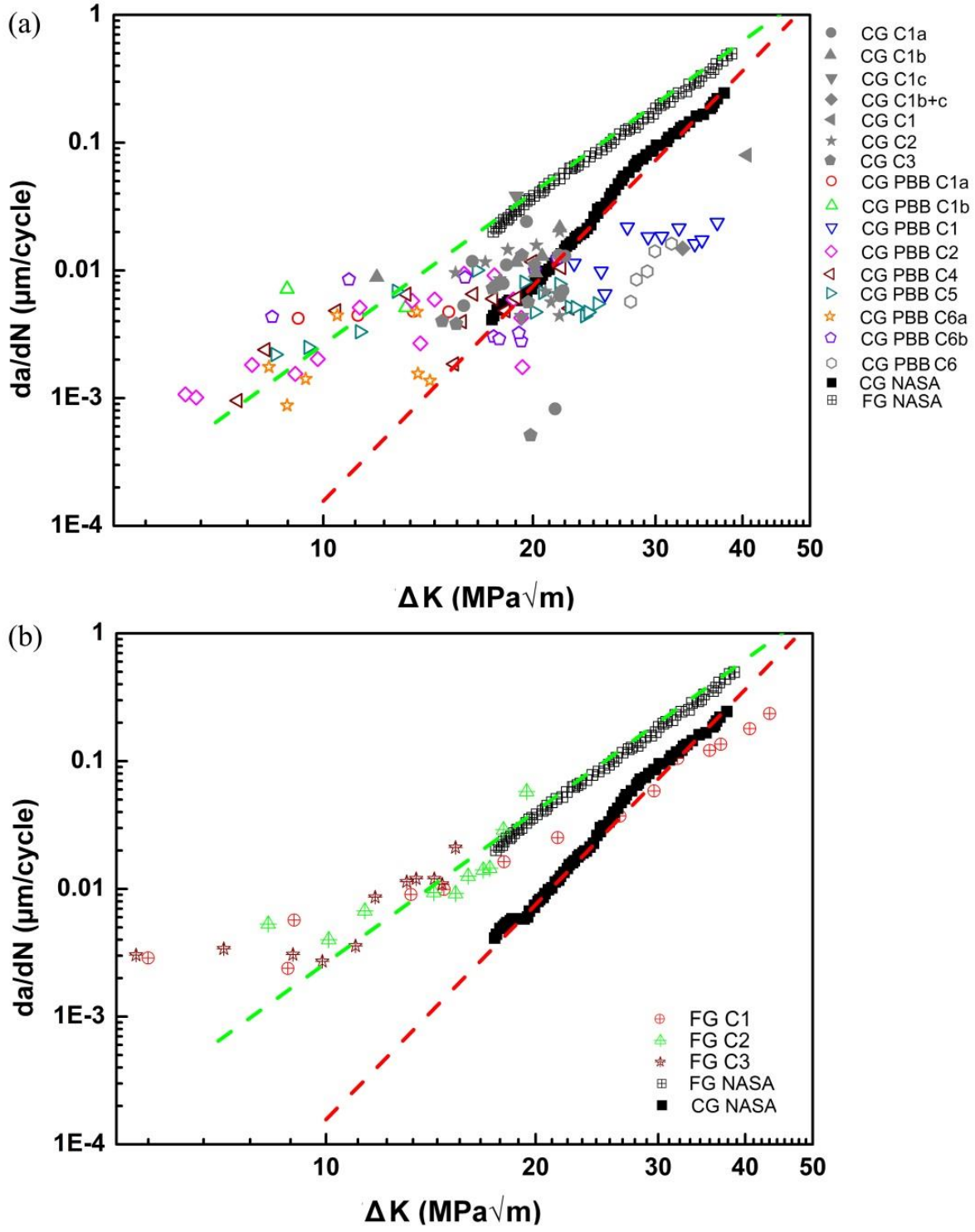

Fig. 4.10 Crack growth rate in (a) CG and (b) FG LSHR alloys. The long crack growth rate of the LSHR alloy was extracted from NASA's report [19].

A summary of crack initiation sites from the EBSD investigation for the CG LSHR is presented in Table 4.2. The measured inclination angles (α_m) between the main crack segment and tensile stress axis within each crack-initiating grain are also listed in the table. By comparing the measured inclined angle with the calculated inclination angle (α_c) between the possible slip traces of the {111} slip planes and the tensile stress axis, it is possible to identify the active primary slip system associated with the crack segment. Additionally, the calculated SF (μ_c) for each active primary slip system associated with crack initiation and the highest SF (μ_h) in the crack- initiating grains are presented in the table as well. As shown in Table 4.2, cracks predominantly initiate from TBs. The TBs and slip bands associated with crack initiation are usually associated with the primary slip system with the highest SF under the applied load conditions, and the SF of the active primary slip system is usually greater than 0.45. However, it is also found that some of the TBs associated with crack initiation are related to the slip systems with second highest SF. It appears that the slip traces in both matrix and twin corresponding to the primary slip systems associated with TB cracking have a similar inclination angle relative to tensile stress axis and parallel to the TB, although the SF of these slip systems is not always the highest within the crack-initiating grains. The slip traces corresponding to the highest SF slip systems in the twinning-related grains where crack CG C1a (PBB) and C6b (PBB) initiated are not parallel to the TB according to the calculated inclination angle. These slip traces which are non-parallel to TB appear to be less favourable for crack initiation. It seems that high resolved shear stress acting on the primary slip systems indicated by high SF in matrix and twin simultaneously is not sufficient to initiate a crack at the TB, it still requires active primary slip systems parallel to the TB.

Fig. 4.11 (c) presents the calculated slip traces for the {111} slip planes within the cracked grains near to crack initiation sites and grains adjacent to the crack path on the contrast band map with the overlapped grain boundaries. The ID of the investigated grains is also labelled in Fig. 4.11 (c). Generally, the crack segment within each grain is parallel to one of the calculated slip traces, indicating TB and/or slip band cracking and the cracks propagating along the slip bands/TBs, even though there is a slight deviation between the calculated slip traces and the actual crack segments. The calculated inclination angle α_c and the measured inclination angle α_m along with the maximum SF of the slip systems on each {111} plane within investigated grains are listed in Table 4.3. Similar to crack initiations shown previously, it is found that the SF of the active primary slip system associated with the crack segment in each cracked grain is not always the highest under the investigated conditions.

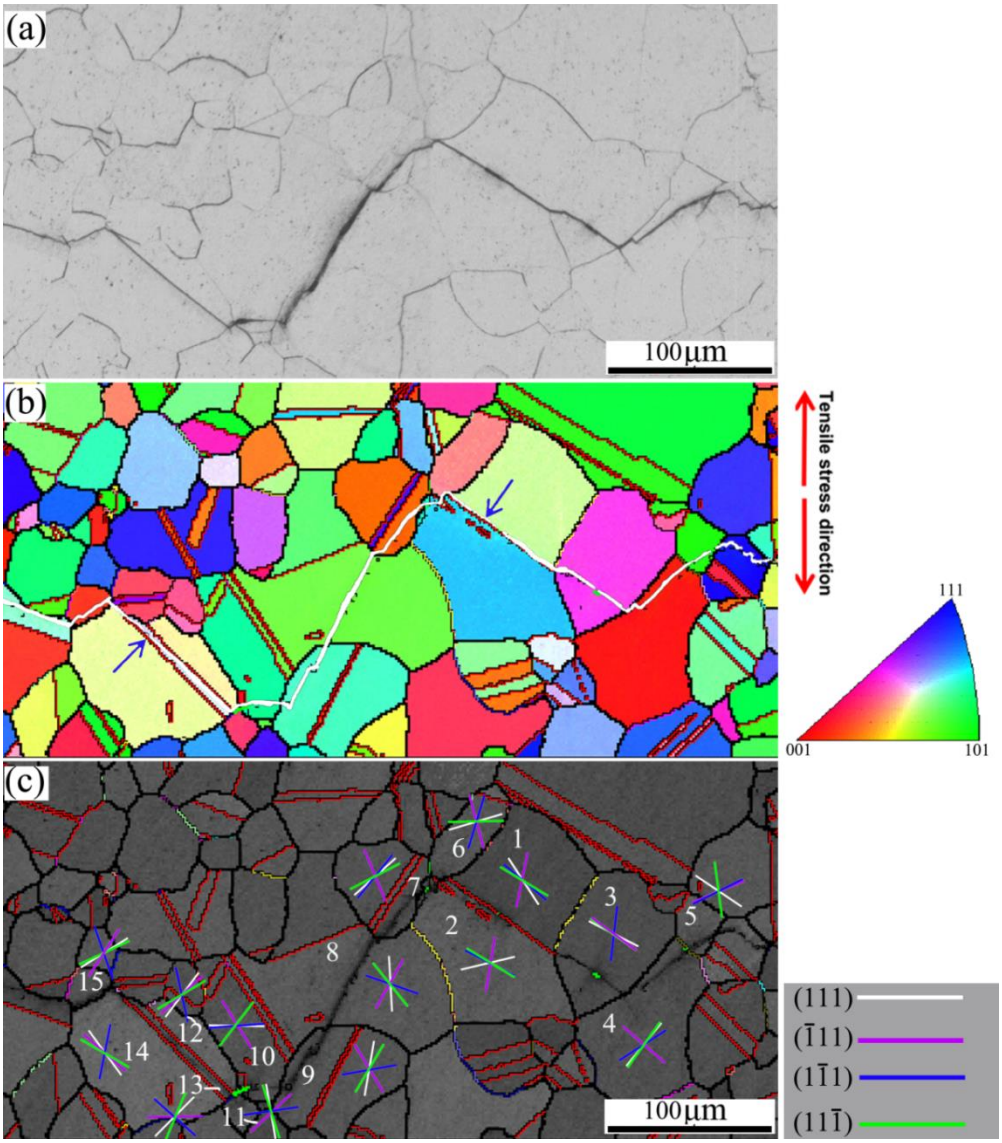

Fig. 4.11 (a) Microstructure around crack CG C1 (PBB); (b) grain orientation map and (c) band contrast map around the crack CG C1 (PBB) overlapped with random high angle grain boundaries and special grain boundaries. Black lines in (b) and (c) represent the random high angle grain boundaries, and the red lines present the Σ3 twin boundaries. Crack path is outlined by white line in (b), and the calculated slip traces in the grains containing or adjacent to crack path are labelled in (c).

As shown in Fig. 4.11 (c), a small deflection occurs when the crack propagates into grain 3 just after initiation due to the similar inclination angle of the active primary slip system in grain 3 and the crack-initiating twinning-related grain. Significant deflection occurs when the crack propagates from grain 3 into grain 4 and from crack-initiating twinning-related grain into grain 7. The zig-zag crack path in grain 4 is associated with the two active primary slip systems with very similar values (the highest SF and the secondary highest SF shown in

Table 4.3), which assists the occurrence of the deflection. The crack deflects at the boundary of the crack-initiating twinning-related grain/grain 6 as the primary slip systems are not easily activated in grain 6 indicated by the relatively low SF. Therefore the crack propagates into grain 7 where the primary slip system with a relatively high SF is activated. Crack deflection within grain 2 associated with a slip system with lower SF occurs to facilitate the crack propagating into grain 7. Similar apparent deflections can also be observed when a crack propagates into nearby grains after initiation at the TB of grain 13/grain 14. Crack coalescence occurs at grain 8 (according to replica observations) where the active slip system is associated with relatively low SF but the resultant slip band is geometrically favourable for crack coalescence as it has a small inclination angle to both approaching crack segments in grain 7 and grain 9 respectively.

Table 4.2 Summary of crack initiation sites in the interrupted test for CG PBB specimen

Crack ID	Crack initiation site	Crack initiated grain size	Matrix/Twin	μ_c	α_c	α_m	μ_h	β
C1a	TB	105.8	Matrix	0.451	121.2	121.5	0.494	130
			Twin	0.452	121.2		0.496	117
C1b	TB	84.5	Matrix	0.497	131.7	130	−	−
			Twin	0.495	131.3		−	−
C2	TB	37.9	Matrix	0.478	55.1	58.5	−	−
			Twin	0.479	55.7		−	−
C3	Slip band	111.4	/	0.489	131	130.2	−	−
C4	TB	75.9	Matrix	0.473	132	132.5	−	−
			Twin	0.471	132		0.476	126
C5	TB	101.9	Matrix	0.483	38.5	41.2	−	−
			Twin	0.488	39.3		−	−
C6a	TB	58.1	Matrix	0.490	51.6	50.8	−	−
			Twin	0.490	51.9		0.495	78.2
C6b	TB	109.2	Matrix	0.481	126	126.9	0.494	124
			Twin	0.480	126		0.492	116

Note: β is the calculated inclined angle between the tensile stress axis and the slip trace corresponding to the slip system with highest SF; − means the SF of the slip system associated with crack initiation is the highest SF in the crack-initiating grain.

Table 4.3 Summary of μ_c, α_c, and α_m in the grains containing or adjacent to crack path in the CG LSHR PBB specimen

Grain ID	Slip system	μ_c	α_c	α_m	Grain ID	Slip system	μ_c	α_c	α_m
Grain 1	(111)[1-10]	0.257	147.0	121.5	Grain 9	(111)[01-1]	0.058	9.73	31.7
	(-111)[110]	0.141	11.6			(-111)[01-1]	0.348	149	
	(1-11)[011]	*0.494*	*129.9*			(1-11)[110]	0.261	79.9	
	(11-1)[011]	**0.451**	**121.2**			**(11-1)[1-10]**	**0.419**	**30.5**	
Grain 2	(111)[01-1]	0.276	76.6	72.1	Grain 10	(111)[1-10]	0.3061	90.9	85.9
	(-111)[01-1]	0.152	9.4			(-111)[110]	0.427	148.3	
	(1-11)[110]	*0.496*	*117.2*			**(1-11)[011]**	**0.449**	**85.7**	
	(11-1)[1-10]	**0.452**	**121.2**	121.5		*(11-1)[011]*	*0.470*	*37.6*	
Grain 3	(111)[10-1]	0.365	117.0	125.7	Grain 11	(111)[01-1]	0.032	170.2	45
	(-111)[110]	**0.496**	**126.0**			**(-111)[01-1]**	**0.478**	**46.7**	
	(1-11)[-101]	0.232	16.7			(1-11)[110]	0.381	81.7	
	(11-1)[1-10]	0.459	124. 6			(11-1)[1-10]	0.277	162.5	
Grain 4	(111)[1-10]	0.378	39. 2		Grain 12	(111)[10-1]	0.289	36.9	
	(-111)[01-1]	0.457	131.0	140		(-111)[110]	0.496	48.1	
	(1-11)[011]	**0.453**	**57.2**	56.3		(1-11)[-101]	0.145	167.6	
	(11-1)[1-10]	0.407	35.6			(11-1)[1-10]	0.446	59.3	
Grain 5	(111)[1-10]	0.408	124.4	66.8	Grain 13	(111)[1-10]	0.271	44.7	130
	(-111)[101]	**0.461**	**67.3**			(-111)[101]	0.476	89.1	
	(1-11)[110]	0.371	63.5			**(1-11)[110]**	**0.497**	**131.7**	
	(11-1)[101]	0.108	172.4			(11-1)[101]	0.349	22.6	
Grain 6	(111)[01-1]	0.396	73.4		Grain 14	(111)[10-1]	0.280	143.9	130
	(-111)[110]	0.173	165.1			**(-111)[110]**	**0.495**	**131.3**	
	(1-11)[110]	0.246	17.0			(1-11)[-101]	0.138	11.3	
	(11-1)[011]	0.197	88.7			(11-1)[1-10]	0.444	120.0	
Grain 7	(111)[1-10]	0.439	48.2	40.1	Grain 15	*(111)[10-1]*	*0.479*	*57.9*	64
	(-111)[110]	0.229	157.5			(-111)[110]	0.417	33.0	
	(1-11)[011]	**0.466**	**38.8**			(1-11)[110]	0.217	160.6	
	(11-1)[011]	0.420	62.5			**(11-1)[101]**	**0.429**	**65.8**	
Grain 8	(111)[01-1]	0.022	176.8	29.8					
	(-111)[01-1]	**0.310**	**29.1**						
	(1-11)[110]	0.359	109.1						
	(11-1)[1-10]	*0.470*	*141.4*						

Note: Active primary slip systems are highlighted by red bold font, and the slip systems associated with highest SF but not the active slip system are highlighted by blue italic font. The active slip systems related to crack deflection are highlighted by underlined green font.

Moreover, the TB crack initiation can also be seen in Fig. 4.12 as indicated by the red arrows along with the crack segments parallel to or cutting through the TBs. However, it is more interesting to notice that a deceleration of crack propagation for crack CG C5 (PBB) is observed based on the observation of the replicas shown in Fig. 4.12 (c), which is consistent with the crack measurement shown in Fig. 4.7 (b). As shown in Fig. 4.12 (b), the decelerated crack growth of CG C5 (PBB) is associated with the crack propagating into the grains with low SF, especially for the large grain with low SF.

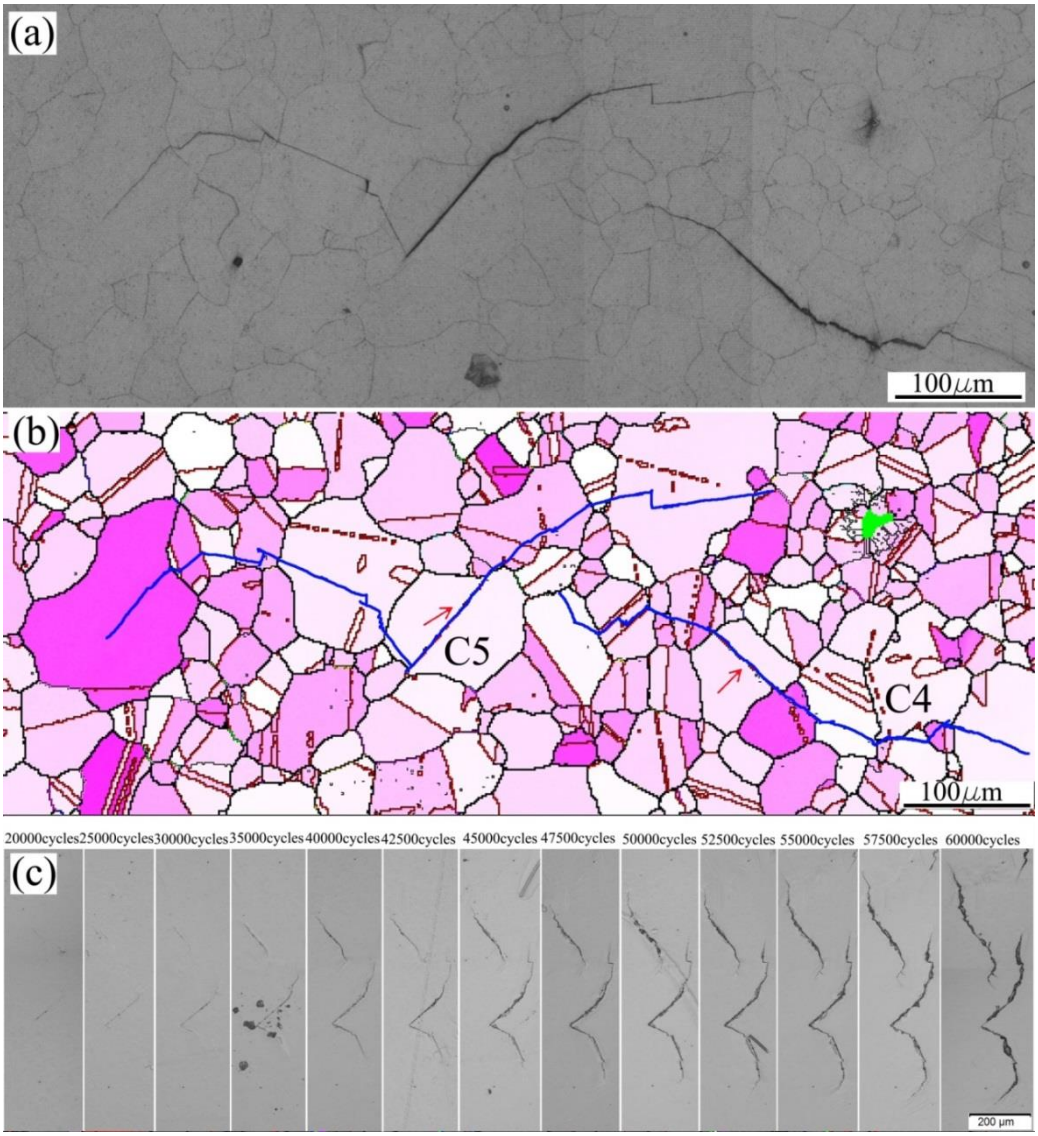

Fig. 4.12 (a) Microstructures around cracks CG C4 and C5 in the PBB specimen, (b) Schmid factor map overlapped with random high angle grain boundaries and special grain boundaries around cracks CG C4 and C5 and (c) evolution of cracks CG C4 and C5. Black lines in (b) represent the random high angle grain boundaries, and the red lines present the Σ3 twin boundaries. Crack path is outlined by blue line in (b).

Figs. 4.13 (a) and (b) present the microstructure and contrast map along with possible slip traces for the region containing the crack-initiating grain in the FG LSHR. Table 4.4 summarises the calculated inclination angle α_c and the measured inclination angle α_m along with the maximum SF of the slip systems on each {111} plane within grains of interest. As shown in Fig. 4.13 (a), large crystallographic facet can be seen on the fracture surface, indicating the crack initiation region. Similar to observations in CG LSHR, the slip band (probably a TB) related to crack initiation in grain 1 (Fig. 4.13 (b)) at the notch root surface is not associated with the slip system with the highest SF as shown in Table 4.4, but it is parallel to the TB between grain 3/grain1 and the slip trace associated with the highest SF in grain 3. After initiation, the crack propagates into grain 2 without a deflection at the notch root surface as the slip band associated with activated slip system with the highest SF in grain 2 has the same orientation in relation to the crack segment in the crack-initiating grain. Primary γ′ precipitates which are located at the boundary of grain 1/grain 2 are observed next to the crack path. However, it should be noted that the primary γ′ precipitates and γ matrix are not distinguishable from each other for EBSD indexation as they have the same face centred cubic crystal structure and a similar lattice parameter. Therefore, primary γ′ precipitates appear as grains in the EBSD band contrast map.

Figs. 4.13 (c) and (d) show the microstructure and band contrast map with possible slip traces in cracked grains around a secondary crack adjacent to the fracture surface. Although the crack-initiating grain cannot be identified directly in Fig. 4.13 (c), it is reasonable to infer that the crack may have initiated in grain 4 or grain 7 as labelled in Fig. 4.13 (d) as indicated by the greater opening width of the crack segments in these two grains, and it seems that the crack is more likely to have initiated in grain 4 due to the much larger grain size (compared with grain 7) which is usually associated with crack initiation in polycrystalline Ni-based superalloys. As shown in Table 4.4, whether the crack initiates in grain 4 or grain 7, it is consistent with the previous observation in the CG LSHR concerning crack initiation at a TB where active slip systems are associated with high SF in the matrix/twin and parallel to the TB, or crack initiation at a slip band associated with the highest SF (the highest and second highest SF in grain 7 are nearly the same). In terms of crack propagation after initiation, crack segments which are parallel to the calculated slip traces can be found in grain 6, grain 8, grain 9, and grains 12-14. Some of these crack segments are associated with slip traces with the highest SF (i.e. in grain 8, grain 9 and grain 13), and some of these crack segments are associated with relatively low SF, such as grain 6, probably due to this enabling a

minimisation of the inclination angle between crack segments in neighbouring grains or due to the existence of primary γ′ at the boundary of grain 6. A significant crack deflection is observed in grain 9, and two crack segments in grain 9 are found to be parallel to the calculated slip traces. However, one main crack segment in grain 9 (as indicated by the arrow in Fig. 4.13 (c)) and crack segments in grains 10 and 11 are not closely linked to the calculated slip traces, which may be related to crack coalescence adjacent to grain 11. Similar observations are also found in grains 12 and 14 when the crack approaches another crack tip.

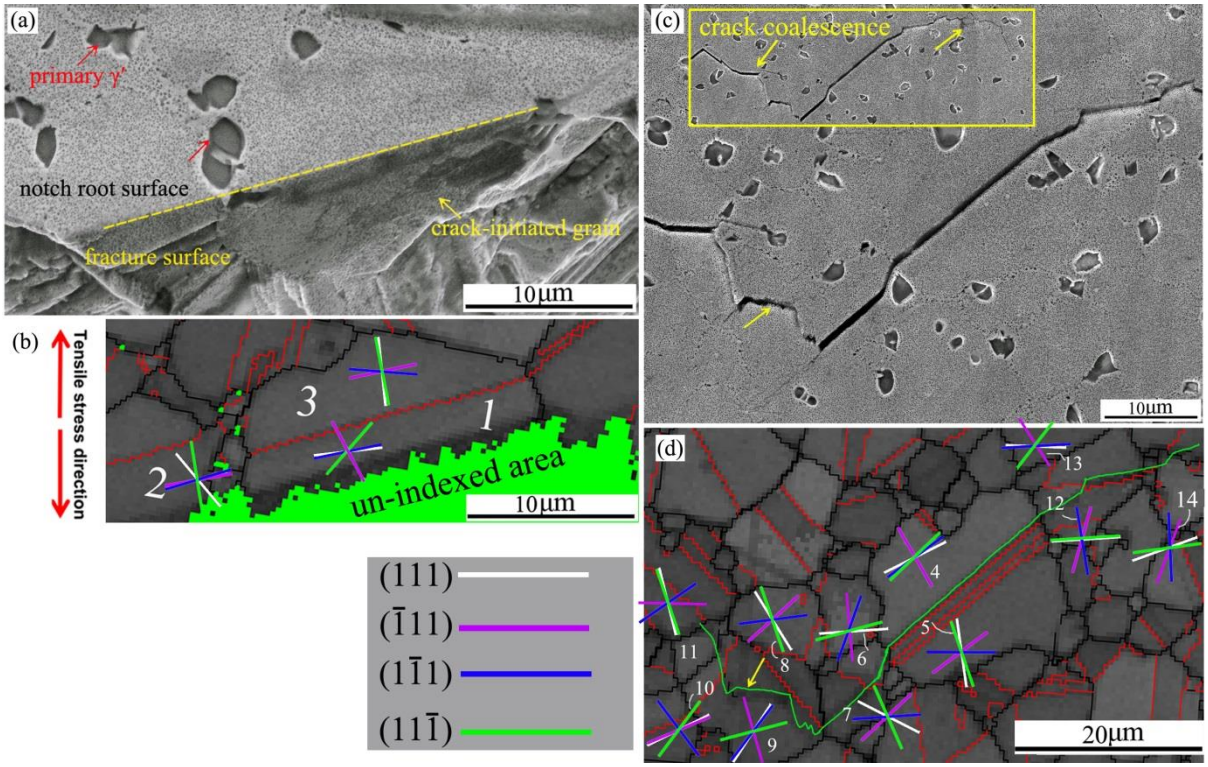

Fig. 4.13 (a) Microstructure around crack initiation region in the fractured FG LSHR; (b) band contrast map around the crack initiation region shown in (a); (c) microstructures around secondary cracks at the notch root surface in the fractured FG LSHR, and a low magnification shot of the full crack path with crack coalescence is inserted in the image; and (d) band contrast map around the secondary cracks shown in (c). Black lines in (b) and (d) represent the random high angle grain boundaries, and the red lines represent the Σ3 twin boundaries. The crack path is outlined by a green line in (d), and the calculated slip traces in the grains containing or adjacent to the crack path are labelled in (b) and (d) respectively.

Table 4.4 Summary of μ_c, α_c, and α_m in the grains containing or adjacent to crack path in the FG LSHR.

Grain ID	Slip system	μ_c	α_c	α_m	Grain ID	Slip system	μ_c	α_c	α_m
Grain 1	(111)[01-1]	0.291	83.6	75.2	Grain 8	(111)[1-10]	0.129	148	47.6
	(-111)[01-1]	0.387	152			**(-111)[01-1]**	**0.494**	**47.9**	
	(1-11)[110]	**0.467**	**78.3**			(1-11)[-101]	0.434	82.7	
	(11-1)[1-10]	*0.489*	*41.3*			(11-1)[101]	0.299	161	
Grain 2	(111)[1-10]	0.328	140	75.4	Grain 9	(111)[01-1]	0.139	33.2	
	(-111)[101]	**0.494**	**79.6**			**(-111)[01-1]**	**0.213**	**164**	166.8
	(1-11)[-101]	0.431	63.2			*(1-11)[011]*	*0.424*	*37.2*	39.7
	(11-1)[1-10]	0.140	171			(11-1)[011]	0.258	75.2	**107.2 (?)**
Grain 3	(111)[1-10]	0.068	174		Grain 10	(111)[10-1]	0.396	63.7	**168.7 (?)**
	(-111)[01-1]	*0.468*	*78.1*			(-111)[110]	0.424	67.1	
	(1-11)[011]	0.434	94.4			(1-11)[-101]	0.417	143	
	(11-1)[1-10]	0.149	169			*(11-1)[1-10]*	*0.425*	*36.9*	
Grain 4	(111)[01-1]	0.437	63.5	51.3	Grain 11	(111)[1-10]	0.126	166	**143.9 (?)**
	(-111)[01-1]	0.352	150			(-111)[101]	0.227	91.2	
	(1-11)[110]	**0.446**	**53.8**			*(1-11)[-101]*	*0.410*	*55.4*	
	(11-1)[1-10]	0.437	46.3			(11-1)[1-10]	0.286	161	
Grain 5	(111)[1-10]	0.061	172	51.3	Grain 12	*(111)[10-1]*	*0.432*	*86.3*	
	(-111)[01-1]	**0.444**	**53.3**			(-111)[110]	0.216	15.7	17.4
	(1-11)[011]	0.298	90.2			(1-11)[110]	0.122	170.7	**64.4 (?)**
	(11-1)[1-10]	0.287	161			(11-1)[101]	0.274	86.2	
Grain 6	*(111)[01-1]*	*0.485*	*86*	20.6	Grain 13	(111)[01-1]	0.412	92.3	83.7
	(-111)[110]	0.068	175			(-111)[01-1]	0.399	147.1	
	(1-11)[110]	**0.244**	**19.8**			**(1-11)[110]**	**0.430**	**86.7**	
	(11-1)[011]	0.415	74.8			(11-1)[1-10]	0.429	37.9	
Grain 7	(111)[1-10]	0.354	117	47.6	Grain 14	*(111)[10-1]*	*0.459*	*70.1*	**35.5 (?)**
	(-111)[01-1]	**0.483**	**47**			(-111)[110]	0.292	20.2	
	(1-11)[011]	*0.486*	*86.3*			(1-11)[110]	0.022	177.6	
	(11-1)[1-10]	0.343	156			**(11-1)[101]**	**0.331**	**82.3**	80.8

Note: Active primary slip systems are highlighted by red bold font, and the slip systems associated with highest SF but not the active slip system are highlighted by blue italic font. The active slip systems related to crack deflection are highlighted by underlined green font. The measured α_m with a "?" means that the smallest difference between α_m and α_c is greater than 15°.

4.4 Discussion

4.4.1 Factors controlling crack initiation

Cracks mainly initiate at stress concentration sites giving rise to strain localisation. It is widely observed that cracks initiate at slip bands close to TBs and/or TBs in the polycrystalline Ni-based superalloys due to their high slip planarity [37, 85, 86]. In this study, crack initiation predominantly occurs at TBs and occasionally occurs at slip bands in

the relatively large grain in the LSHR alloy due to the relatively high volume fraction of TBs caused by the low stacking fault energy. Although primary γ′ was observed next to crack initiating sites in the FG LSHR, there is no evidence to show that primary γ′ has a direct influence on the crack initiation process. Moreover, FG LSHR appears to have a better resistance to crack initiation than CG LSHR indicated by the higher number of cycles to the first observed crack and the fewer cracks observed overall at the end of the interrupted tests.

The better crack initiation resistance in the FG LSHR is correlated to the more homogeneous slip/deformation behaviour. It is well known that grain size has an influence on the slip planarity of the Ni-based superalloys. The coarse grained microstructure is related to the enhanced slip planarity as it provides a longer free slip length for dislocations, and produces longer but more widespread slip bands associated with heterogeneous deformation compared with the fine grained counterpart [130, 134]. The long and widespread slip bands usually act as a favourable stress concentrator, and thereby cause significant strain localisation as more intense back-and-forth dislocation movement is expected to be confined within this region and more dislocations are expected to pile up within the long slip band. Consequently, cracks are inclined to initiate from these long, heterogeneous slip bands.

The presence of a TB further increases the heterogeneity of the slip band distribution, which enhances the strain localisation [108]. It is reported that slip bands parallel to a TB can form easily at the matrix and twin adjacent to the TB and concentrate at the TB due to the high elastic incompatibility stress which is induced to meet the requirement of the discontinuity of stress and displacement across the TB [86, 108]. The concentrated slip bands at the TB which are associated with strain localisation therefore lead to crack initiation at the TB or in the region adjacent to the TB.

The orientation of twin-containing grains in relation to the tensile stress axis is important for crack initiation as it determines the resolved shear stress acting on the primary slip systems. As shown in Table 4.2, the active slip systems for crack initiation in the twin-containing grains are associated with the high resolved shear stress indicated by high SF and parallel to the TB, which is consistent with Miao's study on polycrystalline nickel-based superalloy Rene´ 88DT [86]. However, it seems that activation of the primary slip systems which are parallel to the TB in the matrix and the twin is a more important prerequisite for TB crack initiation, because it is found that the active slip systems associated with crack initiation are not always experiencing the highest resolved shear stress as observed in crack

CG C1a (PBB) (Fig. 4.11) in this study. It seems that having the active primary slip systems parallel to the TB and high resolved shear stress (indicated by high SF) together influence the crack initiation process. It can be therefore concluded that the factors controlling crack initiation in the LSHR alloy are the occurrence of large twin-containing grains and activation of the primary slip systems parallel to the TB in both matrix and twin.

4.4.2 Effects of microstructure on short crack propagation

After crack initiation, cracks mainly propagate along the slip bands and/or TBs associated with high resolved shear stress, which gives rise to crystallographic facets on the fracture surface and zig-zag crack paths until Stage II crack propagation sets in. The crack growth rate after crack initiation in the CG and FG LSHR appears to be similar perhaps due to several competing effects operating simultaneously. It is well known that grain boundaries are effective barriers for slip transmission due to the elastic anisotropy and plastic incompatibility at these regions, and thereby are effective in hindering crack propagation, especially random high angle grain boundaries [118]. From this perspective, the FG LSHR is expected to have better crack propagation resistance due to its higher proportion of grain boundaries. Furthermore, the long, intense and widespread slip bands in the CG LSHR are associated with more dislocation pile ups at grain boundaries, which results in higher stress concentration and thereby activates dislocation sources in the adjacent grains, facilitating crack propagation [76, 130, 134]. However, the coarse grained microstructure is also likely exhibit enhanced slip planarity and hence slip reversibility, which usually produce less strain accumulation within the slip bands, leading to better intrinsic crack growth resistance [9, 37]. In addition, coarse grained microstructures are associated with more tortuous crack path (Fig. 4.7 (c)) due to more significant crack deflection when passing through grain boundaries, which may cause extrinsic shielding due to roughness induced closure and reduction in ΔK due to crack path deviation, both of which will reduce the effective ΔK driving crack propagation [163].

The existence of primary γ' in the FG LSHR appears beneficial in improving the crack propagation resistance during Stage I crack propagation as the slip bands were observed to be terminated at grain boundaries and/or interfaces of γ matrix/primary γ'. Similar beneficial effect of primary γ' on crack growth has also been observed in disc superalloy U720Li [37], although it is reported that some primary γ' precipitates were cut by the crack. This was rarely seen in this study as indicated by the intact primary γ' along the crack path and within the

plastic zone ahead of the crack tip.

As cracks propagate along slip bands and/or TBs in both CG and FG LSHR during Stage I crack propagation, activation of the primary slip systems and formation of slip bands in the grains ahead of the crack tip are critical to crack propagation. High resolved shear stress is generally believed to facilitate the activation of the primary slip systems. Hence the slip systems with high SF are preferentially activated for crack propagation as shown in Tables 4.3 and 4.4. However, it is found that a crack does not propagate exclusively along slip bands with the highest SF primary slip systems according to this EBSD analysis. In some cases, the crack propagates along slip bands with a small inclination angle relative to the previous crack segment, although these slip bands are associated with relatively low SF slip systems as observed at grain 8 in Fig. 4.11 (c) where crack coalescence occurs. Similar short crack propagation along crystallographic facets associated with relatively low SF was also observed in other Ni-based superalloys [116].

It seems that geometrical compatibility of the overall 3D crack path is also an important influential factor when cracks propagate into adjacent grains which may be related to the energy required to produce new cracked surface [114, 164]. As shown in the crystallographic model (Fig. 2.19) proposed by Zhai et al. [114], the tilt angle of the traces of the crack-plane across a grain boundary at the surface and the twist angle of the crack-plane deflection at a grain boundary into the depth are the key factors that control the path and growth rate of a short crack. Large crack-plane twists and tilts when a crack passes through a grain boundary are usually required to fracture a large area at the grain boundary, which could result in crack arrest and/or branching. Conversely, a small crack-plane twist and tilt may enable continuous short crack growth across a grain boundary, which may be not necessarily related to the primary slip systems with the highest SF. Although there is no detailed analysis of the crack-plane twist in depth in this study, one case shown in Fig. 4.8 demonstrates a temporary crack arrest of CG C1a due to the large inclination (or twist) in depth at the crack tip, which is consistent with Zhai's study. Moreover, the frequently observed zig-zag path which is associated with duplex slip band cracking when a crack propagates through a grain boundary could also provide an example of the crack geometrical compatibility as the zig-zag crack path is believed to minimize the energy required to open the grain boundary [116, 164].

4.4.3 Factors controlling Stage I and Stage II crack growth behaviour

As previously mentioned, cracks propagate along the slip bands and/or TBs, producing crystallographic facets and steps on the fracture surfaces, which is a typical feature of the Stage I crack progation. The Stage I crack propagation is quite sensitive to the local microstructures ahead of the crack tip and is closely related to the active slip systems and the development of the plastic zone ahead of the crack tip. At the early stage after crack initaiton, the plastic zone size is relatively small compared with the grain size (usually smaller than a grain) due to the relatively short crack length. Consequently, it is usually associated with the limited active slip systems within the grain containing the plastic zone ahead of the crack tip, resulting in crystallographic crack propagation. With the increase in crack length, the size of the plastic zone increases correspondingly. As a consequence, the plastic zone may encompass several grains where cross-slip/multiple-slip can occur more easlily and frequently. The activation of the cross-slip/multiple-slip and the associated flat fracture feature indicate the onset of Stage II crack propagation. The activation of cross-slip/multiple-slip can be verified by the few slip bands observed at the crack initiation site but a large number of slip bands with different orientation observed at the crack tip as shown in Fig. 4.4.

As shown in Fig. 4.3, Stage I crack propagates a distance of about 10 times the average grain size before the transtion to Stage II crack propagation in both CG and FG LSHR alloys. Transition crack lengths (from Stage I to Stage II type cracking, denoted a_{trans}) were measured from short crack fractography and are shown in Table 4.5. The ΔK corresponding to these transitional crack lengths were calculated using the empirical formula of Scott and Thorpe as shown in Appendix I [161]. The corresponding monotonic ($r_{p,momotonic}$) and cyclic ($r_{p,cyclic}$) plastic zone sizes are calculated using Irwin's approximation based on a plane stress assumption with the following equations [165]:

$$r_{p,monotonic} = \frac{1}{\pi}\left(\frac{K_{max}}{\sigma_y}\right)^2 \tag{4.5}$$

$$r_{p,cyclic} = \frac{1}{\pi}\left(\frac{\Delta K}{2\sigma_y}\right)^2 \tag{4.6}$$

where σ_y is the yield stress of the investigated material.

As shown in Table 4.5, the calculated monotonic plastic zone size ahead of the crack tip is approximately two times the average grain size in both CG and FG LSHR alloys, whereas the

cyclic plastic zone size is generally smaller than the average grain size. Due to the inherent grain size distribution, at the end of the Stage I crack propagation, the crack front grows in a Stage II mode in those relatively small grains, but Stage I crack propagation can still be retained in larger grains. Hence, a mixed Stage I and Stage II crack propagation occurs until the monotonic and cyclic plastic zone ahead of the crack tip is big enough to produce predominantly Stage II crack propagation.

Table 4.5 Approximate Stage I to Stage II transition crack lengths from fractography observations and associated ΔK and plastic zone sizes

Materials	Approximate transition crack length a_{trans} (μm)	Approximate ΔK at a_{trans} ΔK_{trans} (MPa√m)	Corresponding plastic zone size at ΔK_{trans} (μm)		Average grain size (μm)	Grain size range (μm)
			Monotonic	Cyclic		
FG LSHR	105	14.69	17.2	3.5	8.14	4-16
CG LSHR	333	23.9	65.0	13.2	38.38	10-140

4.4.4 Effect of microstructure on fatigue lifetime

Fatigue lifetime is controlled by the fatigue crack initiation lifetime and the crack propagation lifetime. As discussed previously, the FG LSHR possesses better crack initiation resistance and equivalent resistance to Stage I crack propagation but relatively inferior resistance to Stage II crack propagation compared with the CG LSHR. Although the number of cycles to first observed crack is higher in the FG LSHR compared with the CG variant, the difference in crack initiation lifetime between these two LSHR variants only contributes to a small part of the difference in the fatigue lifetime. In light of the equivalent resistance to Stage I crack propagation but relatively inferior resistance to Stage II crack propagation in the FG LSHR, it is believed that much higher fatigue lifetime in the FG LSHR is primarily associated with the far fewer cracks formed. Due to the existence of a large number of cracks in the CG LSHR, frequent crack coalescence occurred during crack propagation, which significantly accelerated the fracture process, although the deceleration of crack propagation caused by the shielding effect of approaching/neighbouring cracks has been reported in some other metallic materials [125, 126].

Apart from the grain size and primary γ′, secondary and tertiary γ′ precipitates also have an influence on crack initiation and propagation processes, which further influences the fatigue lifetime. Depending on the size of secondary and tertiary γ′ precipitates, dislocations have to

bypass the γ′ by shear cutting or Orowan looping mechanism during deformation [1], which influences the slip planarity and thereby influences the crack initiation resistance in Ni-based superalloys. In addition, the size and volume fraction of secondary and tertiary γ′ precipitates usually influence the strength of Ni-based superalloys which is closely related to the strain damage in an individual loading cycle. In this study, the higher fatigue lifetime in the FG LSHR probably also arises from its relatively higher strength brought about by the finer grains and secondary γ′. However, it is difficult to quantify the contribution of secondary and tertiary γ′ precipitates to the fatigue lifetime of the LSHR alloy due to the variation in size and volume fraction of secondary and tertiary γ′ precipitates in this study. Further study concerning the fatigue crack initiation and propagation behaviour in the LSHR alloy by controlling the microstructural variables independently will be helpful to understand the influence of secondary and tertiary γ′ precipitates on slip character and low temperature fatigue resistance.

4.5 Summary

The influence of microstructure on room temperature crack initiation and early short crack propagation in LSHR alloys was assessed by three-point bend loading with a replication procedure in combination with OM, SEM and EBSD observation. Based on the aforementioned results and discussion, the following conclusions can be made:

- FG LSHR alloy possesses a higher fatigue life due to its better fatigue crack initiation resistance and equivalent resistance to Stage I crack propagation compared with the CG LSHR, even though its resistance to Stage II crack propagation is inferior. Frequent crack coalescence occurs in the CG LSHR due to the existence of a large number of cracks, which significantly accelerates the fatigue fracture process and results in a shorter fatigue lifetime. Primary γ′ precipitates improve the resistance to crack propagation in the FG LSHR to some extent as the slip bands usually terminate at grain boundaries or interfaces of γ matrix/primary γ′.
- Cracks mainly initiate from TBs and occasionally initiate from slip bands in relatively large grains with favourable orientation in relation to the tensile stress axis. TB crack initiation is closely related to the activation of the primary slip systems parallel to TB at matrix and twin. These active slip systems are associated with high resolved shear stress indicated by relatively high SF.

- Cracks propagate along slip bands/TBs during Stage I giving rise to crystallographic facets on fracture surfaces. Stage II crack propagation sets in after a crack propagates along crystallographic facets by a distance of ~10 times the average grain size. Crack propagation during Stage I is usually associated with the slip band cracking which correlates to slip systems with high SF. Duplex slip band cracking along slip systems with similar SF occurs to facilitate crack deflection or to allow a crack to pass through grain boundaries.

Chapter 5 Short fatigue crack initiation and early propagation behaviour at elevated temperatures

5.1 Introduction

As shown in Chapter 4, crack initiation and early propagation at room temperature (where effects of oxidation and creep are absent) in the LSHR alloy are predominantly determined by the slip planarity and the orientation of grain/TB relative to tensile stress axis, which controls the intrinsic low temperature fatigue performance. However, the LSHR alloy was designed as a turbine disc alloy to be operated at elevated temperatures, the synergistic interactions arising from fatigue, creep and oxidation are unavoidable during the course of service, despite targeted alloying approaches. Accelerated fatigue crack initiation and propagation processes along with the reduced fatigue life have been frequently observed in the elevated temperature LCF tests for disc alloys, especially when high strain and long dwell were employed during the tests [5, 9, 13, 19, 72, 91, 153, 154, 166]. The accelerated crack initiation and propagation, which are associated with intergranular fracture, are usually ascribed to oxygen attack at GBs by a mechanism of SAGBO [12, 17, 166, 167] or are ascribed to dynamic embrittlement of grain boundaries under stress [15, 16, 168]. However, due to the complex composition of the disc alloys and the variety in test conditions, the activated mechanism responsible for the environmental attack of grain boundary varies from alloy to alloy, and the possible formed oxides during SAGBO are diverse. In this chapter, fatigue crack initiation and early propagation behaviour of the LSHR have been investigated between a temperature range of 650 to 725 ^{o}C which are target operating temperatures for the aeroengine turbine disc rim. An attempt has therefore been made to reveal the role of oxidation at GBs and interfaces of γ/γ′ in the crack initiation and propagation processes. Some aspects of the work detailed in this chapter have been published in the following paper:

R. Jiang, N. Gao, P. A. S. Reed, Journal of Materials Sciences 50 (2015), 4379-4386.

5.2 Experimental procedures

5.2.1 Short fatigue crack tests at elevated temperatures

Short fatigue crack tests for the CG and FG LSHR alloys were conducted at 650 and 725

^{o}C in air and vacuum (~5×10^{-4} mbar) to investigate fatigue crack initiation and early propagation as well as the role of oxidation in these two processes. The specimen dimension and the experimental set-up are the same as the room temperature fatigue tests described in Section 4.2.1. The load was applied by three-point bending to achieve a maximum nominal elastic stress of 1020 MPa at the notch root based on the calculation using simple beam theory for the uncracked ligament. The loading waveform used for the tests at elevated temperatures is 1-1-1-1, which is a lower frequency than the sine waveform used for the room temperature tests. This is a characteristic baseline test frequency often adopted for high temperature tests by Rolls Royce and has also been used to allow comparison with long crack tests discussed in Chapter 6. This 1-1-1-1 trapezoidal loading waveform incorporates a 1s loading ramp from minimum load up to maximum load, a 1s dwell at maximum load, a 1s unloading ramp from maximum load down to minimum load, and a 1s dwell at minimum load. The employed load ratio is also 0.1. Four high intensity quartz lamps were used to heat specimens. The temperature of the specimen was monitored and controlled to an indicated ±1 ^{o}C using a Eurotherm 815 thermo-controller and R-type (platinum + 13%rhodium/platinum) thermocouple which was spot welded to the specimen within the hot zone. For the tests conducted in vacuum, the pressure in the test chamber was pumped down to ~5×10^{-4} mbar before switching on the heating lamps.

Both interrupted and uninterrupted tests were conducted. The uninterrupted tests were carried out to establish the fatigue life of the LSHR alloy under the investigated conditions, which is helpful to reasonably determine the intervals used in the interrupted tests. Generally, the shorter the fatigue life, the shorter the interval that was employed to monitor the crack evolution stages at the notch root. During the re-heating and cooling processes in the interrupted tests, a load that is much lower than the mean load was applied to the specimens, in order to minimize any additional oxidation and mechanical damage brought about during re-heating and cooling processes. Replicas were made when the temperature was cooled to 35 - 40 ^{o}C after interrupting the test, and the process of making a replica was the same as that in the room temperature tests.

5.2.2 Fractography and crack evolution assessment

A JEOL JSM 6500F FEG-SEM was employed to investigate the fractography of the short crack U-notch specimens at an acceleration voltage of 15 kV. Evolution of cracks on the replicas was examined by Olympus BX51 OM and Alicona Infinitefocus Microscopy (AIM).

The morphology of features in the notch root was examined by OM and SEM, with a special focus on the GB oxides formed during the fatigue tests. An energy dispersive X-ray (EDX) spectrometry analysis was carried out using Oxford Inca analysis system to reveal the compositional profile across the grain boundaries and the composition of the GB oxides. The interval between two EDX analysis points was 1 μm.

5.2.3 FIB-TEM characterisation of oxides

TEM foils were extracted from a FG LSHR specimen tested at 725 ^{o}C using FEI NanoLab Dual Beam FIB/SEM system. The areas of interest (AOI) for TEM foil extraction are the grain boundaries with and without apparent oxides as well as the interface of primary γ′/γ matrix. A carbon layer was plated on the areas of interest before the extraction to render an intact AOI. The extracted foil was approximately 100 nm in thickness and was attached to Cu grids with a marker to identify the location of the TEM foil. Examination of the extracted foils was carried out using a FEI Tecnai TF20 FEG TEM with an accelerating voltage of 200 kV. EDX mapping was conducted around grain boundaries with and without apparent oxides as well as the primary γ′/γ matrix interface to reveal the oxide composition along with the element distribution adjacent to oxides. Moreover, the crystal structure of the oxides and the deformation structure such as dislocations and stacking faults were also examined.

5.2.4 EBSD characterisation of orientation-dependent oxidation

EBSD analysis was also conducted on the plain bend bar specimens for the same reasons as stated in the room temperature EBSD characterisation, although one trial EBSD mapping was also conducted at the notch root in the CG LSHR alloy tested at 725 ^{o}C in air. Fatigue tests were conducted on polished plain bend bar specimens with a dimension of 4mm×4mm×53mm at 650 ^{o}C in air and vacuum. However, it is important to note that the plain bend bar specimens used for EBSD analysis were machined from batch 2 LSHR alloy which has an intermediate grain size (i.e. ~16.7 μm) processed by supersolvus heat treatment (due to the limited supply of the batch 1 LSHR alloys). The load was applied to achieve a maximum strain which is close to that in the U-notch specimens (0.81% vs. 0.98% based on finite element simulation). The tests were stopped when a dominant crack appeared based on the intermittent observations of the interrupted tests. The AOI which contain cracks and/or oxides were marked by micro-hardness indentations, and the images corresponding to these regions were taken by OM and/or SEM. After that, further polishing was carried out to

remove the surface oxide layer before conducting EBSD mapping. A step size of 1 μm and a tolerance angle of 2^{o} were employed for the EBSD mapping. After EBSD indexing, the maximum Schmid factors for the grains containing or adjacent to cracks/oxides were calculated using the same methodology presented in Section 4.2.3, to investigate the correlation between grain orientation and oxidation/cracking at elevated temperatures.

5.3 Results

5.3.1 Fatigue life of LSHR alloy at elevated temperatures

Table 5.1 shows fatigue life variation with testing temperature and environment under the 1-1-1-1 trapezoidal waveform. It is found that the fatigue life of LSHR alloy is significantly shortened by higher testing temperature and oxidizing environment, indicating the marked influence of oxidation on fatigue life. The reduced fatigue life with increasing temperature appears to be most pronounced in the FG LSHR. Although the FG LSHR may be expected to show more severe GB oxidation at elevated temperatures, a longer fatigue life is observed at 650^{o}C *cf.* the CG variant. This is ascribed to the higher yield strength of the FG LSHR than that of the CG LSHR [19], resulting in less plastic strain and associated damage in each fatigue cycle that acts to counterbalance the increased GB oxidation effect [5, 137].

Table 5.1 Fatigue life of LSHR alloy at elevated temperatures

Test conditions	Air		Vacuum
	650 ^{o}C	725 ^{o}C	650 ^{o}C
CG LSHR	2460	534 (90*)	16778
FG LSHR	7998	400*	

Note: * represents that the data is from interrupted tests. The interrupted specimens were not fractured, but there were surface cracks with a length longer than half of width of the specimen.

5.3.2 Fractography

Figs. 5.1 - 5.4 present the fractography of the CG and FG LSHR alloys tested in air and vacuum at 650 and 725 ^{o}C. Based on SEM observations, it is found that the intergranular or transgranular features on the fracture surfaces are dependent on the degree of oxidation in the tested specimens which is associated with the grain size of the LSHR alloy, testing temperature and environment. In general, FG LSHR exhibits predominantly intergranular

fracture characteristics, whereas CG LSHR fracture surfaces are mainly characterized by mixed inter-transgranular features in air although the amount of the intergranular features increases with testing temperature.

As shown in Fig. 5.1, cracks appear to initiate from the grain boundary as indicated by the red arrow in the vacuum test at 650 ^{o}C for the CG LSHR, although the intergranular feature is not clearly evident on the fracture surface. After intergranular crack initiation, the crack propagates in a mixed inter-transgranular mode by a short distance (approximately 1-2 grains), and then it converts to completely transgranular propagation. In addition, crystallographic facets can also be seen on the fracture surface, indicating the existence of Stage I crack propagation which is associated with slip band/TB cracking as discussed in Chapter 4. The transition to completely transgranular crack propagation with crystallographic facets also indicates the relatively insignificant influence of oxidation on crack propagation in vacuum (low oxygen partial pressure environment).

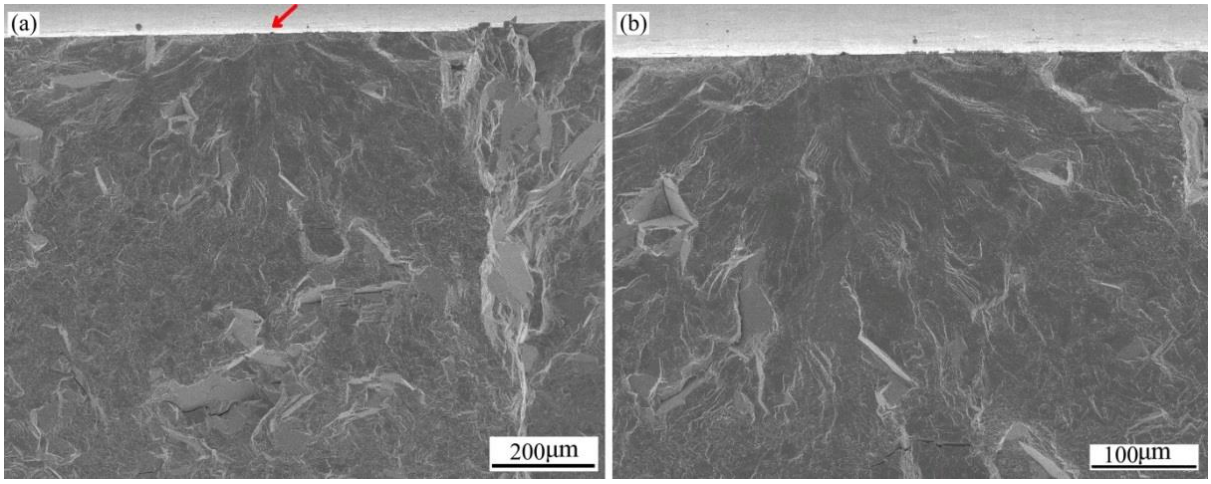

Fig. 5.1 (a) Fractography of the CG LSHR alloy tested at 650 ^{o}C in vacuum and (b) higher magnification of crack initiation site shown in (a).

Fig. 5.2 shows the fractography of the CG LSHR tested at 650 ^{o}C in air, where an increase in intergranular fracture features is seen compared with that of the vacuum test at the same temperature and loading condition. Multiple cracks which are separated by distinct ratchet marks can be seen from the fracture surface shown in Fig. 5.2 (a). It seems that the proportion of intergranular features for an individual crack depends on the sequence of the crack initiation in the test. The earlier the crack initiates, the more significant intergranular features are shown, as in Fig. 5.2 (b). Figs. 5.2 (c) and (d) show the fractography of cracks that

initiated relatively late, which show features similar to that of the vacuum test, i.e. an intergranular crack initiation followed by mixed inter-transgranular and subsequent complete transgranular crack propagation. But the amount of mixed inter-transgranular feature is more significant than that of the vacuum test. Increased intergranular features on the fracture surface indicate a more significant role of oxidation in crack initiation and propagation in these air tests.

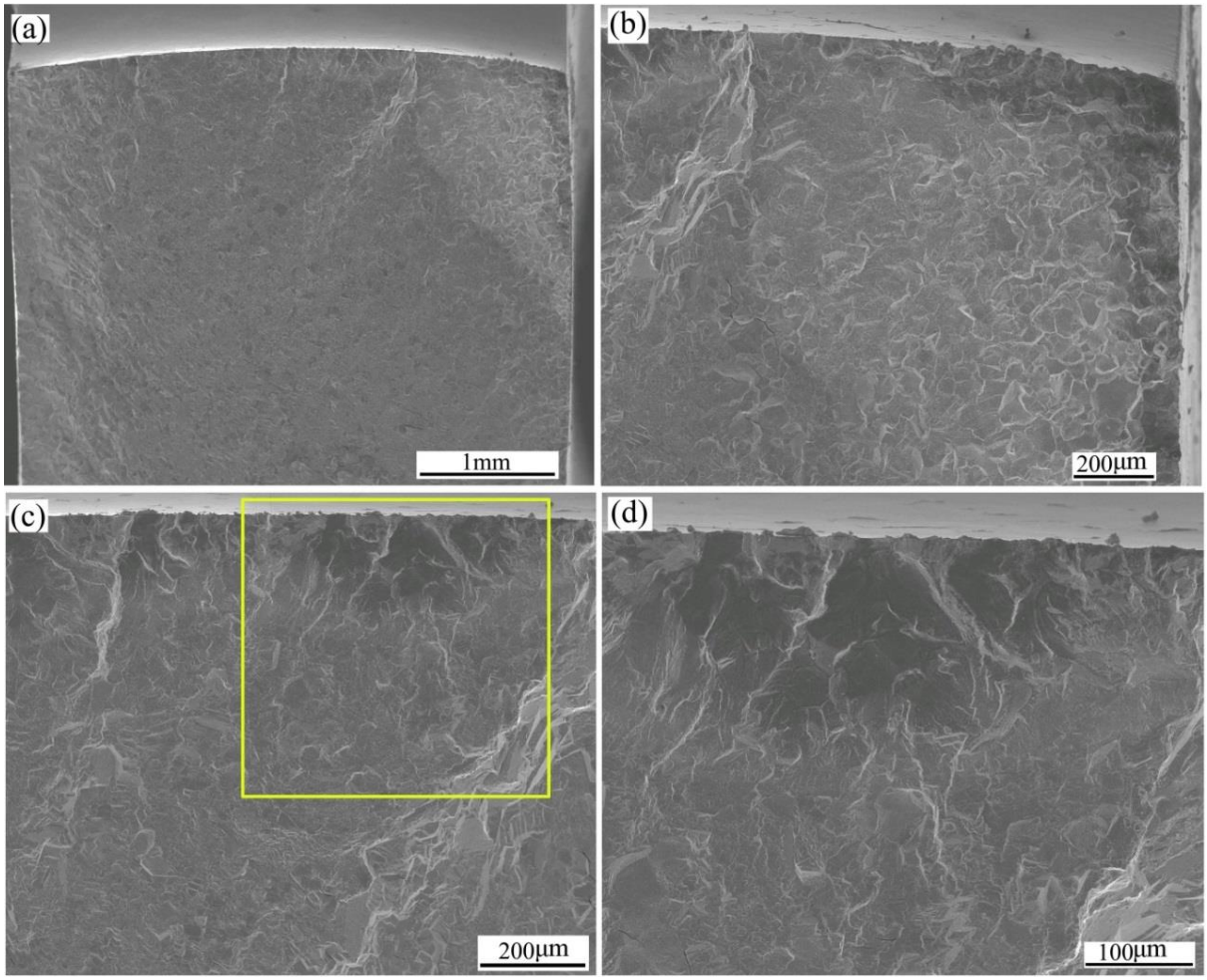

Fig. 5.2 Fractography of the CG LSHR tested at 650 ^{o}C in air: (a) overall view of the fracture surface; (b) predominant intergranular fracture feature on the fracture surface at the corner crack; (c) morphology of intergranular crack initiation followed by mixed inter-transgranular and subsequent complete transgranular propagation and (d) higher magnification of the region highlighted in (c).

As the test temperature was increased to 725 ^{o}C or for the test conducted on the FG LSHR at 650 ^{o}C, the fracture surfaces show predominantly intergranular features (Figs. 5.3 and 5.4), which indicates that a higher temperature and/or a finer microstructure promote the

occurrence of oxidation, giving rise to shorter fatigue life. The more significant degree of intergranular features in the FG LSHR than in the CG LSHR indicates the role of grain boundary in oxidation. In addition, crack propagation along the interfaces of γ matrix/primary γ′ can also be discerned in the FG LSHR as shown in Fig. 5.4 (c). Fractography of the FG LSHR tested at 725 ^{o}C in air is not presented here as this test was not run to fracture, but it can reasonably be inferred that intergranular fracture features would also dominate on the fracture surface.

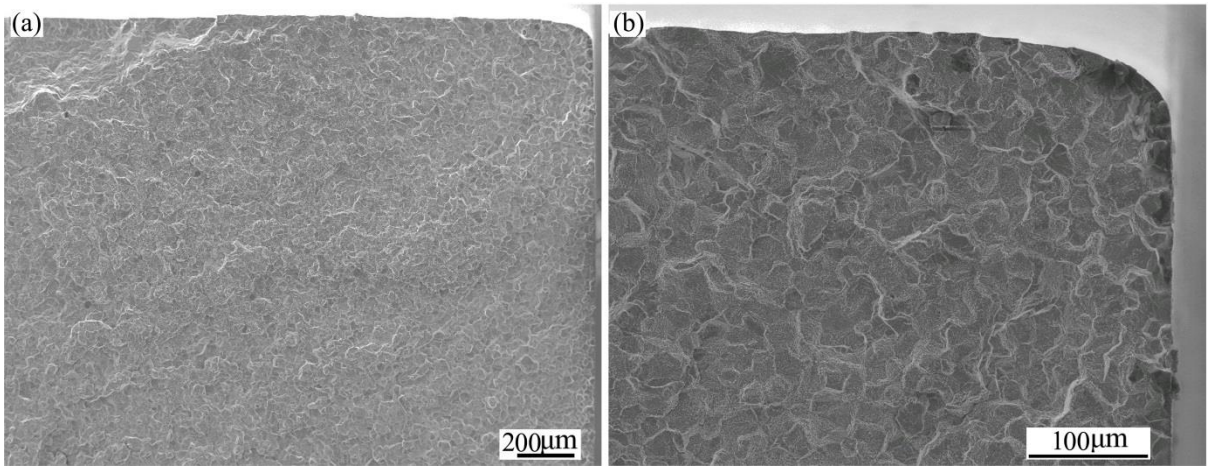

Fig. 5.3 Fractography of the CG LSHR alloy tested at 725 ^{o}C in air: (a) overall view of the fracture surface and (b) intergranular crack initiation and propagation.

5.3.3 Crack evolution at the notch root

OM and SEM were employed to examine the morphology of the notch root of the LSHR alloy tested at elevated temperatures. It is interesting to note that grain boundaries are revealed by the oxidation effect on the polished notch root surface, even for the CG LSHR vacuum test. Bulged oxides can be observed on some grain boundaries. As shown in Fig. 5.5, slip bands, secondary/non-fatal intergranular cracks and grain boundary oxides can be clearly seen in all the tests for both CG and FG LSHR. The slip bands are most evident in the CG LSHR tested in air (Figs. 5.5 (b) and (c)) perhaps due to the balance between the higher expected slip planarity of the coarse microstructure counterbalanced by the lower slip reversibility due to the absorption of oxygen at the slip bands. Plenty of slip bands can also be observed in the CG LSHR tested in vacuum, but the quantity is much less than seen in the corresponding air tests, indicating fewer, more intense slip bands have formed. For the FG LSHR tested in air, only occasional slip bands can be observed due to the more dispersed slip

character of the finer microstructure. Although slip bands are quite common in the CG LSHR, no apparent slip band initiated cracking can be found. The secondary cracks observed at the notch root in the elevated temperature tests are predominantly intergranular, indicating grain boundaries are the weak sites for crack initiation at these elevated temperatures.

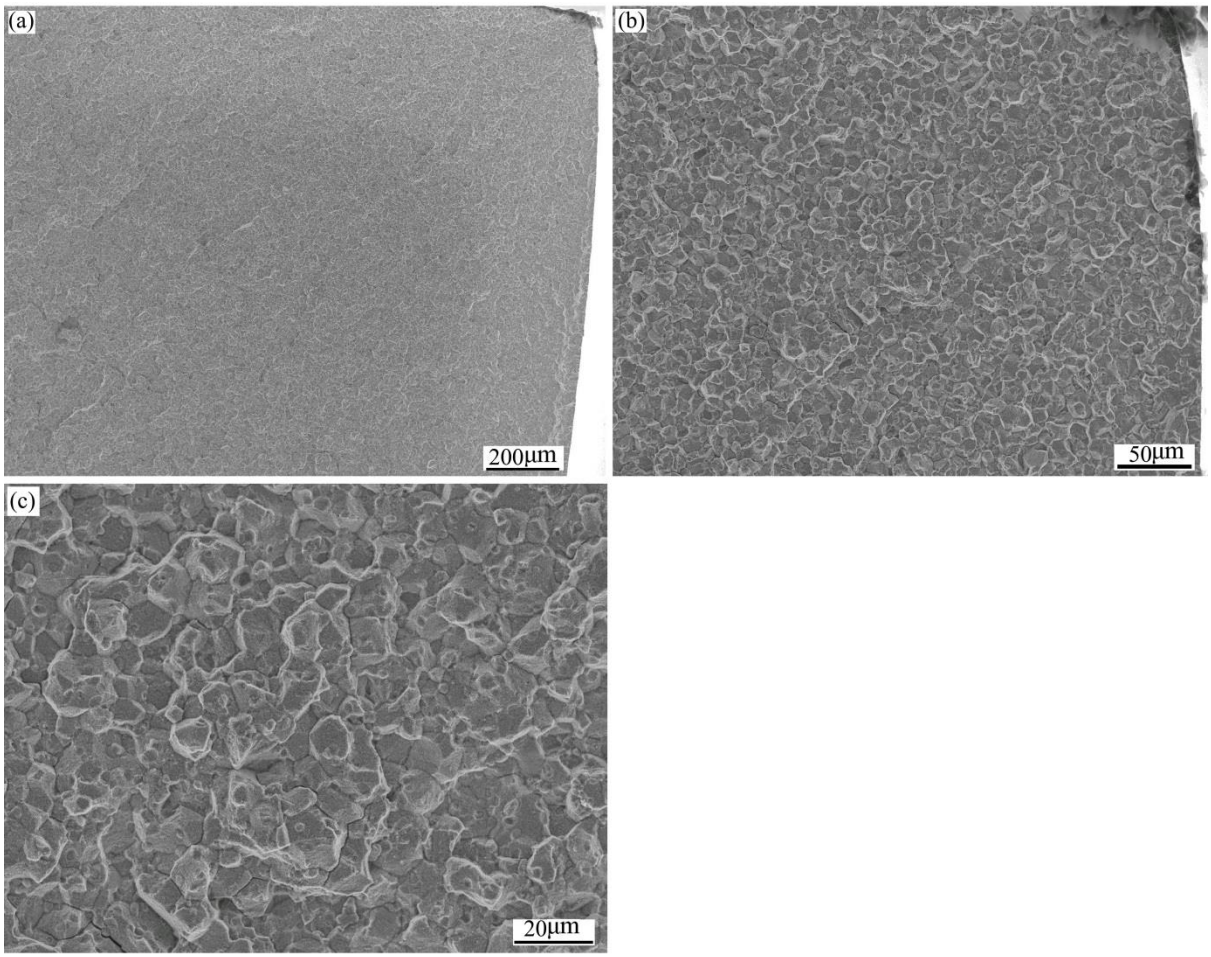

Fig. 5.4 Fractography of the FG LSHR alloy tested at 650 ^{o}C in air: (a) overall view of the fracture surface; (b) completely intergranular fracture surface; and (c) higher magnification of the intergranular fracture surface.

Although intergranular cracks are also observed at the notch root in the vacuum test for the CG LSHR, grain boundary oxides are much less evident than in the air tests either for the CG or FG LSHR. GB oxides are much more common in the FG LSHR as shown in Figs. 5.5 (d) and (e), especially at 725 ^{o}C. Generally, the FG microstructure and higher testing temperature are associated with more marked bulged GB oxides. Apart from GBs, oxides can also be observed at slip bands (Fig. 5.5 (c)) and γ/γ' interfaces (Figs. 5.5 (d) and (e)). Furthermore, it seems that the formed oxides are coarser and distributed more densely along GBs at 725 ^{o}C

than those formed at 650 °C. Additionally, it is found that cracks occasionally cut through primary γ′ (located at grain boundaries) as highlighted by arrows shown in Fig. 5.5 (d).

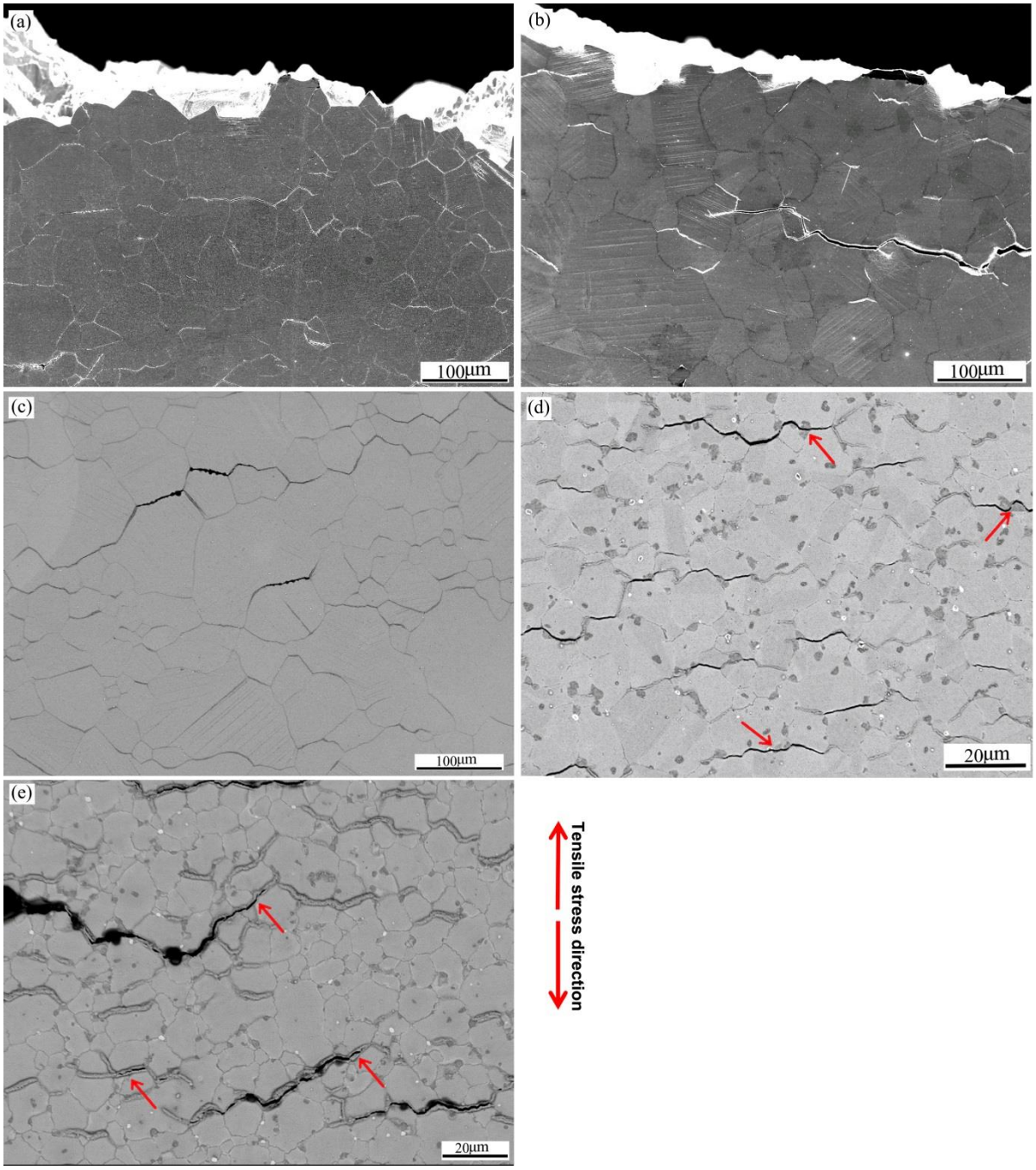

Fig. 5.5 Morphology of notch root in (a) CG LSHR, 650 °C, vacuum; (b) CG LSHR, 650 °C, air; (c) CG LSHR, 725 °C, air; (d) FG LSHR, 650 °C, air and (e) FG LSHR, 725 °C, air.

One more apparent feature of the bulged oxides formed in the air tests is that the oxides are apt to form at those grain boundaries which are inclined *normal* to the tensile stress axis in both CG and FG LSHR. However, it is noteworthy that not all the grain boundaries inclined

normal to this tensile stress axis are decorated with bulged oxides, indicating that GB character or grain orientation may also influence oxide formation. In addition, bulged GB oxide cracking can be found at the notch root as indicated by the arrows in Fig. 5.5 (e), and the cracks propagate along these grain boundaries with bulged oxides. It is noted that the bulged GB oxides ahead of a crack tip are intact. These intact oxides may indicate that the oxide formation occurs prior to crack initiation and it is the bulged oxide cracking which results in crack initiation.

The evolution of the bulged oxides and the cracking of the bulged oxides which causes crack initiation can be observed on the replicas as shown in Fig. 5.6, even though it is difficult to capture the moment of the formation of bugled oxides and its subsequent cracking. The replicas were taken from the notch root of the CG LSHR tested at 650 ^{o}C. The raised parts of the replica (replica bulge) correspond to cracks at the notch root, whereas a "dent" on the replica corresponds to a "bulge" on the notch root surface. The natures of the "dent" and "bulge" have been verified by profile analysis using the Alicona Infinitefocus Microscope. In addition, slip bands can be observed on the replicas. Further examination of these "bulges" on the notch root surface by EDX indicates that they are Co-rich oxide complex (as shown in Fig. 5.8 below). As shown in Fig. 5.6, a crack has already appeared at the notch root surface when the specimen is loaded to 300 cycles, and a long and tortuous "dent" can be discerned on the replica. As loading cycle increases, the replica "dent" and bulge become more evident, which are associated with the growth of oxides on the surface and the continued opening of cracks due to propagation into the depth respectively. More importantly, a transition from "dent" to bulge on the replica is observed with increasing loading cycles, and this transition is believed to be caused by oxide cracking due to the build-up of stress around the oxides.

Fig. 5.7 presents the morphology of the oxides formed at grain boundaries and γ/γ′ interfaces. For the vacuum test, the most common oxides exhibit a somewhat discrete and circular morphology at GBs (Fig. 5.7 (a)) and the oxidised GBs are relatively flat. For the air tests, the oxides at GBs and γ/γ′ interfaces possess a more faceted morphology with a bulged height in both CG and FG LSHR (Figs. 5.7 (b) - (d)). The different morphologies of oxides in the vacuum and air tests indicate the differing degree of GB oxidation and possibly different types of oxides. In addition, the faceted/bulged oxides are also observed within primary γ′ precipitates as shown in Fig. 5.7 (d). Oxide formation within primary γ′ may be associated

with the crack cutting through primary γ′ observed in Fig. 5.5 (d). Along the crack path, some remaining oxide particles are discerned in the rectangle-highlighted region in Fig. 5.7 (d), which also indicates concerning that the grain boundary cracking is related to grain boundary oxidation.

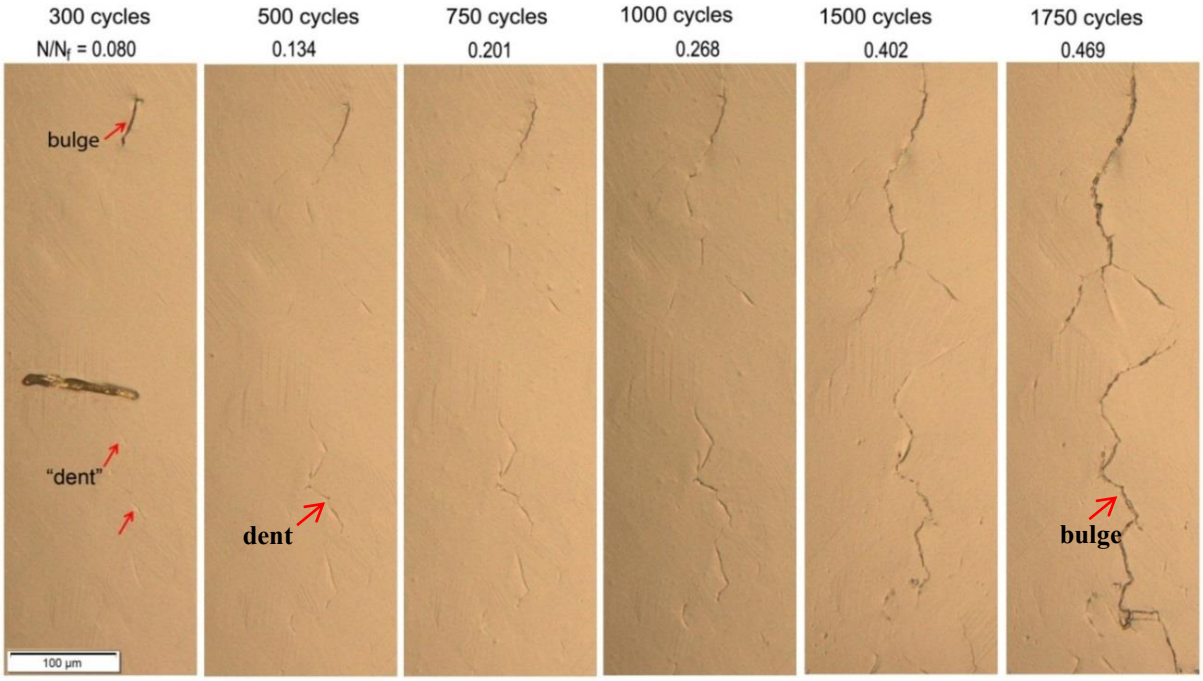

Fig. 5.6 Evolution of cracks on the replicas of the notch root: transition from "dent" (corresponding to oxide) to bulge (corresponding to crack) on the replicas of the CG LSHR tested at 650 ^{o}C. The bulge and "dent" are indicated by the arrows (A replica defect is in the middle of the replica at 300 cycles).

Fig.5.8 presents the morphology of the notch root in the CG LSHR tested at 725 ^{o}C in air and the compositional profiles across the grain boundaries with and without bulged oxides respectively. As mentioned previously, slip bands are observed within the grain of the CG LSHR, and the oxides are apt to form at those grain boundaries inclined normal to the tensile stress axis. Moreover, Fig. 5.8 (b) shows a straight segment of a grain boundary which is partly decorated with bulged oxides. In front of the bulged oxides, the grain boundary is decorated with less bulged and much thinner oxides. It seems that there is a transition between the thin/flat oxides and the wide/bulged oxides.

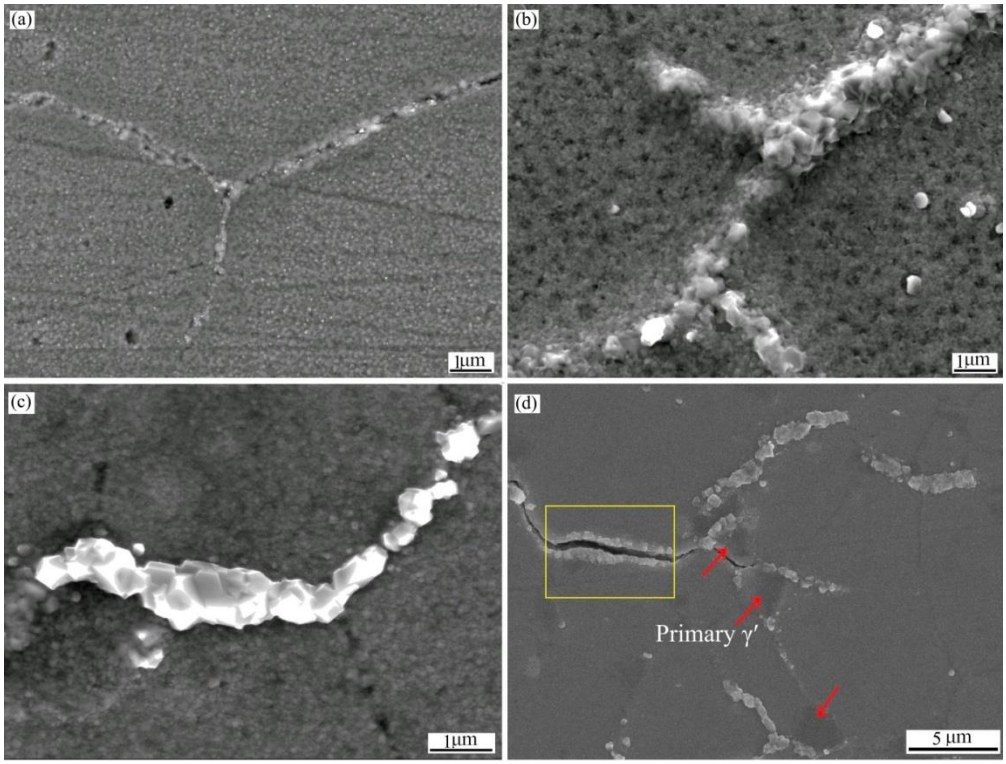

Fig. 5.7 Morphology of oxides at GBs and γ/γ′ interfaces: (a) CG LSHR, 650 ^{o}C, vacuum; (b) CG LSHR, 725 ^{o}C, air; (c) FG LSHR, 650 ^{o}C, air and (d) FG LSHR, 725 ^{o}C, air.

Fig. 5.8 (c) shows the normalized metallic element content (apart from Nb, Ta and Zr) tracking across a GB with a bulged oxide analysed by EDX. "0" in the graph indicates the location of the GB. Significant enrichment of Co and slight enrichment of Cr, along with a depletion of other metallic elements exist at the GB region, indicating that the bulged GB oxide is mainly a Co-rich oxide complex. Fig.5.8 (d) presents the compositional profile across a GB with a thin/flat oxide. A depletion of Co, Cr, W and Mo is observed, whilst an enrichment of Ni, Ti and Al at the GB region is identified, although the extent of this enrichment is not as significant as that of Co at the GB with a bulged oxide. This qualitative variation of the GB compositional profile indicates that the GBs without bulged Co-rich oxide complex are mainly decorated with a Ni/Ti/Al-rich oxide complex. Additionally, it is found that the content of Al is lower than its original content either at GBs or within grains and the content of Cr is relatively higher than its original content within grains, this is believed to be associated with the formation of an internal alumina layer and an outer layer of chromium oxide as observed in other Ni-based superalloys [139, 169, 170]. However, it should be pointed out that the elements in the regions nearby and underneath the GB oxides may also contribute to the composition of the GB oxides due to the relatively large electron

beam size used for EDX analysis in SEM and the large activation volume. The depletion of Ni at the GB with bulged oxides may not be able to rule out the existence of GB Ni oxides as the enrichment of Co in a constant activation volume usually corresponds to a depletion of the matrix element (i.e. Ni). Moreover, the Ni oxide and Co oxide have the same crystal structure and similar lattice parameters, and thereby it is expected that NiO and CoO form a single-phase solid solution scale at surface [17, 106]. Similarly, the depletion of Co and Cr in the Ni/Al/Ti-rich oxide complex may not be able to rule out the existence of Co and Cr oxides in the thin/flat GB oxides. The composition of the bulged oxides and flat oxides at GBs in the FG LSHR is similar to that in the CG LSHR.

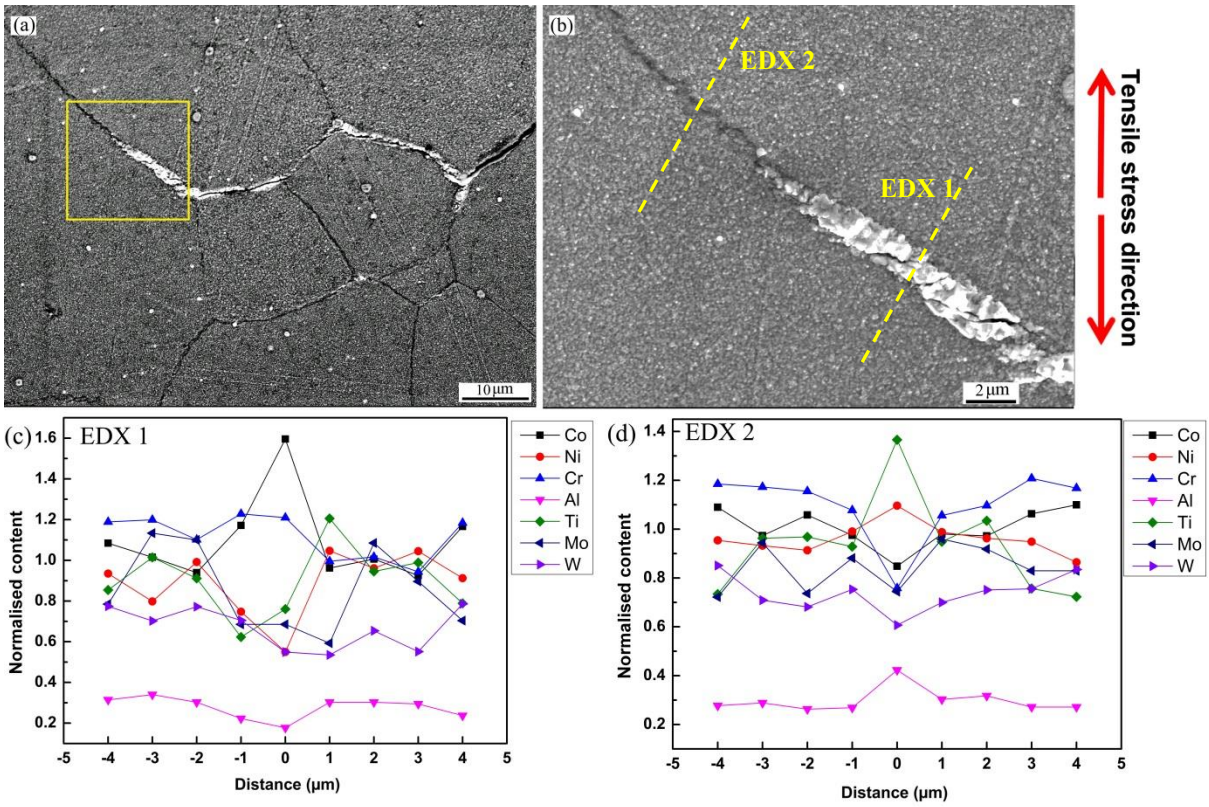

Fig. 5. 8 Morphology of notch root in (a) CG LSHR tested at 725 ^{o}C in air; (b) close-up of the region highlighted by rectangle shown in (a); compositional profile across grain boundary (c) with bulged oxide and (d) without bulged oxide. The EDX analysis regions are indicated by yellow lines shown in (b).

The compositional profile of a grain boundary in the CG LSHR tested in vacuum was also examined, and the result is shown in Fig. 5.9 (b). It is found that the grain boundary is enriched in Cr, which is believed to be associated with the preferential formation of Cr_2O_3 in an environment with low oxygen partial pressure. The normalised content of Cr is generally

greater than 1, indicating that a Cr_2O_3 layer may form both at grain-interior and grain boundary at the notch root surface. Enrichment of W and Mo are also found at the grain boundary, but it is not possible to determine whether there is oxidation of these two elements or they just preferentially segregate at grain boundaries or exist in a form of carbides. The much lower content of Al compared with its original content indicates an Al_2O_3 oxide layer may form underneath the surface Cr_2O_3 layer. In addition, it is interesting to find that the Co-rich oxide complex (containing ~40 wt.% Co indicated by EDX point analysis shown in Fig. 5.9 (c)) also form at certain grain boundaries in vacuum, although there are much fewer incidences of this compared with observations in the air tests.

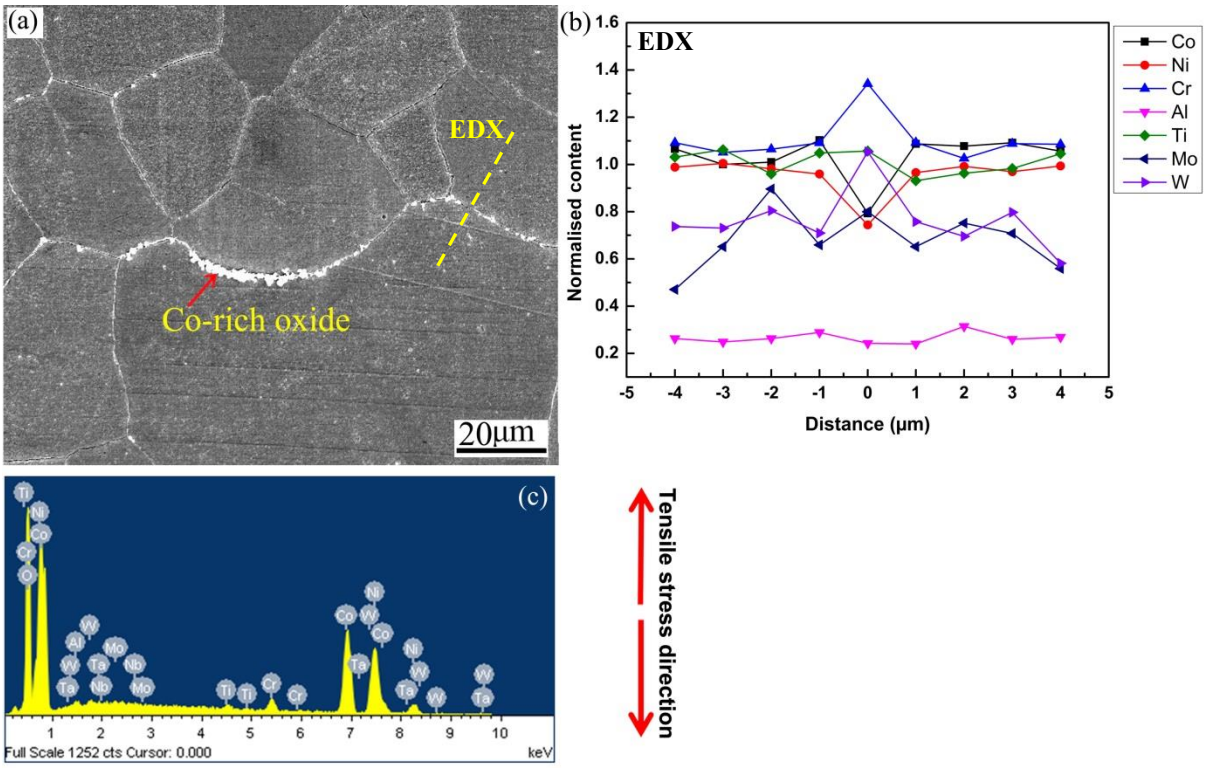

Fig. 5.9 (a) Morphology of notch root in the CG LSHR tested at 650 ^{o}C in vacuum; (b) compositional profile across a grain boundary indicated by the dashed line shown in (a); and (c) EDX spectrum of GB Co-rich oxide indicated by the arrow.

The evolution of cracks at the notch root was observed on replicas under OM. By contrast to the room temperature tests, there are *many* more cracks at the notch root surface at elevated temperatures, and these surface cracks are predominantly intergranular although they change to be transgranular as they propagate into the depth at 650 ^{o}C in the CG LSHR (Figs. 5.1 and 5.2). As shown in Fig. 5.10, cracks initiate relatively late in vacuum. Although slip bands are observed on the replicas, little slip band cracking is discerned, which is consistent

with the observation of the morphology of the notch root. Compared with the crack evolution at room temperature, more crack coalescences occur, and there are more small/secondary cracks in the regions adjacent to the primary cracks. However, a fully quantitative statistical assessment of the crack evolution process was deemed impractical due to the large number of cracks. In addition, the frequent crack coalescence makes the derivation of the da/dN vs. cycles invalid as crack growth is largely controlled by coalescence events.

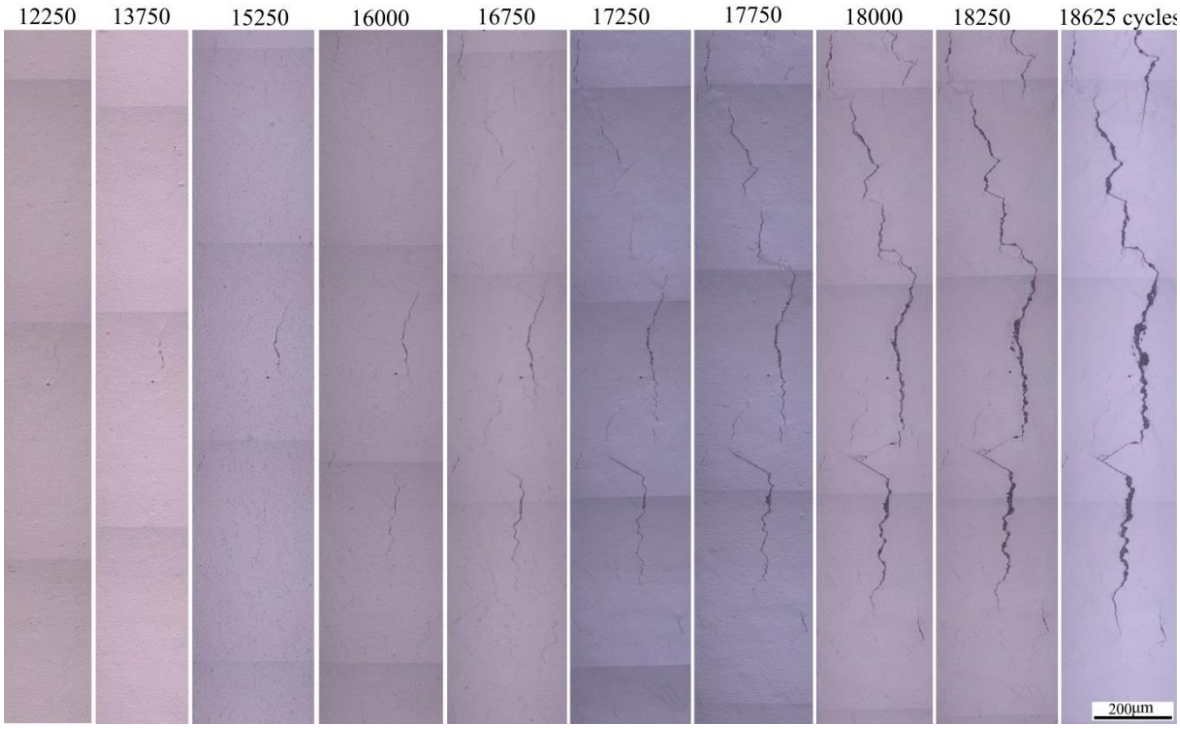

Fig. 5.10 Crack evolution on the replicas for the CG LSHR tested at 650 ^{o}C in vacuum.

As shown in Fig. 5.11, cracks mainly initiate from grain boundary for the CG LSHR tested at 650 ^{o}C in air. Compared with the vacuum test, crack initiation occurs at the early stage of the fatigue life, and more cracks and more frequent crack coalescence can be observed on the replicas. Main crack coalescences can be found on the replicas as shown in Figs. 5.11 (c)-(g), which causes significant increases in crack length.

As the test temperature was increased to 725 ^{o}C or when the test was conducted on the FG LSHR microstructural variant, the number of intergranular cracks becomes more significant, and so crack coalescence occurs even more frequently. The cracks propagate along grain boundaries at both surface and depth (Figs. 5.3 and 5.4). The crack evolution process in the CG LSHR and the FG LSHR at 725 ^{o}C is shown in more detail in Appendix II.

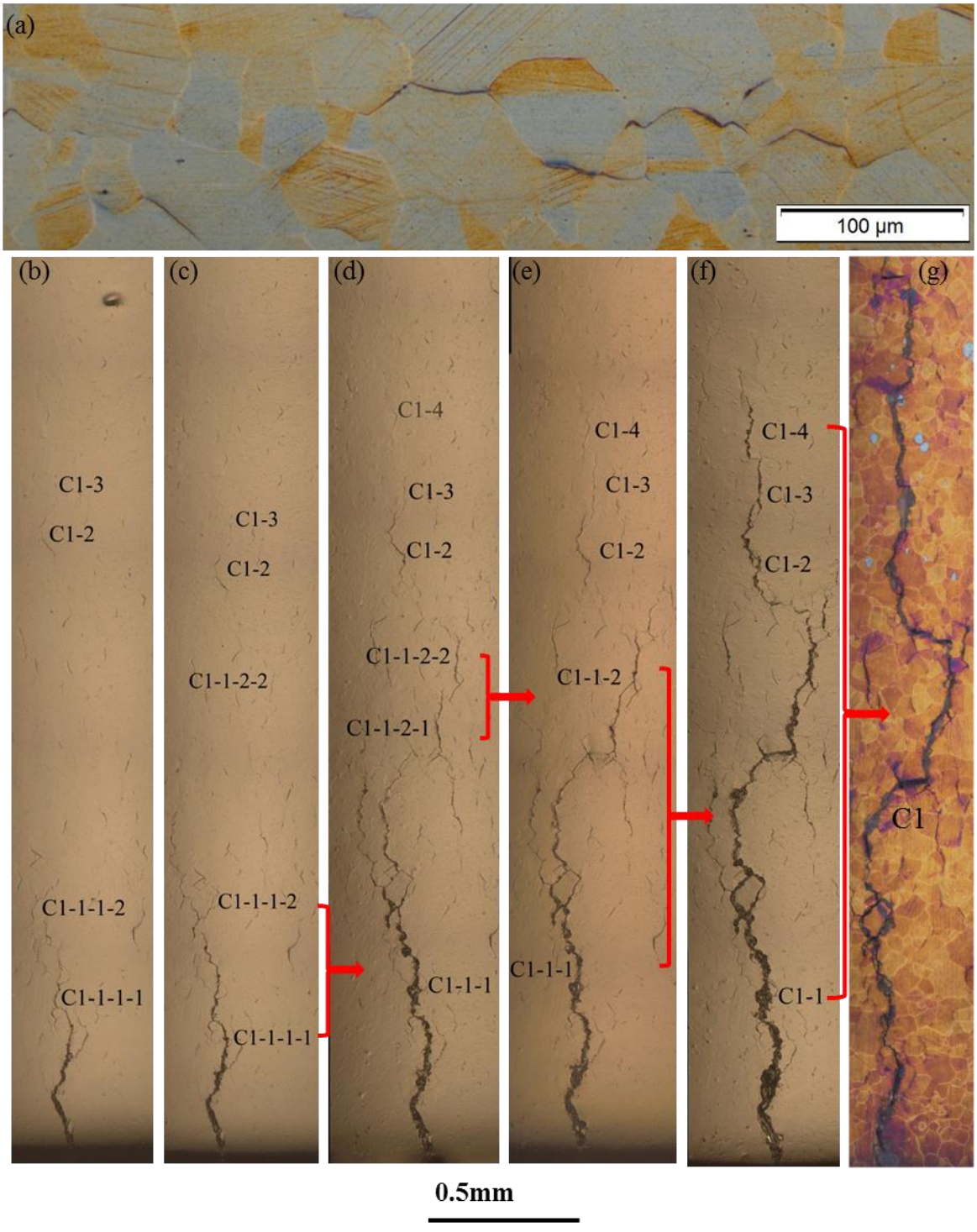

Fig. 5.11 Evolution of cracks at the notch root of the CG LSHR tested at 650 ^{o}C in air: (a) intergranular cracks at 500 cycles; replica made at (b) 1200 cycles; (c) 1500 cycles; (d) 1950 cycles; (e) 2100 cycles; (f) 2400 cycles and (g) metallography of the notch root at 2850 cycles.

5.3.4 Characterisation of oxides at GB and γ/γ′ interface

In order to understand the nature of oxides at grain boundaries and/or γ/γ′ interfaces, a TEM foil which contained a grain boundary with bulged oxides and an oxidized γ/γ′ interface was prepared by FIB. The TEM foil was extracted from FG LSHR tested at 725 ^{o}C. As shown in Fig. 5.12, the bulged oxides can penetrate into the subsurface along a grain boundary (in this sample) by a distance of ~1μm and form an oxide intrusion along the grain boundary. The width of the grain boundary oxides is ~0.5 μm (Figs. 5.12 (b) and (c)). Similarly, oxides at the γ/γ′ interface can also penetrate internally, although the penetration depth appears much shorter (Figs. 12 (b) and (d)). Within the γ grain and primary γ′ at the notch root surface, it seems that the oxides consist of a uniform oxide scale (apart from at GBs) with internal oxide particles underneath the oxide scale. Moreover, secondary γ′ can be seen in Fig. 5.12, although not very clearly. It appears that there is dissolution of secondary (and possibly tertiary) γ′ around the grain boundary ahead of the oxide intrusion as shown in Fig. 5.12 (c).

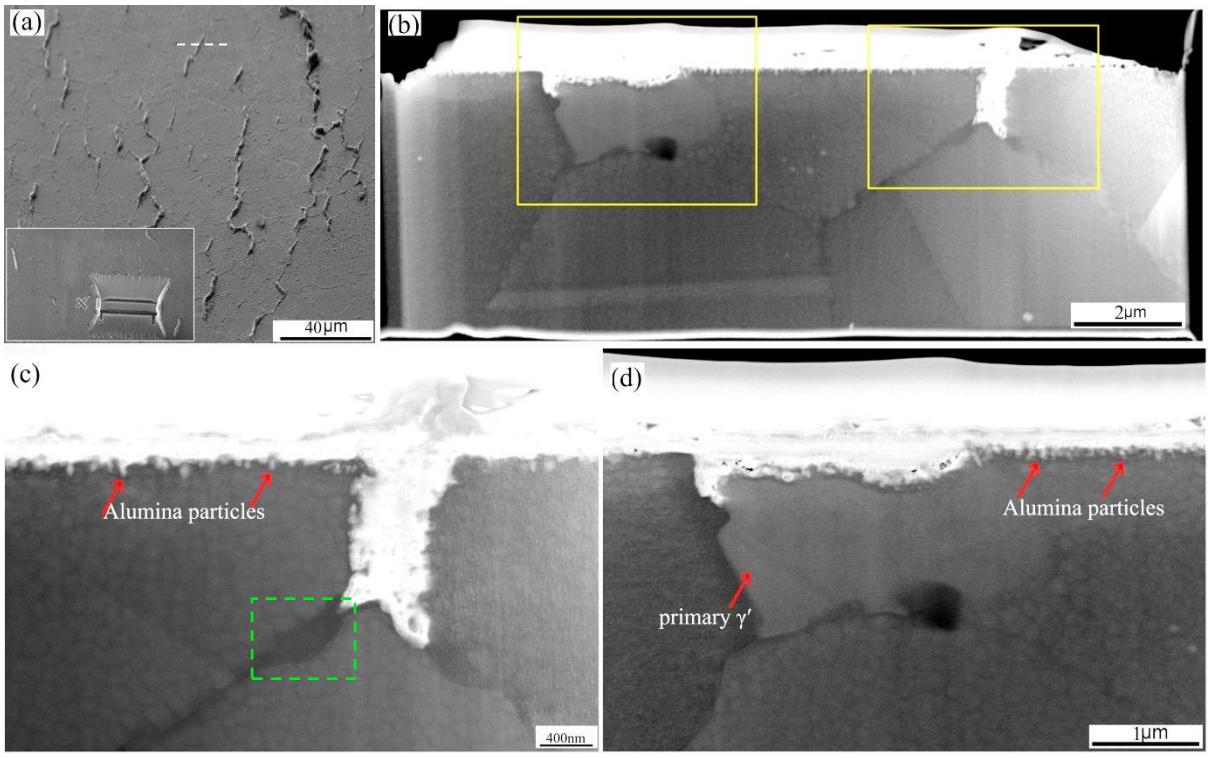

Fig. 5.12 (a) Morphology of the notch root surface in the FG LSHR tested at 725 ^{o}C in air and the extraction site of the TEM foil; (b) full-view of the TEM foil; (c) and (d) close-up of the oxidation at grain boundary and γ/γ′ interface in the regions highlighted in (b), respectively.

Fig. 5.13 shows the penetration of the oxide into the depth direction by sectioning the

tested specimen. In fact, it is found that the penetration depth of bulged grain boundary oxides can range from ~1μm to tens of a μm, which is much longer than that observed in the particular TEM foil we prepared by FIB. The oxide cracking at the surface and the region close to surface can be seen in Fig. 5.13 (b), but the oxides appear to be intact in the further depth, which also indicates the oxide cracking is the main mechanism for crack initiation and propagation.

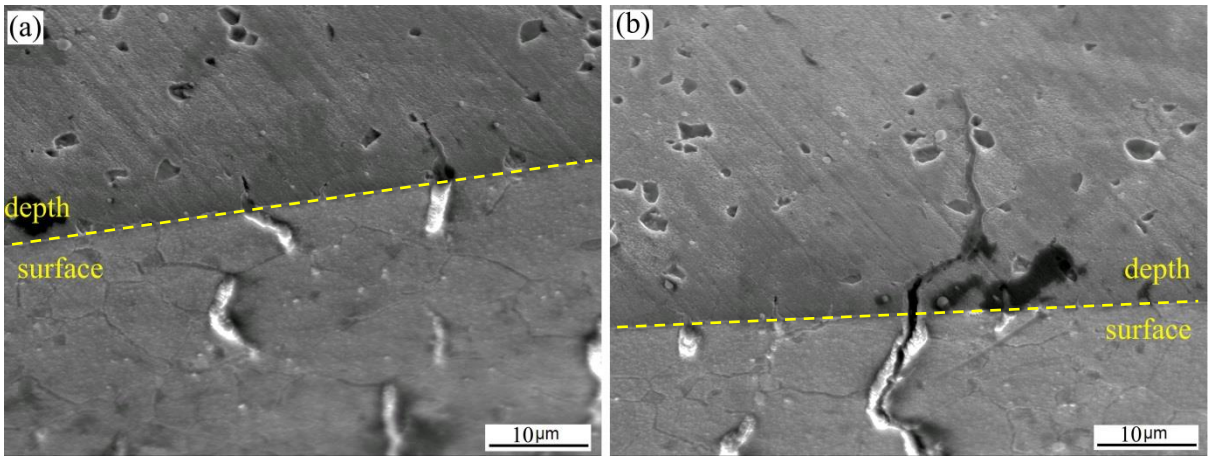

Fig. 5.13 (a) and (b) Penetration of bulged grain boundary oxides observed on the sectioned plane in the FG LSHR alloy tested at 725^{o}C in air.

The composition of the oxides was further analysed by EDX in a TEM. As shown in Fig. 5.14, the oxides at the grain boundary in Fig. 5.12 (c) are enriched in Ni, Co, Cr, Ti and Al. At the outermost surface, the oxides are Ni and Co oxides, and these two oxides typically form a single-phase solid solution scale. Formation of Ni and Co oxides is associated with the dissolution of the γ matrix and γ′ precipitates around GB and the outward diffusion of Ni and Co as indicated by the elemental maps. In addition, an enrichment of Ni and Co at the interfaces of oxides/alloy matrix and GBs ahead of the oxide intrusion can be discerned in the elemental maps. It is interesting to note that the enrichment of Ni and Co and the depletion of Al and Ti at the grain boundaries ahead of the oxide intrusion span a width of approximately 300 nm which is much wider than the GB width and the equivalent diameter of the secondary γ′ precipitate, apparently indicating dissolution of γ′. Underneath the Ni and Co oxide scale, Cr, Ti and Al oxides form, and these oxides penetrate along the grain boundary. The distribution of these three oxides varies from location to location. It seems that more Cr and Ti oxides form at the grain boundary close to outer surface, whereas more Al oxides form at the grain boundary away from the outer surface. The much more evident Al oxide close to the

tip of the oxide intrusion indicates that the formation of Al oxide at this region not only depends on the inward diffusion of O, but also both inward and outward diffusion of Al at the oxidised grain boundary and the grain boundary ahead of the oxide intrusion. Moreover, apart from the regions with oxides, there is no O enrichment at GBs ahead of the oxide intrusion. For the oxide particles underneath the continuous oxide scale within the grains, they appear to be Al oxide.

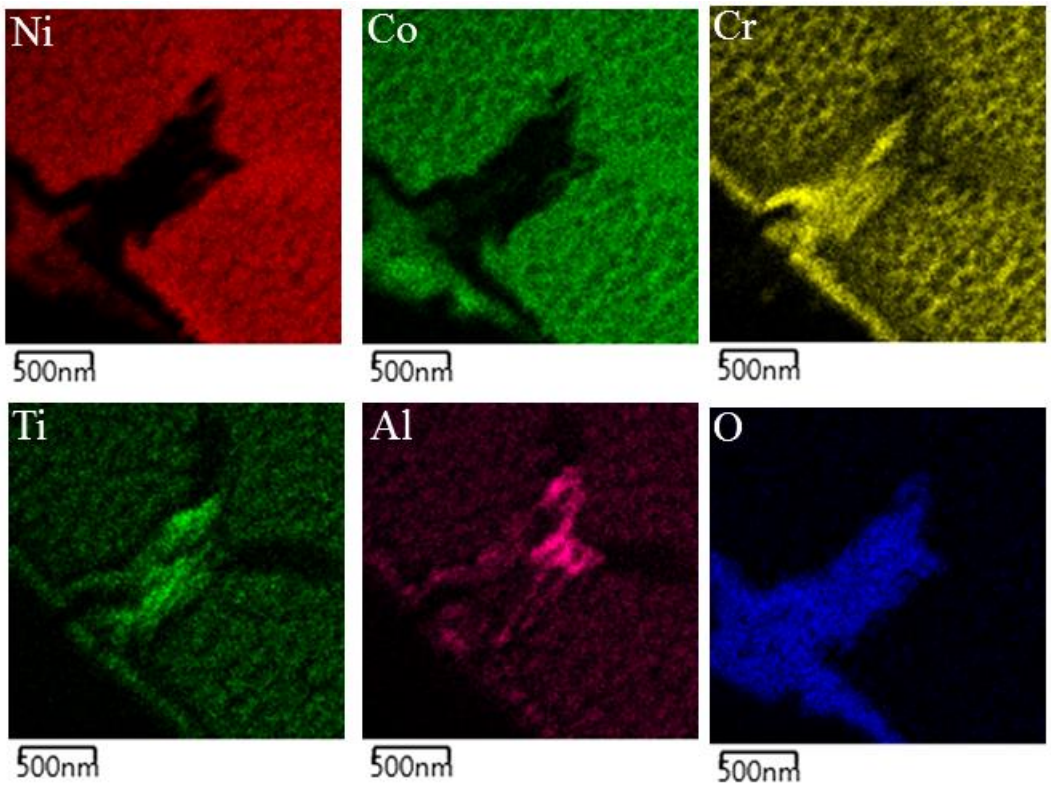

Fig. 5.14 EDX elemental maps of the region around the GB oxides shown in Fig. 5.12 (c).

The element distribution associated with oxides around primary γ′ (Fig. 5.12 (d)) is shown in Fig. 5.15. It is found that similar oxide layers are observed. At the outer surface, it is a Ni and Co oxide layer. However, it is interesting to note the Co oxide layer on the top of the primary γ′ and the Co oxide layer is thicker than the Ni oxide layer. Formation of the Co oxide layer above the primary γ′ may be related to the lateral diffusion of Co as the content of Co in the primary γ′ is much less than that in the matrix (the partitioning ratio of Co (in wt.%) between γ and γ′ is about 2.55 [19]). Underneath the Ni and Co oxides, Cr, Ti and Al oxides form. It is also found that the Al oxide penetrates along the γ′/γ interface. Furthermore, an enrichment of Cr and Co and a depletion of Ni, Al and Ti are found at the γ′/γ interface.

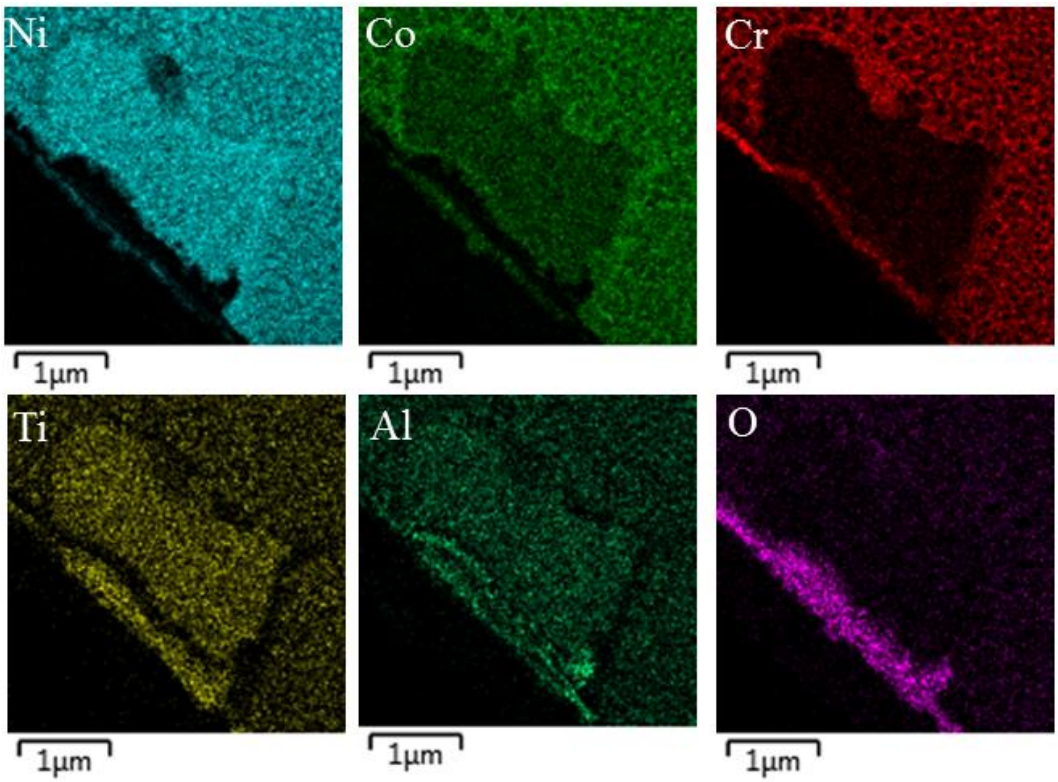

Fig. 5.15 EDX elemental maps of the region around the primary γ′ shown in Fig. 5.12 (d).

5.3.5 Influence of grain orientation on oxide formation and fatigue cracking

As shown previously in Section 5.3.3, oxide formation shows a selectivity of grain boundaries. The formation of grain boundary oxides and their subsequent cracking are closely related to crack initiation and propagation. In order to reveal the dependence of oxide formation and cracking on grain orientation, EBSD analysis has been conducted on the areas containing oxides and cracks.

Fig. 5.16 presents the grain orientation map and SF map for an AOI in the notch root of the CG LSHR tested at 725 ^{o}C in air. The AOI is shown in Fig. 5.16 (a). The crack-initiated sites are indicated by the arrows based on the observation of the replicas taken at this region. The SF is derived by considering the applied tensile stress axis is parallel to the length direction of the specimen. As shown in Fig. 5.16 (c), the crack-initiated sites locate preferentially at the boundaries between high and low SF grains. However, it should be noted that the index rate for this EBSD mapping is relatively low (~60%) due to the notch geometry which makes it difficult to get a good polished surface and shields the signals during EBSD mapping. As a result, further EBSD study was conducted on the plain bend bar specimens.

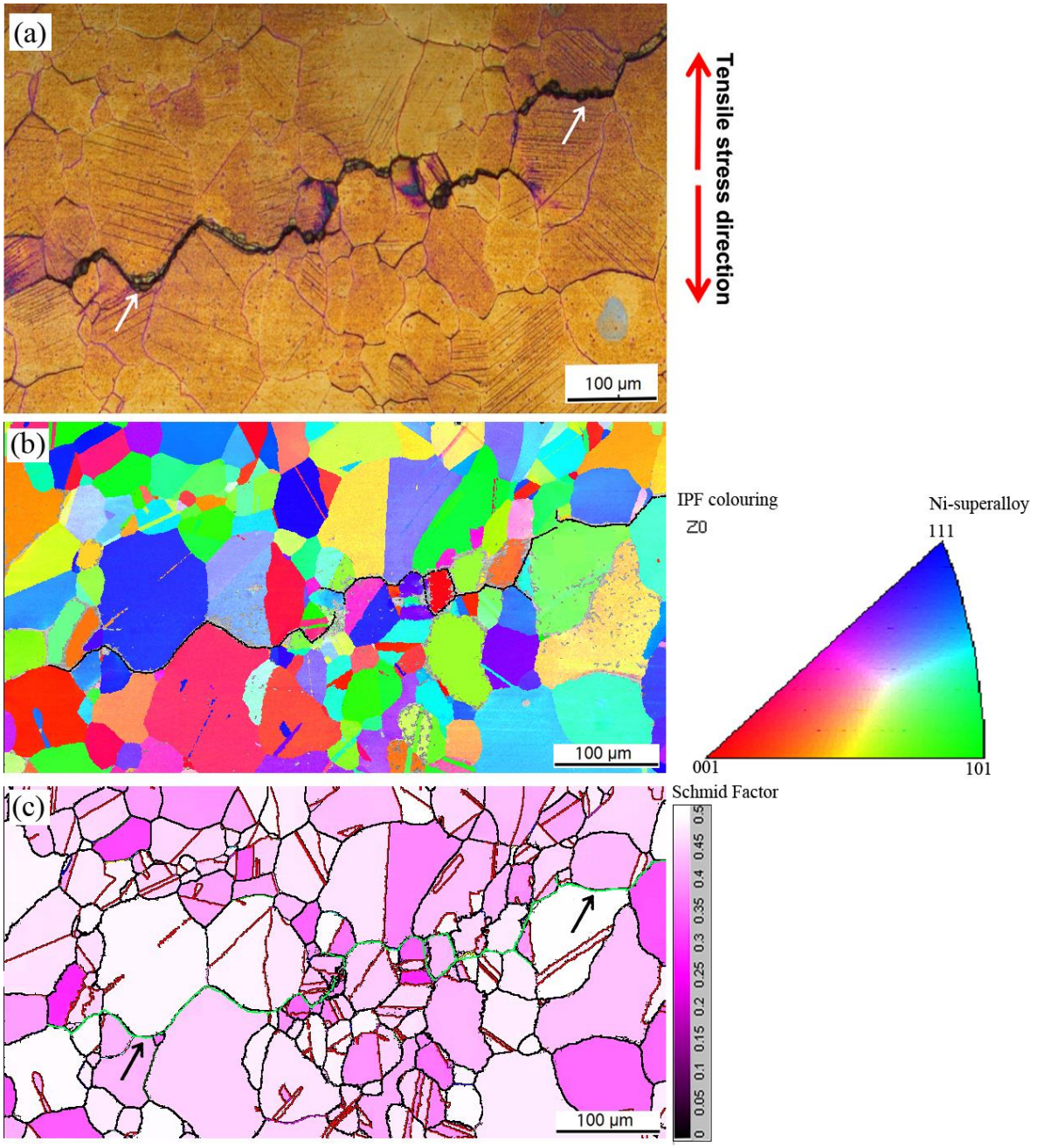

Fig. 5.16 (a) Morphology of GB oxidation and cracking in the LSHR alloy observed under OM in the CG LSHR tested at 725^{o}C in air; (b) grain orientation map and (c) colour-coded SF map of the region shown in (a), crack paths are outlined on the SF map by green lines.

Fig. 5.17 illustrates the dependence of the GB oxidation and cracking on grain orientation in the LSHR alloy. The region containing crack paths and GB oxides on the top central surface was chosen for EBSD mapping as shown in Fig. 5.17 (a). It seems that the grain boundary oxides are more evident in this plain bend bar specimen compared with the CG LSHR U-notch specimen due to the relatively finer grain size. The grain orientation of the

chosen area is shown in Fig. 5.17 (b), exhibiting many twins, and the derived Schmid factor map is shown in Fig. 5.17 (c). It is found that crack paths appear to locate preferentially at the boundaries between high and low SF grains. Similarly, it is found that the oxides also tend to form at high /low SF grain boundaries as indicated by the arrows in Figs. 5.17 (a) and (c).

Figs. 5.17 (d) and (e) show the maximum SF of the grains neighbouring GB oxides in the regions highlighted in Fig. 5.17 (a). It can be found that the formation of bulged GB oxides is associated with the large difference in SF between grains (as indicated by the arrows), rather than the high SF value, as GB oxides are also observed at boundary of grains with low SF. The dependence of GB oxide formation on the difference of the SF may indicate that the oxidation process is related to the strain localisation, because dislocations are expected to pile up at boundaries of grains with a large difference in SF as a result of the hindrance of slip transmission (plastic and elastic incompatibility) at these regions [118, 121]. The higher dislocation density associated with higher local strain can provide short-circuit paths for the diffusion of oxide-forming elements and oxygen, and thereby accelerates the oxide formation. In addition, the formation of oxides within slip bands shown in Fig. 5.5 (c) further verifies that the formation of oxides is indeed related to the local strain.

The distribution of the maximum SF of grains neighbouring the crack paths and ~800 grains in the bulk material is presented in Fig. 5.17 (f). This shows that most of the grains in the bulk material have slip systems associated with the relatively high SF (>0.43) under the applied load conditions, and takes on a unimodal distribution. Conversely, a weak bimodal distribution of the SF of grains neighbouring the crack paths is observed, which is probably related to the fact that the cracked grain boundaries are associated with grains of differing SF. The weak trend of the bimodal distribution indicates that the GB oxidation and cracking may not necessarily require a very large difference in SF between neighbouring grains.

Fig. 5.18 shows the results of the EBSD analysis of the area containing cracks in the batch 2 LSHR tested in vacuum at 650 ^{o}C. It is found that both intergranular and transgranular cracks exist as shown in Figs. 5.18 (a) and (b). However, the grain boundary oxides are not evident based on OM observation. The SF map and the distribution of the SF of the crack-related grains and the bulk material are shown in Figs. 5.18 (c) and (d) respectively. It seems that no bimodal distribution can be observed as in the air test, indicating an insignificant dependence of cracking on grain orientation in vacuum.

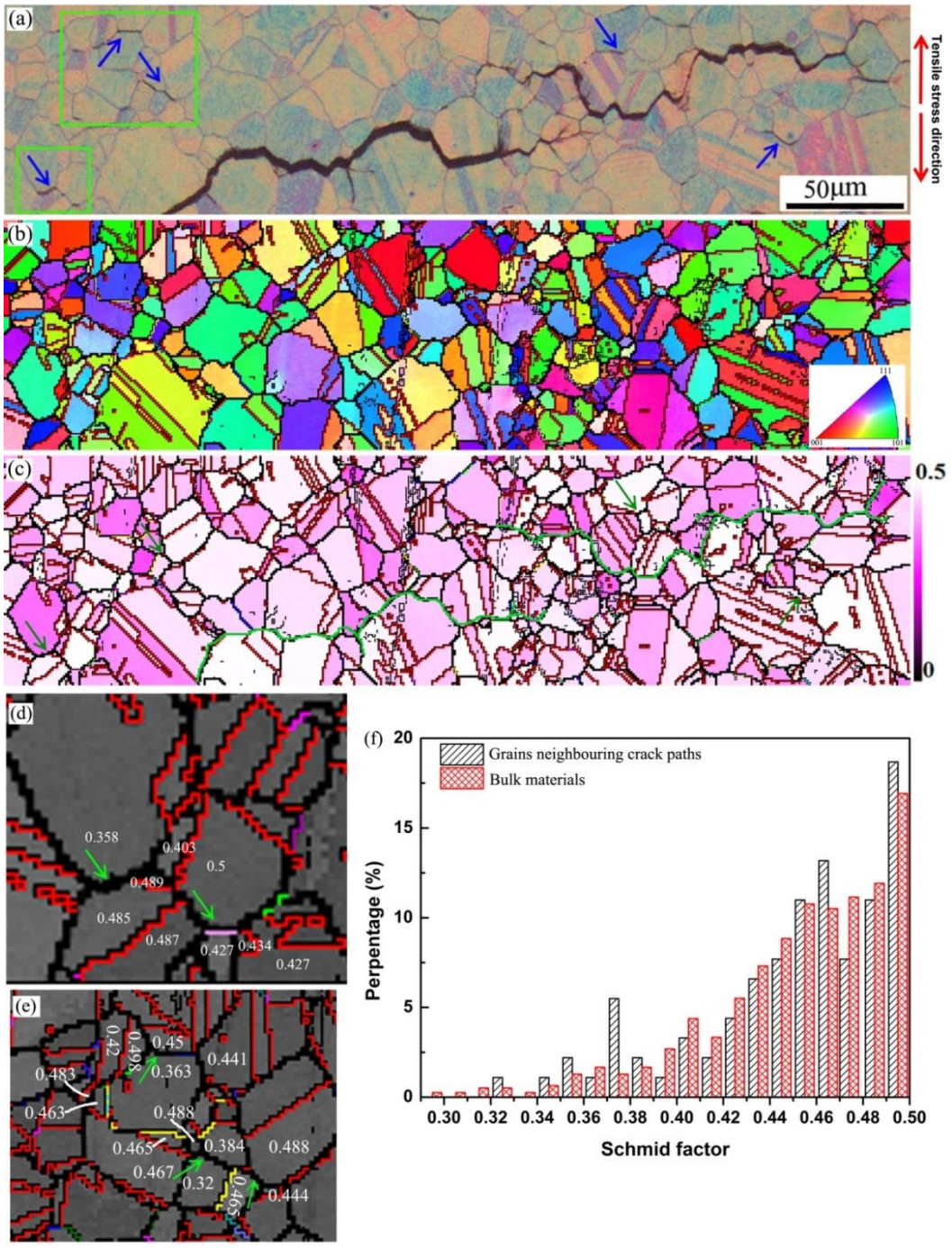

Fig. 5.17 (a) Morphology of GB oxidation and cracking observed under OM in the batch 2 LSHR alloy tested at 650 ^{o}C in air; (b) grain orientation map and (c) colour-coded SF map of the region shown in (a), crack paths are outlined on the SF map by green lines; (d) and (e) maximum SF of the grains of interest highlighted at the bottom and top shown in (a) respectively, the GBs with bulged oxides are indicated by the green arrows; and (f) SF distribution of grains neighbouring the crack paths and bulk materials.

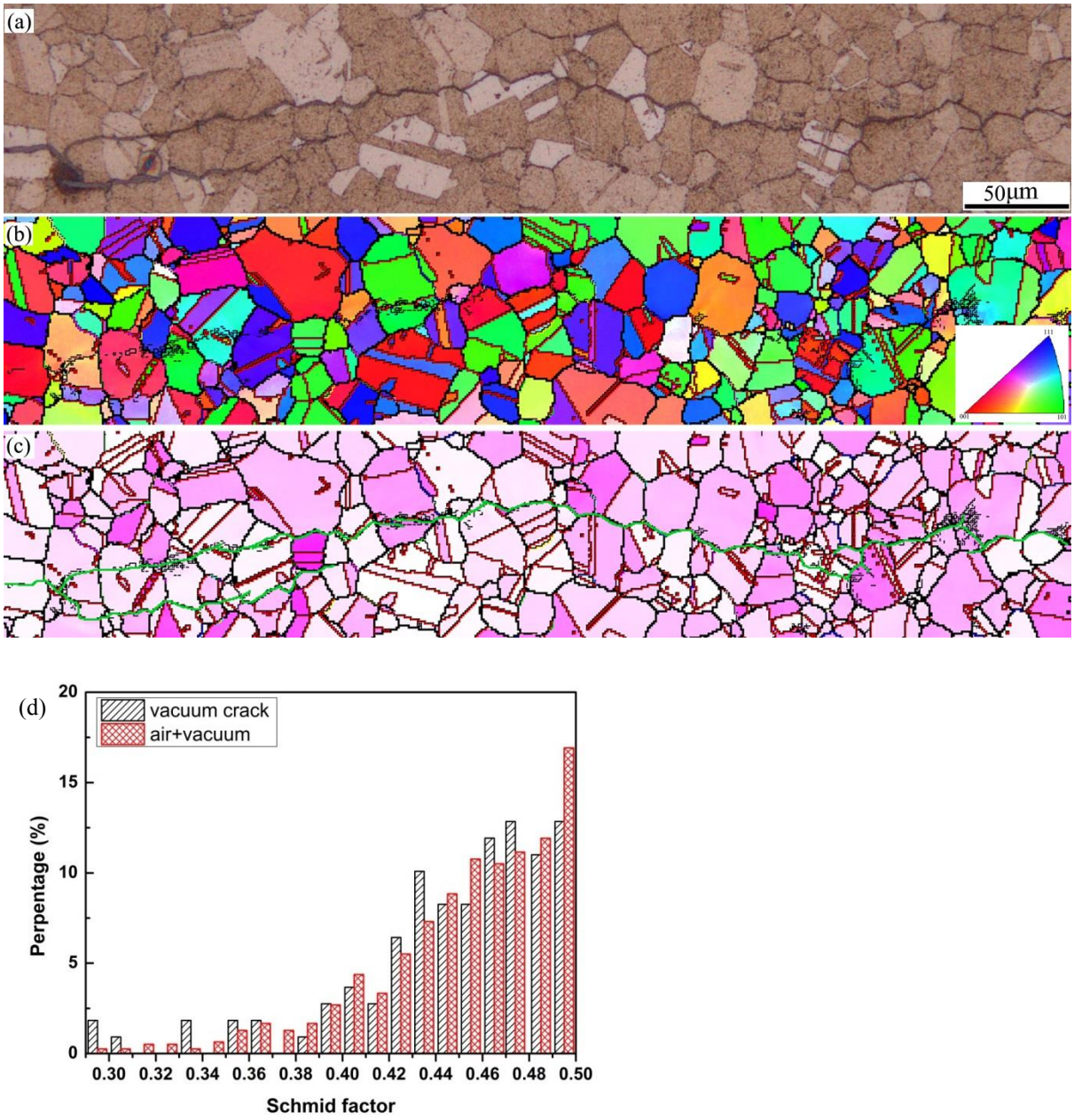

Fig. 5.18 (a) Morphology of GB oxidation and cracking observed under OM in the batch 2 LSHR alloy tested at 650 ^{o}C in vacuum; (b) grain orientation map; (c) colour-coded SF map of the region shown in (a), crack paths are outlined on the SF map by green lines; and (d) SF distribution of grains neighbouring the crack paths and bulk materials.

5.4 Discussion

5.4.1 Effects of oxidation on crack initiation at elevated temperatures

The crack initiation process in the LSHR alloy at elevated temperatures significantly differs from that at room temperature. At room temperature, crack initiation is closely

associated with the slip planarity of the LSHR alloy, and cracks mainly initiate from TBs and occasionally initiate from slip bands in relatively large grains with favourable orientation in relation to the tensile stress axis either in the CG or FG LSHR (Figs. 4.31, 4.11 and 4.12). At elevated temperatures, no slip band/TB cracking is observed, although extensive slip bands can be seen in the CG LSHR. For the FG LSHR, few slip bands can be observed due to its reduced overall slip planarity caused by the finer microstructure. Based on the observation of the notch roots and fracture surfaces, cracks predominantly initiate along grain boundaries in both CG and FG LSHR due to the oxidation effects under the investigated conditions, even though it is reported that crystallographic facet crack initiation and crack initiation at subsurface pore and internal inclusions have also been observed at elevated temperatures for the LSHR alloy [19]. This difference in crack initiation is probably ascribed to the relatively high strain achieved at the notch root in this study, which accelerates the oxidation process by lowering the thermal activation energy and providing more short-circuit paths for the diffusion of oxygen and oxide-forming elements. Crack initiation from subsurface porosity associated with the relatively low strain is observed in other disc alloys such as U720Li [9]. In addition, the oxidation at γ/γ′ interfaces (Figs. 5.5 (d) and (e)) in the FG LSHR also makes these regions become potential crack initiation sites, and the beneficial effects of primary γ′ on resisting crack initiation and propagation observed at room temperature may vanish at elevated temperatures.

The oxide layers formed during the fatigue test basically have the same constituents, i.e. an outermost layer of Ni/Co oxides, an intermediate layer of Cr/Ti oxides and an internal layer of Al oxide with finger-like Al oxide formations, at grain interiors, primary γ′, grain boundaries and γ/γ′ interfaces. However, the significant differences are the depth of Cr/Ti/Al oxide intrusion and the bulged height of Ni/Co oxides along the grain boundaries and γ/γ′ interfaces. The longer oxide intrusion along a grain boundary and the higher bulged height of Ni/Co oxides are usually associated with more significant mismatch strain and hence stress concentration. Therefore, intergranular crack initiation at elevated temperatures is closely related to the formation of the bulged grain boundary Ni/Co-rich oxides and Cr/Ti/Al oxide intrusion and subsequent oxide cracking, rather than the impingement of slip bands at oxygen-attacked grain boundaries. The oxide cracking induced crack initiation can be supported by the transition from a “dent” to a “bulge” on the replicas of the notch root as shown in Fig. 5.6. It should be noted that the impingement of slip bands at grain boundaries may enhance the diffusion of oxide-forming elements and oxygen to some extent as slip

bands can also provide short-circuit diffusion paths as grain boundaries [171]. But it seems that the effect of slip bands on the transportation of the oxide forming elements is quite limited compared with the grain boundaries, indicated by much more marked bulged Ni/Co-rich oxides in the FG LSHR where limited slip bands exist.

It is not rare to see crack initiation assisted by oxide cracking in aeroengine turbine disc alloys. For instance, the porous Ni-oxide or NiO/Cr_2O_3 oxide complex which has a spinel structure is frequently reported to cause crack initiation in disc alloy Inconel 718 [12, 13]. Additionally, the oxidation of Nb carbide to Nb oxide has also been observed as a potent crack initiation source due to the significant volume expansion during the transformation in Inconel 718 [7]. Intergranular crack initiation due to grain boundary oxidation are also observed in other disc alloys, such as Udimet 500 [91], U720Li [9], N18 [92], ME3 [84]. However, the oxides responsible for this intergranular crack initiation vary from alloy to alloy and depend on the test conditions. As shown in this study, the fatigue cracking here is caused by formation of the bulged GB Ni/Co oxides and Cr/Ti/Al oxide intrusion and subsequent cracking of these oxides, which is not widely reported, although it is expected that the formed Ni/Co oxides may produce a surface ridging due to the outward diffusion during this oxide formation [91, 106]. In fact, only Kitaguchi [17] has reported a Ni/Co-rich oxide formed ahead of the crack tip recently in the disc alloy RR1000 which has a similar Co content to the LSHR alloy in this study. Based on the present findings, this suggests that the oxidation of Ni and Co under cyclic load at elevated temperatures may be an important issue in such disc alloys and may accelerate crack initiation and propagation, especially in high Co-containing disc alloys. The use of Co to lower solvus temperature and increase yield strength through increased Co addition is not only a feature of the LSHR alloy investigated in this study but also RR1000 and TMW-4M3 [17, 19, 78].

5.4.2 Effects of oxidation on short crack propagation at elevated temperatures

Short fatigue crack propagation is quite sensitive to the microstructures ahead of the crack tip and the associated deformation behaviour within the plastic zone. However, as temperature increases, this microstructure-sensitive short crack propagation becomes less dependent on the mechanical deformation process ahead of the crack tip, but more relies on the coupled oxidation-deformation interaction. At room temperature, cracks propagate along

the slip bands/TBs at the notch root surface in either CG or FG LSHR alloy, and propagate along the crystallographic facets in the depth direction by a distance of 330±38 μm in the CG LSHR and 105±15 μm in the FG LSHR (Fig. 4.3). The propagation of cracks markedly depends on the cracking of slip bands associated with high SF in the grains ahead of the crack tip. The grain boundaries and primary γ′ precipitates usually act as barriers to crack propagation, because the slip bands usually terminate in front of these regions due to the elastic/plastic incompatibility [37, 86, 108].

At elevated temperatures, the barriers (i.e. grain boundaries and primary γ′ precipitates) to crack propagation at room temperature now become preferential routes for crack propagation due to the selective oxidation at these regions. It is found that nearly all the surface cracks propagate along grain boundaries in the air tests for both CG and FG LSHR alloys, and the majority of surface cracks also propagate along grain boundaries in the vacuum test for CG LSHR. Crack propagation along γ/γ′ interfaces and/or cutting through the primary γ′ in the FG LSHR is also observed due to oxidation. The predominant intergranular crack propagation at the surface is correlated to having sufficient oxygen supply and the highest strain achieved at the notch root surface, both of which can accelerate the occurrence of the oxidation. The crack propagation penetrating into the depth depends on microstructure, test temperature, oxygen partial pressure and the local strain at the crack tip. In general, FG LSHR exhibits predominantly intergranular fracture characteristics, especially at 725 ^{o}C, whereas CG LSHR fracture surfaces are mainly characterized by mixed inter-transgranular features although the degree of intergranular feature increases with testing temperature. This difference between the morphology of fracture surface in CG and FG LSHR is mainly attributed to the more significant grain boundary oxidation occurring in the FG LSHR. In the transgranular fracture surface in the CG LSHR, few crystallographic facets can be observed. The absence of these crystallographic facets at elevated temperatures is believed to be related to the enhanced cross-slip of dislocations and/or other thermally activated dislocation motion such as climb.

The transition from intergranular crack propagation to transgranular crack propagation in the depth direction is a consequence of the competing effects between oxidation and mechanical damage. This transition predominantly depends on temperature and the local strain ahead of the crack tip. Immediately after crack initiation, the mechanical driving force for crack propagation is relatively low. Oxidation therefore has enough time to occur ahead of

the crack tip, and this oxidation process is accelerated by the high temperature and high local strain, resulting in intergranular crack propagation. With increasing crack length, the mechanical driving force for crack propagation increases correspondingly, and the crack propagates at a higher speed and the time for oxidation processes to occur ahead of the crack tip is reduced for the same advancing increment of crack. Hence, the mechanical damage may start to outstrip the evolution of oxidation damage ahead of the crack tip, giving rising to transgranular crack propagation. The higher temperature and local strain ahead of the crack tip can delay this intergranular-transgranular transition to some extent. The influence of local strain on the transition between fracture modes has been further illustrated in a similar study on short crack initiation and propagation in U720Li, where a transition from transgranular fracture to intergranular fracture is seen due to the relatively low initial strain and subsequent increase in local strain ahead of the crack tip (which gives rise to more significant oxidation effect ahead of the crack tip) [9]. However, a similar study on the disc alloy N18 (which has similar grain size to the FG LSHR) yields a predominantly transgranular fracture surface at both 650 ^{o}C and 725 ^{o}C when the same applied load was used, indicating the important influence of alloy composition on the oxidation processes ahead of the crack tip and the corresponding crack propagation modes [2, 92].

The replica of the notch root shows that coalescence of small grain boundary cracks is the main mechanism of crack length increase at the notch root surface at these elevated temperatures, especially in the FG LSHR. Considerable numbers of small grain boundary cracks form in the FG LSHR due to the cracking of the bulged grain boundary oxides. The propagation of these kinds of small cracks is determined by further oxidation occurring at the adjacent grain boundary. From observation of the replica record, it seems that there is no marked individual propagation of these small cracks during the majority of fatigue life before a significant coalescence happens in a relatively short period at the end of fatigue life. This crack growth behaviour is quite different from that observed at room temperature. Although crack coalescence also occurs during crack growth at room temperature, particularly in the CG LSHR, the frequency of this coalescence is much lower. It seems that this crack coalescence is related to the large numbers of cracks initiated (which is associated with the degree of oxidation). As shown in the replicas in Figs. 5.10 and 5.11 as well as Appendix II, crack length increase can be realized by propagation and coalescence in vacuum for the CG LSHR, but there is limited crack length increase by propagation processes in air, especially at 725 ^{o}C and in the FG variant.

In terms of crack propagation, apart from the effect of crack coalescence, crack arrest and retardation due to the shielding effect arising from the presence of neighbouring cracks is also observed at room temperature, but these interactions are not observed in the LSHR alloy at elevated temperatures. Previous work in other alloys (e.g. in austempered ductile irons at room temperature) carried out at Southampton has shown that short crack growth behaviour can be dramatically different where significant micro-crack fields are formed. Where initiation processes were very easy (e.g. cracking of multiple carbides [126]) subsequent crack growth was observed to be extremely slow, as the closely neighbouring cracks robbed surrounding crack tips of the required strain fields to propagate and lifetime was effectively controlled by coalescence events. In some cases a microcracking field can occur ahead of a primary crack tip, contributing significantly to crack propagation resistance [125].

5.4.3 Mechanism of strain (stress)-assisted oxidation

As previously discussed, oxidation, especially at grain boundaries and γ/γ′ interfaces, significantly enhances fatigue crack initiation and propagation in the LSHR alloy at elevated temperatures. The net effect of oxidation on fatigue crack initiation is a function of the microstructures of the investigated alloys, temperature, oxygen partial pressure and applied strain/stress. The effect of oxidation on crack propagation, apart from the aforementioned factors, also depends on crack growth rate which determines the oxidation time possible in each fatigue loading cycle. Generally, fine microstructure, high temperature, high oxygen partial pressure and high applied strain are associated with severe grain boundary and γ/γ′ interface oxidation, producing more significant bulged/wide grain boundary Ni/Co-rich oxides in combination with the longer Ti/Cr/Al oxide intrusion along grain boundaries. On the contrary, coarse microstructure, low temperature, low oxygen partial pressure and low applied strain are associated with less grain boundary attack and less marked grain boundary oxides. Such differences concerning the influence of microstructure, temperature and oxygen partial pressure on grain boundary oxide formation can be easily found by comparing the oxides in Fig 5.5, which can be easily understood in light of the higher diffusivity of oxygen and oxide-forming elements at higher temperature, the increase in short circuit diffusion paths in the finer microstructure (due to the greater grain boundary area) and the higher available oxygen content. Although only one load condition was used in this study, the influence of the applied strain (stress) on oxidation can be seen in Karabela's study on RR1000 which shows the thickness of oxide scale increases with increased applied stress and

the corresponding strain [142]. Moreover, high applied strain enhanced intergranular crack initiation is widely reported [2, 19], which indirectly verifies the effect of applied strain on this oxidation process. Although the detrimental effects of applied strain are widely observed, it is noteworthy that the applied strain/stress can cause a reduction in the duration of the less protective transient oxidation period and promote a faster formation of Cr_2O_3 layer in some cases, and thereby may be beneficial for crack initiation and propagation resistance [145].

The oxidation features (i.e. bulged GB Ni/Co oxides and Cr/Ti/Al oxide intrusion along grain boundary) observed in the LSHR alloy at the notch root surface have a certain similarity to those observed ahead of the crack tip (where a plastic zone exists) observed in RR 1000 [17], but they differ from the surface oxide layers observed in RR 1000 without strain (stress) [172, 173]. In the strain/stress-free RR1000, the oxides formed at the specimen surface consist of a protective Ti-doped Cr_2O_3 layer but with rutile forming on its outer surface and a subsurface Al/Ti oxide layer. Study of the isothermal oxidation of a similar disc alloy, i.e. ME3, also shows a TiO_2-Cr_2O_3 external oxide layer with branched Al_2O_3 internal subscale that extended into a recrystallized γ′ dissolution layer [84]. Generally, in the case where strain/stress is absent, oxidation usually begins with the formation of Ni oxide followed by chromia or Ni-Cr oxide spinel along with the internal Cr_2O_3 or Al_2O_3 scale, which obeys the expected thermodynamic sequence. The discrepancy of oxidation between grain-interior and grain boundaries is insignificant, as the fast formation of the protective Cr_2O_3 or Al_2O_3 scale prevents the inward diffusion of O and outward diffusion of oxide-forming elements such as Ni and Co, which then prevents the further occurrence of internal and external oxidation. However, for strain/stress-assisted oxidation, as shown in this study, the discrepancy of oxidation between grain interior and grain boundary is much more significant than that observed in those strain/stress-free isothermal/dynamic oxidation tests [84, 142, 169, 172, 173]. It is believed that these differences in oxidation are closely related to the accumulated strain or stress concentration around grain boundaries and γ/γ′ interfaces.

It is clear that the global applied strain has an influence on the oxidation process. However, it seems that the oxidation process is more closely related to the accumulated *local* strain in this study as the fatigue process itself is usually associated with strain localisation. In this study, apart from the significant discrepancy between grain-interior and GB oxidation, significant discrepancy of oxidation between different grain boundaries can be observed. As shown in Figs. 5.5 and 5.17, the bulged Ni/Co-rich oxides along with Ti/Cr/Al oxide

intrusion preferentially form at the boundaries between high and low SF grains that are inclined normal to the tensile stress axis. The preferential oxide formation at grain boundaries inclined normal to the tensile stress axis is attributed to the theory that tensile stress is beneficial in accommodating volume expansion during oxide formation/transformation [106]. Meanwhile, the accumulated local strain (or stress concentration) at grain boundaries or other interfaces can change both the thermodynamics and kinetics of the oxidation process to some extent, resulting in more significant oxidation.

Normally, the oxidation of an alloying element M from the superalloy can be presented:

$$\left(\frac{x}{y}\right)M + \frac{1}{2}O_2 \rightarrow \left(\frac{1}{y}\right)M_xO_y \tag{5.1}$$

The corresponding Gibbs free energy of formation of M_xO_y, ΔG_f, can be expressed by the following equation [17, 106, 107, 174]:

$$\Delta G_f = \Delta G_0 + RTln\left(\frac{a_{M_xO_y}^{1/y}}{a_M^{x/y}.P_{O_2}^{1/2}}\right) \tag{5.2}$$

where ΔG_0 is the standard free energy of formation of M_xO_y oxide and the reference status is 1 mole of oxygen. The standard free energies of formation of common oxides in Ni-based superalloy can be found in literature [17, 107]. T is the absolute temperature, and R is the gas constant. a_{MxOy} is the activity of oxide M_xO_y, which is commonly taken to be unity by ignoring the solid solution effect between the oxides. a_M is the activity of the element M in the Ni-based superalloy which is subject to oxidation, and a_M of each reacting solute is assumed to be equal to its atom fraction within the alloy. P_{O2} is oxygen partial pressure, which is 0.2 atm in 1 atm of air. The calculated ΔG_f for the oxides observed in the LSHR alloy are summarised in Table 5.2.

Table 5.2 Calculated Gibbs free energies of formation of oxides in LSHR alloy in air, kJ/mol

	NiO	CoO	Cr_2O_3	Al_2O_3	TiO_2
650 ^oC	-144.8	-150.3	-287.8	-428.4	-349.9
725 ^oC	-137.6	-143.5	-280.0	-417.2	

As shown in Table 5.2, those oxidation processes that are thermodynamically favoured as indicated by the negative value of the Gibbs free energies. However, it should be noted that the oxide nucleation may still need to overcome an additional energy barrier as the formation

of oxide nuclei will create a new interface and also increase the interface energy. In addition, due to the volume expansion during oxide formation, strain may be produced around the oxides, which also increases the energy of the system. On the other hand, the stored energy provided by the accumulated strain (strain energy) can provide an additional driving force to overcome the energy barrier to oxide nucleation. Therefore, the overall Gibbs free energy change ΔG for oxide nucleation can be written as:

$$\Delta G = V\Delta G_V + VG_S + A\gamma - \Delta G_\varepsilon \tag{5.3}$$

where V is the volume of oxide nuclei, ΔG_V is the free energy for the formation of per unit volume of oxide. G_S is the strain energy as a consequence of the volume change due to oxide nucleation. A is the surface area of the oxide nuclei, and γ is the interface energy due to oxide nucleation. ΔG_ε is the strain energy due to deformation brought about by cyclic loading.

In addition, ΔG_V can be expressed by ΔG_f using Equation 5.4

$$\Delta G_V = \frac{\Delta G_f}{m} y\rho \tag{5.4}$$

where m is the mole mass of oxide M_xO_y, and ρ is the density of oxide M_xO_y.

For internal oxidation, such as formation of Cr_2O_3, TiO_2 and Al_2O_3, due to the creation of a new oxide/alloy interface and the large volume change indicated by the large Pilling-Bedworth ratio (as shown in Table 2.4) [106], the influence of the strain energy caused by deformation may play an important role in oxide nucleation process. Hence, the more significant internal oxidation at grain boundaries can be understood in terms of the higher accumulated deformation strain around grain boundaries.

For external oxidation, such as formation of NiO and CoO, the new oxide/gas interface will replace the previous alloy/gas interface, but the surface energy variation for this interface change is quite limited. Moreover, the strain energy caused by volume expansion due to oxide formation is supposed to be insignificant as the constraint for external oxidation is insignificant compared with that for internal oxidation. Thus, the overall free energy change for external oxide nucleation can be simplified as

$$\Delta G = V\Delta G_V - \Delta G_\varepsilon \tag{5.6}$$

Therefore, it seems that the effect of stored strain energy brought about by any deformation

process on external oxidation is not likely to be as significant as it is for internal oxidation. However, the stored strain energy can still influence the external oxidation in an indirect way. Since the stored strain energy can provide additional energy to overcome the energy barrier to internal oxide nucleation, it enhances the propensity to the accelerated internal oxidation of Cr, Ti and Al, which produces an abundance of Ni and Co at subsurface region, especially at subsurface grain boundaries where significant internal oxidation occurs. The abundant Ni and Co will diffuse outward to the surface to form external Ni and Co oxides, and diffuse inward and segregate at internal oxide (i.e. Al_2O_3)/alloy interface (Fig. 5.14). In addition, formation of internal oxides is also related to the diffusion of Cr, Al and Ti, which is closely associated with the defects at these regions.

Diffusion of internal oxide-forming elements (i.e. Cr, Ti and Al) and external oxide-forming elements (i.e. Ni and Co) determines the kinetics of oxidation. As discussed previously, oxidation in the LSHR alloy is thermodynamically favourable, thus, the kinetics, i.e. diffusion of oxide-forming elements, is the rate-determining step for the oxidation process. It is well recognised that grain boundaries and dislocations are short-circuit diffusion paths for oxide-forming elements. Hence, the pile-up of dislocations developed during a deformation process is supposed to accelerate the diffusion process. Meanwhile, the formed internal oxides also produce marked boundaries acting as short-circuit paths due to the very fine grain size of the oxides as shown in Fig. 5.12. In addition, diffusion of oxide-forming elements also occurs through the alloy matrix and oxide grains, but these diffusion processes are insignificant compared with the short-circuit diffusion. As a result, diffusion along the grain boundaries of oxide and the alloy matrix as well as dislocations makes the dominant contribution to both internal and external oxidation.

Based on the above analysis, the influence of strain/stress on the diffusion process can be simplified as the influence of strain/stress on grain boundary diffusivity D_g of the corresponding elements, which can be expressed as a function of the inelastic strain energy density $f(W_p)$ of the particular grain boundary, and can be written as an Arrhenius relationship form as suggested by Ghonem [175]

$$D_g = Dexp\left(-\frac{Q'_g}{RT}\right) = Dexp[-\frac{Q_{g-f(W_p)}}{RT}] \tag{5.7}$$

where Q_g is the activation energy of grain boundary diffusion in the strain/stress-free state, Q'_g is the effective activation energy of grain boundary diffusion for strained/stressed

material. D is diffusion constant. Apparently, the increase in strain energy density yields higher grain boundary diffusivity, and thereby results in accelerated oxidation.

Although the aforementioned discussion only provides a qualitative assessment of the influence of strain/stress on oxidation, it enables an insight into the mechanism of oxidation in the LSHR alloy under strain/stress during short fatigue tests and oxidation-assisted crack initiation and propagation. At the beginning/early stages of fatigue loading at elevated temperatures, surface oxidation occurs to form a thin Ni/Co oxide layer due to the abundance of Ni and Co in alloy matrix and the higher formation rate of Ni/Co oxides indicated by the higher parabolic rate constants (Fig. 2.18). Meanwhile, the strain is accumulating at boundaries between high and low SF grains. Due to the formation of surface Ni/Co oxide layer, the internal oxidation (i.e. selective oxidation of Cr, Ti and Al) starts to occur as a consequence of the reduced oxygen partial pressure at the interface of surface oxide layer/alloy matrix and the enrichment of Cr, Ti and Al underneath the surface oxidation layer. Since there is strain accumulation at grain boundaries, this accelerates the internal oxidation process at these grain boundaries, producing an abundance of Ni and Co by consuming Cr, Ti and Al (which is accompanied by dissolution of γ′ precipitates). The abundant Ni and Co then migrate outward to form Ni/Co oxides by short-circuit diffusion along grain boundaries of oxides and alloy matrix as well as dislocations formed during deformation process, resulting in apparent bulged height at surface grain boundaries. From this point of view, the bulged height of the Ni/Co oxides can be taken as an indicator of the degree of internal oxidation and is associated with the Cr/Ti/Al oxide intrusion depth along grain boundaries. In addition, the abundant Ni and Co also diffuse inwards to the internal oxide/alloy matrix interface where the dissolution of γ′ precipitates is occurring and segregate there. The dissolution of γ′ precipitates ahead of the internal oxide/alloy matrix interface also causes enrichment of Ni and Co at this region. With the loading proceeding, the formed bugled Ni/Co oxides and the Cr/Ti/Al oxide intrusion along the grain boundary start to crack, leading to crack initiation and propagation. When the crack propagates through the formed internal oxide intrusion, the oxygen can quickly access the crack tip which was the internal oxide intrusion tip (i.e. the internal oxide/alloy matrix interface) where it enriches in Ni and Co. At this point, the enrichment of Ni and Co at the crack tip can result in rapid oxidation and form a quasi-surface oxidation layer. Consequently a new cycle of oxidation-oxide cracking-crack initiation and propagation starts.

5.4.4 Effect of oxidation on fatigue life

Due to oxidation enhanced crack initiation and propagation, the fatigue life of the LSHR alloy is significantly reduced by oxidation effects as shown in Table 5.1. Although the FG LSHR is expected to show more severe GB oxidation at elevated temperatures, a longer fatigue life is observed at most testing conditions except the tests at 725 ^{o}C. This is probably ascribed to its higher yield strength over CG LSHR [19], resulting in less plastic strain under these testing conditions and associated damage in each fatigue cycle which acts to counterbalance the increased GB oxidation effect [5, 137]. Similar effects of oxidation on fatigue life have also been observed in other disc alloys such as ME3 [84]. The effect of oxidation was deliberately studied by pre-exposing the LCF specimens at high temperatures for different periods and then conducting LCF tests on these pre-exposed specimens. This work showed that the reduction in fatigue life is determined by the net oxidation effect, i.e. depth of oxide layer and the oxidation affected zone (which is used by these authors to refer the GB carbide dissolution region), rather than simply by temperature or exposure time. By removing the oxide layer and oxidation affected zone in the pre-exposed ME3, the fatigue life was significantly improved and was close to the fatigue life of un-exposed specimens, due to the suppression of intergranular crack initiation and the reduction in crack initiation sites [84].

It is therefore important to improve the intrinsic oxidation resistance of the LSHR alloy and other turbine disc alloys. A trade-off between grain size and precipitate size may need to be made to optimise the combined fatigue-oxidation-creep resistance at elevated temperatures. In addition, it is well known that small angle grain boundaries or special CSL grain boundaries possess higher crystal coherence and lower grain boundary energy than that of random high angle grain boundaries, which makes them more oxidation/corrosion resistant [30]. With an attempt to enhance the oxidation/corrosion resistance of a disc alloy, “grain boundary engineering” may be employed that is supposed to increase the volume fraction of special CSL grain boundaries and/or small angle grain boundaries by thermomechanical processing (as employed in industry) [29, 32, 176]. Moreover, addition of B and Zr is expected to improve the cohesion strength of grain boundaries and should enable an improved oxidation resistance [3, 56].

5.5 Summary

Fatigue crack initiation and early short crack propagation behaviour of the LSHR alloy at elevated temperatures were assessed by three-point bend loading with a replication procedure in combination with OM, SEM and EBSD observation. An attempt has been made to reveal the influences of oxidation on fatigue crack initiation and propagation using FIB-TEM-EDX analysis. Based on the aforementioned results and discussion, the following conclusions can be made:

- Fatigue lives of the LSHR alloy are shortened by high temperature and high oxygen partial pressure, which are associated with more intergranular fracture mechanisms. The FG LSHR possesses a longer fatigue life in most testing conditions although it is expected to be more severely GB oxidized, this is attributed to different strain levels expected in the notch root.
- Plentiful crack initiation mainly occurs at GBs with bulged Ni/Co-rich oxides at elevated temperatures in the LSHR alloy due to oxide cracking. Cracks subsequently propagate along oxidised GBs at surface and exhibit significant crack coalescences at the final stages of fatigue life. In the depth direction, cracks predominantly propagate along grain boundaries in the FG LSHR at the investigated temperatures and in the CG LSHR at 725 ^{o}C, whereas predominantly transgranular propagation after intergranular crack initiation appears in the CG LSHR at 650 ^{o}C either in vacuum or in air.
- The oxides corresponding to crack initiation and propagation consist of bulged surface Ni/Co oxides and Cr/Ti/Al oxide intrusion along grain boundaries and γ/γ' interfaces. The Cr/Ti/Al oxide intrusion enriches in Cr close to surface oxide scale, enriches in Ti in the middle and enriches in Al at the oxide front where is far away from the surface oxide scale. An enrichment of Ni and Co and a depletion of Al and Ti exist ahead of the oxide front due to the Cr/Ti/Al oxide intrusion formation. In addition, Co and Cr are enriched at oxide intrusion/alloy matrix interface.
- Uniform surface oxide scales along with internal oxide particles are observed away from the grain boundaries. The bulged GB Ni/Co oxides and the Cr/Ti/Al oxide intrusion along GB has a width of ~0.5 μm, and can penetrate into the grain boundary by a depth <1 μm to tens of a μm. Formation of bulged Ni/Co and Cr/Ti/Al intrusion are accompanied by dissolution of γ' precipitates.

- Formation of bulged GB Ni/Co-rich oxides and Cr/Ti/Al oxide intrusion is closely related to the strain localisation which is associated with grain orientation and applied stress. The boundaries between high and low SF grains are preferential sites for the formation of bulged Ni/Co-rich oxides and Cr/Ti/Al oxide intrusions. Strain-assisted formation of internal GB Cr/Ti/Al oxide intrusion can facilitate formation of GB bulged Ni/Co-rich oxides by providing abundant Ni and Co.

Chapter 6 Long fatigue crack propagation behaviour at elevated temperatures

6.1 Introduction

Fatigue crack growth rate is an important indicator of propagation behaviour of both short and long cracks, and it is also an important factor when assessing fatigue performance of materials/components, especially in such cases where a damage-tolerant approach is applied in the design of components. The crack growth rate is usually dependant on microstructures of materials/components, loading conditions and service environments. It is well known that short crack growth rate is characterized by its abnormal fast propagation behaviour below the ΔK_{th} and highly fluctuating features due to the significant interaction between local (varied) microstructural features and cracks. However, as shown in Chapter 5, it is difficult to quantitatively assess short crack growth behaviour in the LSHR alloy at elevated temperatures via replica procedures because of the severe grain boundary oxidation (which is associated with a great number of grain boundary cracks) and the frequent crack coalescence events. To enable better understanding the crack propagation behaviour in the LSHR alloy, conventional long crack growth tests have also been conducted on CG and FG LSHR alloy variants at elevated temperatures in air and vacuum under 1-1-1-1 and 1-20-1-1 loading waveforms, to reveal the influence of microstructure on long crack propagation and to elucidate the interaction between damage processes arising from fatigue, oxidation and creep during crack propagation. The long fatigue crack growth data of LSHR alloy obtained by previous PhD and MSc students has also been recapitulated in this chapter. A comparison of fatigue crack growth behaviour between LSHR alloy and N18 has been made. Some aspects of the work detailed in this chapter have been published in the following papers:

S. Everitt, R. Jiang, N. Gao, M. J. Starink, J. W. Brooks and P. A. S. Reed, Materials Science and Technology 29 (2013): 781-787.

R. Jiang, S. Everitt, M. Lewandowski, N. Gao and P. A. S. Reed, International Journal of Fatigue 62 (2014): 217-227.

6.2 Experimental procedures

6.2.1 Crack grow-out test under constant load

In order to investigate the influence of environment, temperature and dwell time on the fatigue crack growth behaviour, a test matrix was designed, which is listed in Table 6.1. The CG and FG LSHR alloys were tested at three temperatures, i.e. 650 ^{o}C, 704 ^{o}C and 725 ^{o}C, in two environments, i.e. air and vacuum with a 1-1-1-1 or a 1-20-1-1 trapezoidal loading waveform. The fatigue tests were performed by three-point bending method on an Instron 8501 servo-hydraulic testing machine with an ESH Ltd. high temperature vacuum chamber attached. Set-up of the fatigue tests, heating of the specimens and the temperature control were the same as detailed for the short crack tests at elevated temperatures described in Section 5.2.1. A schematic diagram of the experimental set-up of the fatigue test along with the specimen dimensions is shown in Fig. 6.1. A notch with a depth of 2.5 mm was machined by electrostatic discharge machining in the middle of specimen, which acted as a stress concentrator to initiate the crack during the fatigue test. Crack length was monitored by direct current potential drop (DCPD) method with pulsed 4 probes, and a calibration check was made by post-test crack length measurement (Details of the calibration for crack length and the ΔK levels can be found in the literature [177]). The fatigue crack growth rates da/dN were derived from the curve of the variation in the electrical potential with time by secant method after a post-test calibration for crack length had been carried out.

Table 6.1 Long fatigue crack test matrix for LSHR alloy

	Test type	Temperature and Environment					
		Air			Vacuum		
		650 ^{o}C	704 ^{o}C	725 ^{o}C	650 ^{o}C	704 ^{o}C	725 ^{o}C
CG LSHR	da/dN 1-1-1-1	√	√√	√	√		√
	da/dN 1-20-1-1	√		√	√		√
FG LSHR	da/dN 1-1-1-1	√	√√	√	√	√	√
	da/dN 1-20-1-1			√			

Note: the "√" stands for the tests have been done in the University of Southampton, and the "√√" stands for the tests reported in NASA's paper on the same material [19]

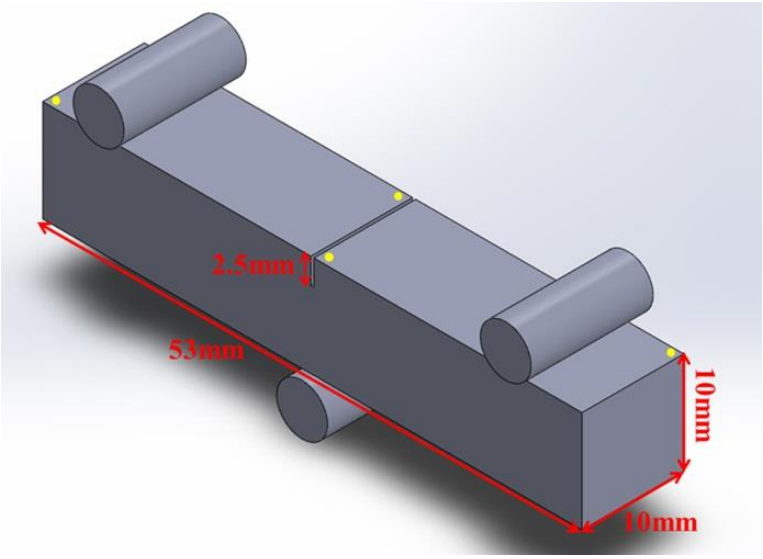

Fig. 6.1 Schematic diagram of experimental set-up of the fatigue tests. The 4 yellow circles indicate the position of pd wires.

For tests carried out in air, pre-cracking was carried out using a load shedding method with a sine waveform, stress ratio of 0.1, a frequency of 20 Hz and an initial ΔK of 20 MPa√m. The ΔK was stepped down in 10% increments after the crack had grown through four plastic zone sizes until ΔK ≈15 MPa√m was achieved, which ensured that crack growth out would occur from a microscopically sharp crack away from any residual effects induced in the machining of the notch, and then the specimen was heated by four high intensity quartz lamps. When the required temperature (650 ^{o}C, 704 ^{o}C or 725 ^{o}C) was attained, the cyclic loading was changed to the appropriate trapezoidal loading waveform 1-1-1-1 or 1-20-1-1 and the cracks were allowed to propagate to failure under constant load amplitude (increasing ΔK conditions).

The procedures for the vacuum tests were almost the same as that of the air tests except that the evacuation process was applied after pre-cracking. At the end of the pre-cracking stage the ESH Ltd. chamber was evacuated until a pressure equal to or less than 5×10^{-4} mbar was achieved. Heating was then applied to raise the specimen to the required testing temperature, which was accompanied by out-gassing of the chamber and an increase in pressure. Crack growth out using the required trapezoidal loading waveform 1-1-1-1 or 1-20-1-1 was only commenced once the vacuum had recovered to 5×10^{-4} mbar. The crack was then allowed to propagate to failure under constant load amplitude. For tests of CG LSHR specimens in vacuum, crack grew considerably slowly at ~15 MPa√m, and hence a higher

initial ΔK (18 - 20 MPa√m) was used to obtain crack growth.

6.2.2 Constant ΔK test

In order to investigate the influence of frequency on the crack propagation behaviour, a crack growth test was conducted under a range of frequencies, i.e. 0.011 - 20 Hz, using trapezoidal waveforms and sine waveforms at a constant ΔK of 25 MPa√m with a load ratio of 0.1. Specifically, the applied loading waveforms are as follows, trapezoidal 1-90-1-1, 1-20-1-1, 1-1-1-1, 0.25-0.25-0.25-0.25 and sine waveforms with a frequency of 2, 4, 8, 20 Hz. The specimen set-up, pre-cracking procedure and measurement of crack length are the same as described in the long fatigue crack growth tests under constant load in Section 6.2.1. The constant ΔK was realized by the loading shedding method as the crack grows. The reason for choosing a ΔK of 25 MPa√m is that this value is well within the mid-power law region of the da/dN versus ΔK plot [154]. After pre-cracking, the specimen was heated to 650 ^{o}C and held at this temperature for 5 minutes to homogenize the temperature across the specimen. The sequence of applied loading waveforms was 1-1-1-1, sine 20 Hz, 1-20-1-1, sine 4 Hz, 1-90-1-1, sine 2 Hz, 0.25-0.25-0.25-0.25, sine 8 Hz. This arrangement of loading waveform sequence was to produce beach-marking on the fracture surface via the change in crack propagation mode caused by the step change of testing frequency and waveform. At each applied frequency, the crack was allowed to grow an increment of 0.4 - 0.6 mm, and finally grew out at a frequency of 8 Hz under constant load with a sine waveform after growth for the appropriate increment at the constant ΔK. The crack length was recorded as a function of time by the DCPD method, and then the crack growth rate can be derived from the crack length versus time curve. In order to avoid any artefact of transient fluctuation in crack growth rate when changing the loading waveform, obvious transition regions (i.e. nonlinear region) in the crack length vs. time curve were excluded in the crack growth rate derivation.

6.2.3 Fractography

After fatigue tests, both a Wild M420 macroscope and JEOL JSM 6500F FEG-SEM were employed to investigate the fractography of fractured surface. The wild M420 macroscope was used to obtain a photograph of the overall fracture surface. The microstructural features on the fractured surface at different ΔK levels were observed by FEG-SEM at an accelerating voltage of 15 kV.

6.2.4 Sectioning fracture surfaces

The fractured specimens were metallographically sectioned in a direction perpendicular to the fracture surface to examine the microstructure of the material in the vicinity of the crack surface and to investigate the interaction between secondary cracks and precipitates/grain boundaries. To maintain the integrity of the fracture surface and provide edge retention during sectioning, specimens were plated with Ni using Watt's solution (500ml H_2O, 150g $NiSO_4 \cdot 6H_2O$, 20g $NiCl_2 \cdot 6H_2O$, 20g H_3BO_3) at a temperature range of 40 - 60 ºC, using a 99.9% pure Ni anode, and a current density of 40 mA/cm^2 for 90 minutes. The experimental apparatus is shown in Fig. 6.2 [2]. The metallographically sectioned specimens were mounted in Bakelite resin and ground, polished and etched with the same procedure as described in Section 3.3.1 before being observed under the OM and the FEG-SEM.

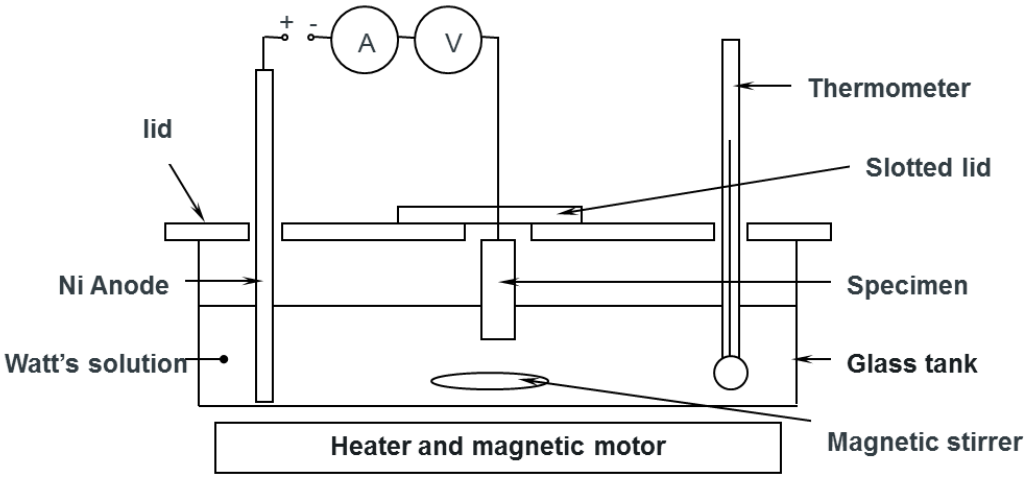

Fig. 6.2 Schematic diagram of the Ni-plating apparatus [2].

6.2.5 Measurement of roughness of fracture surfaces

In order to measure the roughness of the fracture surfaces, three images of the fractured surface at a given ΔK were taken by tilting the specimen stage along Y axis to ±5 degrees in the JEOL JSM 6500 FEG-SEM, and then the 3-D fracture surface was reconstructed from the tilted SEM images automatically by Alicona MEX software, from which the roughness of fracture surface can be measured. For CG LSHR fractured specimens, the tilted images were taken under a magnification of 100 times, whereas a magnification of 750 times was used for FG fractured specimens to obtain a sufficient area of fracture surface for roughness measurement as well as high-quality images in which individual grain dimensions can be

distinguished.

The roughness of the fractured surface is characterized by the average roughness (R_a) in this study. The definition of R_a is given in Equation 6.1, and demonstrated in Fig. 6.3 [178]. R_a is calculated as the area between the roughness profile and its mean line divided by the evaluation length, L. The R_a was measured under profile analysis mode in the MEX software with primary filtering which can reflect the fluctuation of fracture surface accurately. In each image, four sets of parallel lines were drawn individually, and the arrangement of each set of parallel lines was intercepted by 45 degrees as shown schematically in Fig. 6.4. The value of R_a was taken as the average of the measurements of the four sets of parallel lines.

$$R_a = \frac{1}{L}\int_0^L |r(x)|dx \tag{6.1}$$

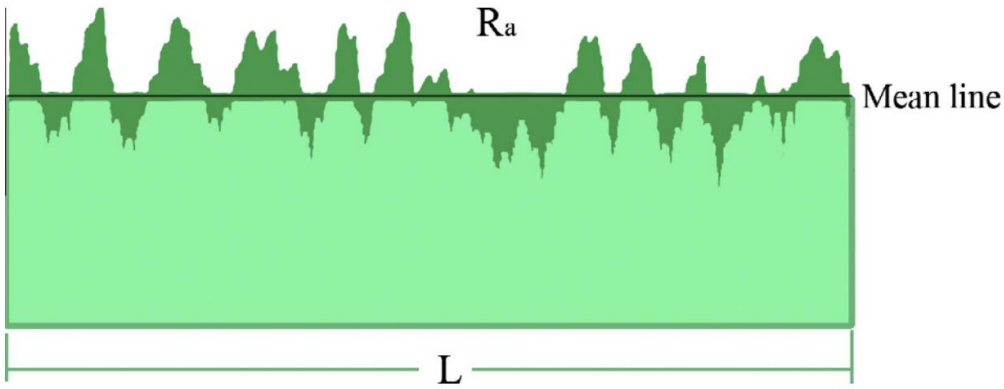

Fig. 6.3 Graphical representation of surface roughness Ra [178].

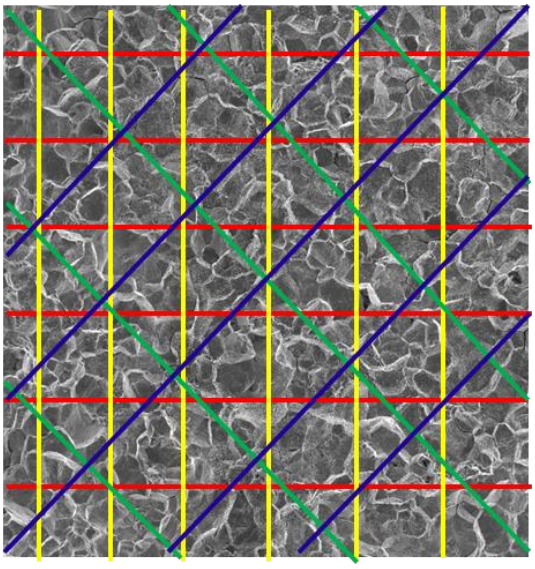

Fig. 6.4 Schematic diagram of the parallel lines used for roughness measurement.

6.2.6 Statistics of secondary cracks

The length and amount of secondary cracks on the fracture surface of the CG LSHR alloy specimens tested in air were measured by Image J. software to investigate the correlation between the number/quantity of secondary cracks, stress intensity level and roughness of fracture surface as well as the degree of grain boundary oxidation. The amount of secondary cracking was expressed as length per unit area. The images used for measurements of secondary cracks were similar to those for the roughness measurement, i.e., a magnification of 100 times for CG LSHR alloy. The images were enlarged in the image analysis software to some extent to allow small secondary cracks to be discerned more easily. For each specimen, two images at a given stress intensity level were analysed. Due to the comparatively low magnification used for measurement of secondary cracks, some short cracks may have been neglected to enable maximizing the observation area in one field of view. In those transgranular fracture specimens, it is difficult to obtain an accurate measurement of secondary cracks because these secondary cracks are quite short and hard to distinguish under the given magnification. For each secondary crack observed on the fracture surface, a line was drawn along the crack by using a drawing tool in the image analysis package, and then the length of these secondary cracks could be measured. In terms of cracks at triple grain boundaries or crack branches, they were simply taken as two individual cracks. This simplification would influence the calculated average length of secondary cracks somewhat, but would not influence the amount estimate of secondary cracks.

6.3 Results

6.3.1 Fatigue crack growth rate

As shown in Fig. 6.5, the effects of environment and dwell time on the FCG rate in the CG LSHR superalloy at 650 ^{o}C and 725 ^{o}C are illustrated respectively. It is found that the FCG rate varies by one or two orders of magnitude at a given ΔK level depending on the investigated conditions. The influence of environment on FCG rate is very evident, either at 650 ^{o}C or 725 ^{o}C. Fatigue cracks propagate at a higher rate in air at the investigated temperatures, especially when a dwell time of 20s at the peak load is introduced in the tests. The dwell is detrimental to the fatigue resistance of LSHR alloy when the tests are carried out in air, whereas it has little influence on the FCG rate in the vacuum tests, either at 650 ^{o}C or 725 ^{o}C, indeed a slightly beneficial effect can be discerned at 725 ^{o}C, which indicates that the

creep process is not activated or has little contribution to FCG rate.

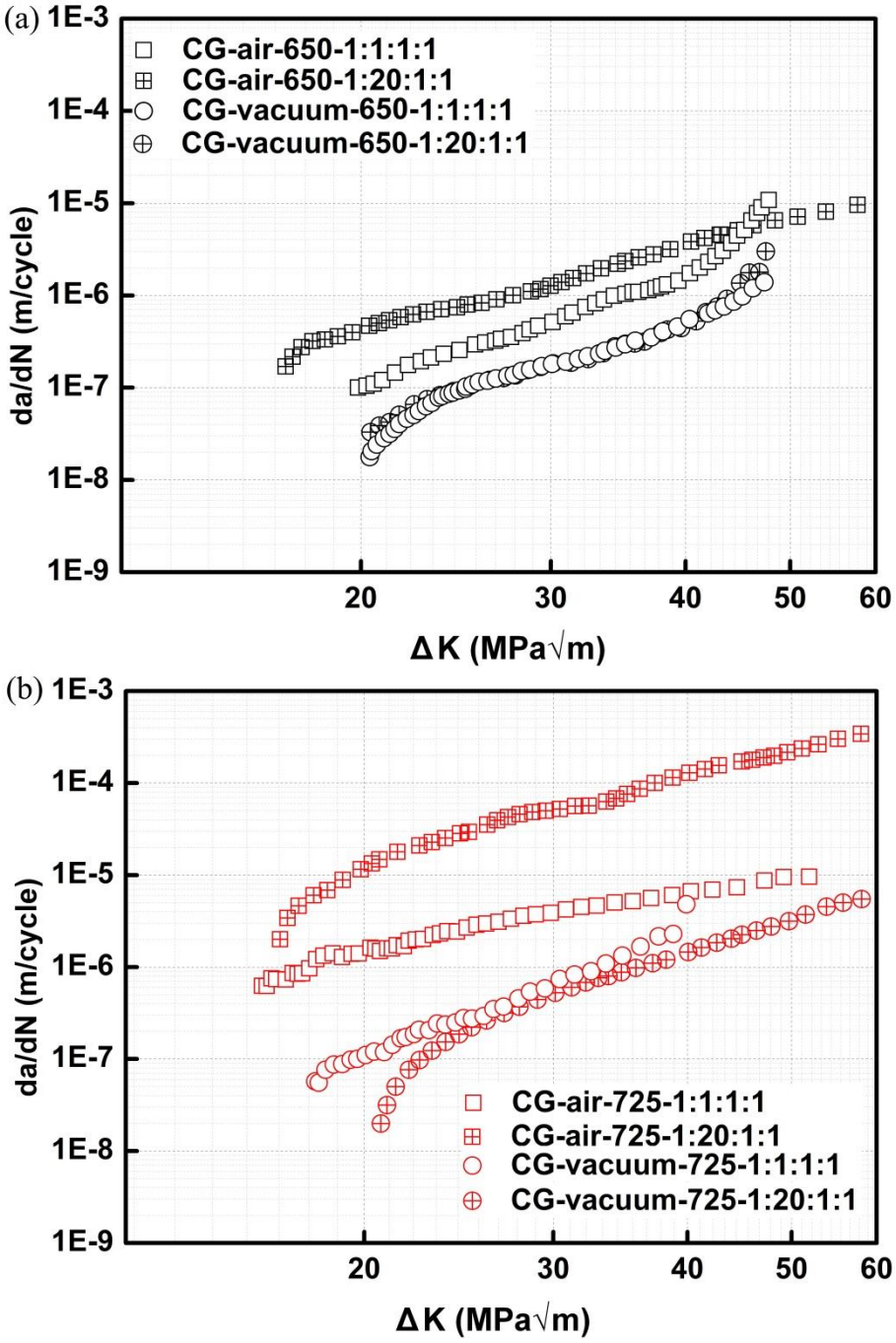

Fig. 6.5 Effects of environment and dwell time on fatigue crack growth rate of CG LSHR alloy tested at (a) 650 ^{o}C and (b) 725 ^{o}C.

By plotting Figs. 6.5 (a) and (b) in the same graph, it is expected to find out the effect of temperature on the FCG rate in the CG LSHR alloy and compare the significance of the influences of environment and dwell time on FCG rate at different temperatures. As shown in Fig. 6.6, the higher temperature significantly enhances crack propagation either in air or

vacuum, with an extremely significant influence when the tests were carried out in the air with a 20s dwell at the peak load, which indicates the oxidation makes a great contribution to the FCG rate for those air tests because of the higher diffusivity of oxygen and longer diffusion time possible at the crack tip. The influence of temperature on FCG rate is much less significant in vacuum although the faster fatigue crack propagation at higher temperature in the vacuum tests is observed. Additionally, it is found that the influences of environment and dwell time on FCG rate are much more marked at higher temperature.

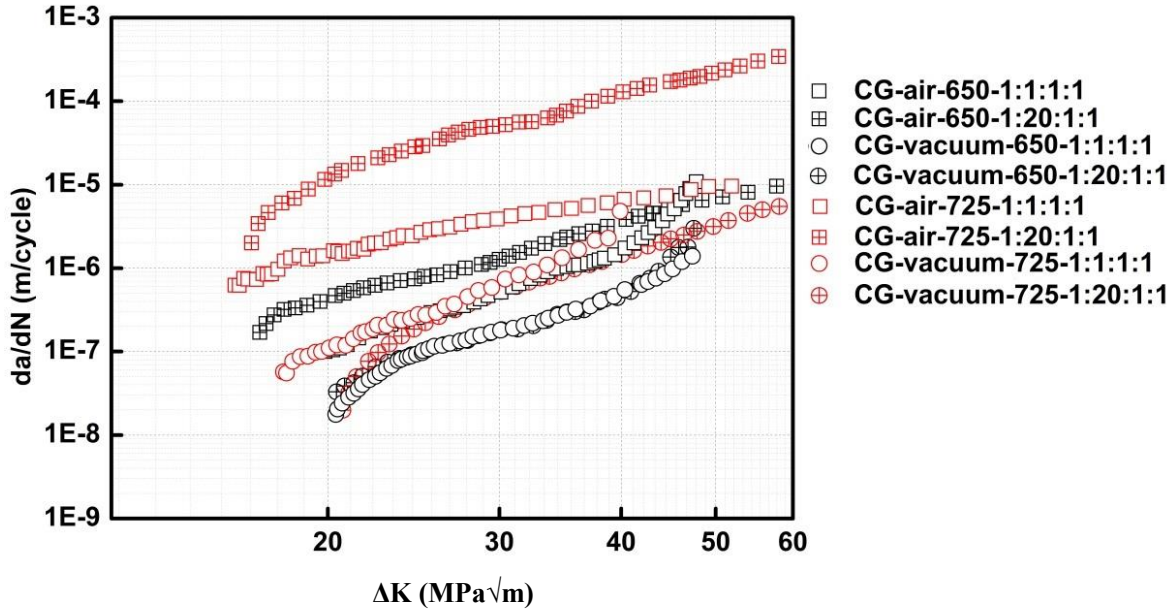

Fig. 6.6 Fatigue crack growth rate of the CG LSHR alloy.

The FCG rate of FG LSHR alloy is presented in Fig. 6.7. Similar to the CG results, FCG rate is significantly higher in air than that in vacuum, and the high temperature and long dwell stimulate the fatigue crack propagation further. The fastest FCG rate occurs in the air test at 725 ^{o}C with a dwell time of 20s at the peak load. Compared with air tests, FCG rate is much slower in the vacuum tests, and the influence of temperature on the FCG rate seems to be more complicated than that in the air tests. As the testing temperature increases from 650 to 704 ^{o}C, the FCG rate decreases approximately by a factor of 5. With further increases in the testing temperature to 725 ^{o}C, the FCG rate is accelerated, and close to that at 650 ^{o}C.

As shown in Fig. 6.8, the influences of microstructure on the FCG rate of the LSHR alloy are illustrated. Compared with the FCG rate in FG LSHR tested at 650 ^{o}C with 1s dwell, the FCG rate in CG LSHR tested under identical conditions is about one order of magnitude lower either in air or vacuum, which means coarse grains are beneficial in improving the

fatigue crack growth resistance of the LSHR alloy. The overlap of da/dN vs. ΔK curves of the FG vacuum test and CG air test in Fig. 6.8 (a) indicates the beneficial effect of vacuum (or absence of oxidation) on FCG rate is similar to that of increasing the grain size under the investigated conditions. As shown in Fig. 6.8 (b), the influence of the microstructure on the FCG rate is significant as well for air tests at 725°C.

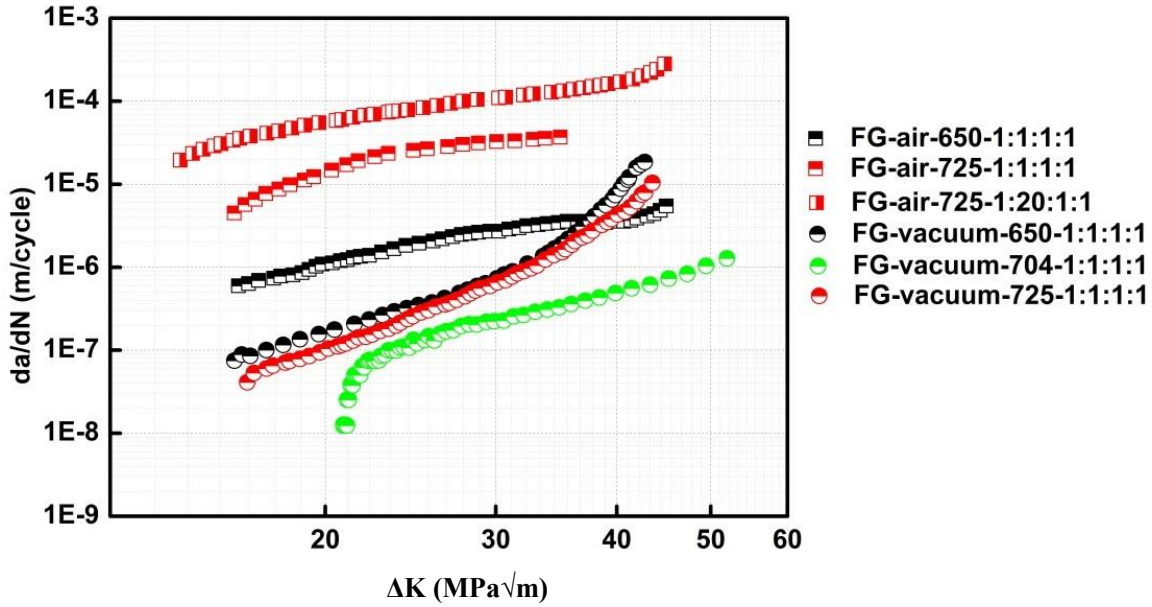

Fig. 6.7 Fatigue crack growth rate of the FG LSHR superalloy.

6.3.2 Fractography and morphology of sectioned fracture surface

Optical overviews of the fracture surfaces of the LSHR specimens tested under the investigated conditions are presented in Figs. 6.9 - 6.11. As indicated in the overall fractography, the edge of the EDM slot, pre-cracking region, fatigue crack grow-out region and final fracture region can be seen clearly. Additionally, it is found from the fracture surfaces that not all cracks are symmetrical to varying degrees, especially for tests carried out in air at 725 °C (shown in Fig. 6.10), indicating that the crack propagation has not been uniform across the breadth of the test specimens. The different stress intensity factor range levels are also marked on the overall fractography.

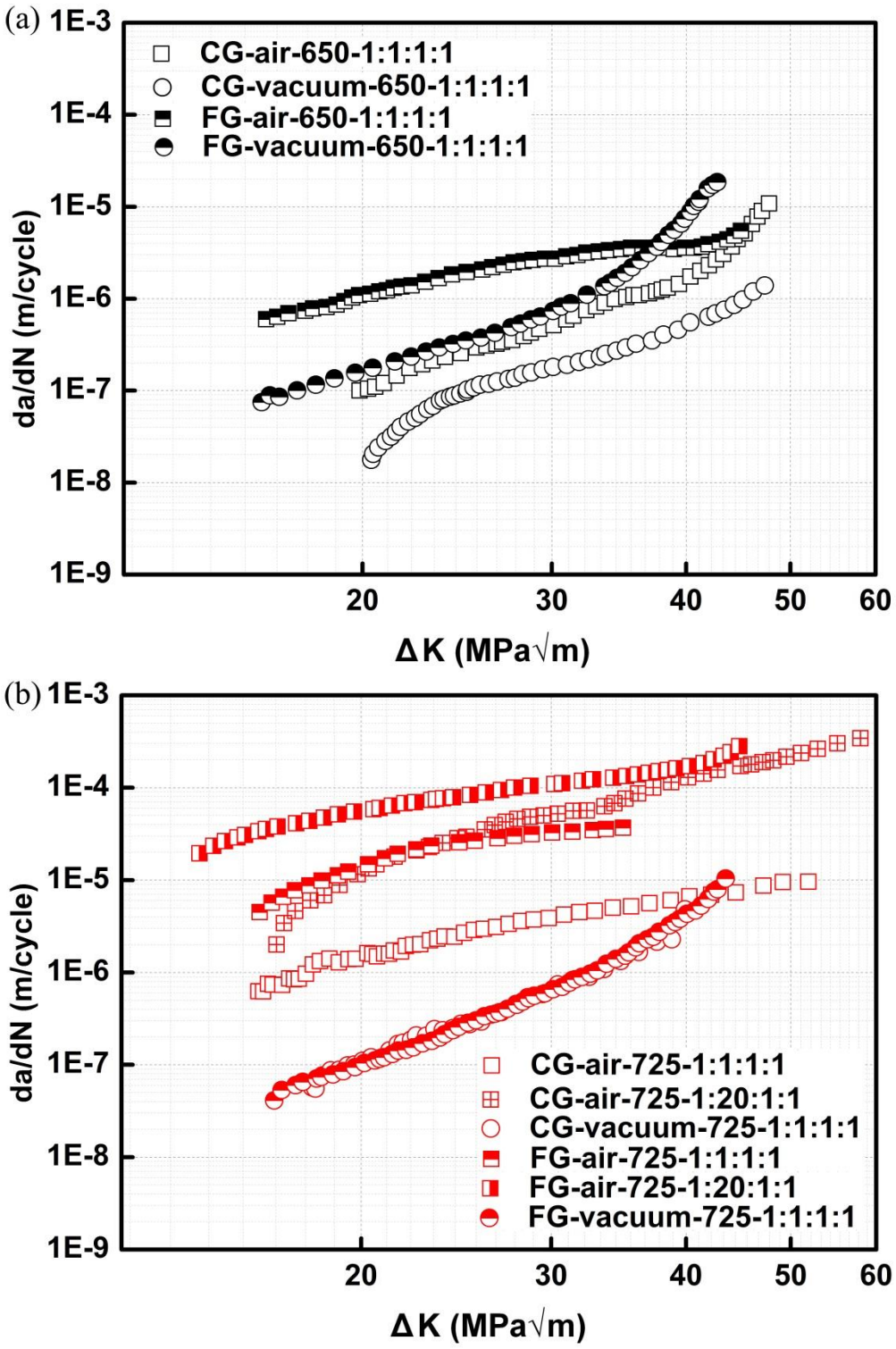

Fig. 6.8 Influences of microstructure on the fatigue crack growth rate of the LSHR alloy at (a) 650 ^{o}C and (b) 725 ^{o}C.

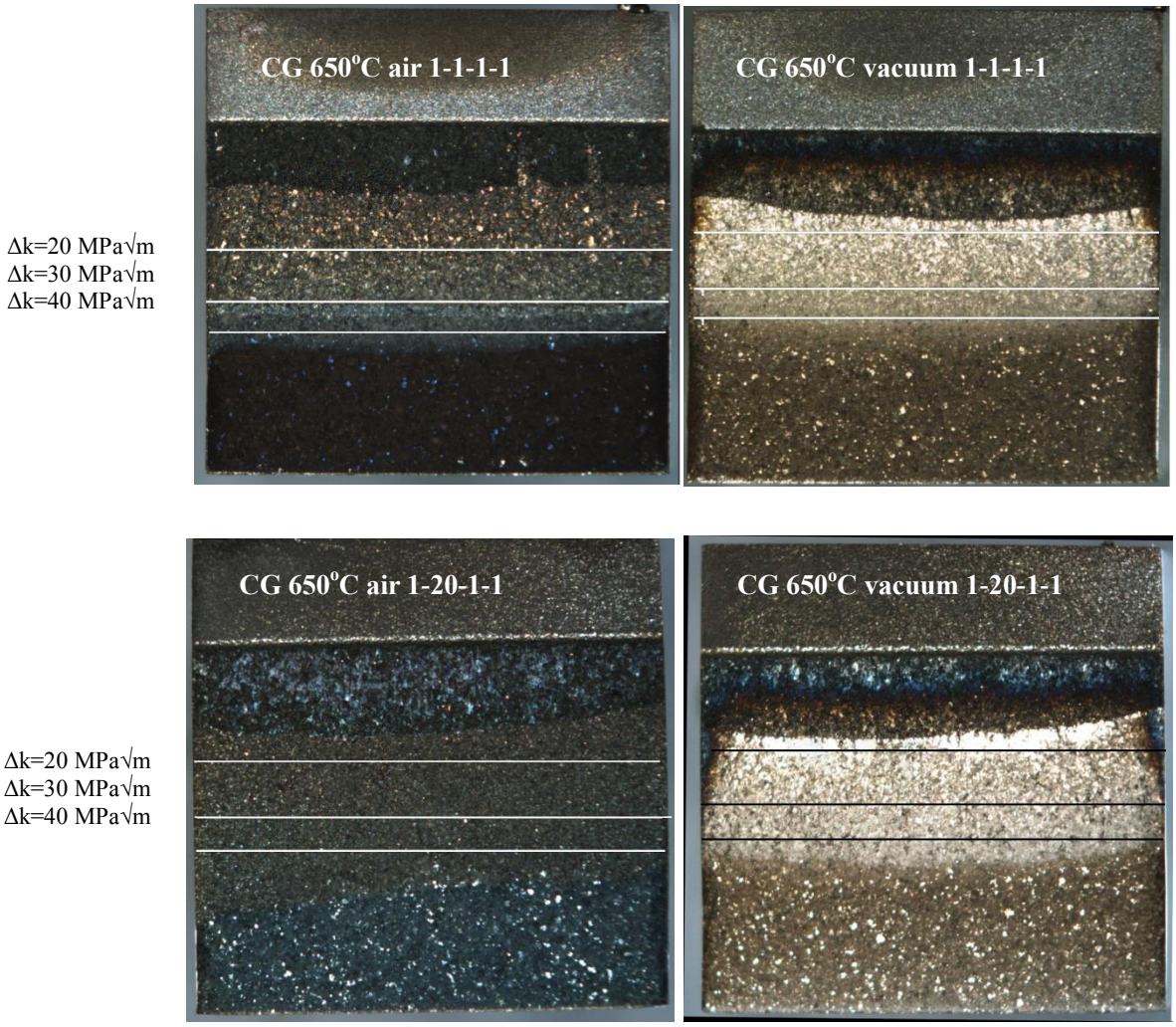

Fig. 6.9 Optical overview of fracture surface of the CG LSHR alloy tested at 650 °C.

The detailed features on the fracture surfaces were examined by SEM, and the results are presented in Figs. 6.12 - 6.19. As shown in Figs. 6.12 and 6.13, intergranular fatigue fracture is the dominant fracture mode for CG LSHR air tests, especially when the ΔK is at a low level. With increasing ΔK, the proportion of transgranular features on the fracture surface is increased, and this phenomenon is most marked for test carried out at 650 °C with a 1s dwell (Figs. 6. 12 (a) and (b)). In such a test, the fracture surface is almost transgranular when ΔK reaches to 40 MPa√m, and the crystallographic facets and steps can be discerned. For other air tests of the CG LSHR alloy, crystallographic facets and steps can be found at high ΔK levels as well (as shown in Fig. 6. 12 (d)). Another evident characteristic of the micro-fractography is the long and tortuous secondary cracks at high ΔK level. Due to this development of secondary cracks, a cluster of grains are decohered from the surface and leave a pit on the fracture surface (in Figs. 6. 12 (d) and 6. 13 (b) and (d)), which makes the fracture surface extremely rough. The quantitative measurement of roughness of fracture

surface and secondary cracks will be illustrated in the following sections. With increasing testing temperature or introduction of a dwell time of 20 seconds at maximum load, the intergranular fracture feature becomes more prominent, although the effect of dwell time at 650 ^{o}C is not as apparent as that at 725 ^{o}C. Similar to the effects of increasing ΔK on secondary crack evolution, the increase in temperature or introduction of long dwell can also promote formation and development of secondary cracks.

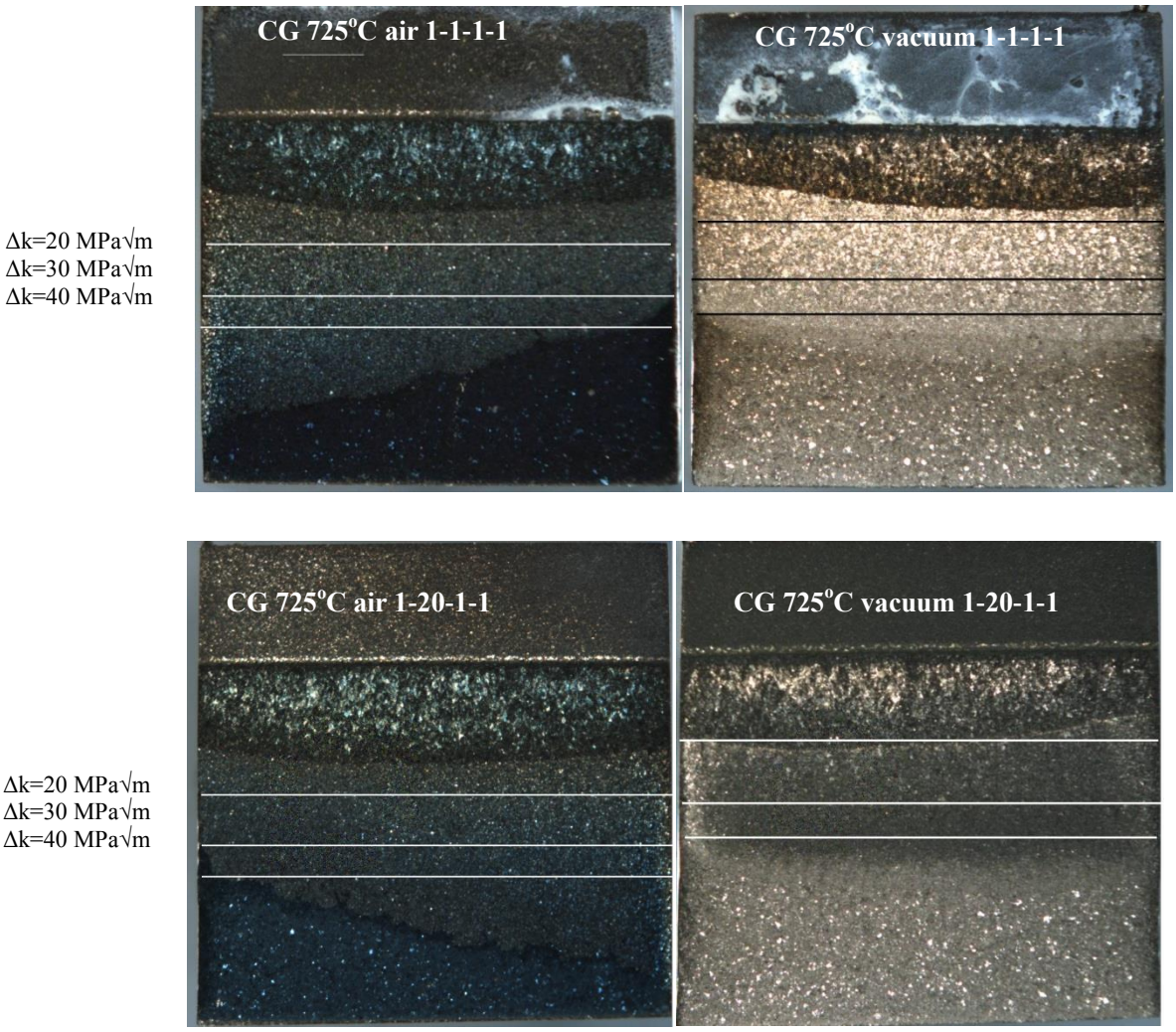

Fig. 6.10 Optical overview of fracture surface of the CG LSHR alloy tested at 725 ^{o}C.

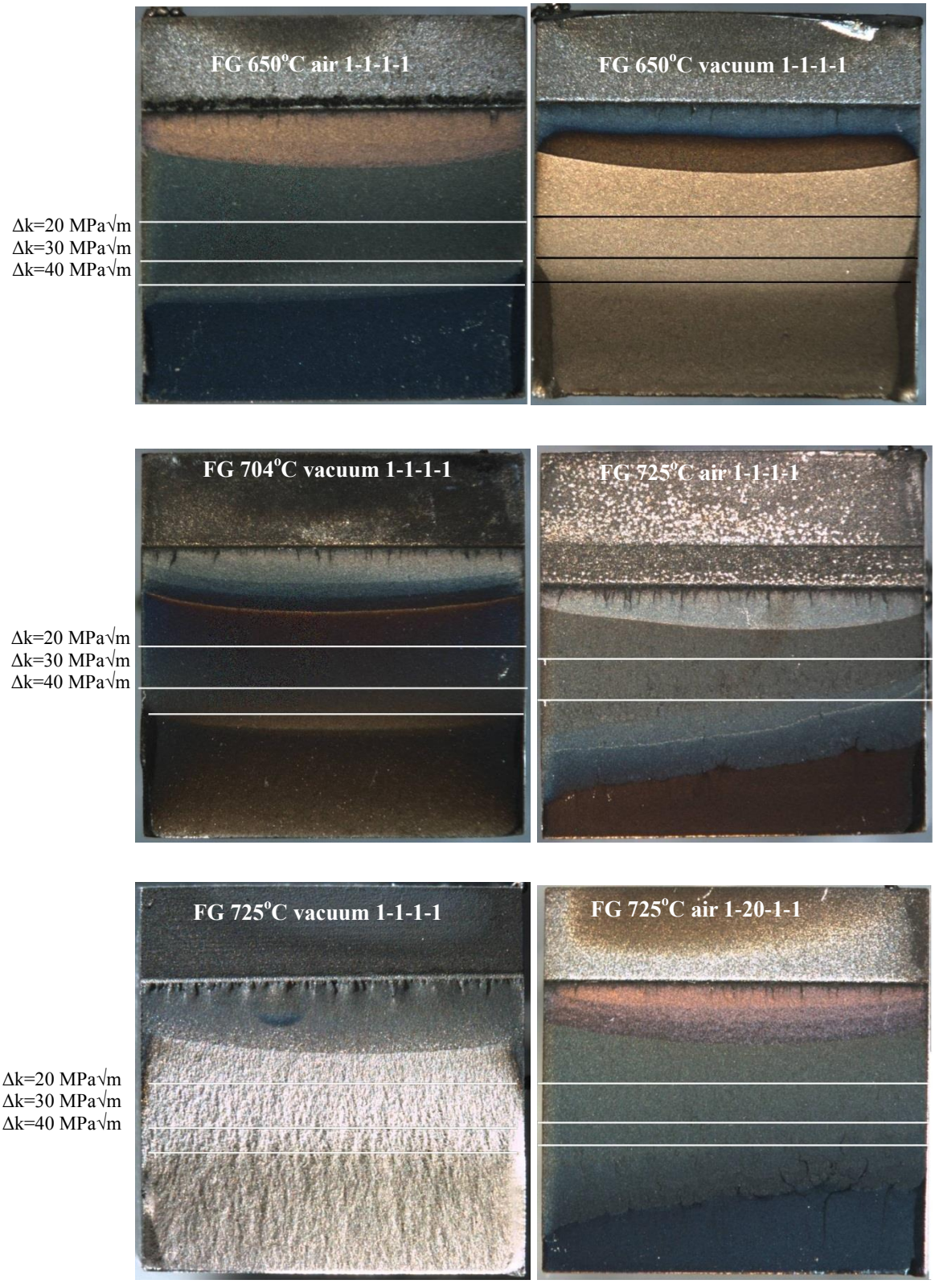

Fig. 6. 11 Optical overview of fracture surfaces of the FG LSHR alloy.

As shown in Figs. 6.14 - 6.16, the fracture features of the vacuum tests for CG LSHR are quite different from those of the air tests. In the vacuum tests, the fracture surfaces are principally transgranular, and the specific features vary from test to test depending on the testing condition. In addition, the secondary cracks are much shorter and straighter, and are not as developed as those in the air tests. In the vacuum test at 650 ^{o}C (Fig. 6.14), there are some crystallographic facets and steps on the transgranular fracture surface accompanied by some evidence of slip bands, as shown in Fig. 6.16 (a), and the crystallographic facets are more evident on the fracture surface of the test with a dwell time of 20s. In the vacuum test at 725 ^{o}C with 1s dwell (Figs. 6.15 (a) and (b)), the fracture surface is quite flat and featureless except some evidence of striations (in Fig. 6.16 (b)), whereas the fracture surface of the test with a dwell time of 20s becomes rougher, and takes on a feature of mixed failure modes (transgranular and intergranular) with a more predominant transgranular fracture feature at high ΔK level as shown in Figs. 6.15 (c) and (d).

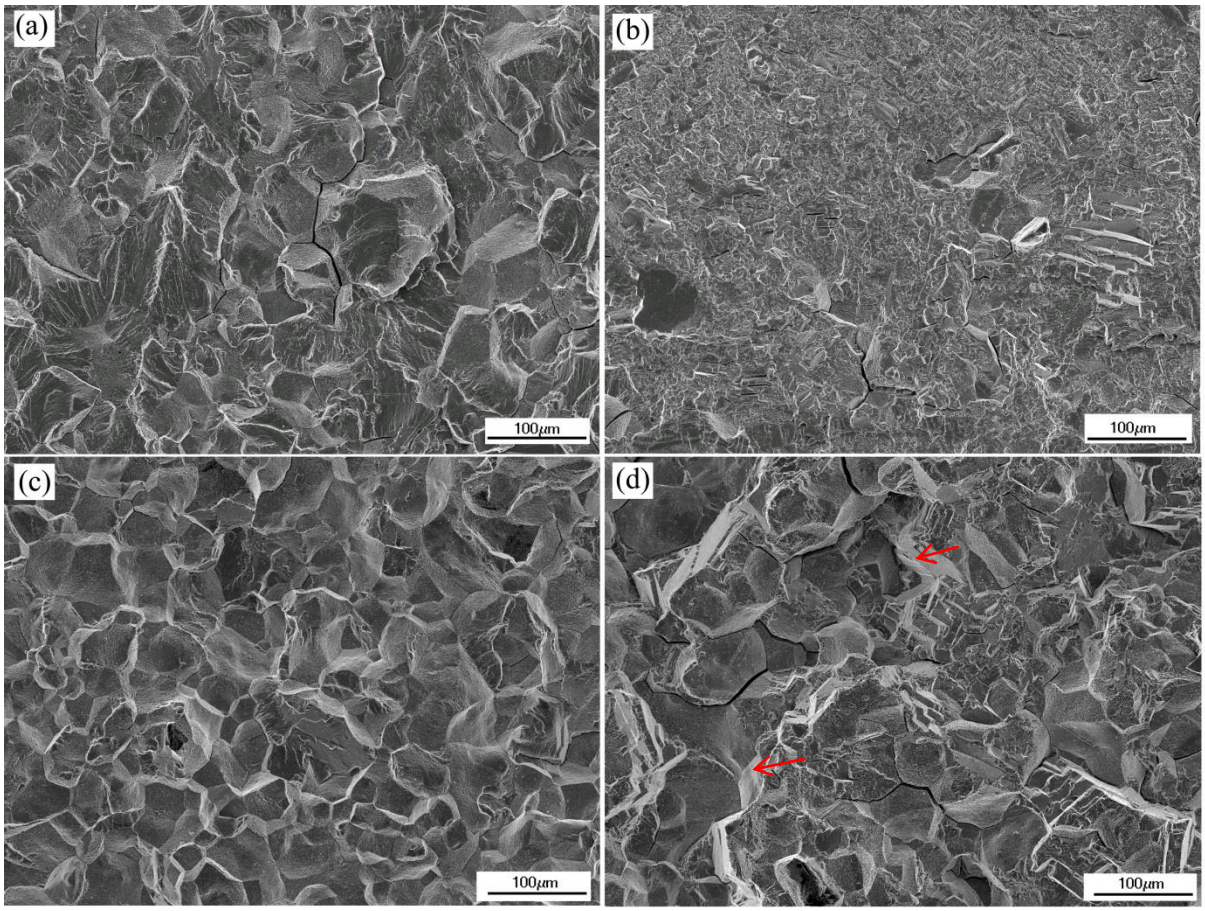

Fig. 6.12 Fractography of the CG LSHR tested in air at 650 ^{o}C: (a) 1-1-1-1, ΔK=20 MPa√m, (b) 1-1-1-1, ΔK=40 MPa√m, (c) 1-20-1-1, ΔK=20 MPa√m and (d) 1-20-1-1, ΔK=40 MPa√m.

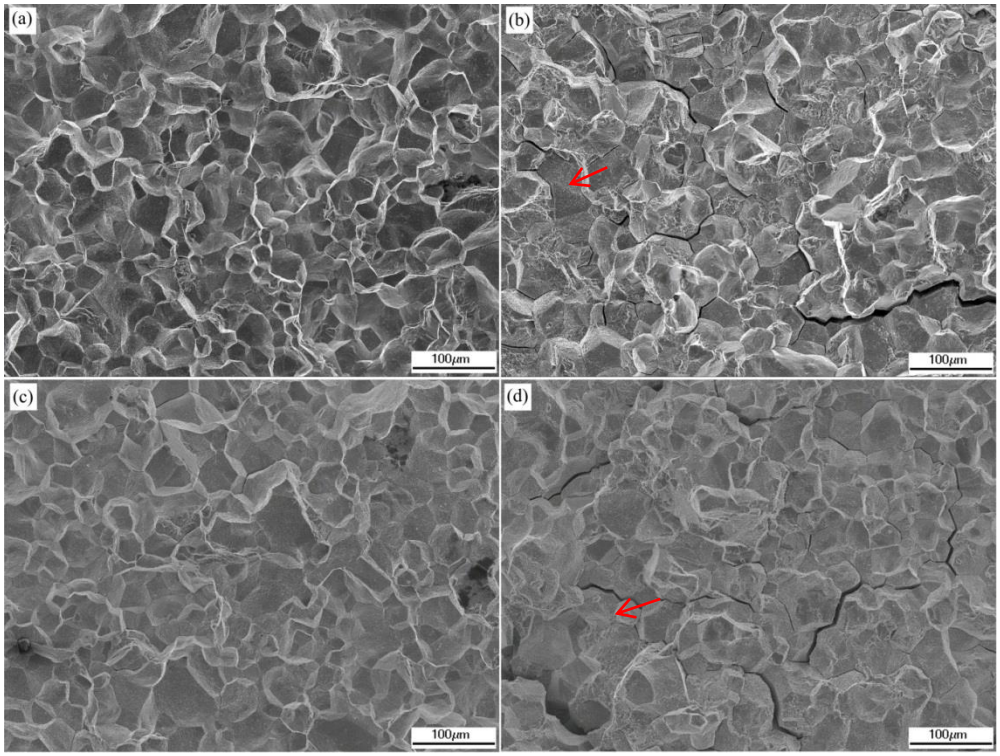

Fig. 6.13 Fractography of the CG LSHR tested in air at 725 ^{o}C: (a) 1-1-1-1, ΔK=20 MPa√m, (b) 1-1-1-1, ΔK=40 MPa√m, (c) 1-20-1-1, ΔK=20 MPa√m and (d) 1-20-1-1, ΔK=40 MPa√m.

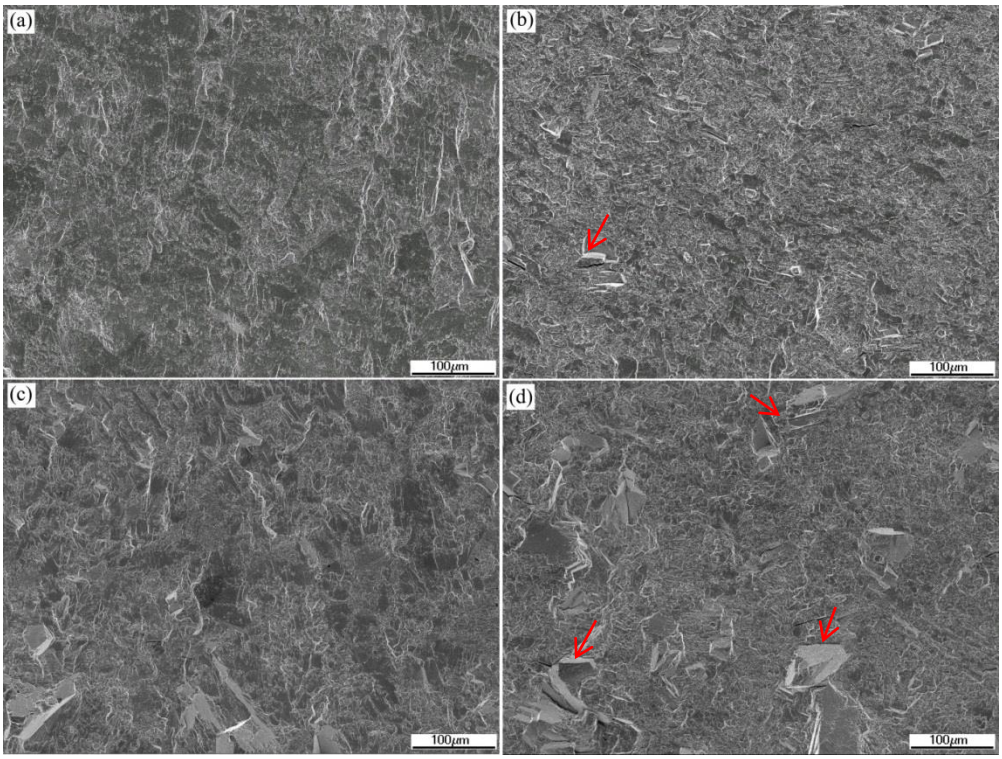

Fig. 6.14 Fractography of CG LSHR tested in vacuum at 650 ^{o}C: (a) 1-1-1-1, ΔK=22 MPa√m, (b) 1-1-1-1, ΔK=44 MPa√m, (c) 1-20-1-1, ΔK=22 MPa√m and (d) 1-20-1-1, ΔK=44 MPa√m.

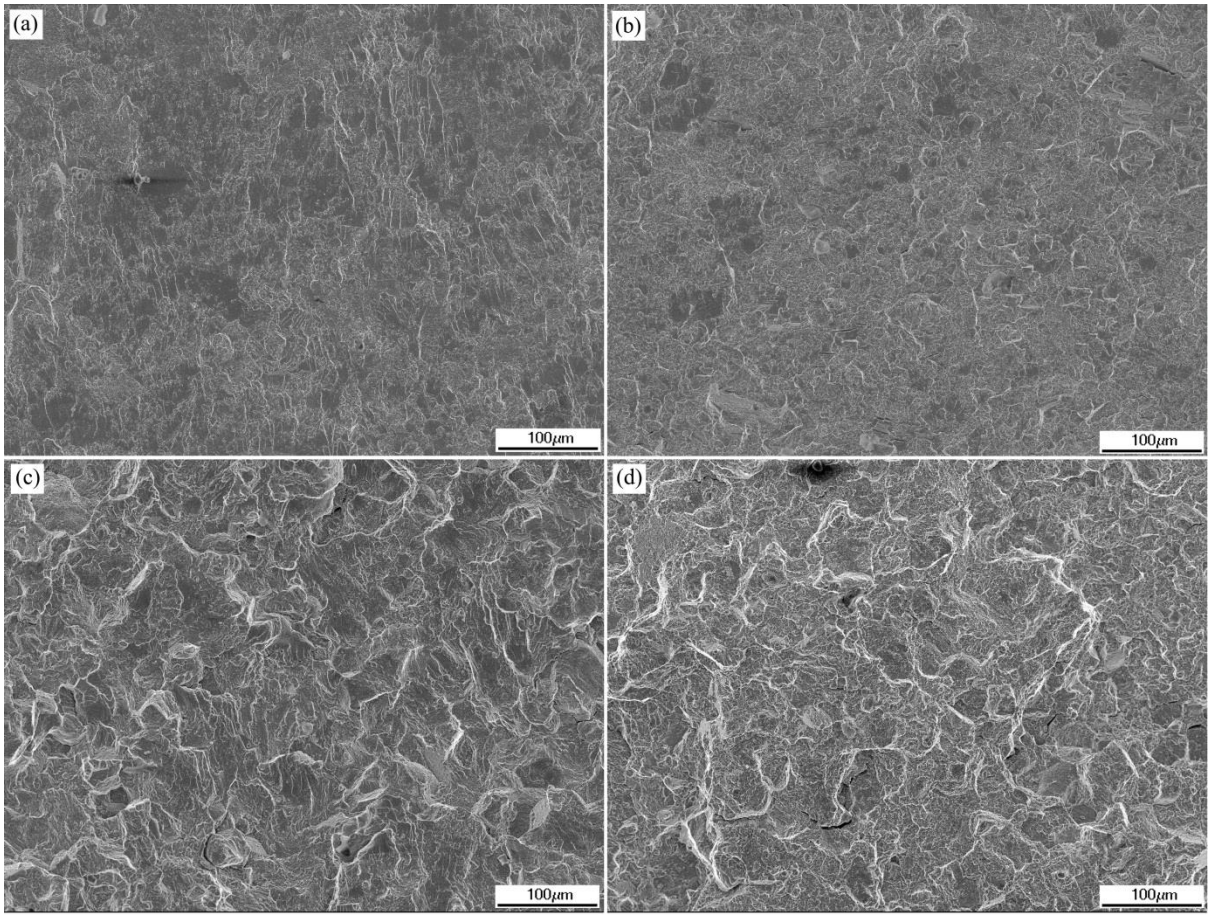

Fig. 6. 15 Fractography of CG LSHR tested in vacuum at 725 ^{o}C: (a) 1-1-1-1, ΔK=20 MPa√m, (b) 1-1-1-1, ΔK=40 MPa√m, (c) 1-1-1-1, ΔK=20 MPa√m and (d) 1-1-1-1, ΔK=40 MPa√m.

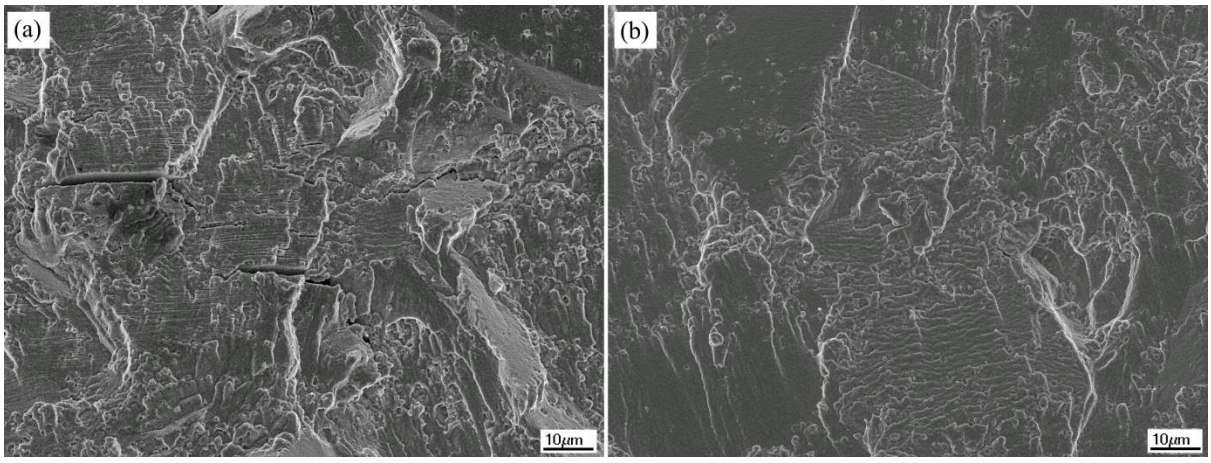

Fig. 6.16 Striation at fracture surfaces of CG LSHR: (a) 650 ^{o}C, vacuum, 1-20-1-1, ΔK=22 MPa√m and (b) 725 ^{o}C, vacuum, 1-1-1-1, ΔK=20 MPa√m.

For the FG LSHR tests, the fracture failure modes are similar to CG LSHR, i.e., predominantly intergranular fracture with longer and more tortuous secondary cracks on the fracture surface in the air tests and predominantly transgranular fracture with shorter and straighter secondary cracks in the vacuum tests, as shown in Figs. 6.17 - 6.19. Additionally, the amount of secondary cracks appears much greater in the air tests. However, unlike CG LSHR air tests, the intergranular characteristics of fracture surfaces in the FG LSHR air tests (Figs. 6.17 and 6.18) are less evident, and the individual grains cannot be seen clearly due to the existence of primary γ′. As ΔK increases in the air test at 650 ^{o}C, the intergranular fracture characteristics become less predominant, and the fracture surface becomes smoother with no obvious crystallographic facets (in Fig. 6.17 (b)). By increasing the temperature and/or introducing a dwell time of 20s at the peak load, the fracture surface becomes completely intergranular with apparent secondary cracks as shown in Fig. 6.18. In addition, evidence of decohesion of primary γ′ from the fracture surface can be observed (in Fig. 6.18 (e)).

As shown in Figs. 6.19 (a) and (b), the transgranular fracture surfaces in the vacuum tests at 650 ^{o}C with a dwell of 1s are quite flat and featureless, and the secondary cracks on the fracture surface are short and straight. As temperature increases to 704 ^{o}C and further to 725 ^{o}C, the fracture surfaces become much rougher, especially at high ΔK level at high temperature as shown in Fig. 6.19 (f).

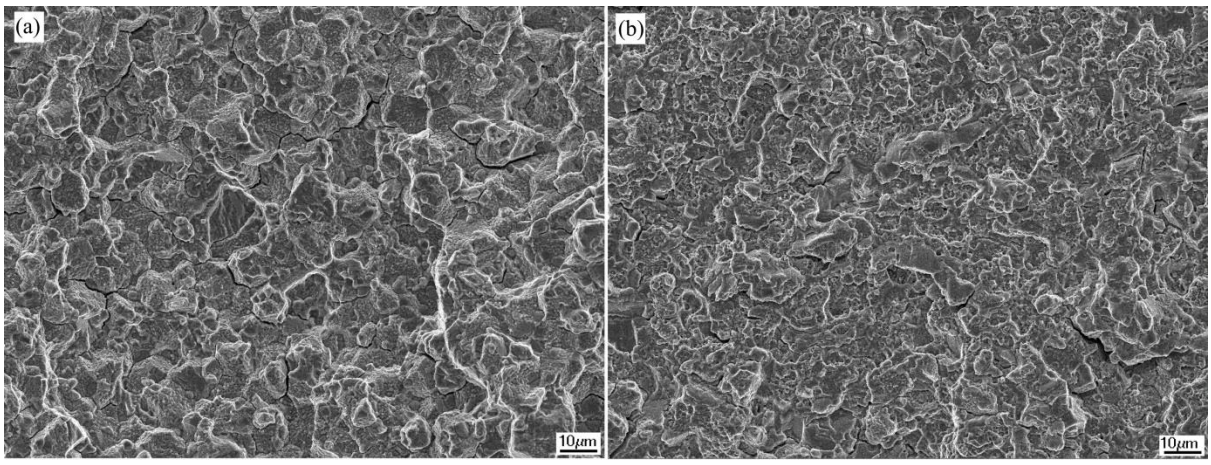

Fig. 6.17 Fractography of FG LSHR tested in air at 650 ^{o}C under a loading waveform of 1-1-1-1: (a) ΔK=20 MPa√m and (b) ΔK=40 MPa√m.

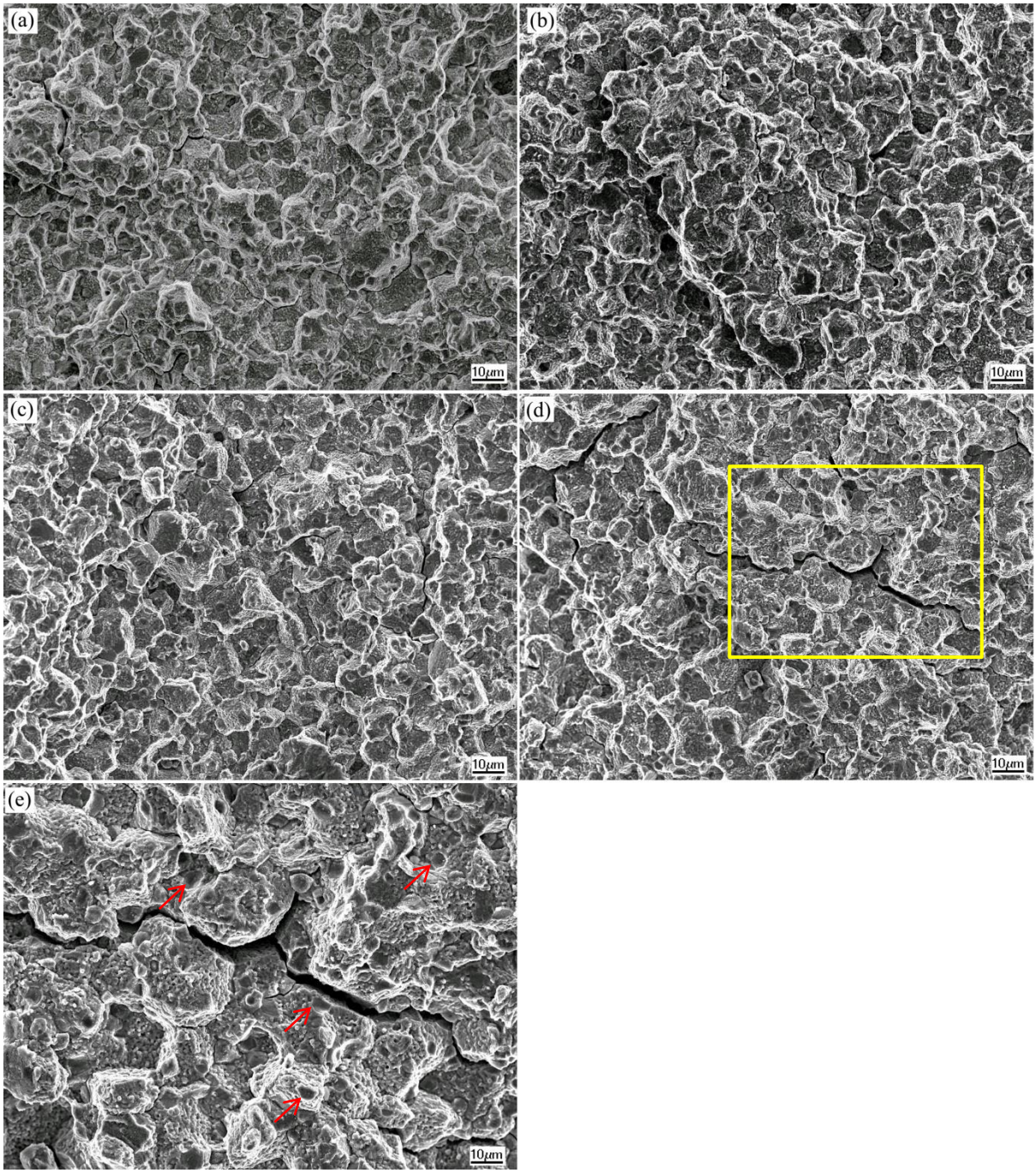

Fig. 6. 18 Fractography of FG LSHR tested in air at 725 ^{o}C: (a) 1-1-1-1, ΔK=20 MPa√m, (b) 1-1-1-1, ΔK=40 MPa√m, (c) 1-20-1-1, ΔK=20 MPa√m, (d) 1-20-1-1, ΔK=40 MPa√m and (e) close-up of the region highlighted by yellow rectangle in (d).

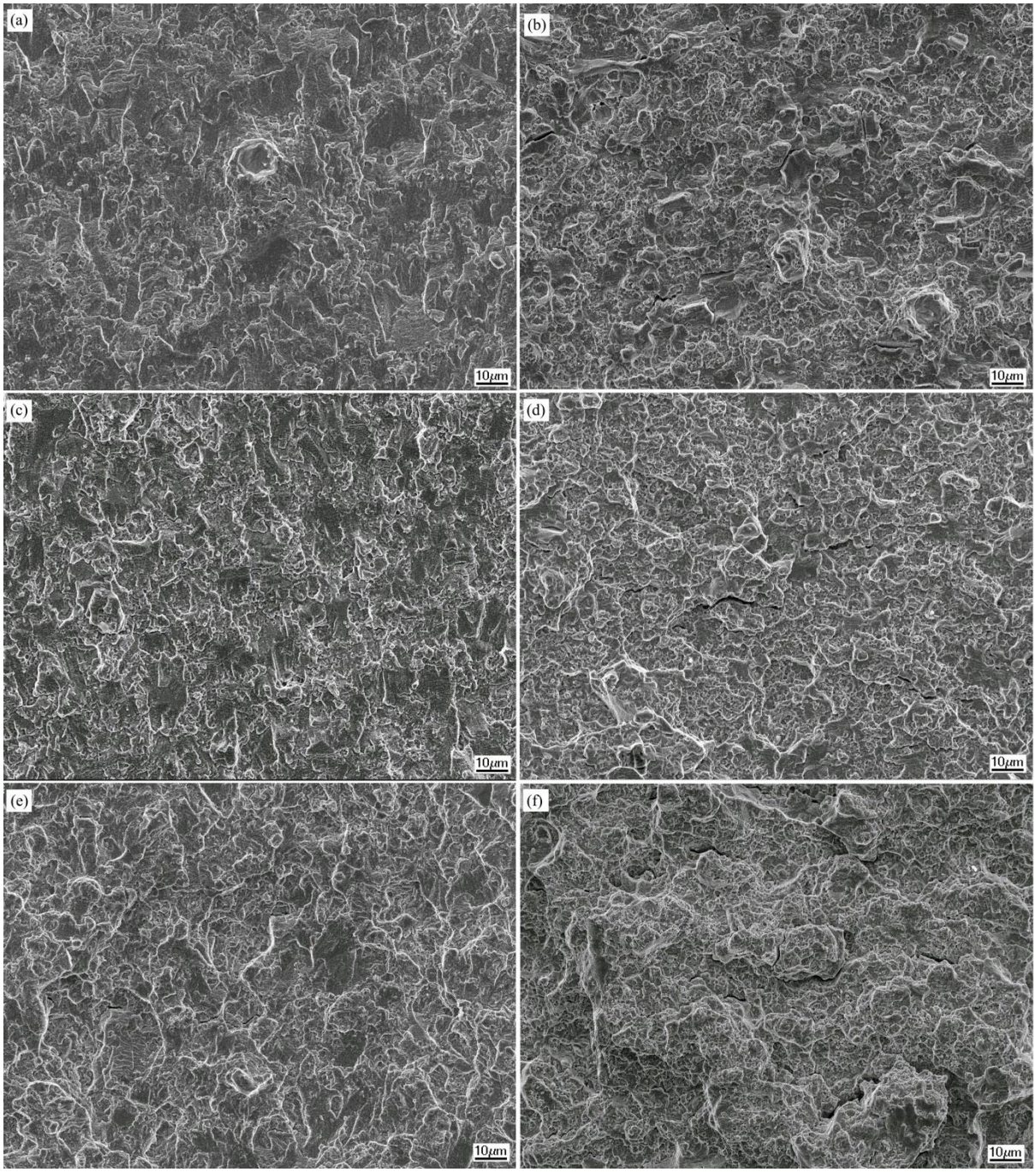

Fig. 6.19 Fractography of FG LSHR tested in vacuum under a 1-1-1-1 loading waveform: (a) 650 ^{o}C, ΔK=20 MPa√m, (b) 650 ^{o}C, ΔK=40 MPa√m, (c) 704 ^{o}C, ΔK=20 MPa√m, (d) 704 ^{o}C, ΔK=40 MPa√m (e) 725 ^{o}C, ΔK=20 MPa√m and (f) 725 ^{o}C, ΔK=40 MPa√m.

Fig. 6.20 shows the morphology of sectioned fracture surfaces of the CG and FG LSHR tested at 725 ^{o}C in air under the 1-20-1-1 waveform. As shown, the secondary cracks on the fracture surface can penetrate into the subsurface by several grains (Figs. 6.20 (a) and (e)). From the observation of all the sectioned fracture surfaces, the penetration depth of the

secondary crack is associated with the testing environment and temperature. Generally, it is more common to see the secondary cracks penetrate subsurface by a longer distance in the 725 ^{o}C air test with a 20s dwell at the peak load. A further examination of the secondary cracks by SEM indicates that these secondary cracks formed in the air tests are filled with oxides, and an enrichment of Co and Cr in these oxides is found by the EDX analysis. It is arguable whether these oxides formed before or after the secondary cracking at the grain boundaries. However, the oxides without cracking at the tip of a secondary crack with cracked oxides in the wake (Figs. 6.20 (d) and (f)) indicates that the formation of such oxides is more likely prior to the appearance of secondary cracks and that oxide cracking may contribute to the development of secondary cracks.

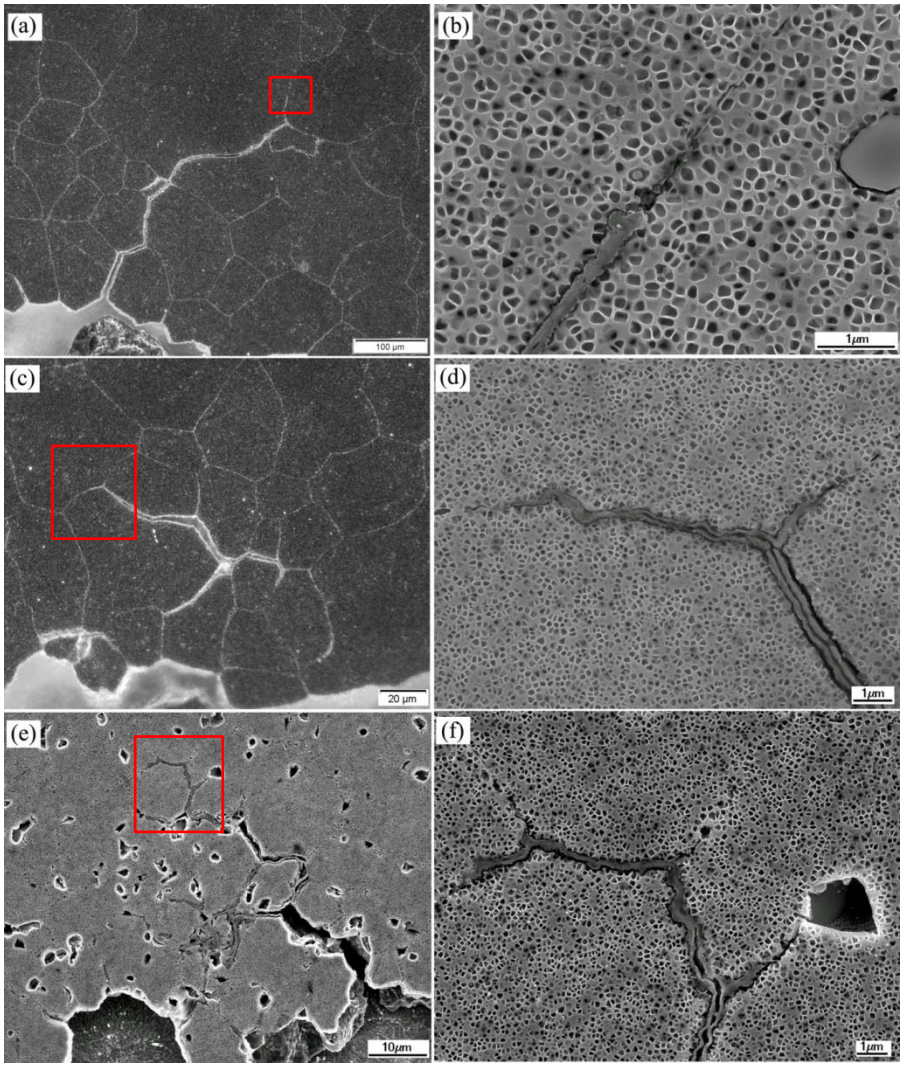

Fig. 6.20 Morphology of sectioned fracture surface in (a), (c) CG and (e) FG LSHR tested at 725 ^{o}C in air under the 1-20-1-1 waveform; (b), (d) and (f) close-ups of the highlighted regions shown in (a), (c) and (e) respectively.

As shown in Fig. 6.21, an interaction between secondary cracks and precipitates is discerned. It is clearly seen from Fig. 6.21 (a) that the secondary crack is deflected around the primary γ′ and then the crack has branched. Figs. 6.21 (c) and (e) show that the secondary cracks are blocked by borides $(W,Mo,Cr)_3B_2$ and carbides respectively which have been identified previously [19] and are confirmed by the EDX analysis in this study (as shown in Figs. 6.21 (d) and (f)).

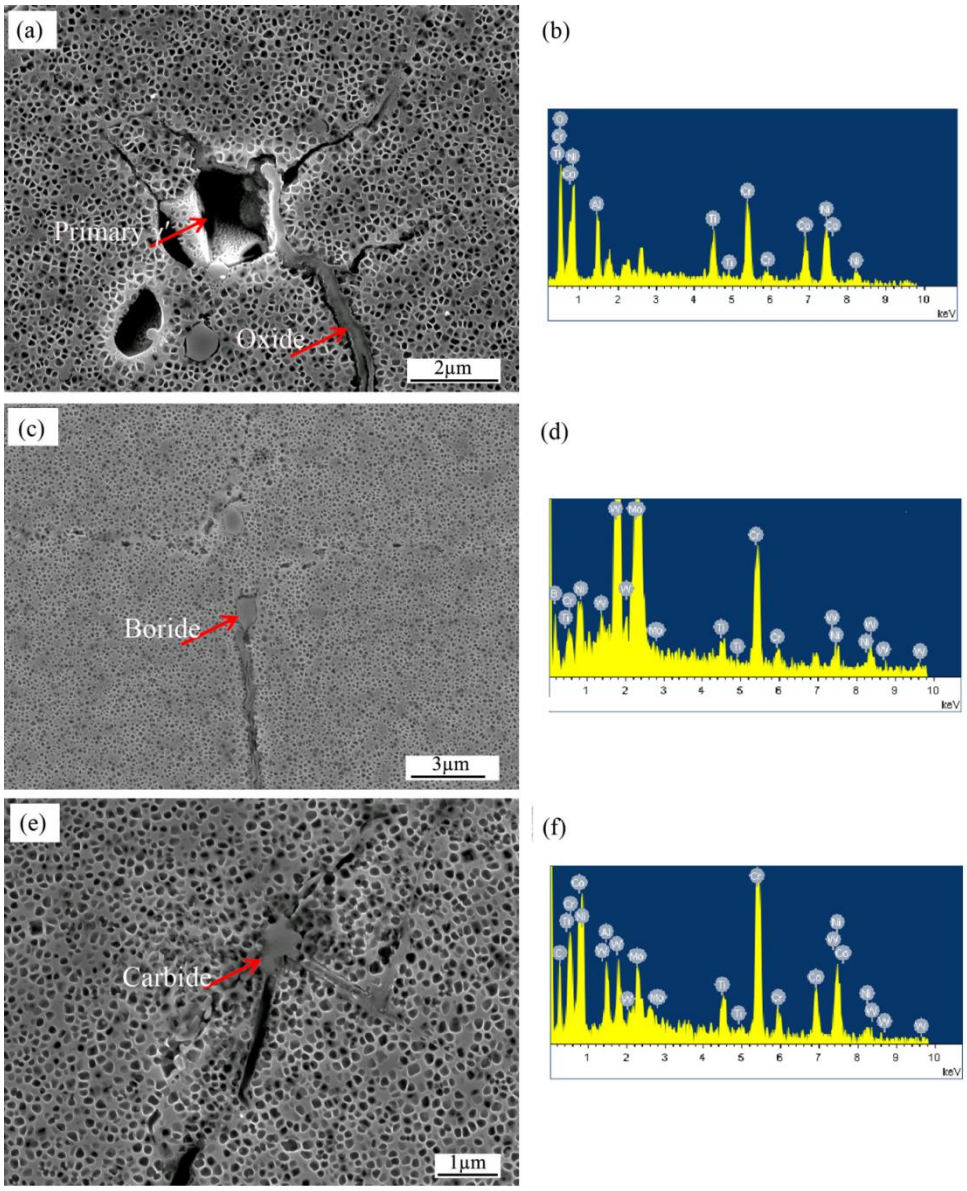

Fig. 6.21 Secondary cracks (a) are deflected and/or branched around primary γ′ in the FG LSHR tested at 725 ^{o}C in air with a 20s dwell, (c) are blocked by borides in the CG LSHR tested at 725 ^{o}C in air with a 20s dwell, (e) are blocked by carbides in the CG LSHR tested 725 ^{o}C in vacuum with a 20s dwell; (b), (d) and (f) the energy dispersive X-ray spectra of oxide, boride and carbide shown in (a), (c) and (e) respectively.

6.3.3 Influence of frequency on crack growth rate

In order to investigate the influence of frequency on the long fatigue crack growth behaviour, a crack growth-out test under a constant ΔK of 25 MPa√m with a series of loading frequencies was conducted. Fig. 6.22 shows the recorded crack length vs. loading time at the investigated frequencies after a post-test calibration, where the influence of the loading frequency can be clearly seen. Generally, there is a faster crack growth rate on the basis of time for the crack that grew under a sine waveform with a higher frequency as indicated by the slope in the graph. The final rapid increase in crack length corresponds to the grow-out region under a constant load with a sine waveform of 8 Hz, and this high crack growth rate is caused by the increase in the crack driving force, i.e. ΔK, due to the increase in crack length.

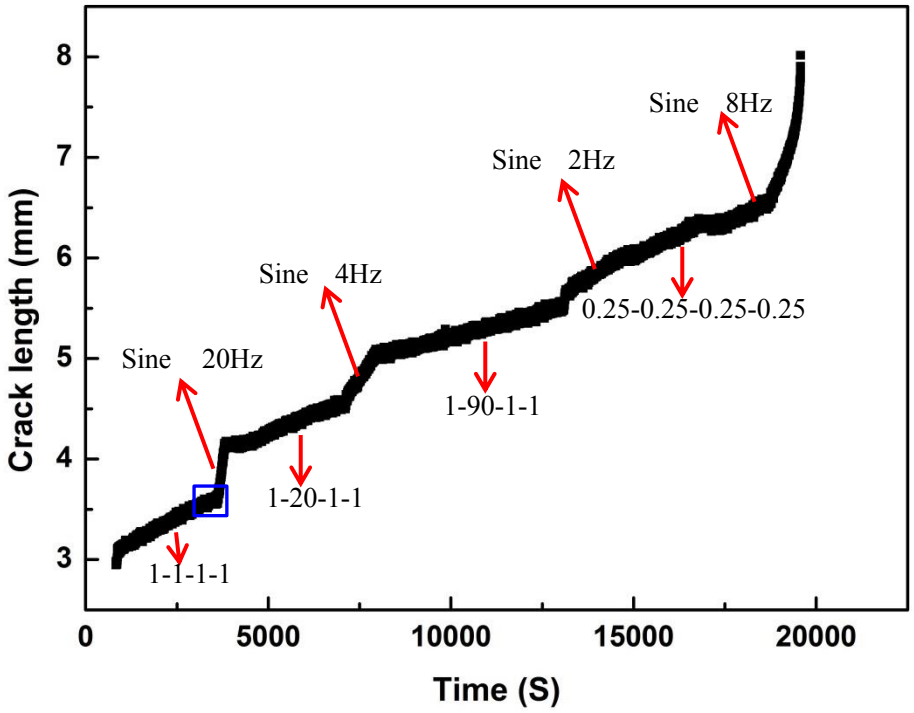

Fig. 6. 22 Fatigue crack growth behaviour of the LSHR alloy at a constant ΔK of 25 MPa√m under different loading frequencies. A transition region that is discarded in the crack growth rate derivation is indicated by a rectangle.

Fig. 6.23 presents the influence of frequency on the crack growth rate. As shown in Fig. 6.23 (a), a transition frequency of 1 - 2 Hz can be identified. When the loading frequency is lower than 2 Hz, the crack growth rate on the basis of time is insensitive to frequency, indicating the dominance of time-dependent crack growth behaviour below this frequency range. On the contrary, the crack growth rate on the basis of time increases almost linearly

with frequency when loading frequency is greater than 2 Hz, indicating the cycle-dependent crack growth behaviour in this frequency range. Similarly, by plotting the crack growth rate on the basis of cycle as shown in Fig. 6.23 (b), it is possible to make the same interpretation and identify the same transitional frequency range of 1 - 2 Hz at a ΔK of 25 MPa√m.

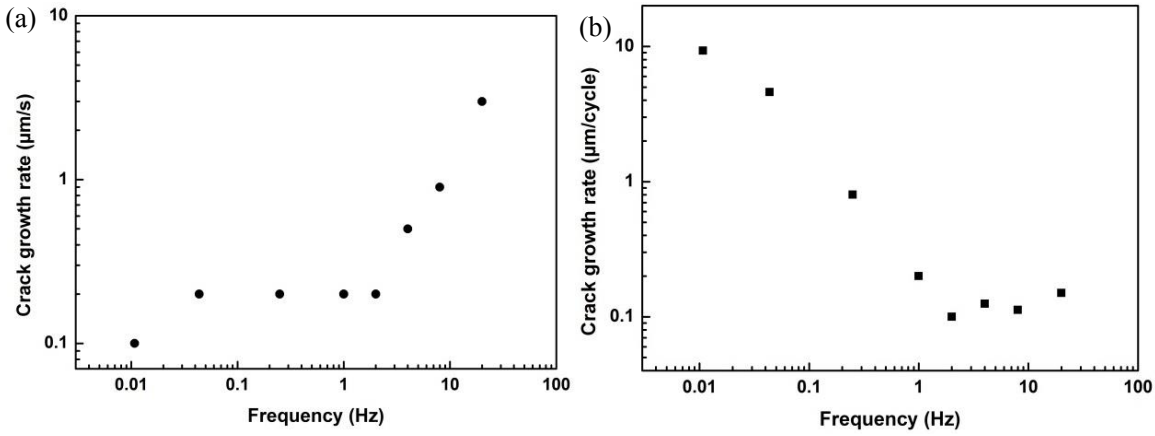

Fig. 6.23 Influence of frequency on crack growth rate on the basis of (a) time and (b) cycle.

As shown in Fig. 6.24, the boundaries between two adjacent regions tested by two different frequencies can be clearly distinguished from the overview of the fracture surface under either OM or FEG-SEM apart from those regions produced by the transitional frequencies. It is found from Fig. 6.24 (b) that the fracture surfaces are predominantly intergranular in these regions where low loading frequency trapezoidal waveforms were applied, whereas these regions tested by sine waveforms with relatively high frequencies are characterised by the transgranular fracture features. At these regions where transitional frequencies were applied, the boundary between adjacent regions is quite blurred and the fracture surface takes on mixed intergranular and transgranular features.

By observing the fracture surface at higher magnification under FEG-SEM, the transition between intergranular fracture and transgranular fracture can be clearly seen when the loading frequency was changed from time-dependent region to cycle-dependent region, and vice versa, as shown in Fig. 6.25 (a). Unlike time or cycle-dependent crack growth regions, in these regions where transitional frequencies were applied, the fracture surfaces turn to be mixed inter-transgranular and the boundary between these regions is not easily distinguishable, which is clearly shown in Figs. 6.25 (c) and (d). Additionally, a transition from intergranular fracture to mixed inter-transgranular facture is observed as shown in Fig. 6.25 (b).

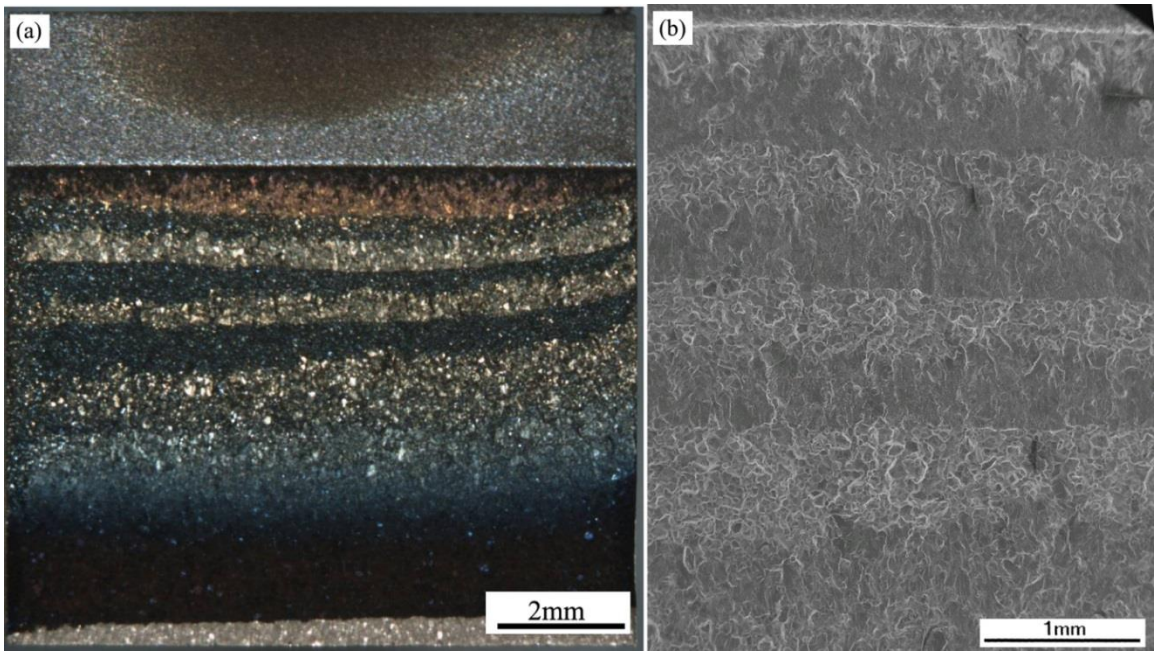

Fig. 6.24 Overview of the fracture surface of the constant ΔK test under (a) OM and (b) FEG-SEM.

6.3.4 Roughness of fracture surface

Fig. 6.26 presents the roughness of fracture surface of CG LSHR alloy tested under different conditions. As shown in Fig. 6.26 (a), the roughness of fracture surface for air tests varies from 20 μm to 50 μm approximately, and increases with the increasing ΔK, apart from the test at 650 ^{o}C with a dwell of 1s, in which the roughness decreases with ΔK. By increasing the temperature or introducing the dwell period, the roughness of the fracture surface increases to some extent, which can also be observed on the fractography in Figs. 6.12 and 6.13. Comparing the roughness of fracture surface between air tests at 650 ^{o}C with a dwell time of 20s and 725 ^{o}C with a dwell time of 1s, it seems that the effect of dwell time on the roughness of fracture surface is more significant. Fig. 6.26 (b) shows the variation of roughness of fracture surface with ΔK in the CG vacuum tests. It can be found that the roughness of fracture surface of vacuum tests is much lower than that of air tests, which is consistent with the fractography observation shown in Figs. 6.14 and 6.15. The roughness of fracture surface for vacuum tests varies from 12 μm to 30 μm, and also increases with ΔK. Similarly to air tests, increasing temperature and/or prolonging dwell time causes the increase in roughness of fracture surface, and the influence of dwell time is greater than temperature at these investigated conditions when making a comparison between vacuum tests at 650 ^{o}C with a 20s dwell and that at 725 ^{o}C with a 1s dwell.

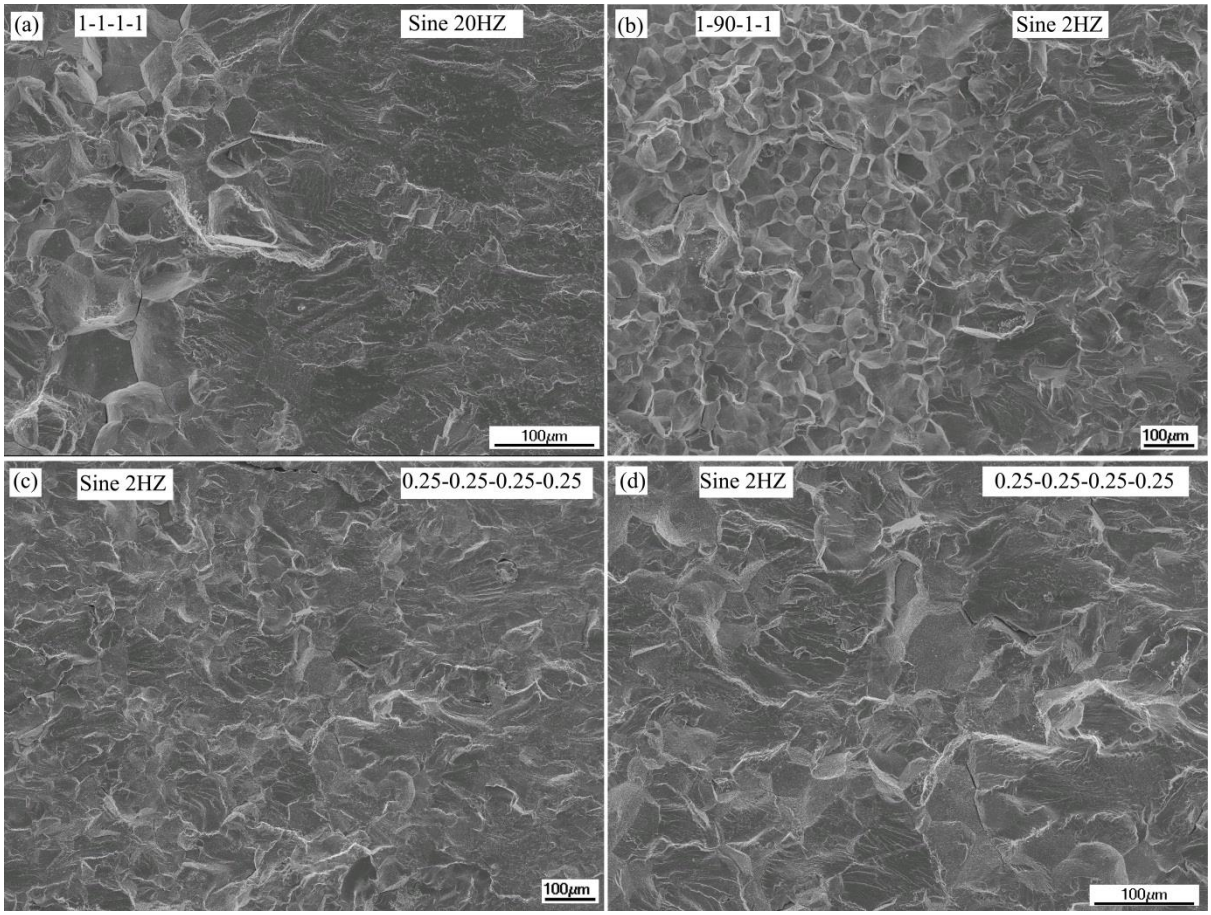

Fig. 6.25 Morphology of the fracture surface of the constant ΔK test: (a) transition from intergranular to transgranular fracture when the loading waveform was changed from 1-1-1-1 to sine 20 Hz; (b) transition from intergranular to mixed inter-transgranular fracture when the loading waveform was changed from 1-90-1-1 to sine 2 Hz; (c) and (d) mixed inter-transgranular region tested under loading waveforms of sine 2 Hz and 0.25-0.25-0.25-0.25.

6.3.5 Secondary cracks on the fracture surface

As shown in the fractography of the tested LSHR alloy (Figs. 6.13, 6.18 and 6.20), secondary cracks are well developed on the fracture surfaces, especially when tested in air at higher temperature with a 20s dwell at peak load. Fig. 6.27 presents the quantitative statistical results of the amount and average length of secondary cracks in the CG LSHR air tests. As shown in Fig. 6.27 (a), the amount of secondary cracks increases with ΔK. The influence of stress intensity is rather significant at high temperature (i.e. 725 ^{o}C) or with a long dwell. For air test at 650 ^{o}C with a dwell time of 1s, the amount of secondary cracks increases slightly with ΔK. The influences of temperature and dwell time on the amount of secondary cracks are similar to the trends in roughness of fracture surface, i.e., dwell time has a greater effect

than temperature. Fig. 6.27 (b) shows the variation of the average length of secondary cracks with ΔK. It is found that the variation trend resembles that of roughness of fracture surface. The average length of secondary cracks in the air tests increases with ΔK, with an exception of the test at 650 ^{o}C with 1s dwell. Similarly, the temperature and dwell time have significant impacts on the average length of secondary cracks, and the influence of dwell time seems to be greater. It is worth mentioning that the average length of secondary cracks should be interpreted carefully in light of the accuracy of the measurement method with respect to measuring the cracks at triple grain boundaries or crack branches (therefore the standard deviation of the measured average length of secondary cracks has not been presented).

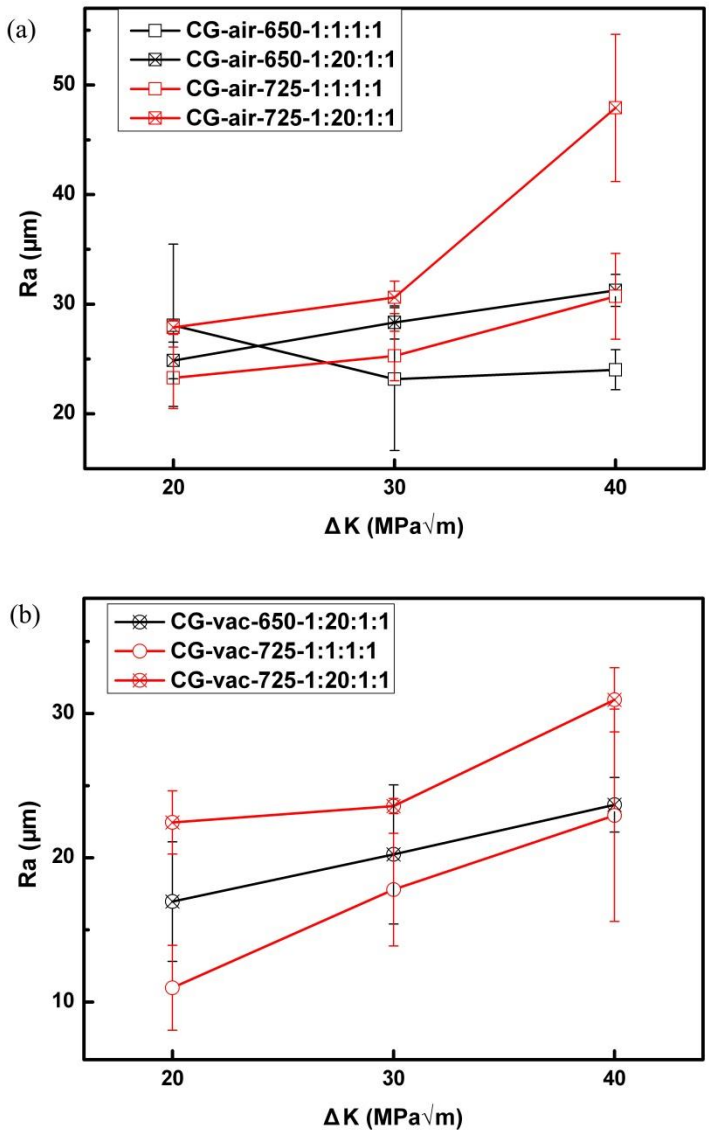

Fig. 6.26 Roughness of fracture surface of CG LSHR alloy tested in: (a) air and (b) vacuum.

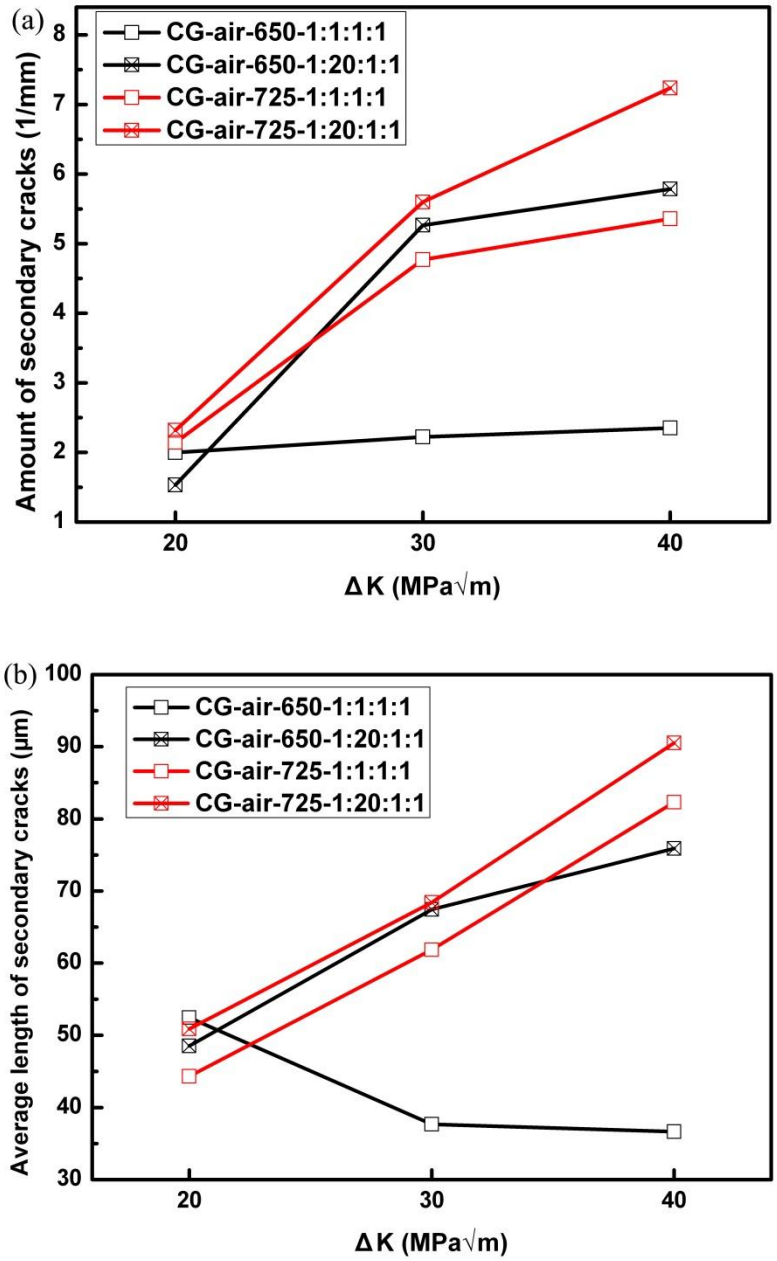

Fig. 6.27 (a) Amount and (b) average length of secondary cracks on the fracture surface in the CG LSHR alloy air tests.

As shown in Fig. 6.28, a correlation between the roughness of the fracture surface, average length of secondary cracks and fatigue crack growth rate can be identified in the CG LSHR air tests, i.e. a higher fracture surface roughness and/or average length of secondary cracks is generally associated with a higher fatigue crack growth rate. It is evident that the fastest fatigue crack growth is observed in the 725 ^{o}C dwell test which has the roughest fracture surface and longest secondary cracks according to these quantitative measurements. The increase in the roughness of fracture surface and/or average length of secondary cracks is

therefore associated with an increased testing temperature and an introduction of a dwell at the maximum load. It is worth mentioning that the trend in the 650 ^{o}C test with a 1s dwell is clearly different from the other three tests, and is related to the observed transition from a predominantly intergranular fracture mode to a mainly transgranular fracture mode as ΔK increases for this set of test conditions. This is believed to relate to the mechanically driven (cycle-dependent) crack growth mechanisms outstripping any oxidation enhanced (time-dependent) processes.

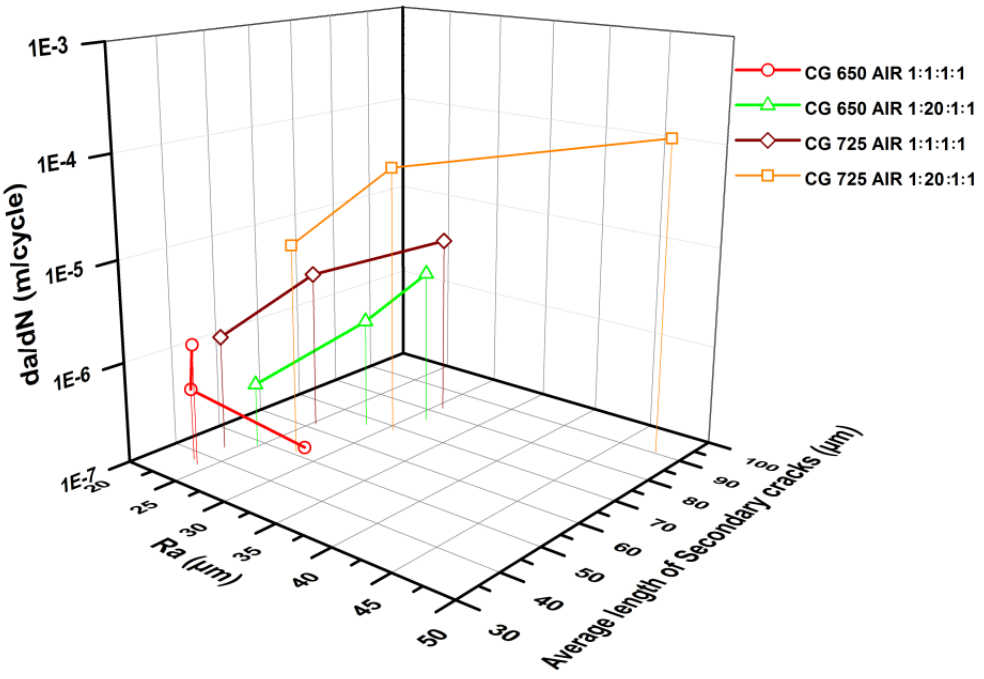

Fig. 6.28 Correlation between the roughness of the fracture surface (Ra), average length of secondary cracks and fatigue crack growth rate (da/dN) in the CG LSHR air tests at 650 and 725 ^{o}C with 1-1-1-1 and 1-20-1-1 trapezoidal loading waveforms.

6.4 Discussion

6.4.1 Oxidation versus creep mechanism

Fatigue crack growth at elevated temperatures is a complicated process as the simultaneous processes of oxidation and creep/stress relaxation may also occur under the cyclic load depending on the testing conditions and the properties of the investigated materials. The results of fatigue crack growth tests in this study show that the crack propagation behaviour in the LSHR alloy is closely related to microstructure, testing environment and temperature,

loading frequency and dwell time at the peak load. Specifically, the finer microstructure, higher temperature, oxidizing environment as well as lower loading frequency and longer dwell at the peak load result in enhanced crack growth rate along with a more intergranular fracture morphology. It is believed that the dramatic increase in the FCG rate in the LSHR alloy with temperature and/or introduction of a dwell at the peak load in air is principally caused by the oxidation of the grain boundary ahead of the crack tip, although it is reported that the decrease in yield strength with temperature and creep processes may also contribute to the degradation of fatigue properties of Ni-based superalloys [36, 136, 179, 180].

It is well known that there is generally an inverse relationship between crack growth and strength [179]. The reduced yield strength at high temperature can result in a larger plastic zone (and crack opening) at the crack tip, and thereby promotes fatigue crack propagation. However, it is reported that there is only a slight decrease in yield strength of the LSHR alloy with increasing temperature within the test temperature range (e.g., a decrease of 22 MPa between 650 ^{o}C and 704 ^{o}C in the CG LSHR alloy, and 13 MPa in the FG LSHR alloy within the same temperature range as shown in Table 3.6) [19]. Hence it can be inferred that the reduction in yield strength plays an insignificant role in the FCG behaviour at the investigated temperatures. Moreover, the higher yield strength but poorer crack growth resistance observed in FG LSHR at elevated temperatures also indicates that the yield strength is not the determining factor of the FCG behaviour under the investigated conditions.

It seems that creep process also has little influence on the FCG behaviour of the LSHR alloy as indicated in the FCG data of the CG LSHR vacuum tests at either 650 ^{o}C or 725 ^{o}C (Fig .6.5 (a)), where the introduction of a 20s dwell does not cause a noticeable increase in the FCG rate. The transgranular features and the absence of the micro-voids on the fracture surface in the vacuum tests further indicates the limited and/or inactivated creep process during fatigue crack propagation in the LSHR alloy. In fact, the LSHR alloy is characterised by its exceptional creep resistance at elevated temperature according to the work conducted at NASA [19], and better creep resistance has been recently reported in the CG LSHR alloy compared with disc alloy N18 under creep-fatigue testing conditions [181]. Creep processes are therefore not the main contributor to the degraded fatigue properties of the LSHR alloy at high temperature and long dwells.

As shown in Figs. 6.5 and 6.7, the oxidizing environment in combination with higher temperature and an introduction of dwell of 20s at the peak load stimulates fatigue crack

growth to a significant extent associated with the evident intergranular fracture features, which can be linked to the evident oxidation of the grain boundary ahead of the crack tip and the resultant decreased strength of the grain boundary promoting intergranular crack growth. The effects of oxidation on FCG are dependent on the availability of oxidizing species, and hence oxygen diffusion in the region ahead of the crack tip, which is closely related to the oxygen diffusivity, diffusion time and available diffusion paths [43, 182]. The higher diffusivity of oxygen at higher testing temperature and the longer diffusion time per loading cycle (by introducing a 20s dwell in a loading cycle) will enhance these oxidation effects, resulting in acceleration of the FCG. Hence the highest FCG rate occurred in the air tests at 725 ^{o}C with a dwell of 20s in both CG and FG LSHR alloys. The higher FCG rate observed in the FG LSHR than in its CG variant under the same testing conditions is linked to the greater number of grain boundaries available for preferential oxidation at the crack tip.

The oxidation assisted crack growth mechanism can be further verified by the oxides observed at the tip of secondary grain boundary cracks in the sectioned fracture surface as shown in Fig. 6.20. Although it is still arguable whether the oxides form prior to or after the secondary crack formation, it is reasonable to assume that if the oxides form later than the emergence of secondary cracks, then the oxides will form on the two freshly cracked surface and grow toward to each other as the loading cycle proceeds. If such a scenario is true, then it fails to explain the intact/uncracked oxides located at the secondary crack tip. Actually, as observed in the short fatigue crack tests at elevated temperatures in Chapter 5, formation of grain boundary Co/Ni-rich oxide plus Cr/Ti/Al oxide intrusion along grain boundaries and oxide cracking is the principal mechanism of the crack initiation and subsequent propagation in air. It is therefore reasonable to believe the same grain boundary oxidation mechanism ahead of the crack tip can also occur and contribute to long crack propagation. In addition, a recent study on the oxidation ahead of the crack tip in disc alloy RR1000 also shows that an oxide intrusion consisting of layered oxides in the thermodynamic sequence of CoO, NiO, Cr_2O_3, TiO_2 and Al_2O_3 which is observed ahead of the propagating crack tip at elevated temperatures [17], indicating that strain/stress assisted grain boundary oxidation is the main mechanism responsible for the enhanced crack growth rate. Even though the experimental results have confirmed the formation of oxides ahead of the propagating cracks, some questions remain with respect to the oxidation assisted crack growth due to stress assisted grain boundary oxidation, e.g. how do the oxides form and how does oxygen diffuse along the grain boundary. Further study on diffusion of oxygen ahead of the crack tip using oxygen

isotope (^{18}O) and secondary ion mass spectrometry (SIMS) is being carried out in a joint research project with Warwick University and Loughborough University, and will be simply depicted in Chapter 8-Future work.

6.4.2 Effect of microstructure on crack growth

A coarse grained structure is beneficial in improving fatigue crack growth resistance of the LSHR alloy in this study (shown in Fig. 6.8), which is consistent with NASA's previous findings [19]. By comparing fractography of CG and FG LSHR tested at 650 ^{o}C in air with a 1s dwell, it is found that there are some crystallographic facets and steps on CG LSHR fracture surfaces at a high stress intensity factor range (ΔK = 40 MPa$\sqrt{m}$), whereas no such features can be found on FG LSHR fracture surface. The differences in fatigue crack growth behaviour between CG and FG LSHR alloys tested under the same conditions are mainly determined by oxidation effects and ease of deformation. It is well known that the grain boundary is a region with more vacancies and dislocations compared with the interior of the grain which can provide a short-circuit diffusion path for oxidizing species. Therefore an enhanced oxidation effect occurs in the FG LSHR alloy due to its greater grain boundary area, which makes a contribution to faster fatigue crack growth, even though the cracks could be temporarily arrested or deflected by grain boundaries and/or primary γ′ decorating the grain boundaries.

In addition to any oxidation effect, the grain size has two opposing effects on fatigue crack growth [37, 76, 130, 132-134]. On the one hand, the grain size determines the amount of grain boundaries acting as barriers to dislocation motion, and crack growth barriers as well, particularly for transgranular crack growth. Materials with larger grains give a lower degree of discontinuity due to less grain boundaries, which makes transgranular cracks able to propagate more continuously resulting in poorer crack growth resistance. On the other hand, a coarse grain size can promote planar slip (indicated by crystallographic facets and steps on fracture surface as shown in Figs. 6.12 (b) and (d)) which may enhance slip reversal and reduce intrinsic damage accumulation, leading to decreased rate of fatigue damage accumulation. Furthermore, larger grains have also been associated with a more tortuous crack path due to Stage I crystallographic propagation, giving increased crack tip deflection and hence shielding which will result in better crack growth resistance [129, 131]. Although an extrinsic crack closure effect is not possible to discern directly in this study, it is quite evident that the enhanced slip planarity (supported by evidence of crystallographic facets and

steps on fracture surface) in combination with improved oxidation resistance due to less grain boundary area for preferential attack by oxidizing species contribute to improved fatigue crack growth resistance in the CG LSHR.

The size of γ′ is also expected to influence fatigue crack growth. Depending on the size of γ′, the dislocation passes the γ′ precipitates by a shearing or looping mechanism, which promotes planar slip or wavy slip and influences the fatigue crack propagation behaviour. Additionally, the stress relaxation caused by a dislocation climb mechanism when dislocations encounter coarse tertiary γ′ has also been reported to impact the fatigue crack growth [40, 137]. According to NASA's research, the tertiary γ′ size correlates well with stress relaxation and fatigue crack growth rate during a dwell fatigue test for supersolvus heat treated LSHR alloy [40]. The coarser the tertiary γ′, the more marked stress relaxation, which in turn reduces the local stress ahead of the crack tip and thereby lowers the crack growth rate correspondingly. Although dislocation climb is also expected to occur when dislocations encounter secondary γ′, the correlation between secondary γ′ and stress relaxation/crack growth rate is quite weak [40], indicating that the tertiary γ′ rather than secondary γ′ is the key microstructural variable controlling stress relaxation and dwell fatigue crack growth. In this study, there is no expected significant difference in the size of tertiary γ′ since the employed aging heat treatments are identical, which indicates the tertiary γ′ distribution should be similar. It is therefore expected that this should make no contribution to the discrepancy of fatigue crack growth behaviour in the CG and FG LSHR alloys. Additionally, the primary γ′ in the FG LSHR superalloy is observed to be able to block or deflect the cracks as shown in Fig. 6.21 (a), but it seems that such crack arrest or deflection has an insignificant effect on the overall fatigue crack growth.

6.4.3 Fractography and fracture mechanism

It is established that the fatigue fracture modes consist of intergranular fracture (time-dependent), transgranular fracture (cycle-dependent) and a mixture of both. Transgranular fatigue includes Stage I/mode II fracture where the crack propagates along specific crystallographic planes and Stage II/mode I fracture where the applied stress is normal to the fracture surface [8, 9, 37, 129]. As shown in Figs. 6.12 - 6.19, the fracture surfaces are mainly intergranular for air tests either in CG or FG LSHR alloys, while predominantly transgranular for vacuum tests. As ΔK increases, the percentage of transgranular region on the fracture surfaces in LSHR alloy 650 ^{o}C air tests rises to some extent, which is not found in U720Li

and RR1000 when tested under the same conditions [129, 158]. Additionally, the crystallographic facets and steps on fracture surfaces at ΔK=40 MPa$\sqrt{m}$ and beyond are quite distinct in the CG LSHR 650 ^{o}C air tests, which is not found in the FG LSHR specimens nor in U720Li and RR1000 tested under the same conditions. In terms of the vacuum tests, the crystallographic facets can also be discerned on the fracture surfaces in CG LSHR alloy tested at 650 ^{o}C, but not in FG specimens. Through making a comparison in composition and microstructures among U720Li, RR1000 and LSHR alloy [2, 158], it can be easily seen that the grain size of CG LSHR is significantly larger than the other two disc alloys, and the stacking fault energy is lower due to the higher content of Co which can effectively decrease stacking fault energy in Ni-based superalloys, thus promoting stable dissociated partial dislocations. As illustrated previously in Section 6.4.2, the coarse grain size is also able to promote slip planarity, which usually causes the formation of crystallographic facets. The decrease in stacking fault energy makes dislocation motion more difficult due to the existence of stable partial dislocations separated by a low energy stacking fault, and thereby hinders dislocation cross-slip and confines dislocations to move along specific crystallographic planes, which also promotes formation of crystallographic facets. One other aspect is that the diffusion of oxidizing species is not as significant in the CG LSHR alloy as in U720Li and RR1000 due to less grain boundaries being available for short-circuit diffusion. It is generally accepted that the fracture mode in fatigue tests is dependent on the relative strength between grain boundary and grain. The diffusion of oxidizing species in materials can cause grain boundary oxidation, and further cause intergranular fracture. For those FG materials, such as U720Li and RR1000, the diffusion of oxidizing species is rather fast due to the high fraction of grain boundary, thus the fracture mode is almost completely intergranular without crystallographic facets and steps when tested in air. However, for CG LSHR alloy, the diffusion rate of oxidizing species at the crack tip is comparatively low, and may indeed lag behind the crack growth rate when ΔK is high, hence, these part of the materials ahead of the crack tip fracture under a quasi-vacuum/low oxidation condition, and take on a mixture of intergranular and transgranular characteristics or even become completely transgranular. Similarly, the crystallographic facets and steps on the fracture surface in the CG LSHR vacuum tests at 650 ^{o}C are also caused by the coarse grain microstructure and low stacking fault energy. It is interesting to note that the transition of intergranular fracture to transgranular fracture also occurs in FG LSHR alloy 650 ^{o}C air test, even though its grain size is only just slightly greater than that of U720Li and RR1000, but no clear crystallographic facets can be found on fracture surface. As the temperature increases, the

diffusion of oxidizing species becomes more significant and the mobility of dislocations is enhanced, therefore few transgranular regions with facets and steps can be found in the air tests at higher temperature or with a dwell period, and there are no crystallographic facets observed on the fracture surfaces in the vacuum tests at 725 ^{o}C.

Roughness of fracture surface is an important parameter which is believed to be related to the deformation behaviour and fracture modes, as well as roughness induced crack closure phenomena during fatigue tests [132, 133, 183, 184]. Normally, the roughness of fracture surface may expect to scale with grain size for intergranular fracture, whereas any roughness would be expected to be usually less than the grain size for transgranular fracture (if the effects of secondary cracks were not taken into consideration). In light of the close correlation between fracture modes and roughness of fracture surface, Antunes [184] suggested that the roughness of fracture surface can be used as an alternative or as a complement to standard fractography. As shown in this study, the roughness of fracture surface does correlate to fracture mode, with an additional effect of secondary cracks. Fig. 6.26 shows the roughness of the fracture surface in the CG LSHR air and vacuum tests. It is found that the roughness of the fracture surface in the vacuum tests (which correspond to predominantly transgranular fracture) is basically lower than that of air tests (which correspond to mainly intergranular fracture). The influence of fracture mode on roughness of fracture surface can also clearly be seen in the air test at 650 ^{o}C with a 1s dwell, in which the roughness of fracture surface decreases with increasing ΔK due to the increasing percentages of transgranular regions on the fracture surface. For those air tests at higher temperature and/or with a dwell time of 20s, the roughness is significantly higher due to the enhanced intergranular fracture along with the well-developed secondary cracks which can cause a cluster of grains to separate from main fracture surface and lead to a pit formation. Based on current results, a boundary between intergranular and transgranular fracture is proposed by a value of roughness of fracture surface for CG LSHR which is shown in Fig. 6.29. For fracture surface with a R_a lower than this value, the fracture surface is increasingly transgranular as R_a decreases. Conversely, for a fracture surface with a R_a higher than this value, the fracture surface is increasingly intergranular as R_a increases. As mentioned previously, the influence of secondary cracks on roughness of the fracture surface should be taken into consideration as well, and such an influence can be found in Fig. 6.26 (a) and Fig. 6.27 (b), where both the roughness of the fracture surface and the average length of secondary cracks show the same variation trend with ΔK. Therefore, it can be concluded that the roughness of fracture surface is to some

extent correlated to the degree of development of secondary cracks for completely intergranular fracture surfaces, whereas it depends on the relative proportion of intergranular and transgranular fracture surface for the mixed fracture situation. For the completely transgranular fracture surface, the roughness is determined by the amount of crystallographic facets and steps on the fracture surface which is caused by slip heterogeneity.

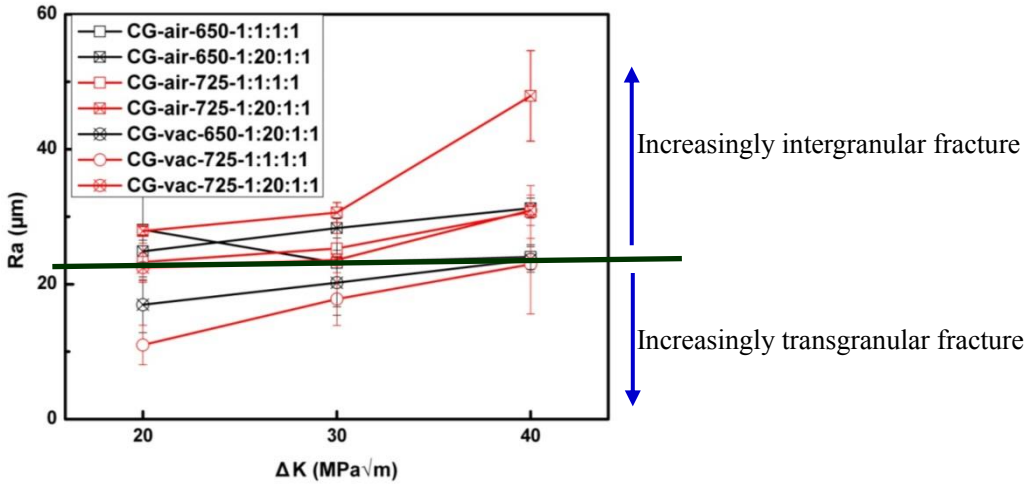

Fig. 6.29 Roughness of fracture surface with a defined boundary between intergranular and transgranular fracture.

Grain boundary cracking is a notable characteristic for air tests in both CG and FG LSHR alloys, whereas it is rarely seen in the vacuum tests. The quantitative statistics of secondary cracks in the CG LSHR air tests indicates that both amount and average length of secondary cracks increase with ΔK apart from the average length in the 650 ^{o}C air test with a dwell time of 1s. On the basis of this study, it seems that the amount and length of secondary cracks has a direct correlation with grain boundary oxidation. As shown in Fig. 6.27 (a), the amount of secondary cracks is significantly lower in the CG LSHR air test at 650 ^{o}C with a 1s dwell in which the fracture surfaces are mixed intergranular and transgranular along with predominantly transgranular fracture at higher ΔK due to less significant effect of grain boundary oxidation compared with the other three tests. Additionally, there is no secondary grain boundary cracking observed in the vacuum tests, which also indicates the role of grain boundary oxidation in formation and development of such secondary cracks. Therefore, the amount of grain boundary secondary cracks can be taken as an indicator of the degree of oxidation of grain boundary in some way. In addition, the amount of secondary cracks is thought to be a better indicator of the actual crack driving force in NASA's reported research since it is a reflection of the underlying visco-plastic redistribution of the crack tip stress and

strain fields occurring during the extended hold times. In such a situation the linear elastic fracture mechanics crack driving force parameter, K_{max}, may fail to describe the actual crack tip driving forces due to the stress relaxation which has occurred [40].

6.4.4 Comparison of FCG rate between disc alloys

To better understand fatigue crack growth behaviour in different disc alloys and the influences produced by different compositions at elevated temperatures, a comparison in fatigue crack growth rate between FG LSHR and N18 was made in light of their similar grain microstructures (e.g. similar grain size [2, 92, 181]). As shown in Fig. 6.30, both high temperature and oxidizing environment promote fatigue crack propagation in these two superalloys, and the influence of temperature on fatigue crack propagation is more significant in air compared with that in vacuum. It appears that N18 possesses a better FCG resistance under the investigated conditions. As shown in Fig. 6.30 (a), the fatigue crack growth rate in the LSHR alloy is higher than that observed in N18 tested at either 650 or 725 ^{o}C in air, even though there is no 20s dwell at the peak load in the 650 ^{o}C test for the FG LSHR alloy (a 20s dwell should enhance fatigue crack growth rate in air). The LSHR alloy also shows a higher fatigue crack growth rate at 650 ^{o}C in vacuum. Although the fatigue crack growth data of the LSHR alloy is obtained from a 1-1-1-1 loading waveform, it is expected that such data is comparable to N18 fatigue crack growth data as a 20s dwell at the peak load has no significant influence on fatigue crack growth of LSHR alloy in vacuum based on the data presented in Section 6.3.1. For the vacuum 725 ^{o}C test, the fatigue crack growth rate of N18 in Paris regimes is higher than that of FG LSHR, which may be caused by the creep damage during the dwell period in N18.

The typical fractography of the fractured N18 tested in air and vacuum are shown in Figs. 6.31 and 6.32 respectively. The fractography of the FG LSHR tested under corresponding conditions can be found in Figs. 6.17 - 6.19. It is clear that the air tests of these two superalloys produced mostly intergranular fracture surfaces with minor transgranular features in the 650 ^{o}C tests, and extensive secondary grain boundary cracking can be found at high ΔK level. As shown in Figs. 6.31 and 6.17, the transgranular features on the fracture surfaces in the 650 ^{o}C air tests for these two superalloys can be clearly discerned although mostly intergranular failure is occurring, and the proportion of transgranular features on the fracture surfaces increase with ΔK, particularly in the LSHR alloy. Additionally, the more significant oxidation effect at higher temperature can be deduced from the reduction of transgranular

features on the fracture surfaces. In the vacuum tests, it yielded predominantly transgranular fracture surfaces at 650 ^{o}C in both alloys and 725 ^{o}C in the LSHR alloy. But intergranular fracture surface features were observed in the N18 725 ^{o}C vacuum test, which are quite similar to the fracture surfaces of the N18 725 ^{o}C air test, indicating increasing grain boundary failure processes (presumably creep) had occurred.

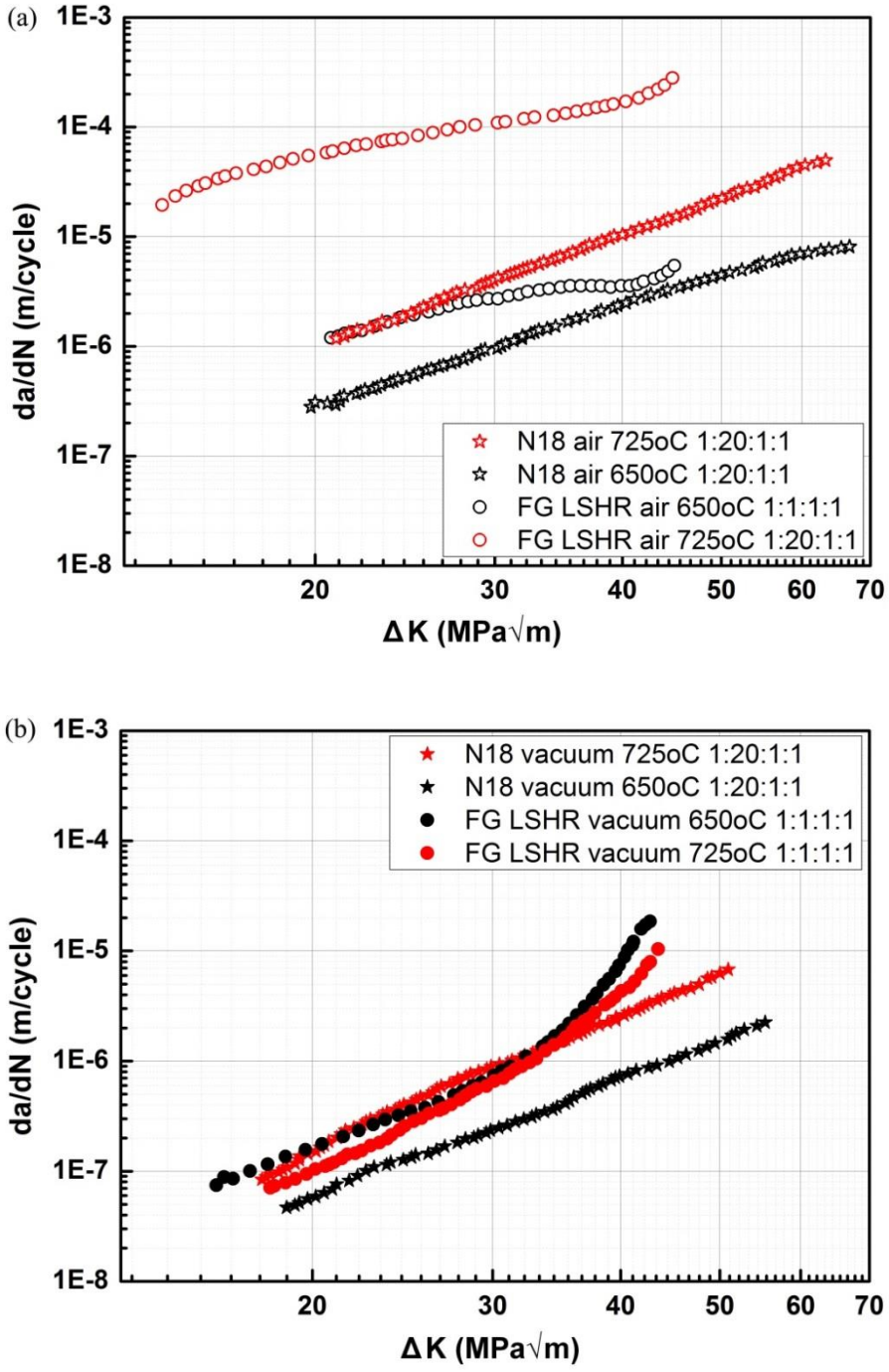

Fig. 6.30 Fatigue crack growth rate in N18 and FG LSHR alloy tested in air and vacuum at 650 and 725 ^{o}C [2, 92, 181].

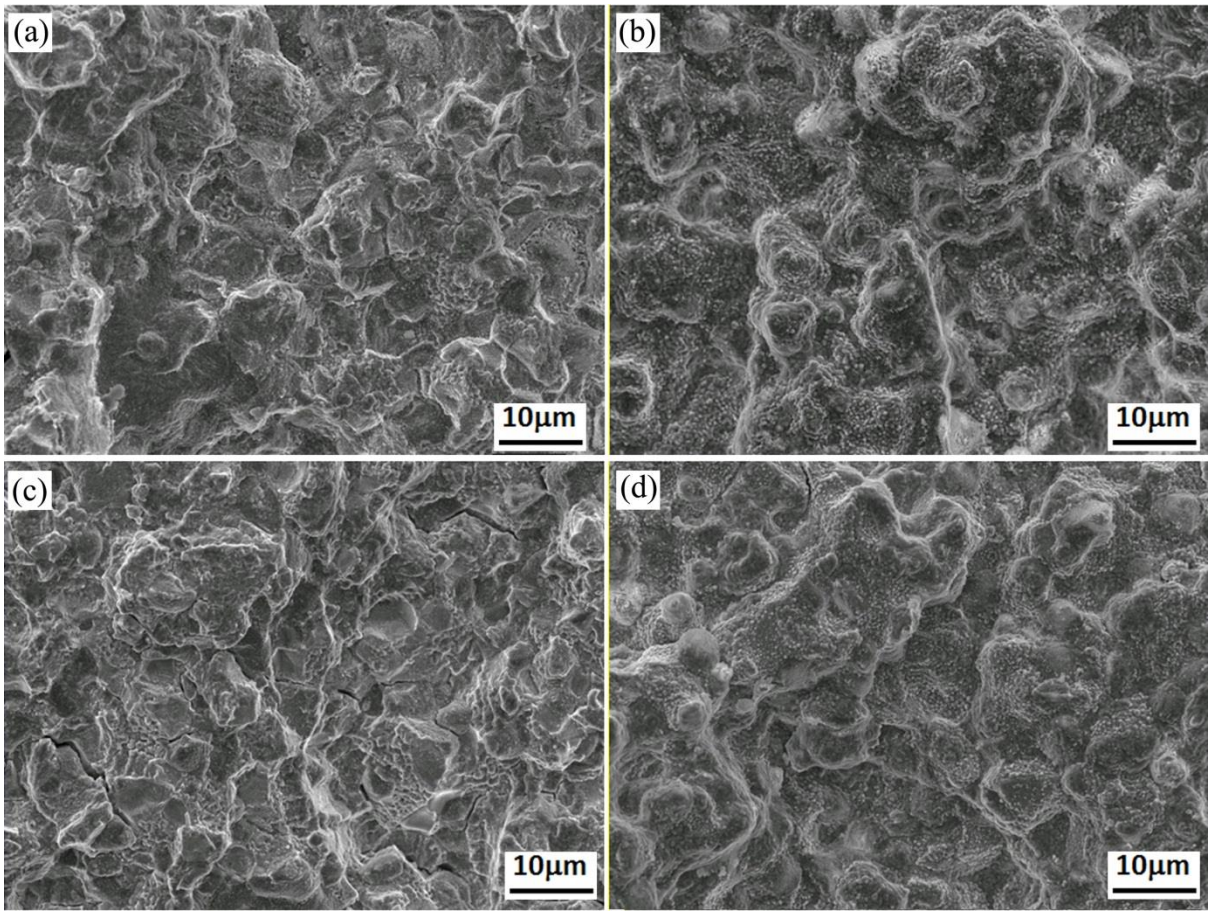

Fig. 6.31 Fractography of N18 tested at 650 and 725 ^{o}C in air with a loading waveform of 1-20-1-1: (a) 650 ^{o}C, ΔK=20 MPa√m, (b) 725 ^{o}C, ΔK=20 MPa√m, (c) 650 ^{o}C, ΔK=40 MPa√m and (d) 725 ^{o}C, ΔK=40 MPa√m [2, 92, 181].

6.4.5 Thermal activation energy for fatigue crack growth

For fatigue crack growth at elevated temperatures in an aggressive environment under cyclic stress, thermally activated processes such as creep and oxidation inevitably make a contribution to growth. Furthermore, the influence of temperature on the yield strength and ultimate tensile strength also plays a role in fatigue crack growth behaviour. In order to investigate the respective influence of thermal activation related processes on fatigue crack growth behaviour, an apparent activation energy analysis was carried out to analyse the data of fatigue crack growth [185]. By assuming that the rate of the thermally activated process is proportional to an Arrhenius term, and then the fatigue crack growth rate can be expressed by the following equation:

$$\frac{da}{dt} \propto k_{FCG} f(a) exp \frac{-Q}{R_g T} \tag{6.2}$$

where *da/dt* is the fatigue crack growth rate; k_{FCG} is a term that contains all non-temperature dependent factors except for the crack length, including loading cycle, the microstructure, monotonic mechanical and deformation properties, etc; *f(a)* is a function of crack length that is related to the compliance of specimen; Q is the activation energy; and R_g is the gas constant (8.31 J/mol•K).

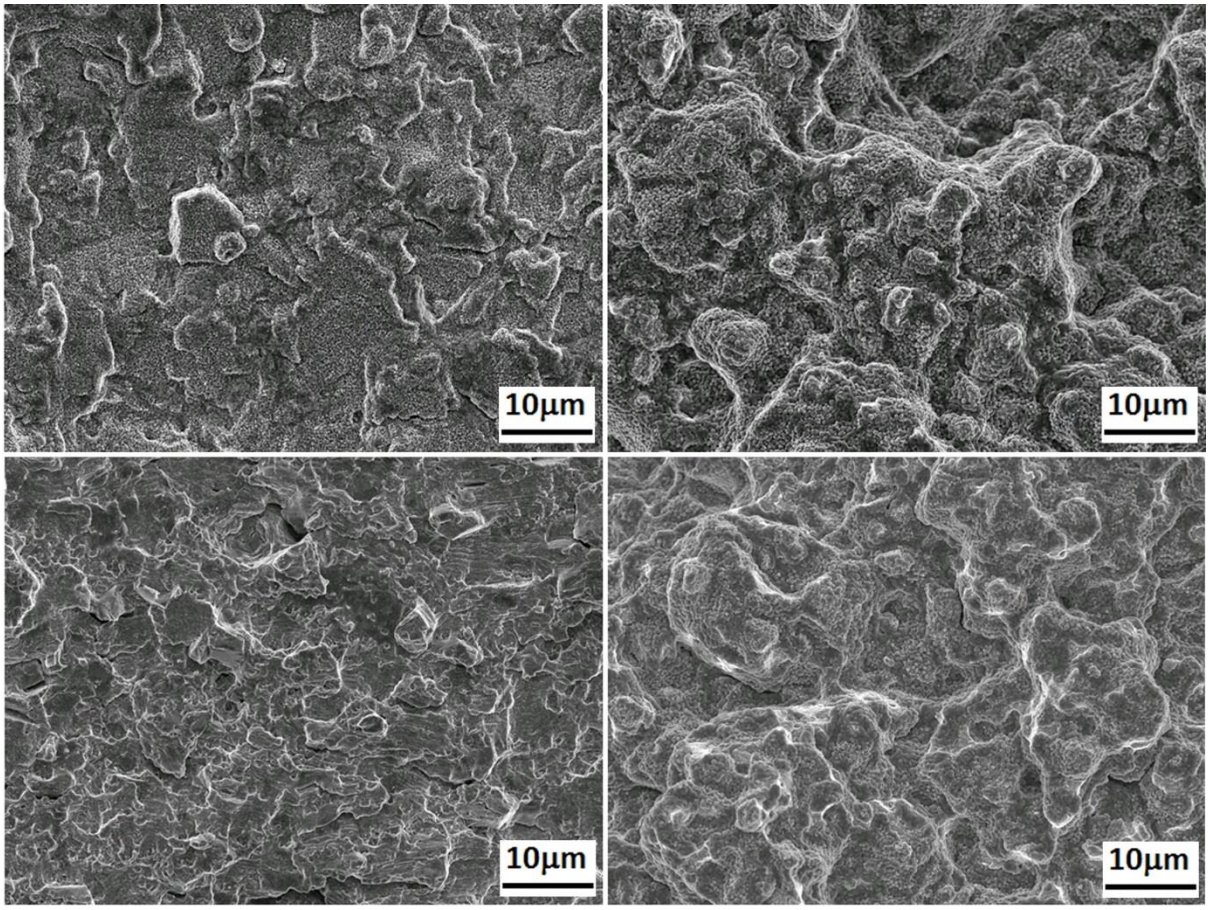

Fig. 6.32 Fractography of N18 tested at 650 and 725 ^{o}C in vacuum with a loading waveform of 1-20-1-1: (a) 650 ^{o}C, ΔK=20 MPa√m, (b) 725 ^{o}C, ΔK=20 MPa√m, (c) 650 ^{o}C, ΔK=40 MPa√m and (d) 725 ^{o}C, ΔK=40 MPa√m [2, 92, 181].

If the product k_{FCG}•$f(a)$ is kept constant and there is little variation in activation energy within a narrow temperature range, the apparent activation energy (E_{app}) of crack growth under fatigue-creep-oxidation conditions can be calculated when fatigue crack growth data from at least two temperatures obtained under otherwise identical testing conditions is known. The equation that derives the apparent activation energy for fatigue crack growth is as follows:

$$E_{app} = \frac{-R_g}{T_2^{-1} - T_1^{-1}} \ln\left(\frac{da}{dN}(T_2) / \frac{da}{dN}(T_1)\right) \quad (6.3)$$

where *da/dN* is the fatigue crack growth rate at T_1 or T_2 at a given ΔK level. In this study, T_1=923.15K, and T_2=998.15K. The known activation energies for basic damage processes such as grain boundary oxidation and creep are listed in Table 6.2 to allow a comparison. However, it should be mentioned that the accuracy of the obtained values of the apparent activation energies might be influenced by the limited amount of experimental data and the expected experimental scatter of the FCG rates. The apparent activation energy method presented here only offers a complementary approach to quantify the effect of temperature and should always be linked to detailed micro-mechanistic evaluations based on observations and analysis of failed specimens under the investigated conditions. Further details of the procedure of apparent activation energy analysis can be found in the literature [185].

Table 6.2 Activation energies for processes contributing to high temperature FCG [185]

Processes contributing to high temperature FCG	Activation energy (kJ/mol)
Grain boundary oxidation	~ 250
Dynamic embrittlement	~ 250
Grain boundary creep	~ 150
Change in static properties	~ 0-60
Grain boundary creep failure + non-thermally activated failure	~ 0-150

The apparent activation energies derived from the fatigue crack growth rates of LSHR alloy and N18 are presented in Fig. 6.33. By making a comparison between the calculated apparent activation energies and the known activation energies for basic damage processes such as grain boundary creep and oxidation, it is possible to shed light on the underlying mechanism of fatigue crack propagation under fatigue-creep-oxidation conditions. As shown in Fig. 6.33 (a), the apparent activation energy falls between 350-400 kJ/mol for the CG LSHR air tests with a dwell of 20s at the peak load, from which it can be inferred that grain boundary oxidation or dynamic embrittlement are the dominant thermally-activated contributors to the fatigue crack growth along with some minor contribution arising from creep damage. In terms of the FG LSHR air tests with a 1s dwell, the apparent activation energy levels of around 250 kJ/mol, indicates the oxidation of the grain boundary as well as fatigue damage is the underlying mechanism for crack growth. Unlike the previous two sets

of fatigue tests, the apparent activation energy for the CG LSHR air tests with a 1s dwell decreases from approximately 230 kJ/mol to 50 kJ/mol as the ΔK increases. Such variation in apparent activation energy indicates the contribution of oxidation to crack growth diminishes gradually with increasing ΔK, which is verified by the transition of fracture mode with ΔK observed in the CG LSHR air test at 650 ^{o}C with a 1s dwell. With regard to the apparent activation of CG LSHR vacuum tests with a 1s and 20s dwell, they are close to each other and basically lower than 150 kJ/mol, indicating the contribution from the changes in static properties. However, the apparent activation energy analysis performed on the FG LSHR alloy vacuum tests yield a negative value which is unexpected, and this might be related to the relatively insignificant influence of the temperature on fatigue crack growth rate in vacuum under 1-1-1-1-1 loading waveform (as shown in Fig. 6.7) and also reflect the possible experimental scatter in determining the fatigue crack growth rate.

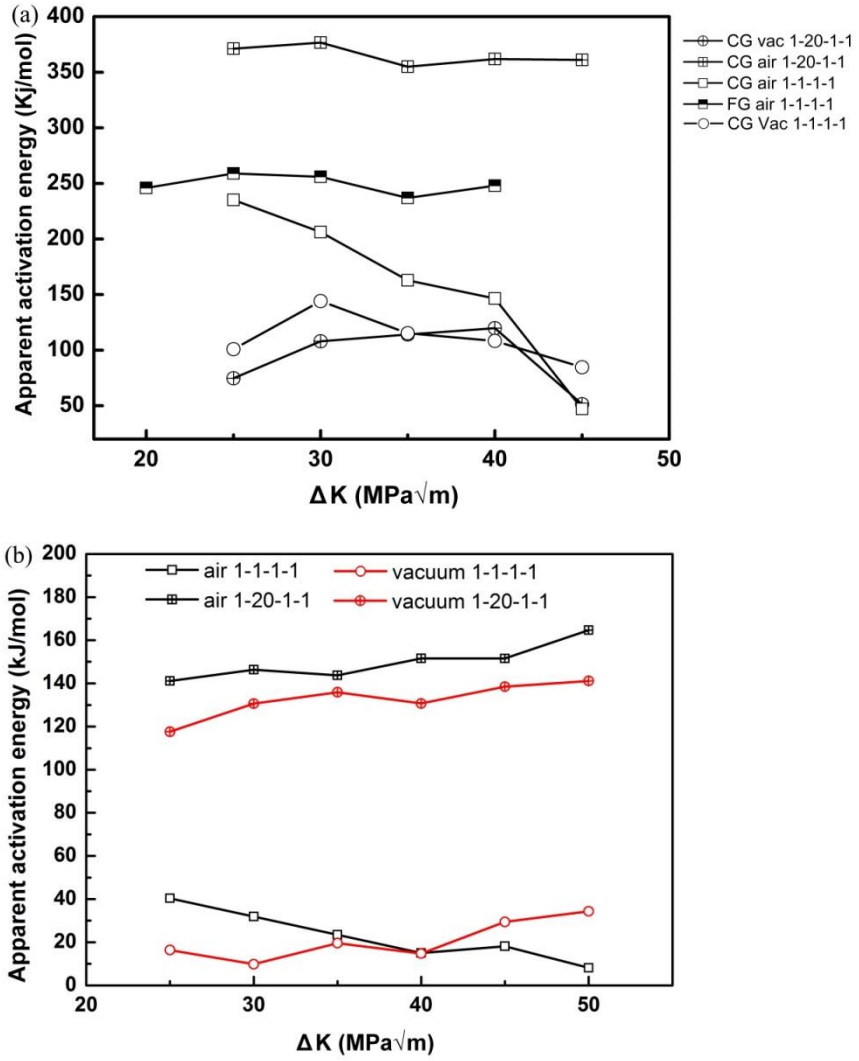

Fig. 6.33 Apparent activation energies for fatigue crack growth in (a) LSHR and (b) N18.

It seems that any additional oxidation brought about by increased dwell time and/or temperature makes little contribution to crack growth rates for N18 under the investigated conditions, this differs from LSHR alloy [181]. It appears that the GB creep process is promoting crack growth when a dwell of 20s at the peak load is introduced during the tests, indicated by the calculated activation energy which is quite close to the reported activation energy of GB creep processes. The increased intergranular features on the fracture surfaces when introducing a 20s dwell in vacuum may also indicate the activation of creep processes, and this change in fracture surface feature is most significant at 725 ^{o}C (where oxidation may be expected to be suppressed). For the tests conducted under a 1-1-1-1 loading waveform, the obtained apparent activation energy is much lower than that of GB creep processes, indicating limited creep is activated. In this case, the slight increase in crack growth rate with temperature may arise from the very slight decrease in yield strength with the increasing temperature (i.e. $\sigma_{0.2\%}$ of N18 is 1031 MPa at 650 ^{o}C, and 1016 MPa at 725 ^{o}C [2]).

6.5 Summary

On the basis of the above experimental results and discussion, the following conclusions can be made:

- The fatigue crack growth rate varies by three orders of magnitude depending on testing conditions and specimen-microstructure. The coarse grained microstructure is beneficial and improves the fatigue crack growth resistance of LSHR alloy due to enhanced crack deflection and slip reversal, whereas the higher temperature, oxidizing environment and dwell time exert a synergistic oxidation effect on LSHR alloy. This causes grain boundary oxidation and leads to significant degradation of fatigue crack growth resistance. The creep process and stress relaxation also make contributions to fatigue crack growth, although their effects are quite limited.
- The fracture surfaces are predominantly transgranular (associated with slower FCG rate) for vacuum tests, whereas they are mainly intergranular (associated with higher FCG rate) for air tests especially at high temperature with a long dwell at peak load because of the enhanced oxidation effects. As ΔK increases, the intergranular features on the fracture surface of specimens tested in air become less significant due to the competition between oxidizing species diffusion rate ahead of crack tip and crack growth rate. Crystallographic facets and steps can be found on the fracture surface at high ΔK level in the CG LSHR tested at 650 ^{o}C because of more significant slip

planarity.

- The amount and average length of grain boundary secondary cracks are basically proportional to ΔK, and closely correlate to grain boundary oxidation. It is proposed that the amount of secondary grain boundary cracks can be taken as an indicator of degree of grain boundary oxidation.
- Roughness of fracture surface is closely related to fracture modes and secondary cracks. For completely intergranular fracture, the roughness of the fracture surface is dependent on the degree of development of secondary cracks; for completely transgranular fracture, the roughness depends on the amount of crystallographic facet and steps on the fracture surface; and for mixed intergranular and transgranular fracture, the roughness is determined by the relative proportion of the transgranular and intergranular regions. The roughness of the fracture surface can be used as an alternative or as a complement to standard fractography.
- The apparent activation energy analysis provides a further insight into the underlying mechanism of FCG in LSHR alloy under fatigue-creep-oxidation conditions, and confirms that oxidation plays an important role in crack propagation when the fatigue tests are conducted in air.
- Compositions have influences on the overall fatigue-creep-oxidation resistance of disc alloys. LSHR alloy is more creep-resistant but less oxidation-resistant in comparison to disc alloy N18.

Chapter 7 Conclusions

Two batches of LSHR alloys processed by separate, different forging processing routes have been used in this PhD programme. It should be highlighted that the majority of experimental tests have been conducted on batch 1 CG and FG LSHR alloys. The microstructures of the LSHR alloys are closely related to the hot working (e.g. extrusion and forging) and solution/aging heat treatments. The LSHR alloy variants possess a relatively high fraction of twin boundaries compared with other turbine disc alloys such as IN718 and U720Li, especially in the FG variant. This is believed to be due to the relatively high content of Co which is expected to reduce the stacking fault energy of this alloy system.

Intrinsic crack initiation and propagation behaviour have been investigated at room temperature where the influences of creep and oxidation damage are absent. Generally, FG LSHR alloy possesses a higher fatigue life due to its better fatigue crack initiation resistance and equivalent resistance to Stage I crack propagation compared with the CG LSHR, even though its resistance to Stage II crack propagation is inferior. Frequent crack coalescence occurs in the CG LSHR due to the existence of a large number of cracks, which significantly accelerates the fatigue fracture process and results in a shorter fatigue lifetime. Primary γ' precipitates improve the resistance to crack propagation in the FG LSHR to some extent as the slip bands usually terminate at grain boundaries or interfaces of γ matrix/primary γ'.

At room temperature, cracks mainly initiate from TBs and occasionally initiate from slip bands in relatively large grains with favourable orientation in relation to the tensile stress axis. TB crack initiation is closely related to the activation of the primary slip systems parallel to TB at matrix and twin. These active slip systems are associated with high resolved shear stress indicated by relatively high SF. Cracks propagate along slip bands/TBs during Stage I giving rise to crystallographic facets on fracture surfaces. Stage II crack propagation sets in after a crack propagates along crystallographic facets by a distance of ~10 times the average grain size. Crack propagation during Stage I is usually associated with slip band cracking which correlates to slip systems with high SF. Duplex slip band cracking along slip systems with similar SF occurs to facilitate crack deflection or to allow a crack to pass through the grain boundaries.

At elevated temperatures (i.e. 650 and 725 ^{o}C), fatigue crack initiation and early short

crack propagation behaviour are closely related to coupled deformation-oxidation damage. Fatigue lives of the LSHR alloy are shortened by high temperature and high oxygen partial pressure which are associated with more intergranular fracture mechanisms. The FG LSHR possesses a higher fatigue life in most testing conditions although it is expected to be more severely GB oxidized, this is attributed to different strain levels expected in the notch root.

Plentiful crack initiation mainly occurs at GBs with bulged Ni/Co-rich oxides and Cr/Ti/Al oxide intrusion at elevated temperatures in the LSHR alloy due to oxide cracking. Cracks subsequently propagate along oxidised GBs at the surface of the investigated specimens and exhibit significant crack coalescence at the final stages of fatigue life. In the depth direction, cracks predominantly propagate along grain boundaries in the FG LSHR at the investigated temperatures and in the CG LSHR at 725 ^{o}C, whereas predominant transgranular propagation after intergranular crack initiation appears in the CG LSHR at 650 ^{o}C either in vacuum or air.

The oxides corresponding to crack initiation and early propagation consist of bulged surface Ni/Co oxides and Cr/Ti/Al oxide intrusion along grain boundaries and γ/γ' interfaces. The bulged GB Ni/Co-rich oxides and the Cr/Ti/Al oxide intrusions along GBs have a width of ~0.5 μm, and can penetrate into the grain boundary between depths of <1 μm to tens of a micron. The Cr/Ti/Al oxide intrusion enriches in Cr close to the surface oxide scale, enriches in Ti in the middle and enriches in Al at the oxide front which is far away from the surface oxide scale. Formation of bulged Ni/Co oxides and Cr/Ti/Al oxide intrusion are accompanied by dissolution of γ matrix and γ' precipitates. An enrichment of Ni and Co and a depletion of Al and Ti exist ahead of the oxide front due to the Cr/Ti/Al oxide intrusion formation. In addition, Co and Cr are enriched at the oxide intrusion/alloy matrix interface. Apart from the significant oxidation at grain boundaries and γ/γ' interfaces, uniform surface oxide scale along with internal oxide particles has been observed within grains and primary γ'.

Formation of bulged GB Ni/Co-rich oxides and Cr/Ti/Al oxide intrusion is closely related to the strain localisation which is associated with grain orientation and applied stress. The boundaries between high/low SF grains are preferential sites for bulged Ni/Co-rich oxides and Cr/Ti/Al oxide intrusion formation. Strain-assisted formation of internal GB Cr/Ti/Al oxide intrusion can facilitate formation of GB bulged Ni/Co-rich oxides by providing abundant Ni and Co.

Due to the significant crack coalescence occurring at elevated temperatures, quantitative

evaluation of crack evolution in terms of individual short crack propagation rates is invalid and offers little insight. Standard long crack growth procedures have instead been adopted to evaluate crack propagation behaviour of LSHR alloy in air and vacuum, in an attempt to reveal the interaction between damage arising from fatigue, creep and oxidation. The obtained fatigue crack growth rate varies by three orders of magnitude depending on testing conditions and specimen-microstructure. The coarse grained microstructure is beneficial and improves the fatigue crack growth resistance of LSHR alloy due to enhanced crack deflection and slip reversal, whereas a higher temperature, oxidizing environment and longer dwell time exert a synergistic oxidation effect in LSHR alloy. This causes grain boundary oxidation and leads to significant degradation of fatigue crack growth resistance. Creep processes and stress relaxation also make contributions to fatigue crack growth, but their effects are quite limited.

The fracture surfaces are predominantly transgranular (associated with slower FCG rate) for vacuum tests. By contrast, the fracture surfaces are mainly intergranular (associated with higher FCG rate) for air tests especially at high temperature with a long dwell at peak load because of the enhanced oxidation effects. As ΔK increases, the intergranular features on the fracture surface of specimens tested in air become less significant due to the competition between oxidizing species' diffusion rates ahead of crack tip and crack growth rate. Crystallographic facets and steps can be found on the fracture surface at high ΔK level in CG LSHR tested at 650 ^{o}C because of the more significant slip planarity exhibited by this microstructure. At lower test temperatures and dwells, cycle-dependent crack growth mechanisms can outstrip any oxidation processes at the crack tip at high ΔK and the fracture mode reverts to transgranular.

Quantitative statistics of secondary cracks on the fracture surfaces and the fracture surface roughness have been conducted to correlate these two features with the effect of oxidation. The amount and average length of grain boundary secondary cracks are proportional to ΔK, and closely correlate to grain boundary oxidation. It is proposed that the amount of secondary grain boundary cracks can be taken as an indicator of degree of grain boundary oxidation. Roughness of fracture surface is closely related to fracture modes and secondary cracks. For completely intergranular fracture, the roughness of the fracture surface is dependent on the degree of development of secondary cracks; for completely transgranular fracture, the roughness depends on the amount of crystallographic facets and steps on the fracture surface; and for mixed intergranular and transgranular fracture, the roughness is determined by the

relative proportion of the transgranular and intergranular regions. The roughness of the fracture surface can be used as an alternative, or as a complement, to standard fractography.

In order to distinguish the influences of oxidation and creep damage on crack propagation, an apparent activation energy analysis has been carried out. It is shown that the apparent activation energy analysis can provide a further insight into the underlying mechanism of FCG in LSHR alloy under fatigue-creep-oxidation conditions, and confirms that oxidation plays an important role in crack propagation when the fatigue tests are conducted in air.

Chapter 8 Future work

8.1 Introduction

As shown in Chapters 5 and 6, oxidation along grain boundaries and γ/γ′ interfaces has significant influence on crack initiation and propagation at elevated temperatures. Formation of bulged Ni/Co oxides in combination with Cr/Ti/Al oxide intrusion in the LSHR alloy preferentially occurs at boundaries between high/low SF grains that are associated with strain localisation, which results in subsequent crack initiation. The crack growth rate is increased by two or three orders of magnitude associated with an intergranular fracture mechanism due to grain boundary oxidation. However, in both the short crack tests and the long crack growth tests, a transition from intergranular fracture mode to transgranular fracture mode was observed at 650 ^{o}C in the CG LSHR when the crack growth rate is relatively high, indicating the mechanical damage ahead of the crack tip can outstrip the oxidation damage. The final failure mechanism under the dwell-fatigue conditions is as a consequence of the competing effects between mechanical and oxidation damage. Hence, further study of strain accumulation at an individual grain level and the oxidation at grain boundaries and γ/γ′ interfaces as well as directly ahead of the crack tip are necessary and helpful to understand the fatigue failure process and underlying mechanisms under dwell-fatigue conditions.

8.2 Characterisation of local plastic strain

As the GB oxidation is related to the strain localisation which is associated with the grain misorientation as shown in Chapter 5, then characterisation of the local plastic strain is helpful to understand the process of oxidation induced crack initiation in the LSHR alloy at elevated temperatures. Therefore, high resolution EBSD will be used to measure the strain distribution (indicated by geometrically necessary dislocation density [186-188]) around the grain boundary oxides and cracks in the LSHR alloy after short crack testing. Furthermore, crystal plasticity model approaches [120, 142] may also be employed to investigate the strain evolution in the LSHR alloy during short fatigue tests.

8.3 Kinetics of grain boundary oxidation under strain/stress

In terms of crack initiation, the bulged Ni/Co oxides and Cr/Ti/Al oxide intrusion are closely related to local strain accumulation, and the formation of Cr/Ti/Al oxide intrusion

promotes the formation of Ni/Co oxides to some extent as it produces abundant Ni and Co as shown in Fig. 5.14. The abundant Ni and Co subsequently diffuses to the surface and forms Ni/Co oxides, resulting in increasing bulged height. Therefore, the bulged height of GB Ni/Co oxides is associated with the Cr/Ti/Al oxide intrusion depth, and it can be taken as an indicator of the degree of grain boundary oxidation. As shown in Fig. 5.12, the bulged height of the Ni/Co oxides can be up to hundreds of a nanometre. Also, the width of the bulged oxides varies between different tests for CG and FG LSHR variants. By characterisation of the evolution of this bulged height and possibly the width of the bulged oxides with time under a sustained loading, it may shed a light on the grain boundary oxidation kinetics under strain (stress) for the LSHR alloy at elevated temperatures. A subsequent high resolution EBSD analysis will be conducted when the sustained load tests are terminated to investigate the effect of grain orientation and local strain accumulation on the oxidation process.

However, it should be pointed out that the aforementioned method may have some limitations, i.e. the bulged height and width of oxide may saturate and may not change any more after certain time, a faster oxidation may happen at a specimen edge due to two-dimensional diffusion, and the residual strain caused by mechanical machining may exert additional influences on the oxidation process.

8.4 Oxidation ahead of the crack tip

The crack growth rate is significantly enhanced by oxidation effects ahead of the crack tip, which is associated with the intergranular fracture mode. As the crack growth rate increases, the time for oxidation to occur within a constant crack length increment becomes shorter, resulting in a diminishing oxidation effect and a transition from intergranular fracture to transgranular fracture. It is hence interesting to know how the interaction between oxidation and mechanical damage occurs ahead of the crack tip. To better understand the oxidation assisted fatigue crack growth at elevated temperatures, a long fatigue crack growth test in oxygen tracing isotope $^{18}O_2$ at certain ΔK levels (i.e. 20 MPa$\sqrt{m}$, 30 MPa$\sqrt{m}$ and 40 MPa$\sqrt{m}$) will be carried out under a trapezoidal waveform of 1-20-1-1, and 1-300-1-1 with a load ratio of 0.1, which includes pre-cracking, crack growth in normal air and crack growth in $^{18}O_2$-enriched environment. The tested specimen with a crack tip prepared in $^{18}O_2$-enriched environment will be sectioned by electro-discharge machining, and then FIB-SIMS will be used to measure the tracer $^{18}O^{2-}$ penetration in and around the crack/crack tip. By conducting such a characterisation, it is believed that it will be possible to reveal the diffusion path of

oxygen inside the material.

TEM/SEM analyses will be carried out to reveal the extent of oxidation and deformation-related damage as well as microstructural changes beyond the crack tip. This includes EDX analyses of alloying element distributions ahead of the crack tip caused by internal oxidation processes. In addition, TEM foils will be extracted at the crack tip using FIB to investigate the correlation between formation of deformation structure (e.g. dislocations and stacking faults) and oxidation. These results will be used to quantify the oxygen-induced damage at selected ΔK levels to feed the coupled deformation-diffusion damage analyses near the crack tip. Moreover, grain misorientation will be determined at the crack tip in the fatigue tested specimens by EBSD to elucidate the effects of grain orientation on the diffusion of oxygen and crack propagation.

Appendix I Stress intensity factor calculation

This appendix provides details of the calculation of the stress intensity factor range ΔK for a semi-elliptic crack.

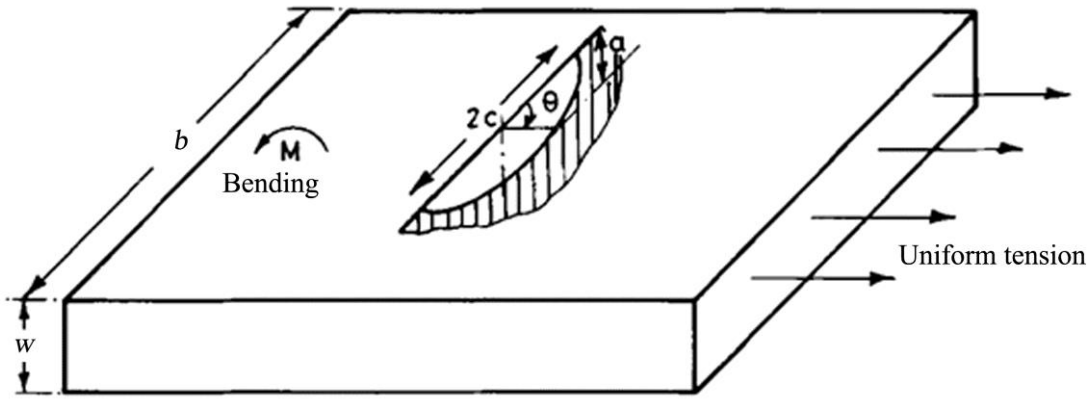

Fig. A1.1 Semi-elliptic crack in a plate [161]

As presented in the review by Scott and Thorpe [161], for a semi-elliptic crack in a plate subjected to bending conditions as shown in Fig. A1.1, the ΔK can be calculated using the following equation:

$$\Delta K = B_w \cdot M_{f(\frac{\pi}{2})} \left[1 - 1.36\left(\frac{a}{w}\right)\left(\frac{a}{c}\right)^{0.1}\right] \frac{1}{E(K)} \Delta\sigma\sqrt{\pi a} \tag{A1}$$

where $\Delta\sigma$ is stress range applied to notch root. The $\Delta\sigma$ used for ΔK calculation was obtained from a finite element simulation for the investigated specimens. The stress distributions at the maximum and minimum load for the CG and FG U-notch specimens as well as CG PBB specimen are shown in Figs. A1.2 - A1.4, respectively. The values of $\Delta\sigma$ are listed in Table A1.1. a is crack depth at the notch root, c is half crack length at notch root surface, w is sample thickness. In this study, all K calculations assume a crack aspect ratio (a/c) of 0.918 based on the observation of serial metallographic sectioning shown in Fig. 4.8. B_w is a correction factor for the finite dimension of the investigated specimens, and it is dependent on crack and specimen dimensions [189]. B_w can be expressed by the following equation:

$$B_w = 1 + \frac{F(\frac{a}{c})G(\frac{c}{b})H(\frac{a}{w})}{(0.2745)^2} \tag{A2}$$

where

$$F\left(\frac{a}{c}\right) = 0.38 - 0.141\left(\frac{a}{c}\right) - 0.366\left(\frac{a}{c}\right)^2 + 0.569\left(\frac{a}{c}\right)^3 - 0.248(\frac{a}{c})^4 \quad \text{(A3)}$$

$$G\left(\frac{c}{b}\right) = -0.0239 + 1.434\left(\frac{c}{b}\right) - 2.984\left(\frac{c}{b}\right)^2 + 7.822(\frac{c}{b})^3 \quad \text{(A4)}$$

$$H\left(\frac{a}{w}\right) = -0.0113 + 0.323\left(\frac{a}{w}\right) + 0.749\left(\frac{a}{w}\right)^2 - 0.535(\frac{a}{w})^3 \quad \text{(A6)}$$

where *b* is the width of samples.

$M_{f(\frac{\pi}{2})}$ is front face correction factor for crack shape and *E(K)* is the elliptic integral of the second kind.

$$M_{f(\frac{\pi}{2})} = 1.13 - 0.07\left(\frac{a}{c}\right)^{0.5} \quad \text{(A7)}$$

$$E(K) = [1 + 1.47\left(\frac{a}{c}\right)^{1.64}]^{0.5} \quad \text{(A8)}$$

Table A1.1 $\Delta\sigma$ for the investigated specimens based on finite element simulation

Specimen	CG U-notch	FG U-notch	CG PBB
$\Delta\sigma$ (MPa)	1370	1365	1160

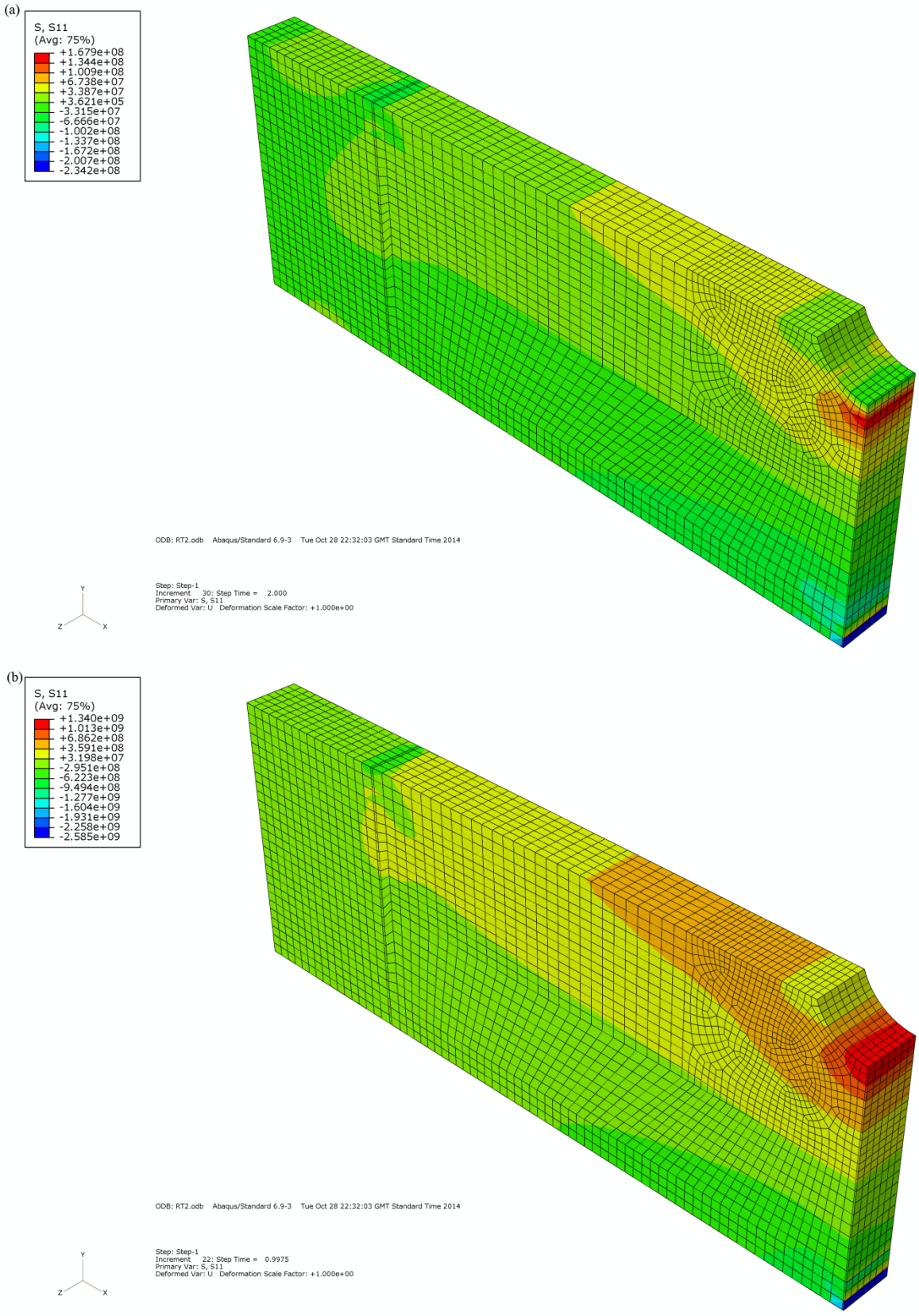

Fig. A1.2 Stress distribution in the CG LSHR U-notch specimen at (a) minimum and (b) maximum load at room temperature.

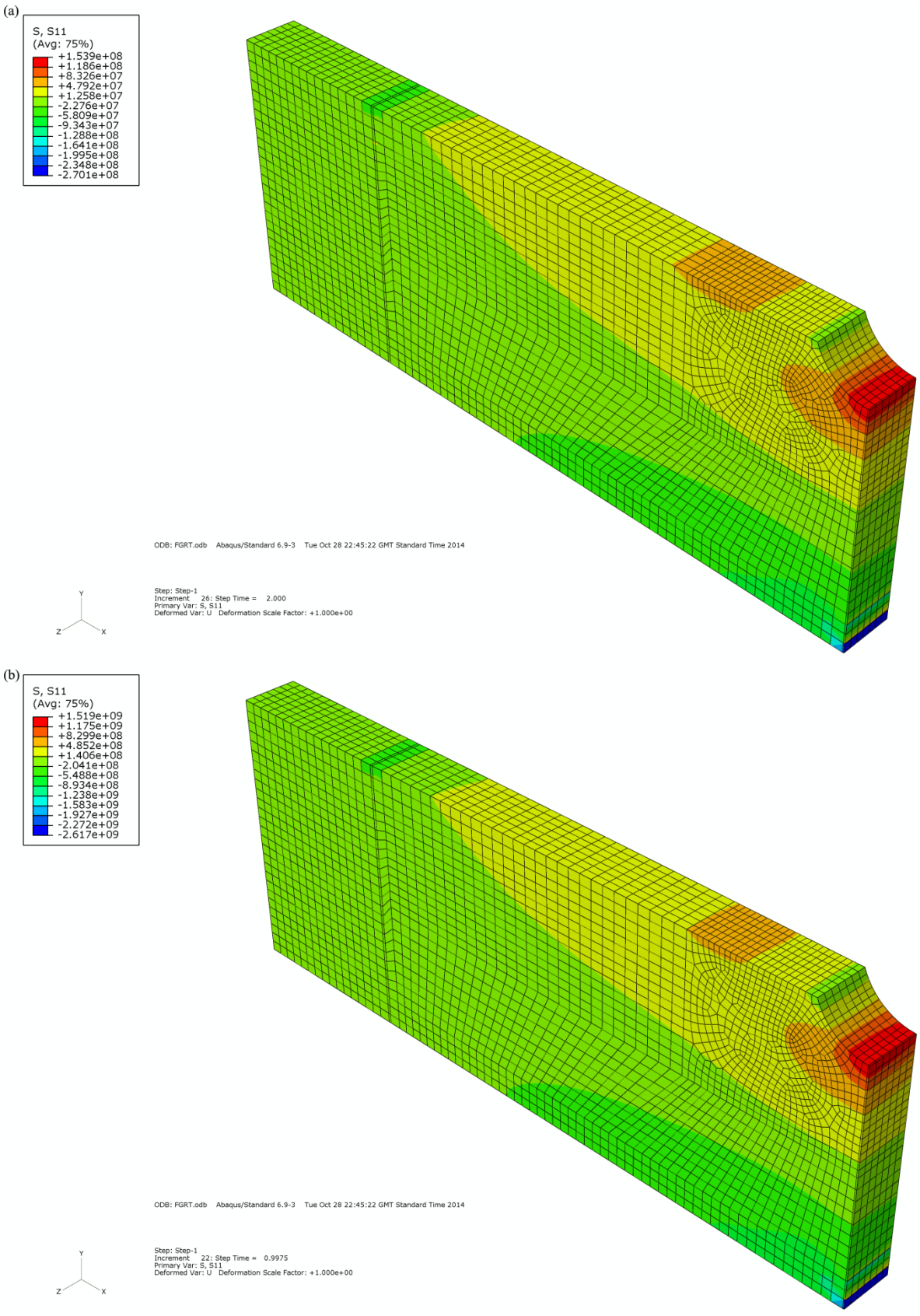

Fig. A1.3 Stress distribution in the FG LSHR U-notch specimen at (a) minimum and (b) maximum load at room temperature.

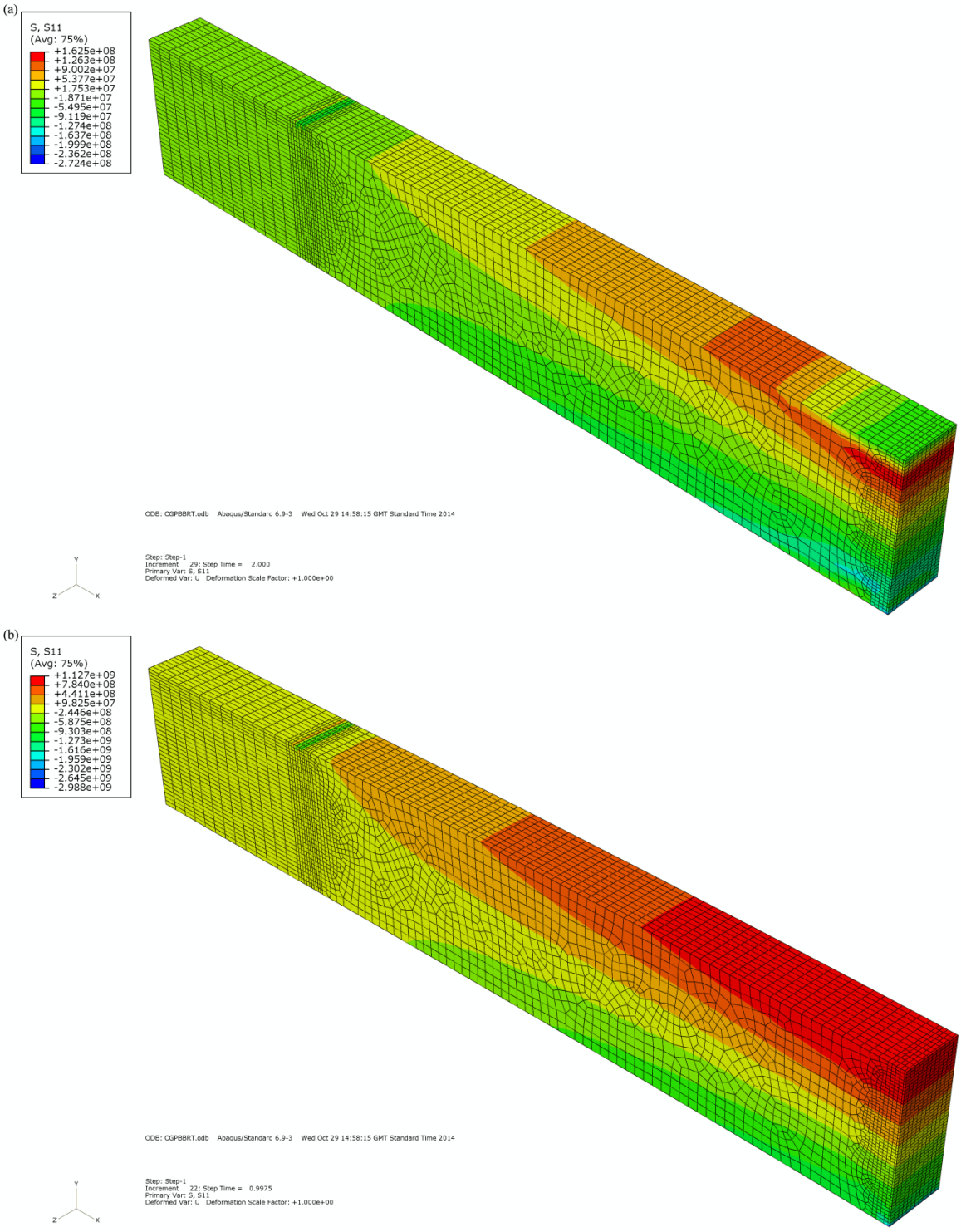

Fig. A1.4 Stress distribution in the CG LSHR PBB specimen at (a) minimum and (b) maximum load at room temperature.

Appendix II Crack evolution at elevated temperatures

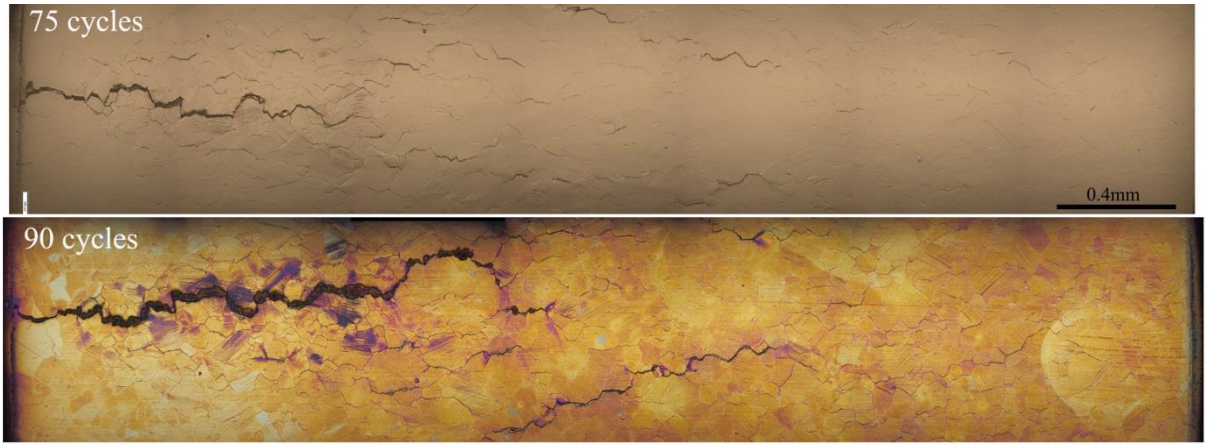

Fig. A2. 1 Crack evolution in the CG LSHR tested at 725 ^{o}C in air.

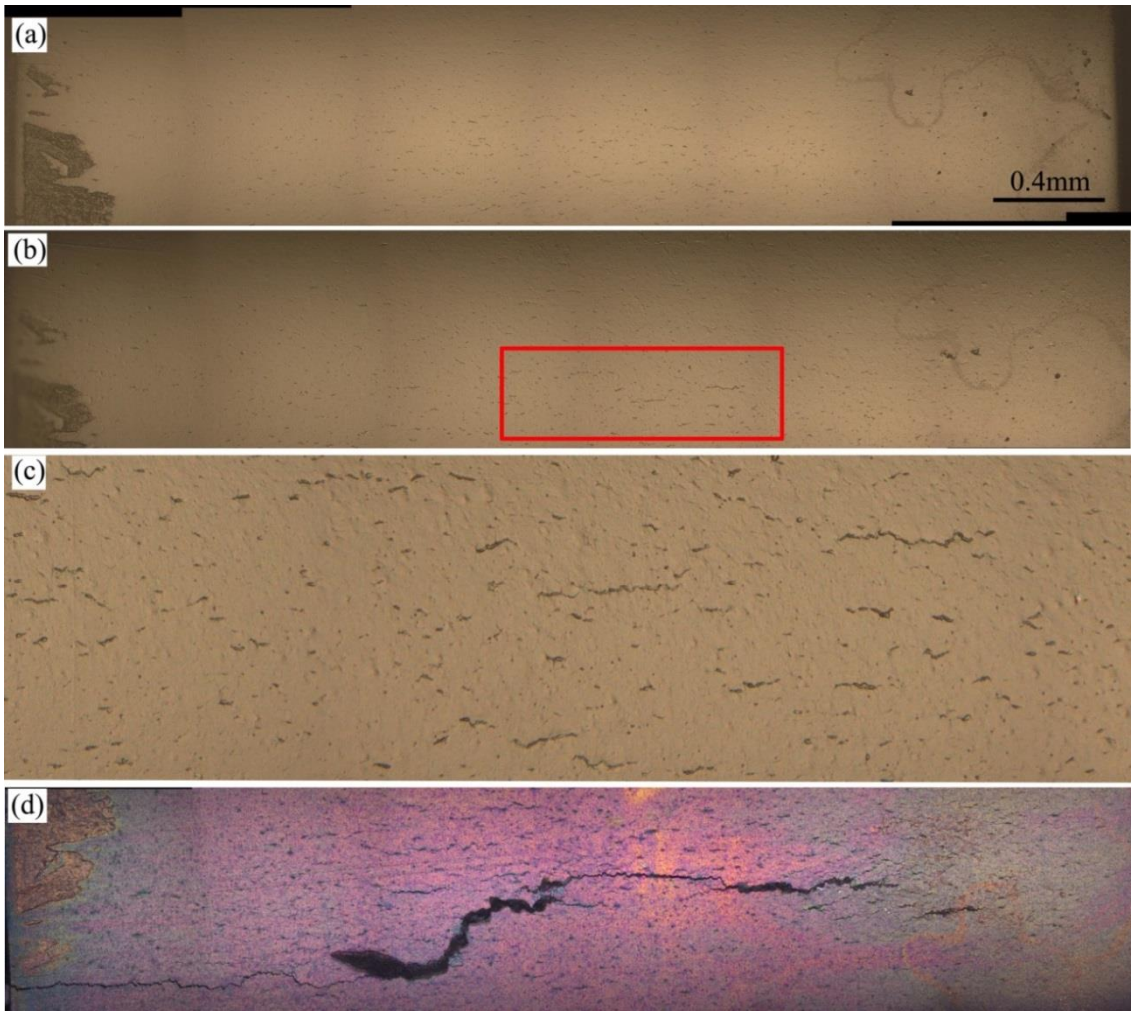

Fig. A2. 2 Crack evolution in the FG LSHR tested at 650 ^{o}C in air: (a) 5000 cycles (b) 6500 cycles (c) close-up of the region shown in (b), and (d) 7250 cycles.

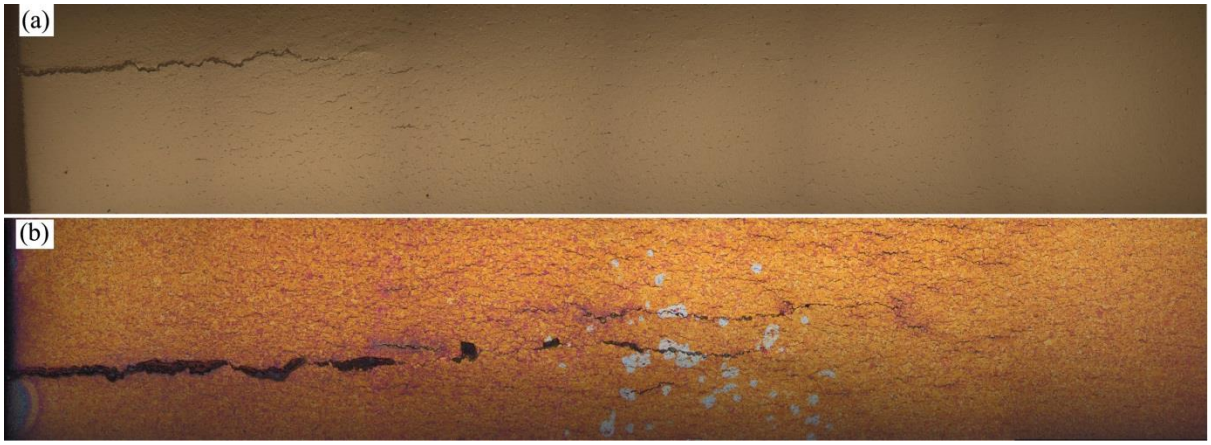

Fig. A2.3 Crack evolution in the FG LSHR tested at 725 ^{o}C in air: (a) 350 cycles and (b) 400 cycles.

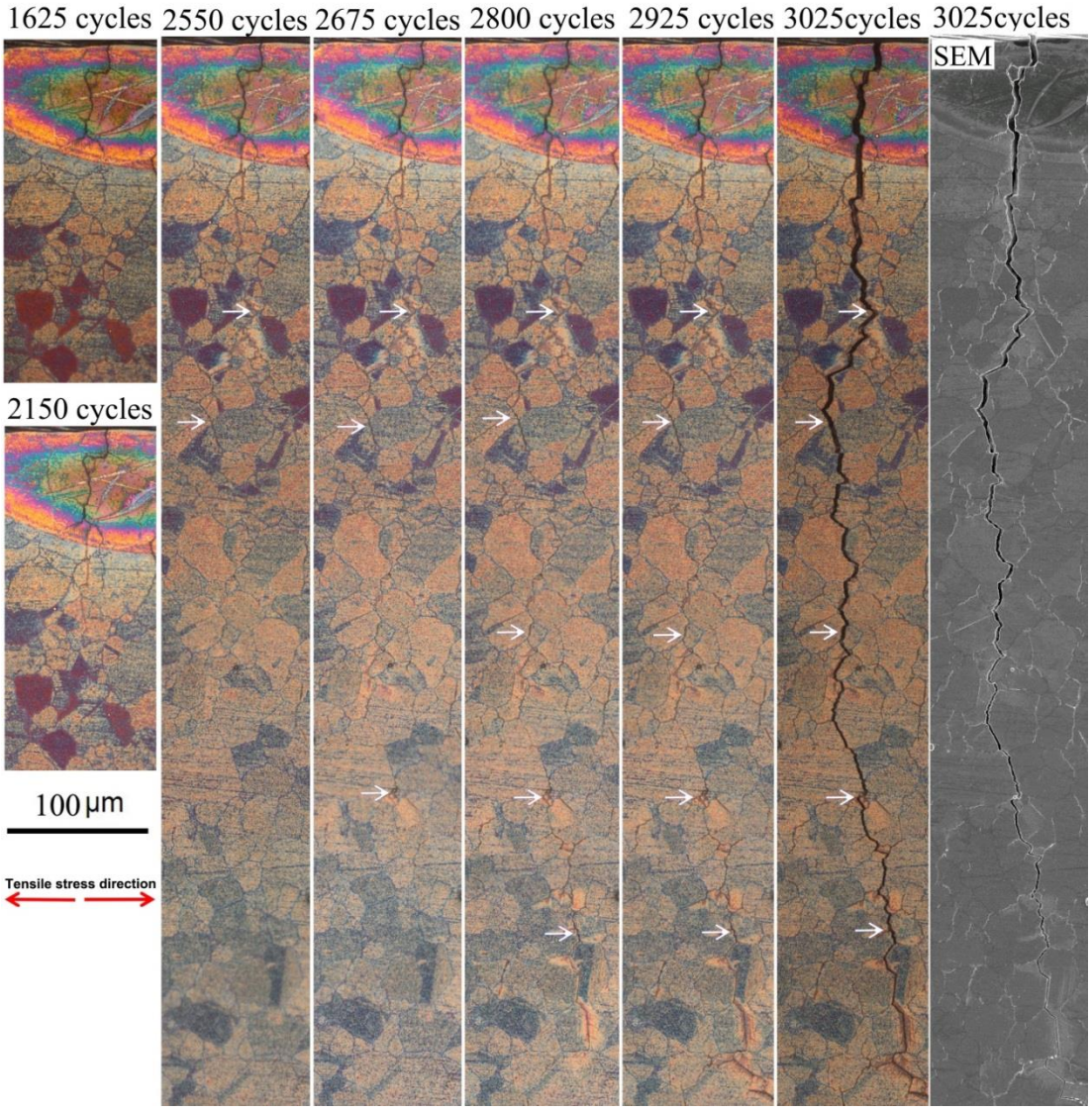

Fig. A2.4 Crack evolution in the batch 2 LSHR tested at 650 ^{o}C in air.

References

[1] R. C. Reed, The Superalloys: Fundamentals and Applications, Cambridge University Press, (2006).
[2] S. Everitt, Developments in advanced high temperature disc and blade materials for aero-engine gas turbine applications, PhD Dissertation, University of Southampton, (2012).
[3] D. G. Leo Prakash, M. J. Walsh, D. Maclachlan, A. M. Korsunsky, Crack growth micro-mechanisms in the IN718 alloy under the combined influence of fatigue, creep and oxidation, International Journal of Fatigue, 31 (2009) 1966-1977.
[4] A. Pineau, S. D. Antolovich, High temperature fatigue of nickel-base superalloys: A review with special emphasis on deformation modes and oxidation, Engineering Failure Analysis, 16 (2009) 2668-2697.
[5] T. P. Gabb, P. T. Kantzos, J. Telesman, J. Gayda, C. K. Sudbrack, B. Palsa, Fatigue resistance of the grain size transition zone in a dual microstructure superalloy disk, International Journal of Fatigue, 33 (2011) 414-426.
[6] J. Gayda, T. P. Gabb, P. T. Kantzos, The effect of dual microstructure heat treatment on an advanced Nickel-based disk alloy, in: K. A. Green, H. Harada, T. E. Howson, T. M. Pollock, R. C. Reed, J. J. Schirra, et al., editors, TMS superalloy 2004, Warrendale (PA): The Minerals, Metals & Materials Society (2004), 323-340.
[7] T. Connolley, P. A. S. Reed, M. J. Starink, Short crack initiation and growth at 600°C in notched specimens of Inconel718, Materials Science and Engineering: A, 340 (2003) 139-154.
[8] H. T. Pang, P. A. S. Reed, Fatigue crack initiation and short crack growth in nickel-base turbine disc alloys-the effects of microstructure and operating parameters, International Journal of Fatigue, 25 (2003) 1089-1099.
[9] H. T. Pang, P. A. S. Reed, Microstructure effects on high temperature fatigue crack initiation and short crack growth in turbine disc nickel-base superalloy Udimet 720Li, Materials Science and Engineering: A, 448 (2007) 67-79.
[10] S. Everitt, M. J. Starink, H. T. Pang, I. M. Wilcock, M. B. Henderson and P. A. S. Reed, A comparison of high temperature fatigue crack propagation in various subsolvus heat treated turbine disc alloys, Materials Science and Technology, 23 (2007) 1419-1423.
[11] P. A. S. Reed, Fatigue crack growth mechanisms in superalloys: overview, Materials Science and Technology, 25 (2009) 258-270.
[12] E. Andrieu, R. Molins, H. Ghonem, A. Pineau, Intergranular crack tip oxidation mechanism in a nickel-based superalloy, Materials Science and Engineering: A, 154 (1992) 21-28.
[13] R. Molins, G. Hochstetter, J. C. Chassaigne, E. Andrieu, Oxidation effects on the fatigue crack growth behaviour of alloy 718 at high temperature, Acta Materialia, 45 (1997) 663-674.
[14] C. K. Sudbrack, S. L. Draper, T. T. Gorman, J. Telesman, T. P. Gabb, D. R. Hull, Oxidation and the effects of high Temperature exposures on notched fatigue life of an advanced powder metallurgy disk superalloy, in: E.S. Huron, R. C. Reed, M. C. Hardy, M. J. Mills, R. E. Montero, P. D. Portella, J. Telesman, TMS superalloy 2012, Champion (PA), The Minerals, Metals & Materials Society (2012), 863-872.
[15] U. Krupp, W. M. Kane, C. Laird, C. J. McMahon, Brittle intergranular fracture of a Ni-base superalloy at high temperatures by dynamic embrittlement, Materials Science and Engineering: A, 387-389 (2004) 409-413.
[16] J. A. Pfaendtner, C. J. McMahon Jr, Oxygen-induced intergranular cracking of a Ni-base alloy at elevated temperatures—an example of dynamic embrittlement, Acta Materialia, 49 (2001) 3369-3377.
[17] H. S. Kitaguchi, H. Y. Li, H. E. Evans, R. G. Ding, I. P. Jones, G. Baxter, P. Bowen, Oxidation ahead of a crack tip in an advanced Ni-based superalloy, Acta Materialia, 61 (2013) 1968-1981.
[18] T. P. Gabb, J. Gayda, J. Telesman, A. Garg, The effects of heat treatment and microstructure variations on disk superalloy properties at high temperature, in: R. C Reed, K. A. Green, P. Caron, T. P. Gabb, M. G. Fahrmann, E. S. Huron, et al., editors, TMS superalloy 2008, Champion (PA), The Minerals, Metals & Materials Society (2008), 121-130.
[19] T. P. Gabb, J. Gayda, J. Telesman, Thermal and mechanical property characterization of the advanced disk alloy LSHR, NASA report NASA/TM-2005-213645 (2005).
[20] S. Semiatin, K. McClary, A. Rollett, C. Roberts, E. Payton, F. Zhang, T. Gabb, Microstructure evolution during supersolvus heat treatment of a powder metallurgy nickel-base superalloy, Metallurgical and Materials Transactions A, 43 (2012) 1649-1661.
[21] P. Veyssiere and G. Saada, Microscopy and plasticity of the L12 γ phase, Dislocations in Solids, 10 (1996) 253-441.
[22] http://www.grc.nasa.gov/WWW/StructuresMaterials/AdvMet/research/turbine_disks.html.
[23] J. Gayda, T. P. Gabb, P. T. Kantzos, Heat treatment devices and method of operation thereof to produce dual microstructure superalloy discs, US Patent, US6660110B1 (2003).
[24] D. Furrer, H. Fecht, Ni-based superalloys for turbine discs, Journal of the Minerals, Metals and Materials Society, 51 (1999) 14-17.

[25] Z. Zhong, Y. Gu, Y. Yuan, T. Yokokawa, H. Harada, On the low cycle fatigue behavior of a Ni-base superalloy containing high Co and Ti contents, Materials Science and Engineering: A, 552 (2012) 434-443.
[26] E. J. Pickering, H. Mathur, A. Bhowmik, O. M. D. M. Messé, J. S. Barnard, M. C. Hardy, R. Krakow, K. Loehnert, H. J. Stone, C. M. F. Rae, Grain-boundary precipitation in Allvac 718Plus, Acta Materialia, 60 (2012) 2757-2769.
[27] D. Crawford, G. Was, The Role of grain boundary misorientation in intergranular cracking of Ni-16Cr-9Fe in 360 °C argon and high-Purity water, Metallurgical Transactions A, 23 (1992) 1195-1206.
[28] G. Palumbo, E. Lehockey, P. Lin, Applications for grain boundary engineered materials, Journal of the Minerals, Metals and Materials Society, 50 (1998) 40-43.
[29] Y. Gao, R. Ritchie, M. Kumar, R. Nalla, High-cycle fatigue of nickel-based superalloy ME3 at ambient and elevated temperatures: Role of grain-boundary engineering, Metallurgical and Materials Transactions A, 36 (2005) 3325-3333.
[30] S. Yamaura, Y. Igarashi, S. Tsurekawa, T. Watanabe, Structure-dependent intergranular oxidation in Ni–Fe polycrystalline alloy, Acta Materialia, 47 (1999) 1163-1174.
[31] T. Watanabe, An approach to grain boundary design for strong and ductile polycrystals, Res Mechanica 11 (1984) 47-84.
[32] N. Souaï, N. Bozzolo, L. Nazé, Y. Chastel, R. Logé, About the possibility of grain boundary engineering via hot-working in a nickel-base superalloy, Scripta Materialia, 62 (2010) 851-854.
[33] U. Krupp, W. M. Kane, X. Liu, O. Dueber, C. Laird, C. J. McMahon Jr, The effect of grain-boundary-engineering-type processing on oxygen-induced cracking of IN718, Materials Science and Engineering: A, 349 (2003) 213-217.
[34] C. H. Radhakrishna, K. Prasad Rao, The formation and control of Laves phase in superalloy 718 welds, Journal of Materials Science, 32 (1997) 1977-1984.
[35] G. Lvov, V. Levit, M. Kaufman, Mechanism of primary MC carbide decomposition in Ni-base superalloys, Metallurgical and Materials Transactions A, 35 (2004) 1669-1679.
[36] J. Guedou, J. Lautridou, Y. Honnorat, N18, Powder metallurgy superalloy for disks: Development and applications, Journal of Materials Engineering and Performance, 2 (1993) 551-556.
[37] H. T. Pang, P. A. S. Reed, Effects of microstructure on room temperature fatigue crack initiation and short crack propagation in Udimet 720Li Ni-base superalloy, International Journal of Fatigue, 30 (2008) 2009-2020.
[38] J. Gayda, P. Kantzos, J. Miller, Quench crack behavior of nickel-base disk superalloys, Journal of Failure Analysis and Prevention, 3 (2003) 55-59.
[39] M. P. Jackson, R. C. Reed, Heat treatment of Udimet 720Li: the effect of microstructure on properties, Materials Science and Engineering: A, 259 (1999) 85-97.
[40] J. Telesman, T. P. Gabb, A. Garg, P. Bonacuse and J.Gayda, Effect of microstructure on time dependent fatigue crack growth behavior in a P/M turbine disk alloy, in: R. C Reed, K. A. Green, P. Caron, T. P. Gabb, M. G. Fahrmann, E. S. Huron, et al., editors, TMS superalloy 2008, Champion (PA), The Minerals, Metals & Materials Society (2008), 807-816.
[41] B. Reppich, Some new aspects concerning particle hardening mechanisms in γ' precipitating Ni-base alloys -I. Theoretical concept, Acta Metallurgica, 30 (1982) 87-94.
[42] B. Reppich, P. Schepp, G. Wehner, Some new aspects concerning particle hardening mechanisms in γ' precipitating nickel-base alloys - II. Experiments, Acta Metallurgica, 30 (1982) 95-104.
[43] J. Gayda, R. Miner, The effect of microstructure on 650 °C fatigue crack growth in P/M astroloy, Metallurgical and Materials Transactions A, 14 (1983) 2301-2308.
[44] T. Billot, P. Villechaise, M. Jouiad, J. Mendez, Creep-fatigue behavior at high temperature of a Udiemt 720 nickel-base superalloy, International Journal of Fatigue, 32 (2010) 824-829.
[45] W. Huther, B. Reppich, Interaction of dislocations with coherent, stress-free, ordered precipitates, Zeitschrift f¨ur Metallkunde, 69 (1978) 628 - 634.
[46] D. J. Crudden, A. Mottura, N. Warnken, B. Raeisinia, R. C. Reed, Modelling of the influence of alloy composition on flow stress in high-strength nickel-based superalloys, Acta Materialia, 75 (2014) 356-370.
[47] T. Kruml, E. Conforto, B. Lo Piccolo, D. Caillard, J. L. Martin, From dislocation cores to strength and work-hardening: a study of binary Ni3Al, Acta Materialia, 50 (2002) 5091-5101.
[48] D. M. Dimiduk, A. W. Thompson, J. C. Williams, The compositional dependence of antiphase-boundary energies and the mechanism of anomalous flow in Ni3 Al alloys, Philosophical Magazine A, 67 (1993) 675-698.
[49] T. Kruml, J. L. Martin, J. Bonneville, On the strengthening of Ni_3Al by hafnium additions, Philosophical Magazine A, 80 (2000) 1545-1566.
[50] B. A. Lerch, N. Jayaraman, S. D. Antolovich, A study of fatigue damage mechanisms in Waspaloy from 25 to 800°C, Materials Science and Engineering, 66 (1984) 151-166.
[51] V. S. Sarma, M. Sundararaman, K. A. Padmanabhan, Effect of γ′ size on room temperature low cycle fatigue behaviour of a nickel base superalloy, Materials Science and Technology, 14 (1998) 669-675.
[52] M. Valsan, D. Sastry, K. Rao, S. Mannan, Effect of strain rate on the high-temperature low-cycle fatigue

properties of a nimonic PE-16 superalloy, Metallurgical and Materials Transactions A, 25 (1994) 159-171.
[53] U. Krupp, Fatigue Crack Propagation in Metals and Alloys, Wiley VCH (2007).
[54] D. Locq, P. Caron, On some advanced nickel-based superalloys for disk applications, High Temperature Materials, (2011) 1-9.
[55] T. Garosshen, T. Tillman, G. McCarthy, Effects of B, C, and Zr on the structure and properties of a P/M nickel base superalloy, Metallurgical and Materials Transactions A, 18 (1987) 69-77.
[56] S. Floreen, J. Davidson, The effects of B and Zr on the creep and fatigue crack growth behavior of a Ni-base superalloy, Metallurgical and Materials Transactions A, 14 (1983) 895-901.
[57] M. H. Yoo, On the theory of anomalous yield behavior of Ni_3Al - Effect of elastic anisotropy, Scripta Metallurgica, 20 (1986) 915-920.
[58] B. H. Kear, H. G. F. Wilsdorf, Dislocation configurations in plastically deformed polycrystalline Cu_3Au alloys, Transactions of the Metallallurgical Society of AIME, 224 (1962) 382-386.
[59] A. E. Staton-Bevan, R. D. Rawlings, The deformation behaviour of single crystal Ni_3(Al, Ti), physica status solidi (a), 29 (1975) 613-622.
[60] S. Suresh, Fatigue of Materials, Cambridge University Press, (2004).
[61] H. Ghonem, T. Nicholas, A. Pineau, Elevated temperature fatigue crack growth in alloy 718-part I: effects of mechanical variables Fatigue & Fracture of Engineering Materials & Structures, 16 (1993) 565-576.
[62] H. Ghonem, D. Zheng, Depth of intergranular oxygen diffusion during environment-dependent fatigue crack growth in alloy 718, Materials Science and Engineering: A, 150 (1992) 151-160.
[63] http://www.ami.ac.uk/courses/topics/0124_seom/index.html.
[64] J. Schijve, Fatigue of Structures and Materials, Springer, (2009).
[65] O. H. Basquin, The exponential law of endurance tests, Proc. Annual Meeting ASTM, 10 (1919) 625.
[66] S. S. Manson, Behaviour of materials under conditions of thermal stress, NACA report 1170 (1954).
[67] L. E. Coffin, The Problem of Thermal Stress Fatigue in Austenitic Steels at Elevated Temperatures, Proc. Symposium on Effects of Cyclic Heating and Stressing on Metals at Elevated Temperatures, ASTM STP 165 (1954) 31.
[68] D. Taylor, J. F. Knott, Fatigue crack propagation behaviour of short cracks: the effect of microstructure, Fatigue & Fracture of Engineering Materials & Structures, 4 (1981) 147-155.
[69] F. M. Yang, X. F. Sun, H. R. Guan, Z. Q. Hu, On the low cycle fatigue deformation of K40S cobalt-base superalloy at elevated temperature, Materials Letters, 57 (2003) 2823-2828.
[70] K. Gopinath, A. K. Gogia, S. V. Kamat, R. Balamuralikrishnan, U. Ramamurty, Low cycle fatigue behaviour of a low interstitial Ni-base superalloy, Acta Materialia, 57 (2009) 3450-3459.
[71] L. Xiao, D. L. Chen, M. C. Chaturvedi, Cyclic deformation mechanisms of precipitation-hardened Inconel 718 superalloy, Materials Science and Engineering: A, 483-484 (2008) 369-372.
[72] S. Antolovich, S. Liu, R. Baur, Low cycle fatigue behavior of René 80 at elevated temperature, Metallurgical and Materials Transactions A, 12 (1981) 473-481.
[73] L. B. Antolovich SD, Cyclic deformation and fatigue in Ni-base alloys, in: Tien JK, Caufield T, editors. Superalloys, supercomposites, and superceramics. New York: Academic Press, (1989) 363-411.
[74] M. D. Sangid, The physics of fatigue crack initiation, International Journal of Fatigue, 57 (2013) 58-72.
[75] R. E. Stoltz, A. G. Pineau, Dislocation-precipitate interaction and cyclic stress-strain behavior of a γ′ strengthened superalloy, Materials Science and Engineering, 34 (1978) 275-284.
[76] R. Keller, W. Zielinski, W. W. Gerberich, On the onset of low-energy dislocation substructures in fatigue: Grain size effects, Materials Science and Engineering: A, 113 (1989) 267-280.
[77] D. Fournier, A. Pineau, Low cycle fatigue behavior of inconel 718 at 298 K and 823 K, Metallurgical Transction A, 8 (1977) 1095-1105.
[78] Y. Yuan, Y. F. Gu, T. Osada, Z. H. Zhong, T. Yokokawa, H. Harada, Deformation mechanisms in a new disc superalloy at low and intermediate temperatures, Scripta Materialia, 67 (2012) 137-140.
[79] Y. Yuan, Y. F. Gu, Z. H. Zhong, T. Yokokawa, H. Harada, Enhanced strength at intermediate temperatures in a Ni-base disk superalloy with high Co addition, Materials Science and Engineering: A, 556 (2012) 595-600.
[80] R. W. Hayes, W. C. Hayes, On the mechanism of delayed discontinuous plastic flow in an age-hardened nickel alloy, Acta Metallurgica, 30 (1982) 1295-1301.
[81] D. J. Lloyd, D. W. Chung, M. C. Chaturvedi, Serrated yielding in a super alloy (40Co-38Ni-17Cr-5Ti), Acta Metallurgica, 23 (1975) 93-100.
[82] B. Max, B. Viguier, E. Andrieu, J. Cloue, A Re-examination of the Portevin-Le Chatelier Effect in Alloy 718 in Connection with Oxidation-Assisted Intergranular Cracking, Metallurgical and Materials Transactions A, 45 (2014) 5431-5441.
[83] Z. Mei, C. Krenn, J. Morris, Initiation and growth of small fatigue cracks in a Ni-base superalloy, Metallurgical and Materials Transactions A, 26 (1995) 2063-2073.
[84] C. K. Sudbrack, S. L. Draper, T. T. Gorman, J. Telesman, T. P. Gabb, D. R. Hull, Oxidation and the effects of high temperature exposures on notched fatigue life of an advanced powder metallurgy disk superalloy, in:

Superalloys 2012, John Wiley & Sons, Inc., 2012, pp. 863-872.
[85] R. R. Stephens, L. Grabowski, D. W. Hoeppner, The effect of temperature on the behaviour of short fatigue cracks in Waspaloy using an in situ SEM fatigue apparatus, International Journal of Fatigue, 15 (1993) 273-282.
[86] J. Miao, T. M. Pollock, J. Wayne Jones, Crystallographic fatigue crack initiation in nickel-based superalloy René 88DT at elevated temperature, Acta Materialia, 57 (2009) 5964-5974.
[87] M. N. Menon, W. H. Reimann, Low-cycle fatigue-crack initiation study in René 95, Journal of Materials Science, 10 (1975) 1571-1581.
[88] J. Hyzak, I. Bernstein, The effect of defects on the fatigue crack initiation process in two P/M superalloys: part I: fatigue origins, Metallurgical and Materials Transactions A, 13 (1982) 33-43.
[89] J. Gayda, R. V. Miner, Fatigue crack initiation and propagation in several nickel-base superalloys at 650°C, International Journal of Fatigue, 5 (1983) 135-143.
[90] Bathias, There is no infinite fatigue life in metallic materials, Fatigue & Fracture of Engineering Materials & Structures, 22 (1999) 559-565.
[91] C. McMahon, L. Coffin, Mechanisms of damage and fracture in high-temperature, low-cycle fatigue of a cast nickel-based superalloy, Metallurgical and Materials Transactions B, 1 (1970) 3443-3450.
[92] R. Jiang, S. Everitt, N. Gao, K. Soady, J. W. Brooks, P. A. S. Reed, Influence of oxidation on fatigue crack initiation and propagation in turbine disc alloy N18, International Journal of Fatigue, 75 (2015) 89-99.
[93] P. Lukas, Fatigue Crack Nucleation and Microstructure, ASM Handbook: Fatigue and Fracture, 19 (1996) 96.
[94] M. Bao-Tong, C. Laird, Overview of fatigue behavior in copper single crystals - I. Surface morphology and stage I crack initiation sites for tests at constant strain amplitude, Acta Metallurgica, 37 (1989) 325-336.
[95] Z. S. Basinski, R. Pascual, S. J. Basinski, Low amplitude fatigue of copper single crystals - I. The role of the surface in fatigue failure, Acta Metallurgica, 31 (1983) 591-602.
[96] J. Polák, J. Man, T. Vystavěl, M. Petrenec, The shape of extrusions and intrusions and initiation of stage I fatigue cracks, Materials Science and Engineering: A, 517 (2009) 204-211.
[97] C. Laird, J. M. Finney, D. Kuhlmann-Wilsdorf, Dislocation behavior in fatigue VI: Variation in the localization of strain in persistent slip bands, Materials Science and Engineering, 50 (1981) 127-136.
[98] R. W. Cahn, P. Haasen, Physical Metallurgy, Cambridge University Press (1996).
[99] D. G. Brandon, The structure of high-angle grain boundaries, Acta Metallurgica, 14 (1966) 1479-1484.
[100] Z. F. Zhang, Z. G. Wang, Comparison of fatigue cracking possibility along large- and low-angle grain boundaries, Materials Science and Engineering: A, 284 (2000) 285-291.
[101] Z. F. Zhang, Z. G. Wang, Dependence of intergranular fatigue cracking on the interactions of persistent slip bands with grain boundaries, Acta Materialia, 51 (2003) 347-364.
[102] W. H. Kim, C. Laird, Crack nucleation and stage I propagation in high strain fatigue - I. Microscopic and interferometric observations, Acta Metallurgica, 26 (1978) 777-787.
[103] W. H. Kim, C. Laird, Crack nucleation and stage I propagation in high strain fatigue - II. mechanism, Acta Metallurgica, 26 (1978) 789-799.
[104] P. Peralta, C. Laird, Compatibility stresses in fatigued bicrystals: Dependence on misorientation and small plastic deformations, Acta Materialia, 45 (1997) 5129-5143.
[105] Z. F. Zhang, Z. G. Wang, Fatigue-cracking characteristics of a copper bicrystal when slip bands transfer through the grain boundary, Materials Science and Engineering: A, 343 (2003) 308-313.
[106] N. Birks, G. H. Meier, F. S. Pettit, Introduction to the High Temperature Oxidation of Metals, Cambridge University Press, 2nd edition (2009).
[107] D. Young, High Temperature Oxidation and Corrosion of Metals, Elsevier Science (2008).
[108] L. L. Li, P. Zhang, Z. J. Zhang, H. F. Zhou, S. X. Qu, J. B. Yang, Z. F. Zhang, Strain localization and fatigue cracking behaviors of Cu bicrystal with an inclined twin boundary, Acta Materialia, 73 (2014) 167-176.
[109] J. Miao, T. M. Pollock, J. Wayne Jones, Microstructural extremes and the transition from fatigue crack initiation to small crack growth in a polycrystalline nickel-base superalloy, Acta Materialia, 60 (2012) 2840-2854.
[110] S. Qu, P. Zhang, S. D. Wu, Q. S. Zang, Z. F. Zhang, Twin boundaries: Strong or weak?, Scripta Materialia, 59 (2008) 1131-1134.
[111] P. Zhang, Z. J. Zhang, L. L. Li, Z. F. Zhang, Twin boundary: Stronger or weaker interface to resist fatigue cracking?, Scripta Materialia, 66 (2012) 854-859.
[112] Y. Gao, J. S. Stölken, M. Kumar, R. O. Ritchie, High-cycle fatigue of nickel-base superalloy René 104 (ME3): Interaction of microstructurally small cracks with grain boundaries of known character, Acta Materialia, 55 (2007) 3155-3167.
[113] T. Connolley, Initiation and growth of short cracks in U-notched bend specimens of superalloy in In718 during high temperature low cycle fatigue, P hD Dissertation, University of Southampton, (2001).
[114] T. Zhai, A. J. Wilkinson, J. W. Martin, A crystallographic mechanism for fatigue crack propagation through grain boundaries, Acta Materialia, 48 (2000) 4917-4927.

[115] M. Marx, W. Schaef, H. Vehoff, Interaction of short cracks with the local microstructure, Procedia Engineering, 2 (2010) 163-171.
[116] W. Schaef, M. Marx, H. Vehoff, A. Heckl, P. Randelzhofer, A 3-D view on the mechanisms of short fatigue cracks interacting with grain boundaries, Acta Materialia, 59 (2011) 1849-1861.
[117] W. Schaef, M. Marx, A numerical description of short fatigue cracks interacting with grain boundaries, Acta Materialia, 60 (2012) 2425-2436.
[118] W. Z. Abuzaid, M. D. Sangid, J. D. Carroll, H. Sehitoglu, J. Lambros, Slip transfer and plastic strain accumulation across grain boundaries in Hastelloy X, Journal of the Mechanics and Physics of Solids, 60 (2012) 1201-1220.
[119] A. Karabela, L. G. Zhao, B. Lin, J. Tong, M. C. Hardy, Oxygen diffusion and crack growth for a nickel-based superalloy under fatigue-oxidation conditions, Materials Science and Engineering: A, 567 (2013) 46-57.
[120] B. Lin, L. G. Zhao, J. Tong, H. J. Christ, Crystal plasticity modeling of cyclic deformation for a polycrystalline nickel-based superalloy at high temperature, Materials Science and Engineering: A, 527 (2010) 3581-3587.
[121] Z. J. Zhang, P. Zhang, L. L. Li, Z. F. Zhang, Fatigue cracking at twin boundaries: Effects of crystallographic orientation and stacking fault energy, Acta Materialia, 60 (2012) 3113-3127.
[122] J. Li, S. J. Dillon, G. S. Rohrer, Relative grain boundary area and energy distributions in nickel, Acta Materialia, 57 (2009) 4304-4311.
[123] D. L. Olmsted, S. M. Foiles, E. A. Holm, Survey of computed grain boundary properties in face-centered cubic metals: I. Grain boundary energy, Acta Materialia, 57 (2009) 3694-3703.
[124] C. Holzapfel, W. Schäf, M. Marx, H. Vehoff, F. Mücklich, Interaction of cracks with precipitates and grain boundaries: Understanding crack growth mechanisms through focused ion beam tomography, Scripta Materialia, 56 (2007) 697-700.
[125] B. Stokes, N. Gao, P. A. S. Reed, Effects of graphite nodules on crack growth behaviour of austempered ductile iron, Materials Science and Engineering: A, 445 - 446 (2007) 374-385.
[126] B. Stokes, N. Gao, P. A. S. Reed, K. K. Lee, Effects of carbides on fatigue characteristics of austempered ductile iron, Metallurgical and Materials Transactions A, 36 (2005) 977-988.
[127] W. Elber, Fatigue crack closure under cyclic tension, Engineering Fracture Mechanics, 2 (1970) 37-45.
[128] P. K. Liaw, Overview of Crack Closure at near-Threshold Fatigue Crack Growth Levels, Proc. Mechanics of Fatigue Crack Closure, ASTM STP 982 (1988) 62.
[129] H. T. Pang, P. A. S. Reed, Microstructure variation effects on room temperature fatigue threshold and crack propagation in Udimet 720Li Ni-base superalloy, Fatigue & Fracture of Engineering Materials & Structures, 32 (2009) 685-701.
[130] D. Krueger, S. Antolovich, R. Stone, Effects of grain size and precipitate size on the fatigue crack growth behavior of alloy 718 at 427 °C, Metallurgical and Materials Transactions A, 18 (1987) 1431-1449.
[131] S. A. Padula Ii, A. Shyam, R. O. Ritchie, W. W. Milligan, High frequency fatigue crack propagation behavior of a nickel-base turbine disk alloy, International Journal of Fatigue, 21 (1999) 725-731.
[132] J. Wasén, E. Heier, Fatigue crack growth thresholds—the influence of Young's modulus and fracture surface roughness, International Journal of Fatigue, 20 (1998) 737-742.
[133] G. Gray, J. Williams, A. Thompson, Roughness-Induced Crack Closure: An Explanation for Microstructurally Sensitive Fatigue Crack Growth, Metallurgical and Materials Transactions A, 14 (1983) 421-433.
[134] S. F. Toh, W. M. Rainforth, Fatigue of a nickel base superalloy with bimodal grain size, Materials Science and Technology, 12 (1996) 1007-1014.
[135] M. R. Winstone, K. M. Nikbin, G. A. Webster, Modes of failure under creep/fatigue loading of a nickel-based superalloy, Journal of Materials Science, 20 (1985) 2471-2476.
[136] H. Yang, R. Bao, J. Zhang, L. Peng, B. Fei, Creep-fatigue crack growth behaviour of a nickel-based powder metallurgy superalloy under high temperature, Engineering Failure Analysis, 18 (2011) 1058-1066.
[137] T. P. Gabb, J. Gayda, J. Telesman, L. J. Ghosn, A. Garg, Factors influencing dwell fatigue life in notches of a powder metallurgy superalloy, International Journal of Fatigue, 48 (2013) 55-67.
[138] J. P. Pédron, A. Pineau, The effect of microstructure and environment on the crack growth behaviour of Inconel 718 alloy at 650 °C under fatigue, creep and combined loading, Materials Science and Engineering, 56 (1982) 143-156.
[139] H. S. Kitaguchi, M. P. Moody, H. Y. Li, H. E. Evans, M. C. Hardy, S. Lozano-Perez, An atom probe tomography study of the oxide–metal interface of an oxide intrusion ahead of a crack in a polycrystalline Ni-based superalloy, Scripta Materialia, 97 (2015) 41-44.
[140] L. Viskari, M. Hörnqvist, K. L. Moore, Y. Cao, K. Stiller, Intergranular crack tip oxidation in a Ni-base superalloy, Acta Materialia, 61 (2013) 3630-3639.
[141] M. Hörnqvist, L. Viskari, K. L. Moore, K. Stiller, High-temperature crack growth in a Ni-base superalloy during sustained load, Materials Science and Engineering: A, 609 (2014) 131-140.

[142] A. Karabela, L. G. Zhao, J. Tong, N. J. Simms, J. R. Nicholls, M. C. Hardy, Effects of cyclic stress and temperature on oxidation damage of a nickel-based superalloy, Materials Science and Engineering: A, 528 (2011) 6194-6202.
[143] B. J. Foss, M. C. Hardy, D. J. Child, D. S. McPhail, B. A. Shollock, Oxidation of a commercial nickel-based superalloy under static loading, The Journal of The Minerals, Metals & Materials Society, 66 (2014) 2516-2524.
[144] L. Viskari, S. Johansson, K. Stiller, Oxygen influenced intergranular crack propagation: analysing microstructure and chemistry in the crack tip region, Materials at High Temperatures, 28 (2011) 336-341.
[145] B. R. Barnard, P. K. Liaw, R. A. Buchanan, D. L. Klarstrom, Affects of applied stresses on the isothermal and cyclic high-temperature oxidation behavior of superalloys, Materials Science and Engineering: A, 527 (2010) 3813-3821.
[146] D. A. Woodford, Gas phase embrittlement and time dependent cracking of nickel based superalloys, Energy Materials: Materials Science and Engineering for Energy Systems, 1 (2006) 59-79.
[147] C. T. Liu, C. L. White, Dynamic embrittlement of boron-doped Ni_3Al alloys at 600°C, Acta Metallurgica, 35 (1987) 643-649.
[148] D. Bika, C. J. McMahon Jr, A model for dynamic embrittlement, Acta Metallurgica et Materialia, 43 (1995) 1909-1916.
[149] P. A. S. Reed, W. F. Gale, J. E. King, Intrinsic thresholds in polycrystalline Udimet 720, Materials Science and Technology, 9 (1993) 281-287.
[150] J. E. King, R. A. Venables, M. A. Hicks, The effects of microstructure, temperature and R-ratio on fatigue crack propagation and threshold behaviour in two Ni-base alloys, Proceedings of the 6th Int. Conf. on Fracture, (1984) 2081-2089.
[151] A. K. Vasudeven, K. Sadananda, N. Louat, A review of crack closure, fatigue crack threshold and related phenomena, Materials Science and Engineering: A, 188 (1994) 1-22.
[152] J. Tong, S. Dalby, J. Byrne, Crack growth in a new nickel-based superalloy at elevated temperature, Journal of Materials Science, 40 (2005) 1237-1243.
[153] S. Dalby, J. Tong, Crack growth in a new nickel-based superalloy at elevated temperature, Journal of Materials Science, 40 (2005) 1217-1228.
[154] J. Tong, J. Byrne, Effects of frequency on fatigue crack growth at elevated temperature, Fatigue & Fracture of Engineering Materials & Structures, 22 (1999) 185-193.
[155] T. P. Gabb, R. A. Mackay, S. L. Draper, C. K. Sudbrack, M. V. Nathal, The mechanical properties of candidate superalloys for a hybrid turbine disk, NASA/TM—2013-217901, (2013).
[156] J.Gayday, T. P. Gabb, Fatigue Behavior of a Third Generation PM Disk Superalloy, NASA/TM—2008-215462, (2008).
[157] W. Ramberg, W. R. Osgood, Description of stress–strain curves by three parameters, NACA Technical Note No. 902 (1943).
[158] H. T. Pang, Effect of microstructure variation on turbine disc fatigue life, PhD Dissertation, University of Southampton (2003).
[159] J. Telesman, P. Kantzos, J. Gayda, P. Bonacuse, A. Prescenzi, Microstructural variables controlling time-dependent crack growth in a P/M superalloy, in: K. A. Green, H. Harada, T. E. Howson, T. M. Pollock, R. C. Reed, J. J. Schirra, et al., editors, TMS superalloy 2004, Warrendale (PA): The Minerals, Metals & Materials Society (2004), 215-224.
[160] M. Goto, D. M. Knowles, Initiation and propagation behaviour of microcracks in Ni-base superalloy Udimet 720 Li, Engineering Fracture Mechanics, 60 (1998) 1-18.
[161] P. M. Scott, T. W. Thorpe, A critical review of crack tip stress intensity factors for semi-elliptic cracks, Fatigue & Fracture of Engineering Materials & Structures, 4 (1981) 291-309.
[162] P. Villechaise, L. Sabatier, J. C. Girard, On slip band features and crack initiation in fatigued 316L austenitic stainless steel: Part 1: Analysis by electron back-scattered diffraction and atomic force microscopy, Materials Science and Engineering: A, 323 (2002) 377-385.
[163] S. Suresh, Fatigue crack deflection and fracture surface contact: Micromechanical models, Metallurgical and Materials Transactions A, 16 (1985) 249-260.
[164] T. Zhai, X. P. Jiang, J. X. Li, M. D. Garratt, G. H. Bray, The grain boundary geometry for optimum resistance to growth of short fatigue cracks in high strength Al-alloys, International Journal of Fatigue, 27 (2005) 1202-1209.
[165] T. L. Anderson, Fracture mechanics – fundamentals and applications, CRC press (1994).
[166] L. Ma, K.-M. Chang, Identification of SAGBO-induced damage zone ahead of crack tip to characterize sustained loading crack growth in alloy 783, Scripta Materialia, 48 (2003) 1271-1276.
[167] C. F. Miller, G. W. Simmons, R. P. Wei, Evidence for internal oxidation during oxygen enhanced crack growth in P/M Ni-based superalloys, Scripta Materialia, 48 (2003) 103-108.
[168] U. Krupp, Improving the resistance to intergranular cracking and corrosion at elevated temperatures by

grain-boundary-engineering-type processing, Journal of Materials Science, 43 (2008) 3908-3916.
[169] J. H. Chen, P. M. Rogers, J. A. Little, Oxidation behavior of several chromia-forming commercial nickel-base superalloys, Oxid Met, 47 (1997) 381-410.
[170] J. Telesman, T. P. Gabb, Y. Yamada, L. J. Ghosn, D. Hornbach, N. Jayaraman, Dwell notch low cycle fatigue behavior of a powder metallurgy nickel disk alloy, in: E.S. Huron, R. C. Reed, M. C. Hardy, M. J. Mills, R. E. Montero, P. D. Portella, J. Telesman, TMS superalloy 2012, Champion (PA), The Minerals, Metals & Materials Society (2012), 853-862.
[171] H. Ghonem, T. Nicholas, A. Pineau, Elevated temperature fatigue crack growth in alloy 718 - part II: Effects of environmental and materials variables, Fatigue & Fracture of Engineering Materials & Structures, 16 (1993) 577-590.
[172] S. Cruchley, H. E. Evans, M. P. Taylor, M. C. Hardy, S. Stekovic, Chromia layer growth on a Ni-based superalloy: Sub-parabolic kinetics and the role of titanium, Corrosion Science, 75 (2013) 58-66.
[173] A. Encinas-Oropesa, G. I. Drew, M. C. Hardy, A. J. Leggett, J. R. Nicholls, N. J. Simms, Effects of oxidation and hot corrosion in a nickel disc alloy, in: R. C Reed, K. A. Green, P. Caron, T. P. Gabb, M. G. Fahrmann, E. S. Huron, et al., editors, TMS superalloy 2008, Champion (PA), The Minerals, Metals & Materials Society (2008) 609-618.
[174] A. Sato, Y. L. Chiu, R. C. Reed, Oxidation of nickel-based single-crystal superalloys for industrial gas turbine applications, Acta Materialia, 59 (2011) 225-240.
[175] H. Ghonem, D. Zheng, Oxidation-assisted fatigue crack growth behaviour in alloy 718-part I. quantitative modelling, Fatigue & Fracture of Engineering Materials & Structures, 14 (1991) 749-760.
[176] L. Viskari, Y. Cao, M. Norell, G. Sjöberg, K. Stiller, Grain boundary microstructure and fatigue crack growth in Allvac 718Plus superalloy, Materials Science and Engineering: A, 528 (2011) 2570-2580.
[177] M. Lewandowski, MSc Dissertation, University of Sputhampton (2011).
[178] Alicona, MEX5.1 Manual, (2008) 72.
[179] T. Yokobori, Fatigue Mechanisms, ASTM STP 675, (1979) 683-706.
[180] H. Yang, R. Bao, J. Zhang, L. Peng, B. Fei, Crack growth behaviour of a nickel-based powder metallurgy superalloy under elevated temperature, International Journal of Fatigue, 33 (2011) 632-641.
[181] S. Everitt, R. Jiang, N. Gao, M. J. Starink, J. W. Brooks and P. A. S. Reed, Comparison of fatigue crack propagation behaviour in two gas turbine disc alloys under creep–fatigue conditions: evaluating microstructure, environment and temperature effects, Materials Science and Technology, 29 (2013) 781-787.
[182] L. G. Zhao, J. Tong, M. C. Hardy, Prediction of crack growth in a nickel-based superalloy under fatigue-oxidation conditions, Engineering Fracture Mechanics, 77 (2010) 925-938.
[183] A. Shyam, W. W. Milligan, Effects of deformation behavior on fatigue fracture surface morphology in a nickel-base superalloy, Acta Materialia, 52 (2004) 1503-1513.
[184] F. V. Antunes, A. Ramalho, J. M. Ferreira, Identification of fatigue crack propagation modes by means of roughness measurements, International Journal of Fatigue, 22 (2000) 781-788.
[185] M. J. Starink, P. A. S. Reed, Thermal activation of fatigue crack growth: Analysing the mechanisms of fatigue crack propagation in superalloys, Materials Science and Engineering: A, 491 (2008) 279-289.
[186] M. Kamaya, A. J. Wilkinson, J. M. Titchmarsh, Quantification of plastic strain of stainless steel and nickel alloy by electron backscatter diffraction, Acta Materialia, 54 (2006) 539-548.
[187] A. J. Wilkinson, G. Meaden, D. J. Dingley, High resolution mapping of strains and rotations using electron backscatter diffraction, Materials Science and Technology, 22 (2006) 1271-1278.
[188] A. J. Wilkinson, G. Meaden, D. J. Dingley, High-resolution elastic strain measurement from electron backscatter diffraction patterns: New levels of sensitivity, Ultramicroscopy, 106 (2006) 307-313.
[189] S. J. Holdbrook, W. D. Dover, The stress intensity factor for a deep surface crack in a finite plate, Engineering Fracture Mechanics, 12 (1979) 347-364.